Investigation of HfO2-based resistive RAM cells by electrical characterization and atomistic simulations

Boubacar Traore

UNIVERSITÉ DE GRENOBLE

THÈSE

Pour obtenir le grade de

DOCTEUR DE L'UNIVERSITÉ DE GRENOBLE

Spécialité : **Nano-Electronique et Nano-Technologies**

Arrêté ministériel : 7 août 2006

Présentée par

Boubacar TRAORÉ

Thèse dirigée par **Dr. Barbara DE SALVO** et
codirigé par **Prof. Yoshio Nishi**

préparée au sein du **Laboratoire composants mémoires au CEA-LETI**

dans **l'École Doctorale EEATS de l'INP Grenoble**

Etude de cellules mémoires résistives RRAM à base de HfO_2 par caractérisation électrique et simulations atomistiques

Thèse soutenue publiquement le **27 Avril 2015**,
devant le jury composé de :

M. Kenji SHIRAISHI
Professeur, Nagoya University (Japon), Rapporteur
M. Salvatore LOMBARDO
Directeur de Recherche au CNR-IMM (Italie), Rapporteur
M. Gérard GHIBAUDO
Directeur de Recherche au CNRS (IMEP-LAHC, Grenoble), Président
M. Damien DELERUYELLE
Maître de conférences, Aix-Marseille Université (Marseille), Examinateur
M. Philippe BOIVIN
Program manager, STMicroelectronics (Rousset), Examinateur
Mme Elisa VIANELLO
Docteur ingénieur de recherche, CEA-LETI (Grenoble), Encadrante
M. Philippe BLAISE
Docteur ingénieur de recherche, CEA-LETI (Grenoble), invité
M. Yoshio NISHI
Professeur, Stanford University (Californie, Etats-Unis), invité
Mme Barbara DE SALVO
Docteur ingénieur de recherche, CEA-LETI (Grenoble), invitée

ABSTRACT

Investigation of HfO_2-based Resistive RAM cells by electrical characterization and atomistic simulations

A large number of application opportunities have opened up for semiconductor memory technologies. Among these technologies, non-volatile NAND Flash memory represents a significant portion in the IC market and has benefitted from the traditional scaling of semi-conductor industry allowing its high density integration for mass market production. However, this scaling limit seems to be approached and there seems to be serious problems beyond the 22 nm node. In an effort to go beyond this scaling limitation, alternative memory solutions are proposed among which Resistive RAM (RRAM) stands out as a serious candidate for NAND Flash replacement. Hence, in this PhD thesis we try to respond to many open questions about RRAM devices based on hafnium oxide (HfO_2), in particular, by addressing the lack of detailed physical comprehension about their operation and reliability. A strong point of semiconductor industry being the continuous scaling of devices and as such the scalability of RRAM through either the reduction of the oxide thickness, the reduction of the device active area or the reduction of the electrode thickness are addressed in this work. The impact of the electrode material on RRAM performance is also studied with a comprehensive analysis of the interface Ti/HfO_2. The process of defect formation and diffusion which are crucial in RRAM operation is also investigated with the aim of gaining more understanding on RRAM switching mechanisms. Special attention is also given to the impact of alloying HfO_2 with other materials for improved RRAM performance and in-depth understanding about the microscopic behavior of data retention is also provided. Finally, one of the main limiting factors of RRAM being the missing unified picture about their operation, our study attempts to give some results based on theoretical calculations about the different switching processes with an emphasis on the conductive filament formation and its possible composition.

RÉSUMÉ

Etude de cellules mémoires résistives RRAM à base de HfO_2 par caractérisation électrique et simulations atomistiques

Avec la prolifération et l'émergence des nouveaux produits électroniques à travers les tablettes, smart phones et autres, des nouvelles opportunités d'applications sont ouvertes pour les technologies mémoires. Parmi ces technologies, la mémoire NAND Flash représente une part importante dans le marché des circuits intégrés et a bénéficié de la traditionnelle miniaturisation de l'industrie des sémiconducteurs lui permettant un niveau d'intégration élevé idéale pour la production de masse. Toutefois, cette miniaturisation semble approcher ses limites physiques et il semble y avoir des sérieux problèmes au-delà du nœud 22 nm. Dans un souci de dépasser cette limite, des solutions mémoires alternatives sont proposées parmi lesquelles la mémoire résistive (RRAM) se pose comme un sérieux candidat pour le remplacement de NAND Flash. Ainsi, dans cette thèse nous essayons de répondre à des nombreuses questions ouvertes sur les dispositifs RRAM à base d'oxyde d'hafnium (HfO_2) en particulier en adressant le manque de compréhension physique détaillée sur leur fonctionnement et leur fiabilité. Un point fort de l'industrie des sémiconducteurs étant la miniaturisation continue des technologies mémoires, et en tant que telle la réduction des tailles de RRAM soit par la réduction de l'épaisseur de l'oxyde, la réduction de la surface active des dispositifs ou la réduction de l'épaisseur de l'électrode sont abordés dans ce travail. L'impact du choix des électrodes sur la performance des RRAM est aussi étudié avec une analyse plus détaillée de l'interface Ti/HfO_2. Le processus de formation des défauts et leur diffusion, deux phénomènes cruciaux dans le fonctionnement des RRAM, est également étudié. Une attention particulière est accordée à l'impact de l'alliage de HfO_2 avec d'autres matériaux pour l'optimisation des performances des RRAM et une étude approfondie sur le comportement microscopique de la rétention des données est aussi fournie. Enfin, l'un des facteurs limitants des RRAM étant l'image unifiée manquante sur leur fonctionnement, notre étude tente de donner quelques réponses basées sur des calculs théoriques sur les différents processus de commutation avec un accent sur la formation du filament conducteur et sa possible composition.

ACKNOWLEDGMENT

"Let us be grateful to people who make us happy; they are the charming gardeners who make our souls blossom", Marcel Proust (1871 – 1922)

"A person who neglects a small gesture is not worthy of a big gesture", Bambara proverb

It happens that only one name appears as the author of this manuscript. However, I can assure that many people coming from different scientific backgrounds and disciplines took part in the project. And, I would like to, in this part, address my sincere thanks and gratitude to everyone that was directly or indirectly involved in this work carried out at CEA-Leti.

First of all, I would like to thank my thesis directors namely prof. Yoshio Nishi and Dr. Barbara De Salvo for their guidance, trust and wisdom throughout my thesis. Despite, sometimes, the long distance that separated us, they remained active and involved in directing the research in a more productive and useful manner. I learned a lot from their wisdom and was impressed by their calmness and understanding. I must say I was fortunate enough to be under their guidance!

Without her energy, commitment, pro-activeness and dedication, this thesis would not have been as it is. I am surely talking about my supervisor Dr. Elisa Vianello. From the start to the end, she was as involved in the thesis as myself and was always searching for new ways, methods, and directions in order to progress as much as we could in the research. I would like to thank her for her supervision, support and for this great moment of research that we spent together. Grazie Elisa!

Sometimes, life brings its lot of surprise and things that we did not expect. When I started my thesis, I never imagined that along the way I would be working with a special person almost on a daily basis for more than 1 year of my thesis. Here, I am certainly talking about Dr. Philippe Blaise. He taught me everything that I needed to know about what happened to be one of the cores of my thesis work: Density Functional Theory (DFT). I never imagined before coming to CEA-Leti that I would be doing so much work based on DFT. I learned a lot from his research method and what is

expected from a good research. In addition to the scientific discussions and exchange that would last for hours in his office or elsewhere, I also enjoyed being with him because at personal level he was a very good person. I will surely miss these discussions and brainstorming and will always remain as special moments in my memory. Merci Philippe!

My thanks also go to all the memory component laboratory personnel. The environment was soothing and conducive for good interpersonal relationship. I would like to thank the head of the laboratory Dr. Luca Perniola for his availability and will to progress research in the memory field. My thanks also go to Dr. Eric Jalaguier, whom I call “camarade”, for his support, good humor, reviews of my papers and availability throughout my thesis. I also thank Dr. Gabriel Molas for his open mind and help. My thanks also go to Gabriele Navarro, Véronique Sousa, Christelle Charpin, Sophie Bernasconi, Alain Persico, Carine Jahan, Jean-François Nodin, Rémy Coquand, Etienne Nowak, Laurent Grénouillet, Cathérine Carabasse. It is possible that I forgot some names, if so I do apologize for that. I would like to also thank Marc Gely who was very involved in the fabrication of the first RRAM devices that I tested at the beginning of my thesis. Despite him being moved to another laboratory of CEA, I would like to address him my thanks. I also thank François Triozon, Benoit Sklenard, and Olga Cueto from the modeling and simulation laboratory.

I would like to thank the personal secretaries of the lab namely Sabine Révol and Brigitte Gaillard for their availability to solve our administrative stuff. It is surely a very difficult task but they were always smiling and ready to help in any way. I really thank them for their good humors and jokes.

I would like to thank K.-H. Xue, the former post-doc student of the project, for the first one year and half that we worked together during my thesis. It was a real pleasure working with him. I also thank L.R.C. Fonseca, from State University of Campinas, for fruitful discussion and exchange. My thanks also go to STMicroelectronics for providing some of the devices that I tested during my PhD work.

Having spent 3 years of thesis, the exchange with current or former PhD students was very important. Among those who have finished their thesis, I would like to thank Thomas Cabout, Manan Suri, Giorgio Palma, Florian Longnos, Quentin Hubert, Julien Philippe, Sara Souiki, Thérèse Diokh, Tsanka Todorva and Murielle Lontsi Fomena for the good moment we have spent together. Among those who are currently doing their thesis, my thanks go to Giuseppe Piccolboni, Mouhamad Alayan, Amine El Kacimi, Marinela Barci, Athanasios Kiouseloglou, Mourad Azzaz, Issam Ouerghi, Jérémy Guy, Adam Dobri, Martin Coue, Daniele Garbin, Thilo Werner and everyone else. I wish them courage and success in their respective works.

Material characterization being an important part in the research on nano-devices, I would like to thank Helen Grampeix, Aurore Bonnevialle, Denis Jalabert, François Pierre for their help and fruitful discussions with regards to phyisico-chemical experiments. I also thank Jacques Cluzel, Alain Lopez, Giovanni Romano, Rabah Kies, Alain Toffoli and Denis Blachier from the test and electrical characterization laboratory.

My thanks also go Prof. Nishi's group at Stanford University. I would like to thank Blanka Magyari-Kope for her support and ideas during the research. Special thanks go to Liang Zhao for all the discussions and electrical characterization experiments that we carried out at Stanford during my stay over there. I would also like to thank the other PhD students: Aryan Hazeghi, Asad Kalantarian who recently graduated, Dan Duncan and HyeRyoung Lee.

I would like to address special thanks to the former scientific director of CEA-LETI, Dr. Simon Deleonibus who was recently retired. I am thankful to all his support and help throughout my thesis. I wish him all the best for this new phase of his life.

I would like to thank the Nanosciences foundation for their financial support of this project and their aim to make Grenoble a center of excellence with new challenging and exciting research topics via the funding of the different chairs of Excellence. I would like to thank its director Alain Fontaine and its entire personnel starting from Marie-Anne Carré, Stéphanie Monfront, Fériel Kouiten to Alix Guillaume.

I am sure that I have met so many other people during my thesis whom I probably did not mention their names but helped directly or indirectly for the project to come to its end. I address them my sincere apologies and thank them for their contribution.

Finally, I would like to thank my family in both Bamako (Mali) and France for their moral support, advice and help to remain strong both mentally and spiritually. Their open mind, sympathy/kindness towards the other and understanding of life surely helped me be the person I am. I would like to address them my sincere gratitude for everything.

Boubacar Traoré

CONTENTS

Introduction

This thesis has been carried on within the framework of the Professor Nishi Chair of Excellence Project supported by the Nanosciences Foundation. The project aimed to bring an important contribution to resistive memory technology physical understanding. To this regard, in this PhD thesis, we will try to respond to many open questions about Resistive RAM (RRAM) devices based on hafnium oxide (HfO_2), in particular, by addressing the lack of detailed physical comprehension about their operation and reliability. As will be detail later, HfO_2 based RRAM devices have shown promising features but still need to be further studied for a comprehensive understanding of the key parameters and issues in their operation.

In Chapter 1 we will give a general overview of non-volatile memory technologies and their market status. The different technologies will be briefly discussed and compared in terms of their strengths and areas for improvement. The chapter comprehensively reviews HfO_2-based RRAMs from materials point of view to their performance and challenges especially with regards to the physical mechanisms behind their operation and the current understanding about them.

For RRAM to be solid a competitor for NAND flash replacement or an element to be used in non Von-Neumann like computing approach such as Neuromorphic computing, the scalability of RRAM need to be fully addressed from different perspectives. In this regard, the scalability of the memory cells can be achieved through either the reduction of the oxide thickness, the reduction of the device active area or the reduction of the electrode thickness. Each type of scaling may have its specific impact on RRAM performance and it is therefore important to look at the different possibilities. Hence, scaling of RRAM will be discussed in Chapter 2.

Since the properties of the switching modes are independent of the oxide material but rather dependent on a combination of both the oxide and the oxide/electrode interface; a comprehensive understanding of the impact of the electrode material will be required for the optimization of the technology. Therefore, Chapter 3 will discuss the effects of electrode material on RRAM performance especially from reliability perspectives (thermal stability and switching variability). A comprehensive

analysis on the HfO_2/Ti interface is performed. The process of defect formation and diffusion which are crucial in RRAM operation is also investigated with the aim of gaining more understanding on RRAM switching mechanisms.

Chapter 4 is devoted to the impact of alloying HfO_2 with other materials for improved performance. The alloying materials of concern are Al_2O_3 and TiO_2. The study provides in-depth understanding about the microscopic behavior of data retention in HfO_2 RRAM devices and the role of the added materials on it.

One of the main limiting factors of RRAM being the missing unified picture about the mechanisms of the resistive switching, Chapter 5 attempts to give some results based on theoretical calculations about the different switching processes with an emphasis on the forming operation. An in-depth theoretical study is provided on the probable composition of CF along with its stability from thermodynamics view. SET and RESET processes are also viewed superficially but with the aim of providing a consistent microscopic picture about RRAM operation.

This manuscript will conclude with a section named “Conclusions and Perspectives” which will synthetize main results as well as give directions for future works.

Chapter I

The memory landscape and RRAM technologies

This chapter provides a general overview of non-volatile memory technologies and their market status. The different technologies are briefly discussed and compared in terms of their strengths and areas for improvement. More focus is given to binary metal oxide resistive random access memories (RRAMs) with an emphasis on HfO_2 as the oxide layer. The chapter comprehensively reviews RRAMs from materials point of view to their performance and challenges especially with regards to the physical mechanisms behind their operation and the current understanding about them.

I.1 IC and memory market

Technology has never been so present and influential on our daily lives starting from mobile phones, tablets to personal computers, digital cameras etc. All these technological commodities contain some sort of computer systems that present features like Input/Output (I/O), processing and storage units. From the introduction of Intel's first 4-bit 4004 microprocessor running at 740 KHz clock frequency in 1971 [1] to the high performance processor i7-4790K running at 4GHz, 22 nm lithography with 3 levels of cache in 2014 [2], microelectronic industry has witnessed a huge success. This success was possible due to not only the miniaturization and high density integration of CMOS logic but also the accompanying development and scalability of memory technologies.

FigI.1 shows the evolution of the worldwide semiconductor market over the past few years. Semiconductor memories (see FigI.2, mainly dominated by DRAM and NAND Flash) represent a significant portion of the IC market [3]. NAND Flash presents a steady growing market share which is expected to exceed that of DRAM in the next few years [4] because of the continual demand for smartphones, tablets and other media devices (FigI.3).

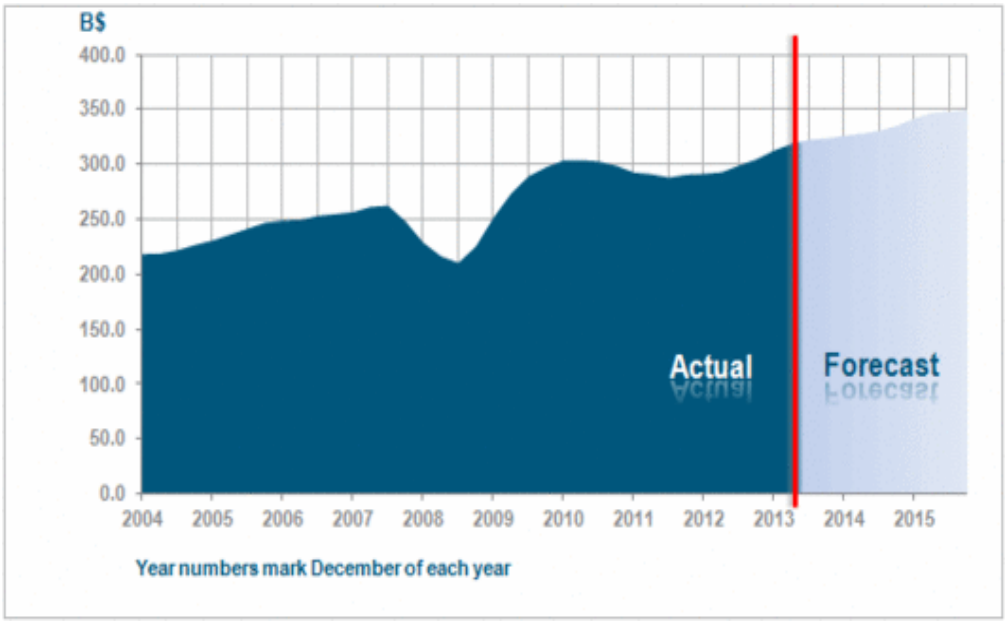

FigI.1. Worldwide semiconductor industry revenue, data from WSTS [5].

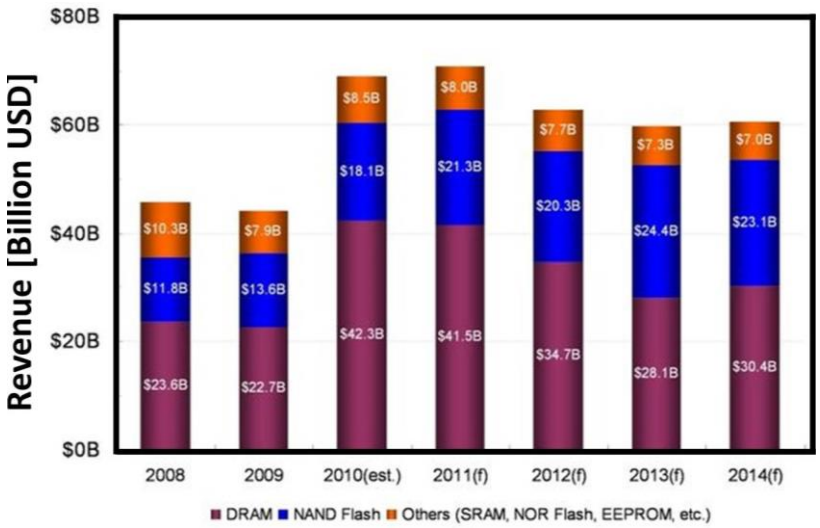

FigI.2. Global semiconductor market; adopted from [3]

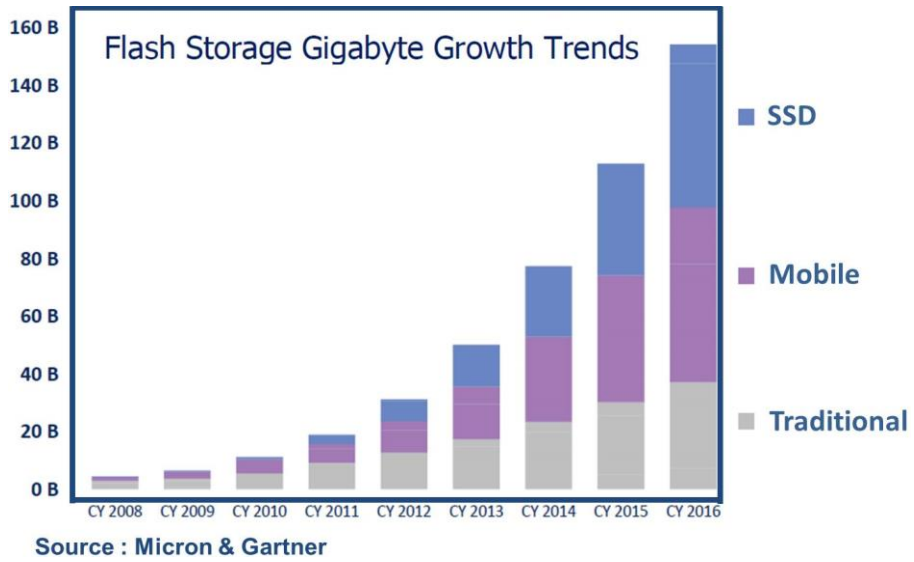

FigI.3. Flash storage gigabyte trends in the next few years; adopted from [6].

I.2 Overview of memory technologies

Generally, memory technologies are categorized into two main types namely "volatile" and "non-volatile" as shown in FigI.4. SRAM (Static Random Access Memory) and DRAM (Dynamic Random Access Memory) are volatile and lose their data when power is turned off. While, charge based memories such as FLASH and RRAM (resistive random access memories) are non-volatile and retain data even after power is turned off.

SRAMs generally use 6 transistors to store information. They present very fast Read/write speeds (1 ns/1 ns) and excellent endurance [7]. However, they are expensive and have low density integration because of their larger feature size ($24F^2$ [7]).They are generally used as cache in computer systems.

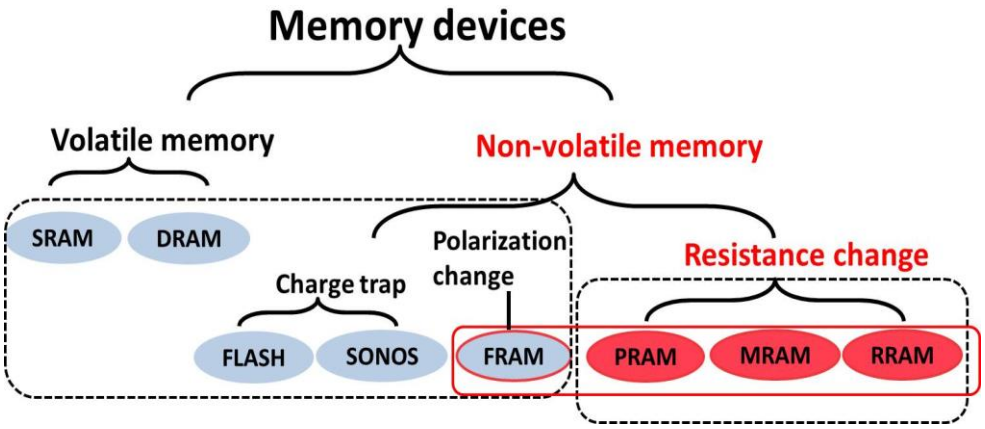

FigI.4. Different categories of memory technologies [5]

DRAMs consist of one transistor and one capacitor (1T1C) to store information. The presence of charge at the terminals of the capacitor corresponds to Logic "1" while Logic "0" corresponds to the absence of charge. Due to its smaller feature size ($6\text{-}8F^2$ [7]), this technology is cheap and present a very high integration density level with very excellent endurance. However, because of the capacitor, DRAM needs to be continually refreshed to retain data while power is still ON. DRAMs are generally used as main memory in computer RAMs.

Non-volatile memory technologies do not need to be refreshed as DRAM and retain data even after power is turned off. Flash has benefitted from the traditional scaling of semi-conductor industry allowing its high density integration for mass market production. However, this scaling limit seems to be approached and there seems to be serious problems beyond the 22 nm node such as severe floating gate interference, lower coupling ratio, short channel effects and low electron charge in the floating gate [8]. Hence, alternative solutions, generally referred to as "Emerging memory devices" or "Disruptive memory technologies" [9], are being sought after for future applications. Among the serious candidates out of these emerging memory devices are resistive memories. Different families of resistive memories exist and are generally classified as FRAM (Ferroelectric Random Access Memory), MRAM (Magnetoresistive Random

access Memory), PRAM (Phase Change Random Access Memory), CBRAM (Conductive Bridge Random Access Memory) and OxRAM (Oxide based Random Access Memory). MRAM products are being used in niche applications [10] while PRAM are announced in commercial production [8].

I.3 Non-volatile memory technologies

I.3.1 Flash

A Flash memory cell is basically a floating-gate MOS transistor in which a floating gate is inserted between the gate of the transistor (control gate) and the transistor channel [11,12] (FigI.5). The floating gate is electrically isolated from the control gate and the channel by two dielectric layers: control oxide and tunnel oxide. When a positive voltage is applied to the control gate, electrons are injected into the floating gate through the tunnel oxide via Fowler-Nordheim (FN) tunneling. The presence of charge in the floating gate which corresponds to Logic "1" shifts the apparent threshold voltage (V_T) seen from the control gate (FigI.5). When a negative voltage applied to the control gate, the trapped electrons are injected back from the floating gate into the substrate via the tunnel oxide and that corresponds to Logic "0".

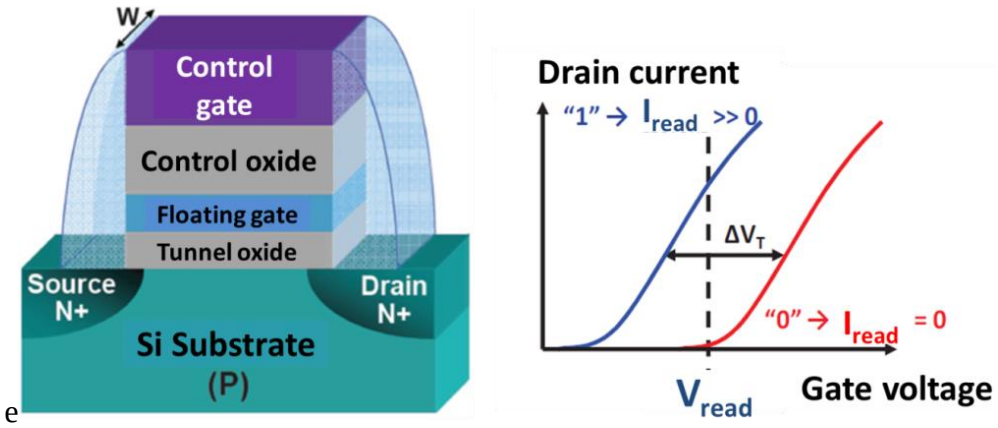

e

FigI.5. (left) Basic structure of Flash memory cell (right) Example of corresponding IV characteristics; adopted from [13].

Flash technology is produced in two different cell array combinations and are referred to as NAND Flash and NOR Flash. The two types are shown in FigI.6. In NOR flash, the transistors are connected in parallel which allow random access to each memory cell but it has lower density. Because of the parallel configuration of the transistors, NOR Flash offers complete random access to data buses of any memory

location (byte addressable). Hence, NOR is suitable for storing codes in embedded systems. Many microcontrollers come with built-in Flash memory [12,14]. The transistors are connected in series in NAND Flash which consumes less space, thus allowing its higher density integration with reduced cost [12]. The higher density of NAND Flash made it suitable as storage media for large files. It is also used in USB drives and SD cards.

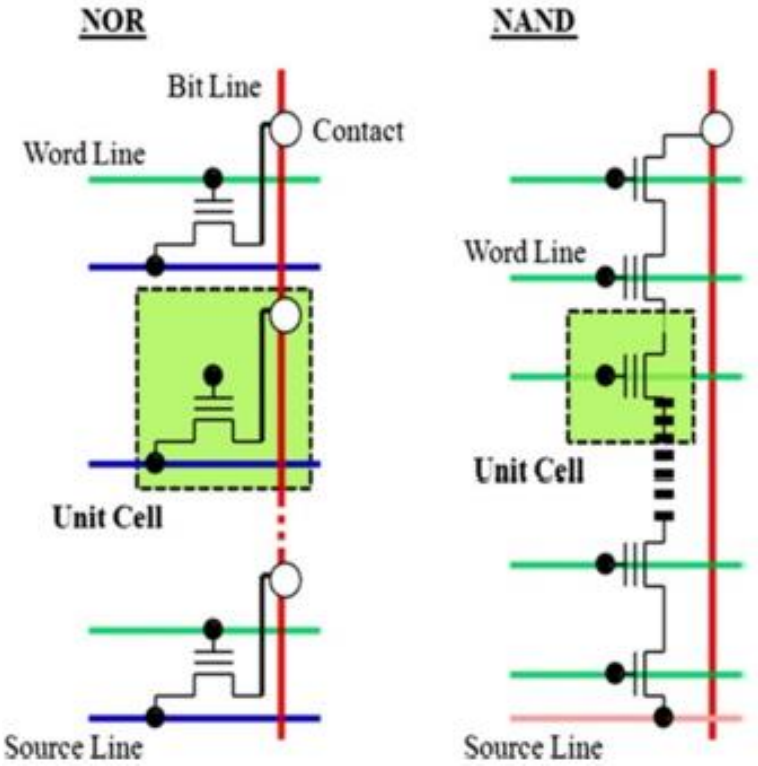

FigI.6. Comparing NOR and NAND Flash array architectures [12]

Over the past years, there have been considerable improvements in Flash technology in order to comply with the requirement of continuous scaling. In order to meet the increasing demand of reduced feature size and the large memory requirement (multi-gigabit) in microelectronic products, Flash technology, using floating gate CMOS, has been scaled over the years in single cell (SC) and multi-level cell configurations. With the announcement of the 32-layer 3D NAND chips by Intel (FigI.7) [15] and the started mass production of the similar 32-layer V-NAND Flash by Samsung (FigI.8) [16], it is very likely that NAND Flash will have few more years before its replacement becomes a reality. This is still true in view of the fact it will probably be possible to keep adding NAND Flash layers up to 100 per die at some point in future [17] [15].

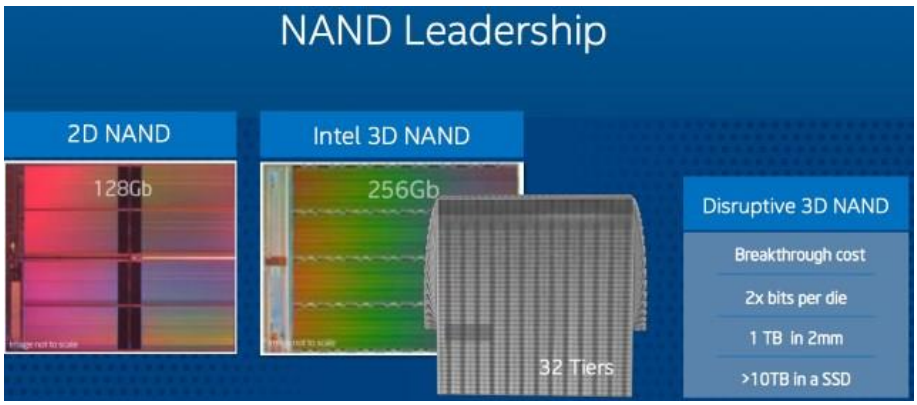

FigI.7. Intel's announced 32-layer 3D NAND Flash; adopted from [15]

FigI.8. Samsung's started mass production 32-layer 3D NAND Flash [18].

Despite the remarkable development and the continuing engineering progress in NAND Flash, it is widely believed that scaling beyond the 22 nm node will be very challenging and serious physical problems will likely appear [19]. In order to comply with the 10 years data retention requirement, the tunnel and control oxides need to be thick enough to prevent charge loss. However, scaling of the tunnel oxide will affect this requirement which is already not easily achieved with the present Flash memories [9]. Stress Induced Leakage Currents (SILC) which affects devices' reliability are of primary concerns in Flash and their amplitude increases by reducing the oxide thickness [20]. Also, few electrons phenomena may be an ultimate intrinsic limit in the scaling of Flash memories [9,21].

In an effort to follow Moore's law, many alternative memory solutions are proposed to hopefully go beyond the scaling limitations and challenges of Flash technology. These alternative solutions are sometimes called universal memories

because they offer the high speed requirement of SRAM, the integration density of DRAM and non-volatility of Flash. Currently, an extensive research is going on each of the memory types and the debate remains open about which technology will win the race. They are described in the following sections.

I.3.2 FRAM

FRAM (Ferroelectric RAM) uses the polarization properties of a ferroelectric material generally made of lead zirconate titanate (PZT) [12] as a memory device (FigI.9). The memory effect is obtained due to two stable states of polarization by the application of the electric field in opposite directions. A hysteresis exists when the field is removed (FigI.9).

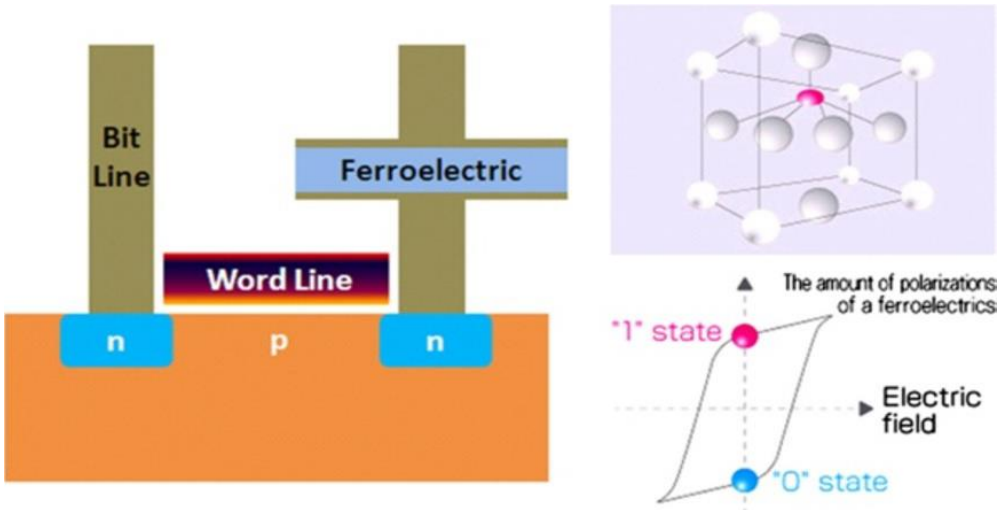

FigI.9. An FRAM device stack, crystal structure and an electric-polarized hysteresis curve are shown; adopted from [12].

I.3.3 MRAM

MRAM for Magnetoresistive RAM uses electrons' spin to store data. The main component of an MRAM is the magnetic tunnel junction (MTJ) which is a sub-100 nm size magnetic element consisting of one of the magnetic layers, called the free layer (FL) [22] which is programmable. A thin insulating barrier separates the FL from a second magnetic layer called the reference layer (RL) which provides a stable reference magnetic orientation required for reading and writing. When the magnetizations (majority electron spins) in the two magnetic plates are parallel then the resistance of the MRAM is lower while if they are oriented in antiparallel direction the resistance of the MRAM is high (FigI.10). Data can be retained in the spin orientations of the fixed

and free ferromagnetic plates and the stored data can be sensed by measuring the tunneling current [23]. Although early MRAM devices suffered from very high write currents, the development of devices based on STT-MRAM (Spin Torque Transfer MRAM) has largely improved the current levels [24]. MRAM strengths being non-volatility coupled with unlimited endurance and high performance characteristics (high speed, low voltage) make them suitable for embedded applications. However, MRAM has low integration density (not as high as DRAM or Flash) [24] and its scalability beyond 20 nm node still remain to be demonstrated [25].

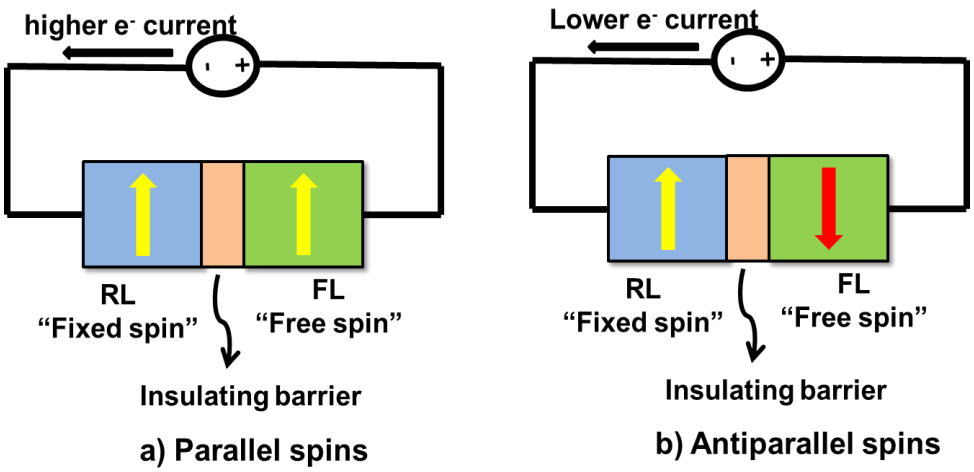

FigI.10. MTJ junction showing (a) parallel and (b) antiparallel spins corresponding to low resistance and high resistance states of an MRAM respectively.

I.3.4 PCM

Among the emerging memory technologies, PCM (Phase Change Memory) or PCRAM (Phase Change RAM) seems to be the most mature technology partly because the materials (such as GST) used in PCM were largely adopted for the development of CDs and DVDs. PCM, whose basic schematic cell is shown in FigI.11, uses chalcogenide based materials that can exist at two different phases namely crystalline and amorphous phases.

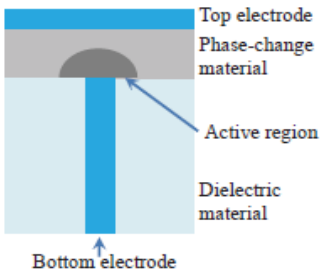

FigI.11. Schematic structure of a PCM cell [26].

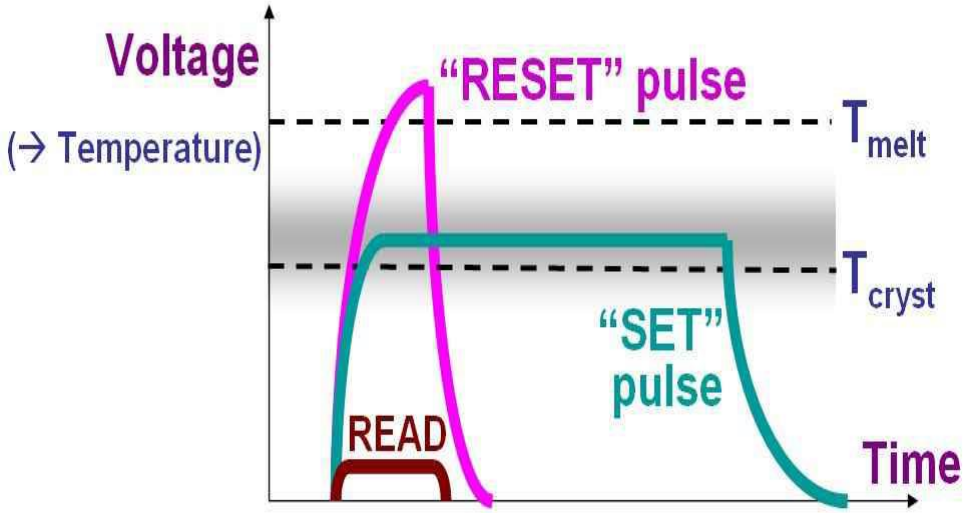

FigI.12. Programming of a PCM cell involving the application of electrical power [27].

A PCM cell programming is driven by current induced joule heating. The resistance of the crystalline phase is low and defines the Logic "1" while that of the amorphous phase is high defining the Logic "0". The resistance change between the two phases can be many orders of magnitude [13]. To SET the PCM cell into low resistive state, an electrical pulse is applied to heat a significant portion of the active region above the crystallization temperature T_{cryst} (FigI.12). For the RESET process (program the cell to high resistance state), a larger current than required during SET is applied and then cut/stopped in order to melt and quench the active region of the cell (FigI.12). Although, the main limitation of PCM cells was the high current required to program the devices to high resistive state, significant improvement have been achieved through the doping the cells with carbon [28] or changing the architecture of the memory cells [29]. FigI.13 shows that scaling PCM cells results in a significant reduction of the melting currents and as such scaling is the main enabler of power performance improvement in PCM cells. Because of its demonstrated switching performance, PCM devices are cited as candidates for DRAM replacement and possible use as Storage Class Memories (SCM) in new generation memory applications [30] [29]. However, despite significant progress in its material engineering and processes, PCM still suffers from high RESET current and some reliability issues [30]. This high RESET current translates into larger memory selector area which occupies the most layout area of the cell [31], thus limiting the integration density of the devices in arrays.

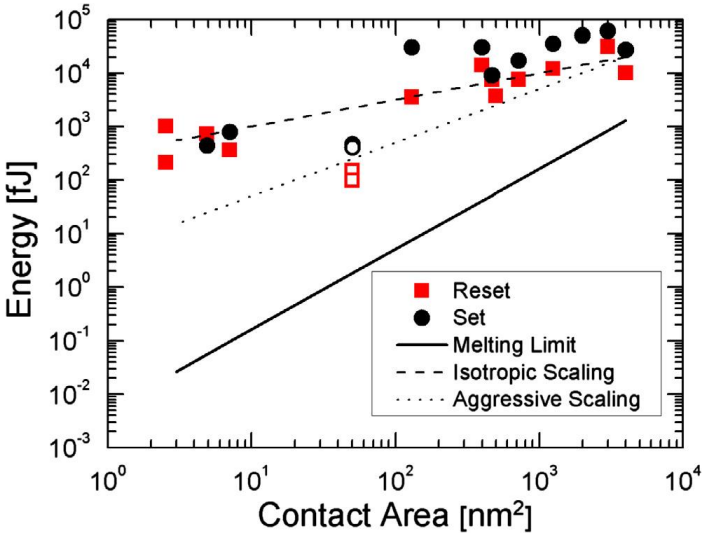

FigI.13. PCM energy consumption as a function of the cell contact area [29].

I.3.5 CBRAM

CBRAM (Conductive Bridge RRAM) or ECM (Electrochemical Metallization Cell) relies on the electrochemical metal deposition and dissolution to perform resistive switching [32]. The memory structure of a CBRAM cell consists of a solid electrolyte sandwiched between two metal electrodes one of which is an electrochemical active metal (generally Ag, Cu) as shown in FigI.14. The basic working principle of a CBRAM cell and the corresponding current-voltage (IV) switching characteristics are shown in FigI.15. Initially, the CBRAM device is at a high resistive state with no electrochemical active metal present in the solid electrolyte. When a sufficient positive voltage is applied to the top electrode, a conductive filament (*CF*) is formed made essentially of the active metal electrode in the solid electrolyte connecting the two electrodes (FigI.15) [33]. SET operation results in the low resistance state of the CBRAM cell and a compliance current (maximum allowable current in the memory cell during low resistance state to avoid permanent breakdown of the device) is enforced to limit current in the device. To bring the device to high resistance state during RESET, a negative voltage is applied to the top electrode which results in the dissolution of the electrochemical active metal in the CF (FigI.15). The two resistance states achieved during SET and RESET operations define the Logic states “1” and “0” respectively. Different materials are used for the solid electrolyte such as chalcogenide (GeS_2) [34], and oxides in oxide based CBRAM [35]. Low voltage, high speed and scalability are some of the performance characteristics demonstrated with CBRAM which make it a potential candidate in embedded non-volatile memory applications. However, CBRAM

devices suffer from high temperature instability especially for cells made of chalgonide based solid electrolytes [36].

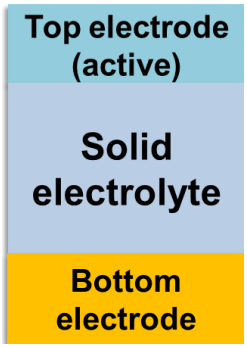

FigI.14. Basic structure of a CBRAM memory cell

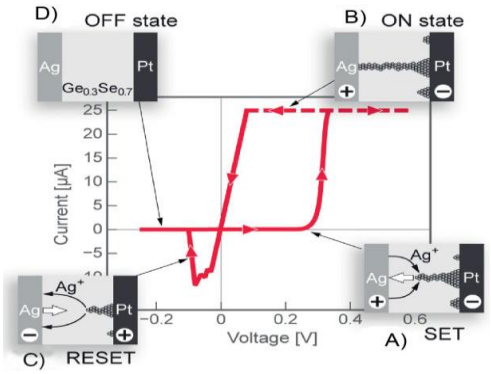

FigI.15. Typical current-voltage (IV) characteristics and basic working principle of Ag/$Ge_{0.3}Se_{0.7}$/Pt CBRAM cell [33].

I.3.6 OxRAM

Oxide based RRAM (OxRAM) are fabricated in a metal-insulator-metal structure similar to a CBRAM cell in which the insulator is an oxide. It relies on the reversible resistance of the oxide layer between two stable states namely low resistance state (LRS or R_{on}) and high resistance state (HRS or R_{off}). Since, oxide based RRAM is the non-volatile memory considered in this thesis, its working principle and performance will be revisited in detail in the next sections. Many interesting switching characteristics such as low voltage, low power, excellent endurence and high thermal stability have been demonstrated with oxide based RRAM making it a very serious candidate for NAND Flash replacement.

Before closing this section, we may look at the different emerging memory technologies in order to highlight their strengths and what they should improve upon for sustainable commercial production. It is intersting to note that all the different emerging technologies are available in commercial products even if for different applications and markets [37]. TableI.1 compares the different memory technologies in terms of both performance and cost. We observe that all the emerging memory technologies compete very well with the well established and mature DRAM and NAND Flash in terms of device performance. However, their main limitation is cost : $10,000/GB for RRAM and FRAM compared with the 1$/GB and $0.1/GB for DRAM and NAND Flash respectively [38]. Hence, at this stage, the new emerging technologies can only be used in niche applications very specific needs that DRAM and NAND Flash barely meet.

Nevertheless, a further analysis of the table points out a very interesting point : the emerging memory devices, exhibit potentially very low operating voltage compared with NAND Flash. Furthermore, they all present very high switching speeds in the vicinity of 10 ns ([39,40] show write speeds less than 10 ns compared to the 75 ns shown in TableI.1 for RRAM). Therefore, these features (low voltage and high speed) play key role market drivers for the emerging memory technologies as shown in TableI.2. Most of the emerging memory technologies have the potential to meet the requirements related to cache memory for entreprise applications (because of their high speed) and embedded Industrial/Transportation systems (for their low power and high speed). However, for NAND Flash replacement beyond the 20 nm node, RRAM seems to be the most serious candidate that stands out because of its demonstrated very high density, high endurance, high speed, low power. For Flash replacement to happen, RRAM will need more maturity; and sound experimental and physical understanding will be highly required. Several research laboratories and companies have been extensively working over the past few years on oxide based RRAM development and optimization. In the following paragraphs and sections, we will look at the state of the art of oxide based RRAM and the level of understanding of the technology from experimental and physical perspectives. For the rest of the chapter and the manuscript, RRAM will always be referring to oxide based RRAM (OxRAM).

	FRAM	MRAM/STT MRAM	PCM	RRAM	DRAM	Flash NAND
Non-volatile	YES	YES	YES	YES	NO	YES
Endurance (Nb cycles)	High (10^{12})	High (10^{15})	Medium (10^{8})	Medium (10^{8})	High (10^{15})	Low (10^{5})
2013 latest technological node produced (nm)	130 nm	90 nm	45 nm	130 nm	30 nm	20 nm
Cell size (cell size in F^2)	Large (15-20)	Large/Medium (6-40)	Medium(6-12)	Medium(6-12)	Small (6-10)	Very small (4)
Write speed (ns)	Medium (100 ns)	High (10ns)	Medium (75 ns)	Medium (75 ns)	High (10 ns)	Low (10,000 ns)
Power consumption	Low	High/Low	Low	Low	Low	Very high
2013 price ($/GB)	High ($10,000/GB)	High ($1,000 - 100/GB)	Medium (few $/GB)	High (10,000 $/GB)	Low (1$/GB)	Very low (0,1 $/GB)

TableI.1. Memory position in 2013; comparison of some of the performance criteria of the different technologies; adopted from [38].

	Average density required	Current memory	2012 TAM in units	2012 ASP ($)	2012 TAM in $	Market drivers for ENVM	Time-to-market for commercial samples
Industrial & Transportation	10 KB - 10 MB	NVSRAM EEPROM BB SRAM	600M	$0.5 - $5	$600M	• Lower power consumption • Higher speed	• FRAM: 2001 • MRAM: 2008 • RRAM: 2013
Smart Card MCU	1 - 15 MB	Flash EEPROM	1B	$0.2 - $0.7	$350M	• Lower power consumption • Lower cost • Increased security	• MRAM: 2014 • PCM: 2014
Cache Memory for Enterprise Storage	4 MB - 8 GB	DRAM BBSRAM NV SRAM	60 - 100M	$4 - $5	$500M	• Lower power consumption • Higher speed	• MRAM: 2010 • PCM: 2014 • RRAM: 2015
Mobile Phones	Few MB - 1 GB	NOR SRAM	1.8B	$1 - $3	$1 - 2B	• Lower power consumption • Lower cost	• PCM: 2010 • MRAM < 2015
Mass Storage	4 GB – 256 GB	NAND	7B	$0.1 - $10	$27B	• Lower power consumption • Higher endurance • Lower cost	• RRAM: 2016

TableI.2. Features that may make emerging non-volatile memories as market drivers in future non-volatile memory applications; adopted from [38].

I.4 Oxide based RRAM

The concept of a resistance with memory is not new and is intimately related to the memristor component. The existence of such a component was postulated in the early 70s by Chua [41] who noticed the absence of a direct relationship between the electric charge (q) and the flux (ϕ) among the four main parameters of a circuit (charge, flux, voltage and current). In order to fill this absence, the theory of memristor was developed. But it was until the years 2000s that the research in the field of devices showing memrsitive effects has received more attention. Although, a first resistive switching effect of NiO film was already reported in 1964 by Gibbons and Beadle [42], one of the most significant milestones in RRAM research was the 2004 IEDM paper of Baek et al. [43] from Samsung in which the resistance switching was demonstrated with a binary transition metal oxide (TMO) integrated in 0.18 µm CMOS compatible process. From there on, research on RRAM has raised more interest and the resistive switching effects were observed in different thin films.

I.4.1 Basics of RRAM operation

As pointed out earlier, Oxide based RRAM are fabricated in a metal-insulator-metal structure in which the insulator is a metal oxide (FigI.16a). Their operation relies on the reversible resistance change of the oxide layer between two stable states namely low resistance state (LRS or R_{on}) and high resistance state (HRS or R_{off}). At pristine state, the oxide layer has a very high resistance value and needs to be preconditioned for resistive switching through an operation called forming/electroforming. Forming is a current controlled soft-breakdown of the oxide layer that causes the creation of a conductive path of low resistance value called conductive filament (CF). During the forming operation, current is limited in order to avoid permanent damage of the device. This maximum current is referred to as the compliance current (I_{comp}) and is limited either by the semiconductor parameter analyzer for 1R devices or by the access transistor for 1T1R devices (devices integrated with a transistor). During RESET, by applying an appropriate voltage, the device can be programmed to high resistance state (HRS or R_{off}) inducing the rupture/disruption of the CF (FigI.17). Subsequent SET (programming the devices to R_{on} involving the reconstruction of the CF as seen in FigI.17) and RESET operations cause the resistive switching between R_{on} and R_{off} respectively. Different switching behaviors are observed in RRAM memory cells namely unipolar and bipolar types of switching. For unipolar devices, the same voltage polarity is used in programming the devices to both low and high resistance states (FigI.16b) while in the case of bipolar devices different voltage polarities are used for the resistive switching (FigI.16c). The type of RRAM switching largely depends on the choice of the electrode materials and will be discussed in the next sections.

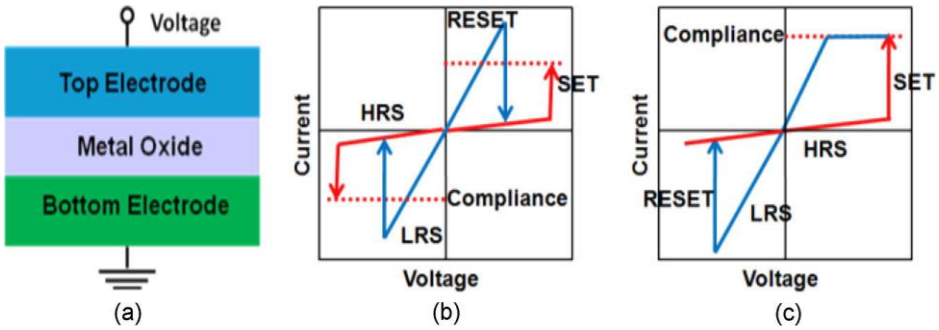

FigI.16. (a) Schematic cell structure of an oxide based RRAM (b) schematic current-voltage (IV) curve of a unipolar RRAM (c) schematic IV curve of a bipolar RRAM [44].

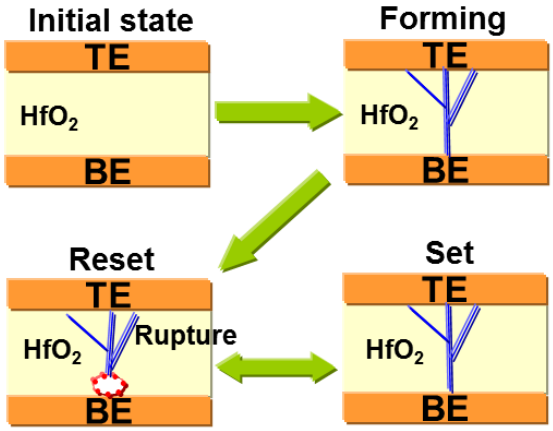

FigI.17. Illustration showing HfO_2 based RRAM cell structure and its working principle.

To complete this introductory section on RRAM operation, FigI.18 shows the definition of the switching voltages and currents that are used to assess the quasi-static (DC) switching characteristics of the devices. $V_{forming}$ or V_F corresponds to the voltage at which an abrupt current increase starts during the forming operation and the maximum current or current limit during this operation is referred to as the compliance current (I_{comp} or I_c). Vreset corresponds to the voltage at which current starts to decrease during the RESET operation and the corresponding current is referred to as the RESET current I_{reset}. Hence, I_{reset} is the maximum current during the RESET operation and its magnitude gives a fairly good estimation of the maximum current that the CF has seen during the forming and SET operations. Similarly, V_{set} is defined in the same way as $V_{forming}/V_F$ except that Vset is much lower than $V_{forming}$ in RRAM.

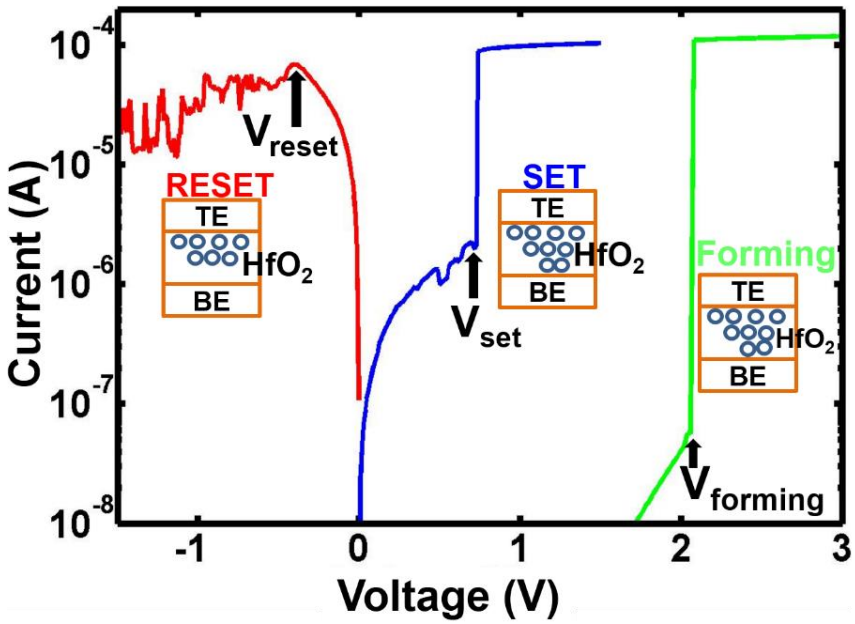

FigI.18. RRAM quasi-static switching voltages definition.

I.4.2 Materials

Several binary metal-oxides have been found to exhibit resistive switching effect with most of the metals being the transitional metals. TableI.3 shows the materials used as binary metal-oxide RRAM as well as the materials used as electrode in the MIM structure. Among these binary metal-oxides, TaO_x, TiO_x, AlO_x, NiO and HfO_x have raised more research interest.

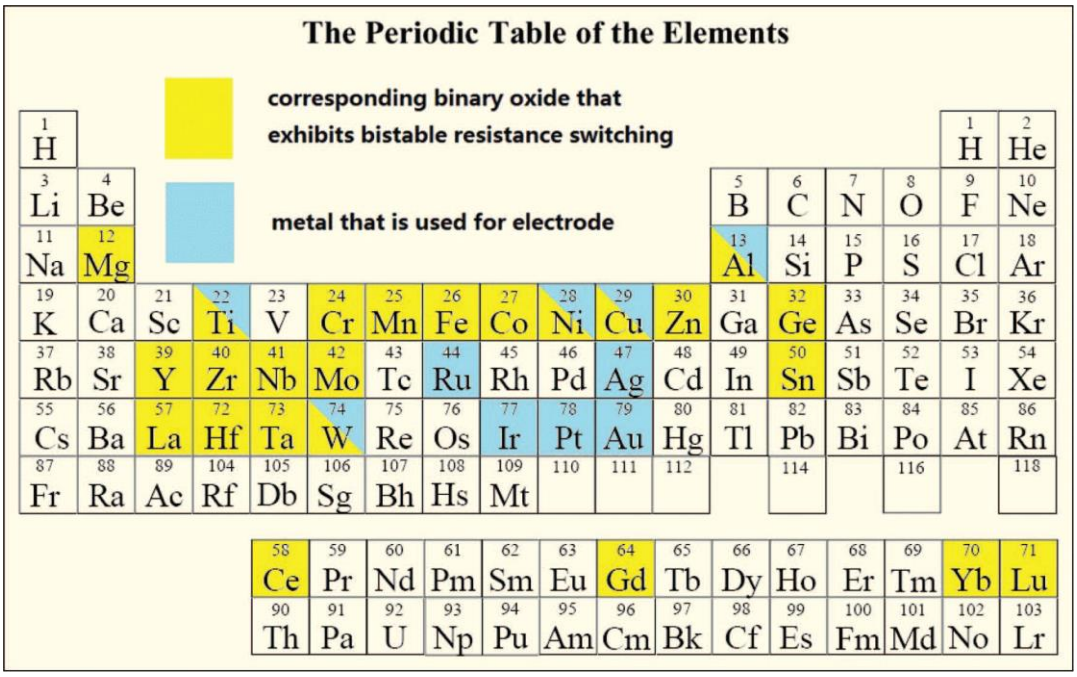

TableI.3. Materials used in the metal-Insulator-metal (MIM) structure of metal-oxides based RRAM [44].

Wu et al. studied Al_2O_3 structure sandwiched between Pt (BE) and Al (TE) with Ti and without Ti interfacial layer between the oxide/Al interface, low RESET currents were obtained [45]. Interestingly, they observed forming-free operation with $Pt/Al_2O_3/Al$ and very low RESET current of ~1µA was achieved. Although, their $Pt/Al_2O_3/Al$ structure was forming-less, the obtained SET voltage of ~ 3.5V still remains high for RRAM in embedded novel low power CMOS applications. However, Kim et al. used Nitrogen doped AlO sandwiched between two Al electrodes (Al/N-doped AlO/Al) to further decrease the SET voltage of the forming-free structure to approximately 2 V [46]. Furthermore, low RESET currents less 30 nA were achieved and multi-bit storage for over 10 years retention at 125°C was projected.

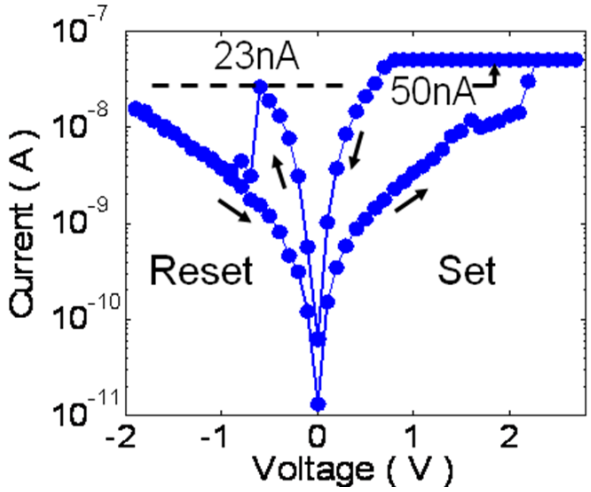

FigI.19. Current-voltage characteristics of forming-free Al/N-doped AlO/Al RRAM devices reported by [46].

NiO based RRAM was among the first binary metal-oxides reported in the literature and Ir, Ni, Au, TiN among others were used as metal electrodes. Most of the reported structures with NiO based RRAM exhibited unipolar resistive switching [47,48,49,50]. Despite the RESET current being much higher in unipolar switching devices [47,48,49,50], Nardi et al. obtained sub-µA RESET currents with TiN/NiO/Au memory cells (FigI.20) [49] and showed that their RRAM device integrated with Si-based select diodes may be scaled down to at least 11 nm node for cross-bar arrays.

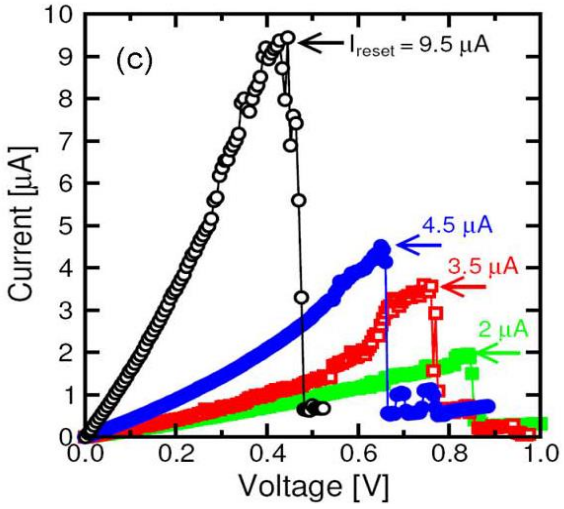

FigI.20. Current-voltage characteristics showing RESET currents as low as 2µA with NiO based RRAM adopted from [49].

TaO_x based RRAM have been extensively studied by Panasonic [51,52] and their embedded RRAM available in commercial microcontroller products is based on the technology [53] as shown in FigI.21. Several electrode materials were studied in [51] to investigate the electrode dependence switching phenomena as shown in FigI.22.

TaO_x RRAM cells showing high endurance (>10^{10} cycles) [54] and 3 multi-bit storage with low power and good retention [55] are also reported.

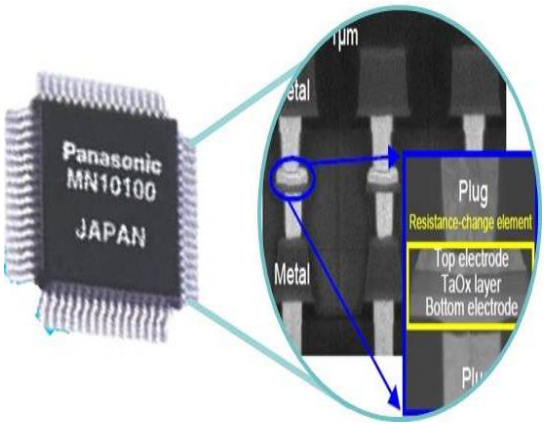

FigI.21. Panasonic commercial microcontroller product based on TaO_x RRAM [53].

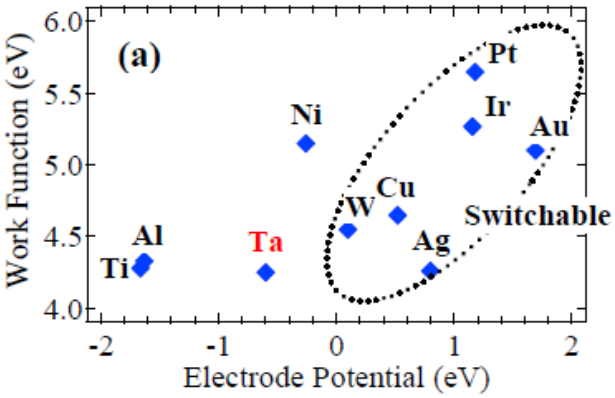

FigI.22. Electrode dependence switching phenomena in TaO_x based RRAM adopted from [51].

TiO_x has also been investigated in the early development of metal-oxide RRAM devices. One of the most significant results obtained with TiO_x based RRAM devices was the identification of the Magneli phase Ti_4O_7 as the conductive filament responsible for resistive switching as shown in FigI.23 [56].

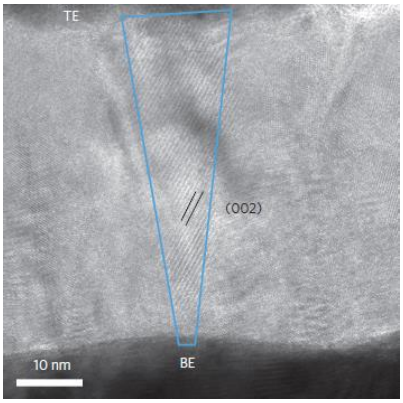

FigI.23. Ti_4O_7 Magneli phase nanofilament observed in Pt/TiO_2/Pt RRAM; adopted from [56].

As for HfO_2, it is probably the most adopted metal-oxide for resistive switching. Several companies [57] and research laboratories [58] have used the HfO_2 solution as the active layer responsible for the memory effect because of, among others, its compatibility with conventional CMOS Back-End-Of-Line (BEOL) process. Very interesting results have been obtained with HfO_2 based RRAM. Scaled devices as small as 10nm x 10nm HfO_2 RRAM with switching speeds less than 10 ns have been demonstrated [39]. Very recently, 2nm ultrathin HfO_2 layer sandwiched between *Pt* and *TiN* electrodes suitable for 3D integration has also been reported [59]. High endurance (>10^8 cycles) [40], low voltage [40,39], very good data retention [60,59], and excellent device yield [61] characteristics are also obtained. Alloying HfO_2 with materials like Al_2O_3, TiO_2 or using bilayers Al_2O_3/HfO_2 have also recently been studied to improve the devices' performance in terms of better switching uniformity, enhanced thermal stability and increased cycling endurance. Hence, among the different metal-oxides, HfO_2 seems to be the most investigated oxide although TaO_x based devices are also under intense study. As such, HfO_2 is the oxide adopted for this thesis work. TableI.4 compares the switching performance of some of the binary metal-oxides in which resistive switching was reported.

	NiO IEDM 2004	Cu_xO IEDM 2005	Ti:NiO IEDM 2007	TaO_x IEDM 2008	Ti/HfO_x IEDM 2008	Ti/HfO_x IEDM 2009 &2010	WO_x IEDM 2010	ZrO_x/HfO_x IEDM 2010	$N:AlO_x$ VLSI 2011	TaO_x/Ta_2O_5 VLSI 2011	Hf/HfO_x IEDM 2011
switching type	unipolar	bipolar	unipolar	bipolar	bipolar	bipolar	bipolar	bipolar	bipolar	bipolar	bipolar
structure	1T-1R	1T-1R	1T-1R	1T-1R	1T-1R	1T-1R	1T-1R	1R	1T-1R	1R	1T-1R
cell area (μm^2)	~0.2	~0.03	~0.49	~0.25	~0.1	0.0009 (30nm)	0.0036 (60nm)	0.0025 (50nm)	~1	~9000	0.0001 (10nm)
speed	~5µs	~50ns	~5ns	~10ns	~5ns	~0.3ns	~50ns	~40ns	N/A	~10ns	~10ns
peak voltage	<3V	<3V	<3V	<2V	<1.5V	<2.5V	<3V	<2V	<2V	<2.5V	<1.5V
peak current	~2mA	~45µA	~100µA	~170µA	~25µA	~200µA	~1mA	~50µA	~50nA	~30µA	~50 µA
HRS/LRS ratio	>10	>10	>90	>10	>100	>100	>10	>10	>100	>100	>10
endurance	10^6	600	100	10^9	10^6	10^{10}	10^6	10^6	10^5	10^{12}	$5x10^7$
retention	300h@ 150°C	30h@ 90°C	1000h@ 150°C	3000h@ 150°C	10h@ 200°C	28h@ 150°C	2000h@ 150°C	28h@ 125°C	28h@ 125°C	3h@ 200°C	30h@ 250°C

TableI.4. Binary metal-oxides with some switching performance characteristics; adopted from [44].

I.4.3 Switching modes of RRAM devices

As mentioned in the RRAM operation section, different switching types are observed in oxide based RRAM devices namely unipolar and bipolar types of switching. This is mainly due to the type of metal electrode used in the RRAM MIM structure. Furthermore, depending on the electrode material used, the properties of the dielectric may change due to more or less defects generation and possible interfacial layer that may be formed at the oxide/metal interface. Hence, by proper engineering and choice of the metal/oxide interface, the switching performance of the memory cells can be improved. Different materials such as Ti, TiN, Zr, Hf, Pt, Ni, Cu, Ir etc. (TableI.3) are used as metal electrodes. Bipolar resistive characteristics have been, among others, observed in TiN/HfO_2/Ti, TiN/HfO_2/Pt [62,63], Pt/HfO_2/TiN [59], TiN/HfO_2/TiN (this work, see chapter III), p+-Si/HfO_2/Ti/TiN, p+-Si/HfO_2/Ta, p+-Si/HfO_2/Pt [65], TiN/HfO_2/Hf [39] memory stacks. On the other hand, Pt/HfO_2/Pt [62,63], TiN/HfO_2/TiN [64] (unlike this work), p+-Si/HfO_2/Ni [65] and Ni/HfO_2/TiN [66] memory stacks showed unipolar characteristics. Interestingly, unlike the bipolar behavior of TiN/HfO_2/Pt reported by [59], Wang et al. reported unipolar switching characteristics for the same memory stack (TiN/HfO_2/Pt) [67]. There is a general trend that we may observe about the switching types of the memory cells depending on the electrode material: When the top electrode (TE) is an oxygen reactive metal like Ti or Hf, the switching type is mostly bipolar while when both TE and BE are symmetrical and less reactive with oxygen the switching type is mostly unipolar or non-polar (switching can occur in either polarity). This trend may explain the non-polarity of TiN/HfO_2/TiN and TiN/HfO_2/Pt as mentioned above. However, given that TiN/HfO_2/Pt stack does not have symmetrical electrodes, the origin of unipolarity of the devices may be more complicated than the simple symmetry arguments of the electrodes. Comparing the results of Zhao et al. [59] on TiN/HfO_2/Pt devices in the bipolar mode to those of Wang et al. [67] in the unipolar mode, it is likely that operating this memory stack in the bipolar mode presents superior performance which is in line with the asymmetry of its electrodes (asymmetry of the electrodes indicates that oxygen ions distribution is not symmetrical on either electrode/oxide interface and hence the polarity of the voltage plays more important role during the switching). The switching characteristics of the devices with different electrodes exhibiting different switching types are compared in [62,63]. Devices with TiN (BE) and Ti (TE) could be formed at low forming voltages compared to Pt (BE) and Pt (TE) based cells. This low forming voltage in TiN/HfO_2/Ti

cells was attributed to the oxygen reactive property of Ti which causes the formation of sub-stoichiometric TiO_x layer at the Ti/oxide interface (FigI.24) [62]. Moreover, [63] shows that the set voltage is also lower for TiN/HfO_2/Ti samples compared to their counterparts Pt/HfO_2/Pt samples (TableI.5) and exhibited better switching endurance and variability. Similarly, Wang et al. also showed that by proper engineering of the anodic interface at the top electrode with the introduction of a thin metal layer (like Ti) or a thin metal-oxide MO_x (like TiO), the device performance could be improved [67]. We have also seen earlier in the Tantalum oxide (TaO_x) section that Panasonic performed a large screening of electrode materials for improved performance. This is an important point: RRAM device performance largely depends on the choice of the electrode material. Hence, the characteristics of RRAM devices are largely influenced by the composition of the memory stack. Due to the attractive switching characteristics of TiN/HfO_2/Ti memory devices as reported among other by [61,68], this memory stack is becoming a dominant choice for future RRAM applications. However, the memory stack not being perfect in terms of all the requirements (uniformity, larger R_{off}/R_{on} ratio etc.), studies are going on with regards to optimizing the HfO_2 layer by alloying it with other materials, doping it or by adding other oxide films for bilayers. In this manuscript, a full chapter is dedicated to the study of electrode impact on RRAM performance.

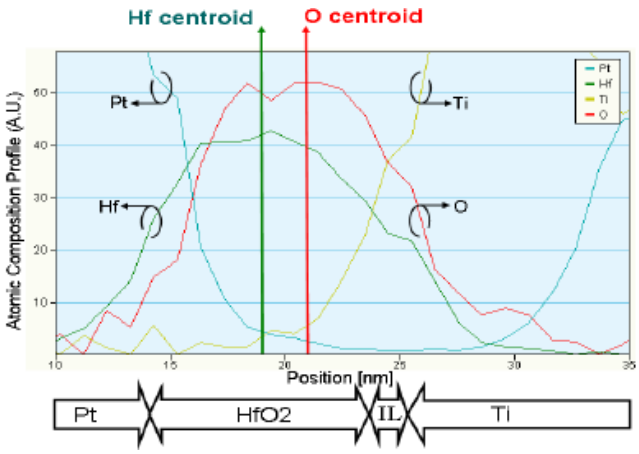

FigI.24. Atomic composition of the Pt/HfO_2/Ti memory stack by EDX. Distribution of oxygen (O) is found to be shifted towards Ti electrode supporting the presence of an interfacial TiO_x layer; adopted from [62].

Capacitors	$V_{Forming}$ [V]	V_{Set} [V]	V_{Reset} [V]	R_{Set} [Ω]	R_{Reset} [Ω]	I_{Reset} [mA]
Pt/HfO_2/Pt	4.3 ± 0.6	2.5 ± 0.9	-0.38 ± 0.09	120	$\sim 4 \times 10^6$	4.2
Ti/HfO_2/TiN	2.0 ± 0.7	0.6 ± 0.4	-0.42 ± 0.06	480	$\sim 4 \times 10^5$	1.2

TableI.5. Comparing the switching characteristics of TiN/HfO_2/Ti and Pt/HfO_2/based RRAM; adopted from [63].

Unipolar	Bipolar
Pt/NiO/Pt [7]	Pt/NiO/$SrRuO_3$ [54]
Pt/TiO_2/Pt [8]	Pt/TiO_2/TiN [55]
Pt/ZnO/Pt [18]	TiN/ZnO/Pt [56]
Pt/ZrO_2/Pt [57]	Ti/ZrO_2/Pt [57]
Pt/HfO_2/Pt [58]	TiN/HfO_2/Pt [59]
Pt/Al_2O_3/Ru [60]	Ti/Al_2O_3/Pt [61]

TableI.6. Switching modes with different memory stacks; adopted from [44].

The origin of the unipolar and bipolar switching in RRAM devices is an active area of research and is not fully understood. Since with same oxide, different switching types are observed just by changing the electrode material, this indicates that the polarity of the switching is not a property of the oxide layer alone but the combination of both the oxide and oxide/electrode interfaces [44]. RRAM operation essentially relies on the migration of oxygen defects (oxygen vacancies V_o and oxygen interstitials O_i) and the formation of CF during the forming operation induces the migration of oxygen ions towards oxide/electrode interfaces or around the CF region under the applied field. In most cases, unipolar switching is observed when a noble metal like Pt or Ru is used as both top and bottom electrodes [44]. When one of the electrodes is replaced by an oxidizable metal like Ti or Hf bipolar mode is observed as shown in TableI.6. Cagli et al. performed systematic study of the switching mode of Pt/HfO_2/Ti, Pt/HfO_2/Pt (unipolar) devices and found that when Ti replaces the top electrode Pt, the switching mode becomes bipolar. Hence, the O reactivity of the electrodes plays a crucial in the switching mode. In unipolar mode where the electrodes are noble and non-reactive with O, during the forming/SET operations that cause the formation of conductive V_o rich CF region, the oxygen ions (Oi^{2-}) preferentially remain dispersed around the CF region and at the electrode/oxide interface [69,44]. During RESET, the O ions at the interface or the region around CF migrate back to the CF region due to the concentration gradient and recombine with it. During this mode, the RESET process usually involves high RESET current (see TableI.5) that raises the local temperature around the CF supporting the thermal dissolution model of the CF [70]. For the bipolar mode, O ions react with the oxidizable electrode (like Ti) creating some O reservoir at the electrode

after the forming/SET operations. During the RESET process, the thermal effect in not enough to drive the O ions back to the CF region and hence the application of field in the opposite polarity is required. This opposite polarity allows the migration of the O ions back to the CF to recombine with it [44]. This picture of RESET in bipolar mode may somehow seem consistent, it is important to note that the mechanisms of switching remain unclear and a microscopic understanding of the origin of the switching modes is an intense field of research.

I.4.4 Uniformity of the switching parameters

RRAM devices switch between two stable resistance states namely R_{off} or HRS and R_{on} or LRS to respectively define the Logic states 0 and 1. The ultimate goal being to integrate the devices into a novel circuit design where these logic states are well defined, the uniformity of the switching parameters especially R_{off} and R_{on} becomes very important. This is because clearly defined logic states reduce the error margins in reading the devices' states and also reduce the complexity of the circuits that would otherwise be needed for error corrections or intelligent reading schemes. Significant fluctuations exist in the values of the switching voltages as well as the resistance values of both R_{on} and R_{off}. The resistance fluctuations may be due to device-to-device variations or cycle-to-cycle variations. Low resistance variation may be due to the change in the filament diameter or the number of CFs responsible for ON state [44]. This R_{on} state is, though, mostly determined by the compliance current [71] which can be properly controlled, for example, by a select transistor as shown in FigI 25. The higher the compliance current, the lower the low resistance state R_{on}. Within the filamentary switching picture, R_{off} fluctuations are essentially due to the change of the thickness of the ruptured CF region (gap thickness). Any small variation in the gap thickness may be magnified due to the exponential dependence of the tunneling current on the distance [44]. It is therefore more difficult to control the R_{off} state since the RESET current is not controlled. FigI.26 shows that the variability of R_{off} is the same and exhibit the same slope of the distribution for all the test conditions. This is in agreement with the recent reported results of Garbin et al. [72] where they observed a plateau in the R_{off} distributions (same variability) irrespective of the test conditions. Therefore, R_{off} variation seems to be an intrinsic property of the HfO_2 layer and its improvement may necessitate further engineering of the dielectric material.

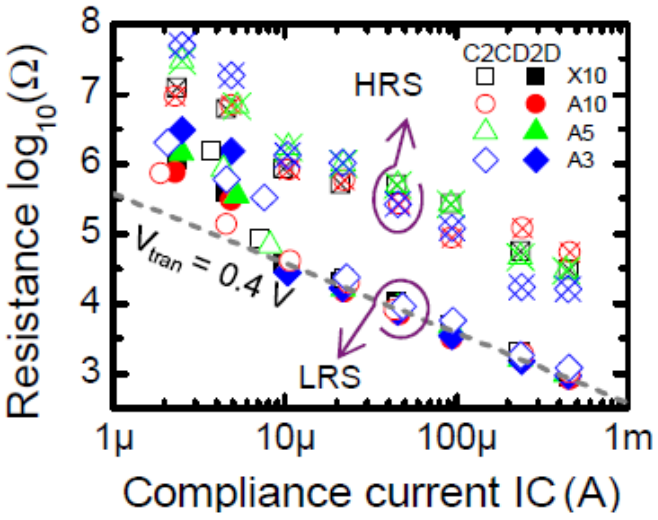

FigI 25. R_{on} or LRS dependence on the compliance current; adopted from [71].

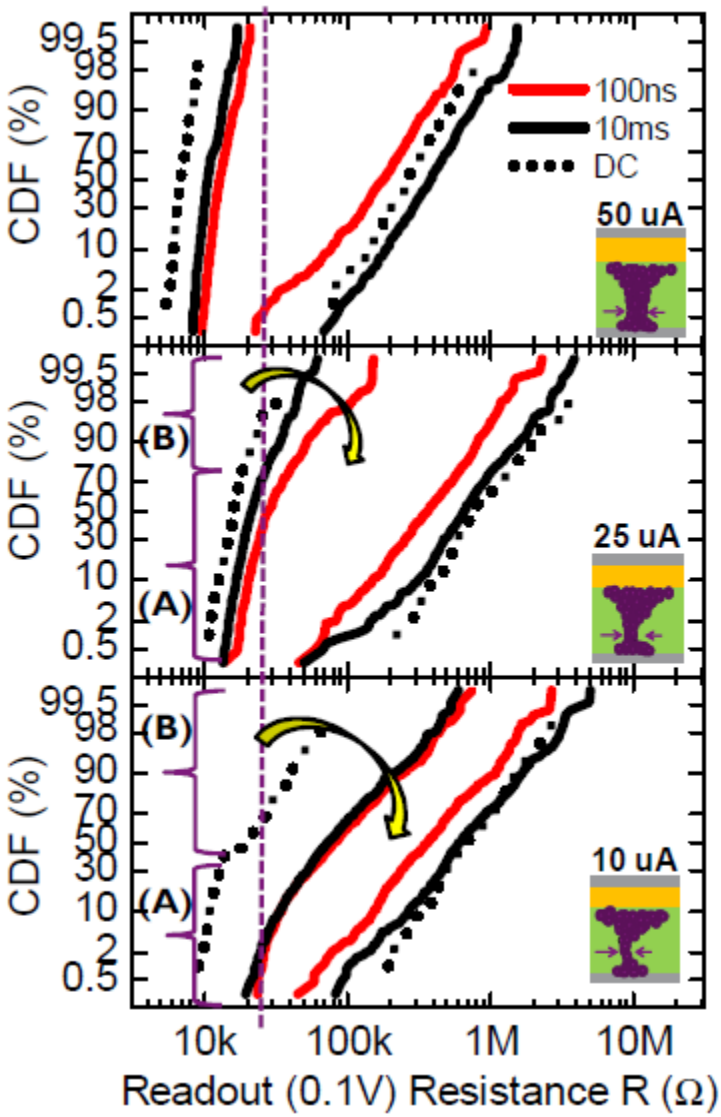

FigI.26. Distributions of LRS and HRS under different conditions with TiN/HfO_2/Hf stack. HRS distributions remain unaffected and the slope of the distribution is almost the same for all test conditions; adopted from [71].

I.4.5 Thermal stability

One important requirement of the non-volatile memories in both embedded and stand-alone applications is the 10 years data retention compliance. Depending on the applications and especially in automotive environments, system temperature can be very high. This raises questions about system's reliability under extreme working conditions. As HfO_2 RRAMs are regarded as potential candidate for future non-volatile memory applications, the memory devices' thermal stability is of great importance. Several groups have investigated the thermal stability of both pure HfO_2 based cells as well as HfO_2 doped or alloyed based devices. FigI.27 shows the evolution of both LRS and HRS during the data retention test performed by Chen et al. [60]. With the retention time, LRS fails towards HRS while HRS keeps on drifting towards higher resistance values and this process is activated in temperature. They extracted similar activation energy for both LRS and HRS failure suggesting that similar failure mechanism is present for both states FigI.27 (right). They attributed the failure of LRS towards HRS to the oxygen vacancy diffusion and two possible cases were proposed (FigI.28) : 1) O atoms scavenged by the Hf cap diffuses back into HfO_2 and recombines with the V_o, thus explaining the failure of LRS towards HRS or 2) the lateral diffusion of V_o out of the CF region. They claim that case (1) would be dependent on the device area because it involves the entire oxide/electrode interface while case (2) would be area independent. The interpretation of the R_{on} retention failure mechanism is also subject to active area of research and the debate remains open about bringing consistent and solid microscopic understanding about it. The retention failure mechanism will be discussed in the chapter on the impact of doping (Chapter IV). From application point of view, one interesting thing to note from the results of Chen et al. [60] is the high activation energies extracted from the test which indicate that $TiN/HfO_2/Hf$ devices are thermally stable.

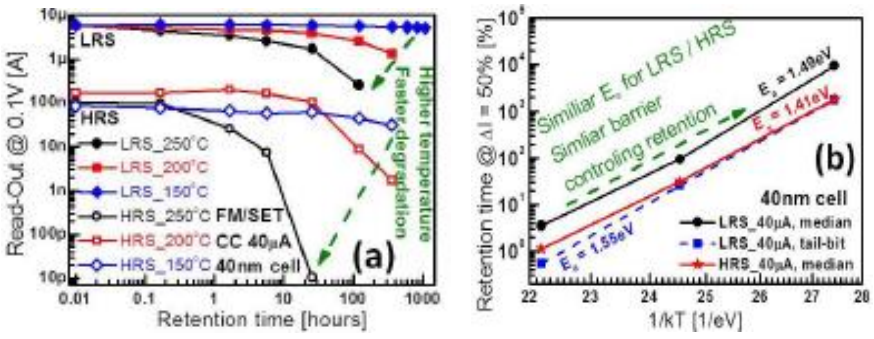

FigI.27. (Left) The evolution of both LRS and HRS with retention time for $TiN/HfO_2/Hf$ devices. LRS fails towards HRS and HRS drifts towards higher resistance values. (Right) Extracted activation for HRS and LRS using the Arrhenius equation; adopted from [60].

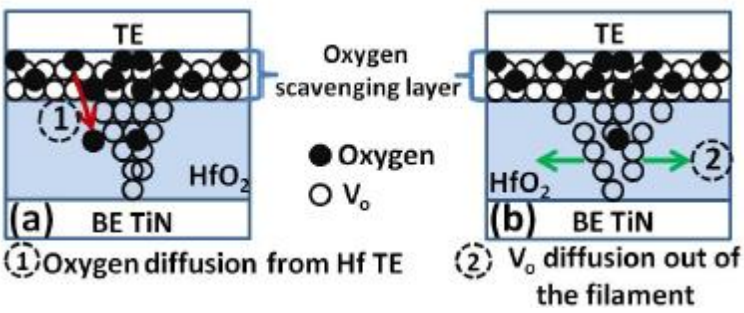

FigI.28. Possible retention degradation mechanism in HfO_2 RRAM (a) O scavenged by the Hf cap layer diffuses back into HfO_2 and recombine with V_o; this is area dependent (b) LRS failure to HRS due to lateral diffusion of V_o and this scenario is area independent; adopted [60].

Similarly, Lee et al. [73] demonstrated long data retention performance of $TiN/HfO_2/Ti$ devices at 200°C while Cabout et al. [74] reported excellent retention performance of both LRS and HRS of the same memory stack for 68 days at 150°. However, the results shown in FigI.27 suggest an LRS failure towards HRS. This trend may not always be true when LRS is very stable with thicker CF size. Indeed, Yu et al. performed Monte-Carlo simulations to study the low resistance state retention performance of HfO_2 based RRAM and found that the thermal stability of the LRS state largely depends on the CF size (indirectly the compliance current) [75]. The lower the value of the initial state of the resistance before the test (thicker CF size), the longer the retention time (more stable) of the device will be. Thicker CF corresponds to a lower resistance value which is achieved by enforcing higher compliance current through the devices. This may have other effects such as the increase of RESET current to reprogram the devices to high resistance state. Nevertheless, it is important to note that the profile of the resistance evolution during the data retention test is largely dependent on the conditions at which the devices were programmed.

As we have seen in the previous section, the choice of the electrode material plays an important role in RRAM performance and so ultrathin Pt/HfO_2(~2nm)/TiN devices were investigated by Zhao et al [59] and good thermal stability was demonstrated even though the extrapolated 10 years retention was at 20°C. This may not be sufficient for applications requiring 10 years data retention at a temperature of at least 85°C. However the use of ~2nm HfO_2 oxide opens the way for ultra-scaling of RRAM devices. For a direct comparison of the electrode impact on data retention, [62] looked at the R_{on} retention of $Pt/HfO_2/Pt$ and $TiN/HfO_2/Ti$ samples and found that $TiN/HfO_2/Ti$ devices exhibited better thermal stability. Therefore, not only the

introduction of Ti improved the devices' switching characteristics but also enhanced their thermal stability as well.

The impact of alloying HfO_2 with Al_2O_3 and the bilayer Al_2O_3/HfO_2 devices were also respectively investigated in [76] and [77]. For both stack structures, the data retention performance of the memory stack was improved compared with HfO_2 alone.

I.4.6 Endurance

The assessment of HfO_2 based RRAM devices in terms of their endurance performance and the associated failure mechanisms is also necessary for a thorough reliability study. Earlier endurance tests on $TiN/HfO_2/Ti$ memory cells were generally limited to 10^6-10^7 cycles [61,78] which were just sufficient to demonstrate their higher cycling ability compared to NAND Flash memories. However, for RRAM to be envisaged as DRAM replacement, excellent endurance (10^{15} to 10^{18} cycles) will be required. Recently, Chen et al. demonstrated cycling endurance of over 10^{10} cycles with $TiN/HfO_2/Hf$ memory stack [79]. This will still need to be improved by adopting some intelligent characterization techniques. FigI.29 shows the cycling endurance of some of the RRAM technologies. We note that $TiN/HfO_2/Ti$ stack endurance needs further improvement.

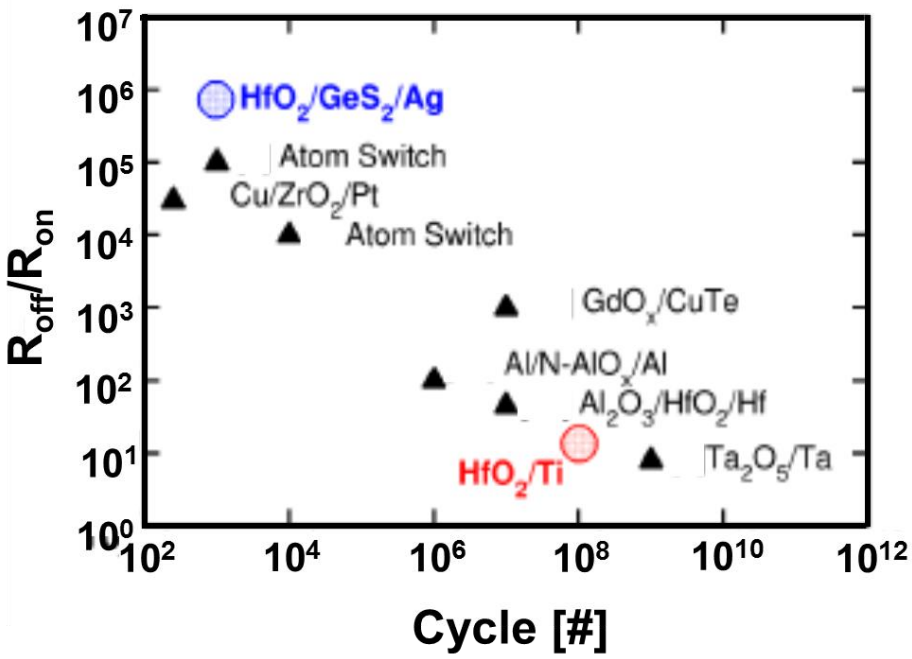

FigI.29. Endurance performance of some of the RRAM technologies; adopted from [40].

It often happens that LRS fails towards HRS (gets stuck to HRS) during the endurance test (FigI.30 left). Chen et al. attributed this failure to a progressive degradation of V_o diffusion barrier in the CF due to high local temperature [80]. It could also be due to the reinforcement of the interfacial layer between the oxidizable electrode and the HfO_2 layer making it difficult to SET [44]. The endurance failure also occurs in the opposite direction whereby the devices get stuck to LRS State (FigI.30 right). Wong et al. attempted to explain this phenomenon by 3 possible ways : (1) too many V_o generated at or near the electrode/oxide interface; (2) too many V_o generated in or near the CF; or (3) too many V_o generated inside the HfO_2 matrix [44]. Although, the devices fail during the endurance, Chen et al. observed that the failed devices could be recovered after the test using DC sweeps [79] indicating that the endurance failure is not permanent. Hence, there is still more to understand about the devices failure mechanisms and it is becoming more complex to decouple phenomena due to the presence of many failure modes.

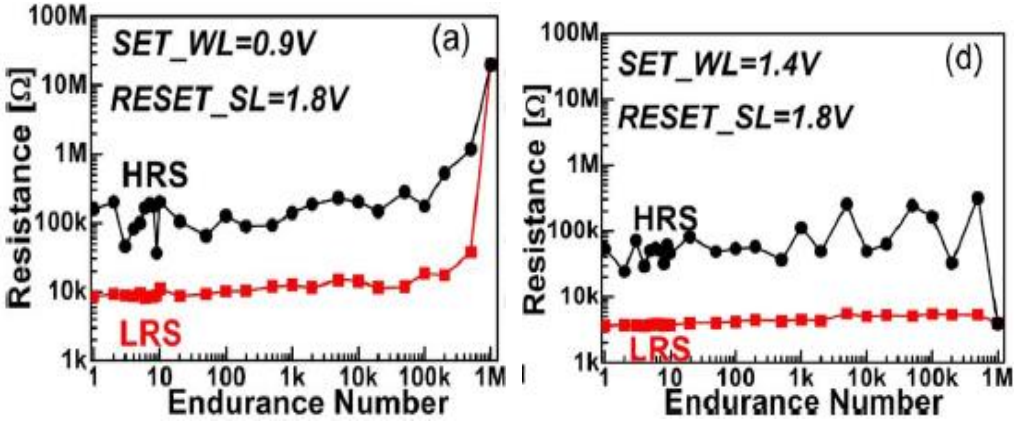

FigI.30. Different endurance failure modes (left) failure stuck at HRS (right) failure stuck at LRS; adopted from [79].

I.4.7 Mechanisms of switching

The simplicity of RRAM devices structure (MIM structure) is in contrast with the acquired understanding about the mechanisms responsible for the resistive switching. The fact that resistive switching phenomena have been observed in so many materials has also contributed to the difficulty about having a consensual physical picture. Nevertheless, as far as binary metal-oxides sandwiched between electrodes are concerned, filamentary resistive switching, as shown in FigI.31, is widely accepted [81,82,83,44]. In filamentary switching, localized conductive paths called conductive

filaments (CF) serve as conductive medium for the RRAM during the low resistance state LRS or R_{on} and the rupture of the CF bring the devices to HRS or R_{off}. The main argument behind filamentary switching is through the experimental observation that devices' low resistance state R_{on} is area independent as shown in FigI.32. The area independence of R_{on}, indeed, supports conduction through localized regions but not sufficient to explain the dependence of R_{off} on area for some RRAM cells (FigI.32 left). However, recent physical characterization experiments using HRTEM and CAFM techniques also support the idea of localized conductive regions in the oxide layer after electroforming [84].

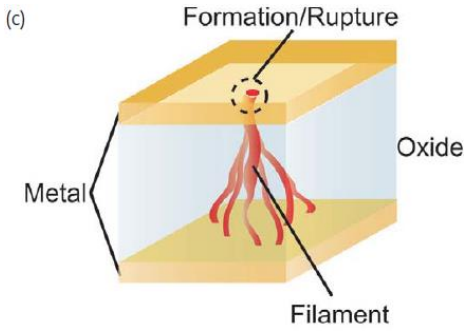

FigI.31. Filamentary conductive path in a metal-oxide-metal structure [85].

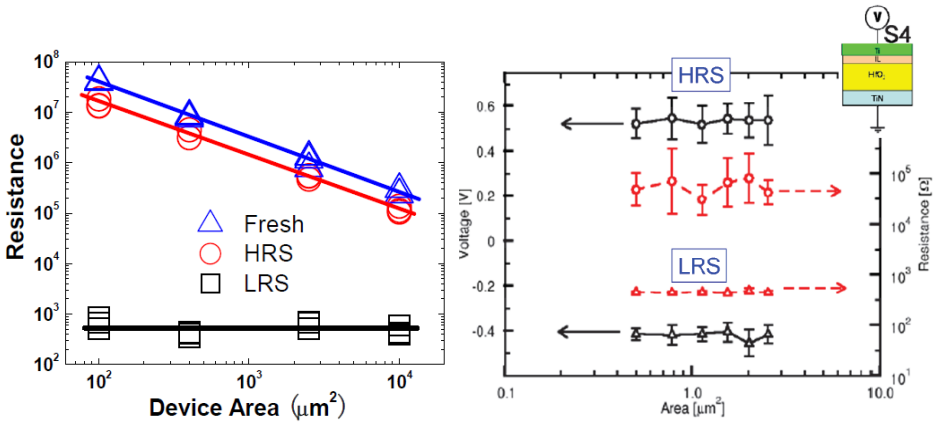

FigI.32. Electrical characterization data showing the no dependence of LRS on area (left) from [86] and (right) from [62].

I.4.7.1 Forming mechanism

In general, RRAM devices need to be preconditioned for resistive switching through the operation of forming. Statistical consideration of the dielectric breakdown through time dependent dielectric breakdown (TDDB) data shows an exponential dependence of forming time on applied voltage which indicates that the forming process in not a one event/simultaneous process but a process resulting from an upsurge of defects [87,44]. Hence, forming process is stochastic in nature but the conclusion is not

enough in understanding the origin of the soft breakdown of the dielectric leading to CF formation. Several models are proposed in the literature about the formation of these conductive filaments in binary metal-oxides RRAM. Some of them are briefly described in the following:

Bersuker et al. identified the grain boundaries (GB) in HfO_2 as constituting leakage paths that ultimately transform into the CF during the forming process [88] which is consistent with GB assisted filament formation reported by Lanza et al. [89]. This filament is an aggregation of oxygen vacancies with charge +1 (V_o^{1+}). With the field applied and under temperature, V_o^{2+} migrate and segregate at GB and these charged V_o^{2+} are then converted to V_o^{1+} by capturing electron from the cathode . The released O^{2-} ions migrate towards the anode creating an interfacial layer. The conduction through these V_o^{1+} vacancies is achieved via trap assisted tunneling (TAT) according to:

$$V_o^{1+} + e^- \rightarrow V_o^0 \rightarrow V_o^{1+} + e^- \qquad \text{(I. 1)}$$

This forming model is similar to what has been proposed by Vandelli et al. [90].

Zhao et al. [91], inspired from the work of Jeong et al. [92], explained the forming process, using $Pt/TiO_2/Pt$ stack), through the formation of oxygen ions and oxygen vacancies at the anode. The oxygen vacancies migrate towards the cathode and grow into a cone-shaped CF of Ti_4O_7 with the larger side of the cone at the cathode. The O ions are removed from the oxide and chemisorbed at the GB of Pt electrode near the anode interface. Jeong et al. working on similar $Pt/TiO_2/Pt$ stack further elaborates on the Ti ions [92]. The Ti ions in the oxygen deficient regions might be reduced to fulfil the local charge neutrality by capturing electrons from the cathode, according to

$$T_i^{4+} + ne^- \rightarrow T_i^{(4-n)+} \qquad \text{(I. 2)}$$

Theses reduced valence states of Ti ions with the oxygen vacancies can form metallic phase in the form $TiO_{2-n/2}$ for approximately n > 1.5. According to Waser et al., this conductive $TiO_{2-n/2}$ forms a sort of "virtual cathode" that moves towards the anode [32].

The common point about all these models which is consensual and widely accepted is that the conductive region or CF is oxygen deficient, rich of oxygen vacancies. The models do not agree about the charge state of this V_o rich region and which V_o type migrates during the CF formation. Also, what this V_o rich region looks like, its composition and morphology is very unclear. Another point that the majority of the models does not consider or mention is the possible migration/diffusion of the metal electrode into the oxide layer during the CF formation. In the case of $TiN/HfO_2/Ti$

based RRAM, this scenario may not be completely excluded as is proposed by Privitera et al. working on TiN/HfO_2/Ti devices through the experimental EELS STEM technique [93].

I.4.7.2 Nature of CF

As mentioned in the previous section, the widely accepted model about metal-oxide based resistive switching is that conduction occurs via localized conductive filament CF. Furthermore, another accepted picture about this CF is that it is rich of oxygen vacancies. However, it remains unclear whether this CF is a rich metal cation precipitate, a sub-oxide, a mixture of sub-oxides and electrode atoms etc. In order to partly elucidate some of these open questions that are very active areas of research, some experimental and theoretical works have been carried out.

As far the experimental works are concerned, the important milestone was the identification of the Magneli phase Ti_4O_7 by Kwon et al. as the conductive filament in Pt/TiO_2/Pt stack using in-situ TEM [56]. This result gave more credit to the widely accepted picture of the predominance of oxygen vacancies in the CF region. Calka et al. also performed physico-chemical characterization on TiN/HfO_2 memory stack using the CAFM (Conducting Atomic Force Microscopy) diamond tip as the top electrode [84]. They identified CF region that are HfO_{2-x} defective in oxygen and spreading along both grain and GB in the oxide layer as shown in FigI.33. Their result confirmed the role of GB in the CF formation and the oxygen deficiency of the CF region. However, they did not identify a particular phase for the conductive filament.

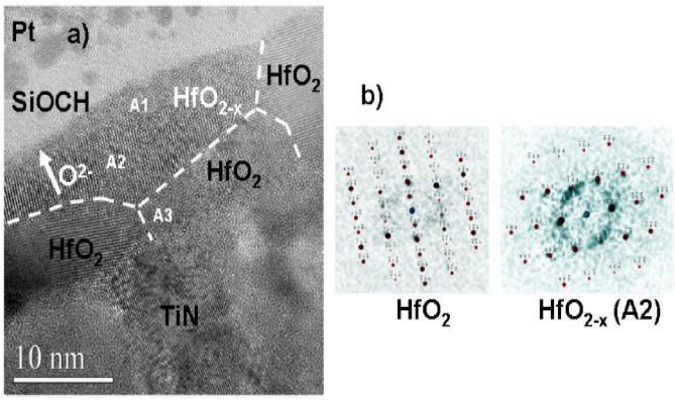

FigI.33. High-Resolution TEM image of the HfO_{2-x} conductive region. GB are represented by dashed lines and the amorphous regions are labelled A; adopted from [84].

As for the theoretical calculations, Park et al investigated the effect of oxygen vacancy ordering in rutile TiO_2 and found that ordered V_o chain could serve as a conductive channel during the switching (FigI.34) [94]. According to the authors, the V_o ordering serving as a conductive channel is compatible to the Magneli phase conductive CF which is known to have a long range of order of successive oxygen vacancies. Cartoixa et al. also investigated the transport properties of V_o filament in HfO_2 and concluded that even a single vacancy filament could sustain conduction [95].

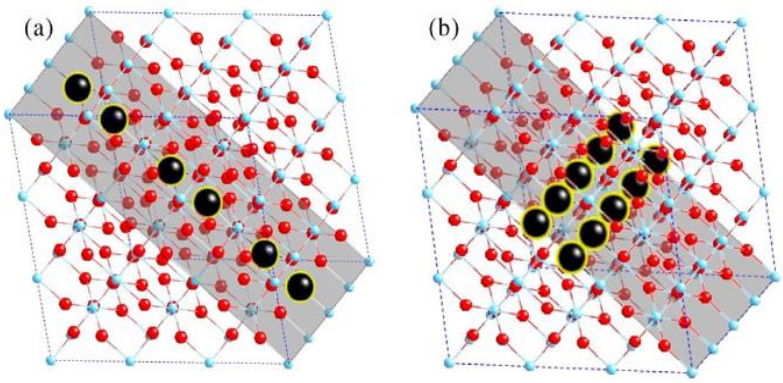

FigI.34. Oxygen vacancy channel in rutie TiO_2 serving as a conducting channels [94].

Recently, McKenna investigated the nucleation and growth of metal-rich precipitates in HfO_x sub-oxides [96]. He calculated an optimal HfO_x stoichiometry with x in the range 1.50 – 1.75 for efficient nucleation and growth of Hf-rich clusters which may serve as precursors for the growth of CF during forming. However, his calculations do not provide information about what would be the stoichiometry of the CF. Therefore, more theoretical studies are needed in order to have better insight about the structure and stoichiometry of the CF.

I.4.7.3 Conduction mechanisms

In order to engineer and fabricate optimized RRAM devices, understanding their conduction mechanism and the properties of the CF become necessary. This may be achieved through careful physical and electrical characterization techniques. In literature, intensive efforts have been devoted to understanding the properties of the CF by studying the temperature dependence of the devices' state and through some other novel techniques such as complex impedance spectroscopy and low-frequency noise measurements. In general, Ohmic type of conduction is observed in LRS (not always) while there is a huge controversy about HRS. Among the conduction mechanisms

proposed for HRS are Pool-Frenkel (PF) [97] , Space Charge Limited Current (SCLC) [98], Trap Assisted Tunneling (TAT) [99], Schottky emission [51]. FigI.35 shows the different conduction mechanisms that are possible in RRAM devices. The predominance of one type compared to the other may be due to the electrode/oxide interface properties, the fabrication process, defect density, trap energy levels etc. [44].

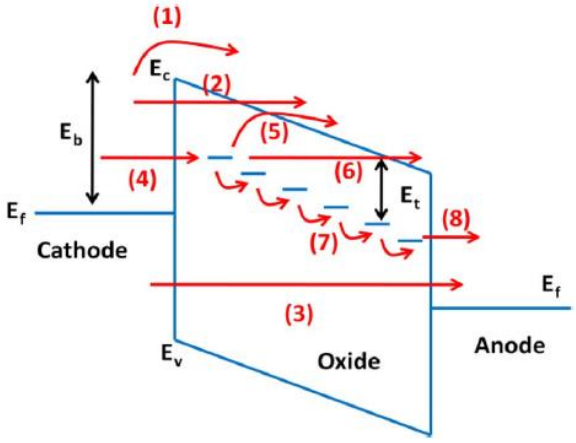

FigI.35. Schematic of possible electron conduction paths in RRAM. (1) Schottky emission (2) Fowler-Nordheim FN tunneling from cathode into conduction band CB(3) Direct tunneling (4) tunneling from cathode to trap (5) Pool-Frenkel emission : emission from trap to CB (6) FN from trap CB (7) trap to trap hopping in the form of Mott hopping (8) tunneling from trap to anode; adopted from [44]

Nevertheless, Yu et al. studied the conduction properties of HRS in Pt/HfO_2/TiN memory stack and fitted their experimental data to both Pool-Frenkel (PF) and Trap Assisted Tunneling models (TAT) [99]. By analyzing the fitting parameters extracted from their experimental data, they concluded that the extracted trap energy and the HfO_2 dielectric constant with the PF model were unreasonable and that TAT was the dominant transport mechanism at low bias. Walczyk et al. studied the temperature dependence of both HRS and LRS in TiN/HfO_2/Ti devices and used the quantum-point contact (QPC) model to fit their data [100]. They found that R_{on} has a weak metallic-like characteristics and that the QPC model can be consistently applied to both LRS and HRS. This goes in line with the results of Prócel et al. who also showed that the QPC model agrees well with the conduction behavior of both LRS and HRS for their TiN/HfO_2/Hf devices [101]. On contrary, Kim working on Mo/HfO_2/Mo devices showed that the conduction in the high resistance state HRS was Pool-Frenkel type mechanism while LRS exhibited Ohmic conduction behavior. For LRS, Privitera et al. also observed metallic-like behavior for TiN/HfO_2/Ti and TiN/HfO_2/Hf RRAM cells where the devices' resistance increased with temperature [93]. However, the

semiconducting like behavior of LRS observed by De Stefano et al. [64] working on TiN/HfO_2/TiN devices contrasts the usual metal-like Ohmic conduction behavior observed in the low resistance state of most RRAM devices. Similarly, Jiang et al. observed different conduction mechanisms in LRS state depending on the deposition condition of their Pt/HfO_2/Ti devices [102]. When HfO_2 was deposited by Pulsed Laser Deposition (PLD), both LRS and HRS exhibited semiconductor like behavior while when HfO_2 was deposited by sputtering, HRS had semiconductor like behavior and LRS a metal-like behavior. Lin et al. reported Schottky emission mechanism for HRS with Pt/ZrO_2/Pt RRAM [103] while Lee et al. reported SCLC conduction for both LRS and HRS states [73].

It is remarkable that there are so many conduction mechanisms reported in the literature. This is probably due to the fact that many parameters play crucial roles in RRAM switching such as the oxide deposition conditions, the oxide/electrode interface, the programming conditions (high vs. low compliance currents) etc. Hence, despite the widely accepted filamentary model of the metal-oxide RRAM devices, the diversity of the conduction mechanisms observed in the literature is a fair reflection of the difficulty involved in finding consistent physical mechanism for their operation. Unfortunately or fortunately, this step will have to be overcome for RRAM to hold promise for becoming a credible choice for NAND flash replacement and future low power non-volatile memory applications.

I.5 Opportunities for RRAM

In this information technology era, a large number of application opportunities have opened up for semiconductor memory technologies. FigI.36 shows a range of applications in which non-volatile memories play a key role. With the concept of internet of things (IoT) where the core computing data centers connect billions of devices to which it is expected that trillions of other smart devices will be connected with the whole system forming this unprecedented large network of devices, ultralow power circuits and memory technologies are required [104]. In addition, a wider space has opened up in the traditional memory hierarchy due to the rate improvement in microprocessor speeds that by far exceed those of DRAM memory and the storage media such as the Hard Disk Drive (HDD) as shown in FigI.37. This speed/capacity gap is a bottleneck for high performance computing but at the same time necessitates the search for new generation of memory technologies the so called storage class memories

(SCM). Solid States Drives (SDD) based on NAND Flash have been used to speed up the computing performance by allowing faster data access time compared to HDD but this will not be sufficient for very high speed systems. As such, non-volatile RRAM technologies have a huge potential to be used in any of the memory hierarchy in addition to the NAND Flash replacement that is generally mentioned. The research and development in the field is in steady progress and the storage capacity follows a somehow exponential increase as is supported by FigI.38. In less than 8 years of intensive R&D in the field, RRAM has surpassed the demonstrated storage capacity of the more mature PCM technology and is approaching the 128 Gb of NAND Flash. Hence, the perspectives for RRAM to be the technology of choice, for at least one or most of the new non-volatile market opportunities, are promising. However, RRAM technology will first have to gain more maturity and a solid understanding about its switching mechanisms will be required. Finally, the emergence of a high density array with excellent device yield, repeatability and reliability will surely help pave the way for its transition towards commercial mass-scale production.

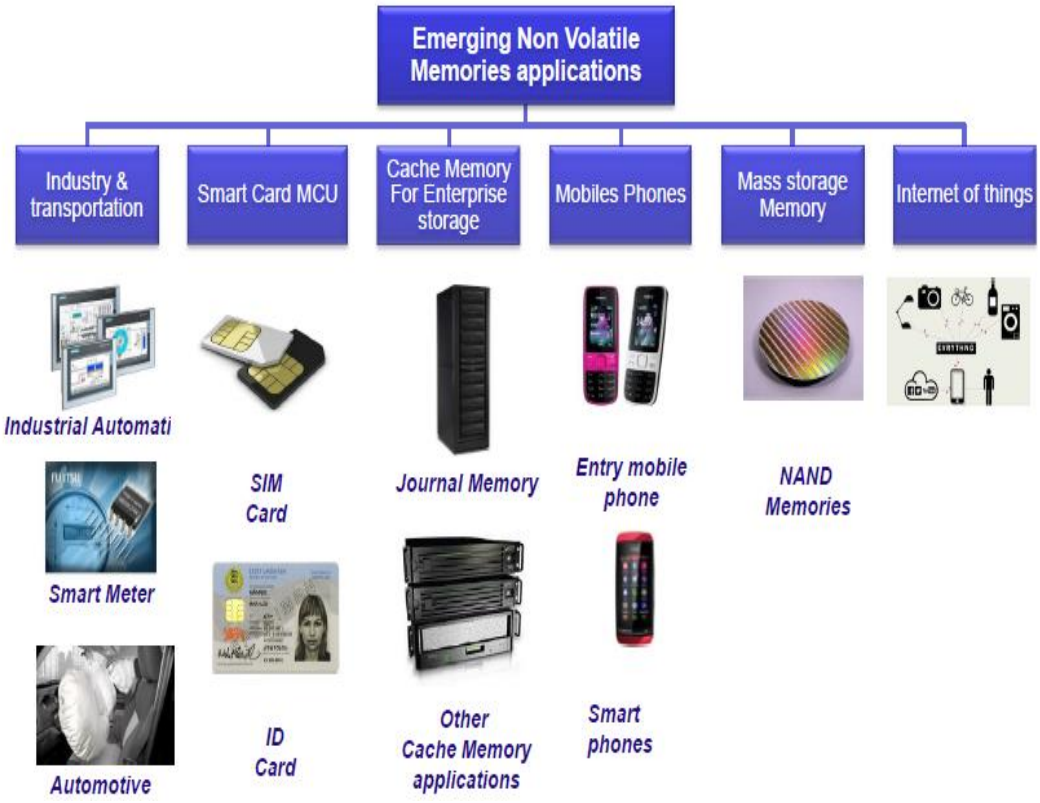

FigI.36. Emerging non-volatile memory applications; adopted from [38].

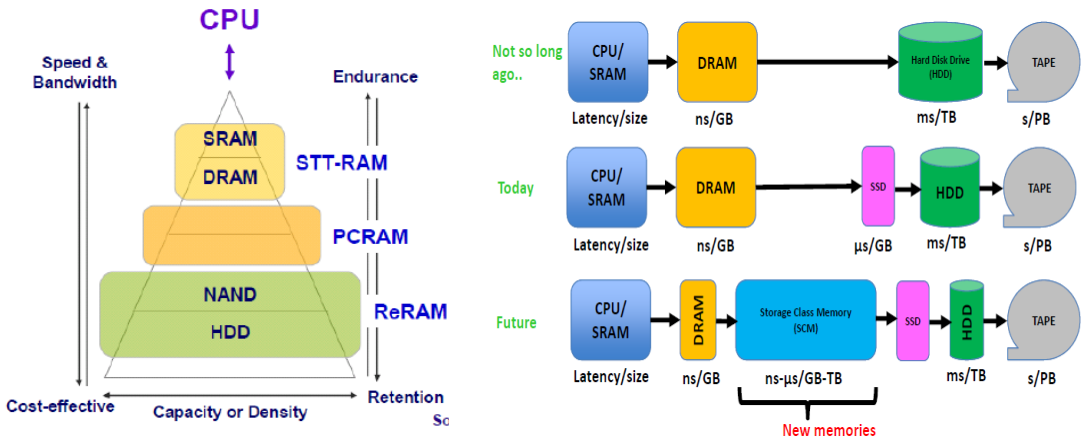

FigI.37. Memory hierarchy in computing landscape; (left) from [38] and (right) from [105].

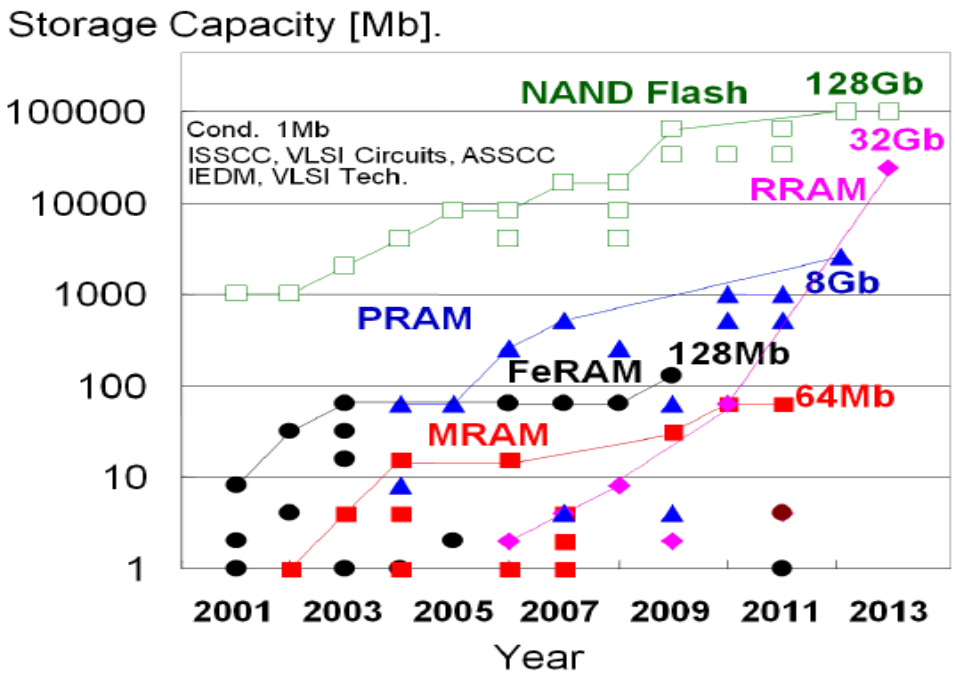

FigI.38. Non-volatile memory trend; adopted [106].

References

[1] CPU World, 2014. [Online]. http://www.cpu-world.com/CPUs/4040/

[2] Intel, 2014. [Online]. http://ark.intel.com/products/80807

[3] ChannelTimes, 2010. [Online]. http://www.channeltimes.com

[4] IC Insights, 2012. [Online]. http://www.icinsights.com

[5] World semiconductor trade statistics (WSTS). [Online]. https://www.wsts.org/

[6] Glen Hawk, "Now is the Time for Flash Storage", 2012, Micron technology, Inc.

[7] S. Natarajan, S. Chung, L. Paris and A. Keshavarzi, "Searching for the dream embedded memory," *IEEE Solid Stat. Circ. Mag*, pp. 34 - 44, 2009.

[8] M.H. Kryder and C.S. Kim, "After Hard Drives—What Comes Next?," *IEEE Trans. Magnetics.*, vol. 45, no. 10, 2009.

[9] B. De Salvo, *Silicon Non-Volatile Memories : Paths of Innovation*, Wiley, Ed. USA, 2009.

[10] MRAM : SERIAL AND PARALLEL MEMORY PRODUCTS, December 2013. [Online]. http://www.everspin.com

[11] R. Bez, E. Camerlenghi, A. Modello and A. Visconti, "Introduction to Flash Memory," *Proceedings IEEE* , vol. 91, no. 4, 2003.

[12] J. S. Meena, S. M. Sze, U. Chand and T. -Y. Tseng, "Overview of emerging nonvolatile memory technologies," *Nanosc. Resear. Lett.*, vol. 9, p. 526, 2014.

[13] Q. Hubert, Optimisation de mémoires PCRAM pour générations sub-40 nm : intégration de matériaux alternatifs et structures innovantes, 2013, Thesis dissertation.

[14] S.K. Lai, "Brief history of ETOX NOR flash memory," *J. Nanosci. Nanotech.*, vol. 12, no. 10, pp. 7597–7603, 2012.

[15] J. Hruska. EXTREMETECH, 2014. [Online]. http://www.extremetech.com/

[16] Samsung, 2014. [Online]. http://www.samsung.com/

[17] S. Lawson. PCWorld, 2014. [Online]. http://www.pcworld.com/

[18] Samsung Tomorrow, 2014. [Online]. http://global.samsungtomorrow.com/

[19] International technology Roadmap for Semiconductors, 2012. [Online]. http://www.itrs.net

[20] E.F. Runnion, S.M. Gladstone, R.S. Scott Jr., D.J. Dumin, L. Lie, J.C. Mitros, "Thickness dependence of stress-induced leakage currents in silicon oxide," *IEEE TED*, pp. 993 - 1001, 1997.

[21] G. Molas, D. Deleruyelle, B. De Salvo, G. Gibaudo, M. gely, L. Perniola et al., "Degradation of floating-gate memory reliability by few electron phenomena," *IEEE TED*, vol. 53, pp. 2610 - 2619, 2006.

[22] A.V. Khvalkovskiy, D. Apalkov, S. Watts, R. Chepulskii, R.S. Beach, A Ong et al., "Basic principles of STT-MRAM cell operation in memory arrays," *J. Phys. D: Appl. Phys.*, vol. 46, no. 074001, 2013.

[23] B.F. Cockburn, "Tutorial on magnetic tunnel junction magnetoresistive random-access memory," *Memory Tech. Desig. Test.*, pp. 46-51, 2004.

[24] W.J. Gallagher, "Emerging Nonvolatile Magnetic Memory Technologies," *IEEE Inter. Conf. Solid Stat. Integ. Circu. (ICSICT)*, pp. 1073 - 1076, 2010.

[25] G. Prenat, G. Di Pendina, C. Layer, O. Goncalves, K. Jaber, B. Dieny et al., "Magnetic memories : From DRAM replacement to ultra low power logic chips,"

Design, Automation and Test in Europe Conference and Exhibition, p. 1, 2014.

[26] M. Di Ventra and Y. Pershin , "Memory effects in complex materials and nanoscale systems," *Avances in Physics*, no. 2, p. 60, 2011.

[27] G.W. Burr, M.J. Breitwisch, M. Franceschini, D. Garetto, K. Gopalakrishnan, B. Jackson et al., "Phase change memory technology," *Journ. Vacu. Scien. tech. B.*, vol. 28, pp. 223 - 262, 2010.

[28] Q. Hubert, C. Jahan, A. Toffoli, G. Navarro, S. Chandrashekar, P. Noe et al., "Carbon-doped $Ge_2Sb_2Te_5$ phase-change memory devices featuring reduced RESET current and power consumption ," *IEEE ESSDERC*, pp. 286 - 289, 2012.

[29] A. L. Lacaita and A. Redaelli, "The race of phase change memories to nanoscale storage and applications," *Microelec. Eng.*, vol. 109, pp. 351 - 356, 2013.

[30] D. Ielmini and A. Lacaita, "Phase change materials in non-volatile storage," *Materialstoday*, vol. 14, no. 12, 2011.

[31] H.-S.P. Wong, S. Raoux, S. Kim, J. Liang, J.P. Reifenberg, B. Rajendran et al. , "Phase ChangeMemory," *Proceedings IEEE*, vol. 98, no. 12, 2010.

[32] R. Waser and M. Aono, "Nanoionics-based resistive switching memories," *Nat. Mater.*, vol. 6, pp. 833 - 840, 2007.

[33] R. Waser, R. Dittmann, G. Staikov, and K. Szot, "Redox-based resistive switching memories – nanoionic mechanisms, prospects, and challenges," *Adv. Mater.*, vol. 21, pp. 2632–2663, 2009.

[34] C. Gopalan, Y. Ma, T. Gallo, J. Wang, E. Runnion, J.Saenz et al., "Demonstration of conductive bridging random access memory (CBRAM) in logic CMOS process," *Solid-Stat. Elec.*, vol. 58, pp. 54 - 61, 2011.

[35] K. Aratani, K. Ohba, T. Mizuguchi, S. Yasuda, T. Shiimoto, T. Tsushima et al., "A novel resistance memory with high scalability and nanosecond switching," *IEEE IEDM*, pp. 783 - 786, 2007.

[36] E. Vianello, G. Molas, F. Longnos, P. Blaise, E. Souchier, C. Cagli et al., "Sb-doped GeS_2 as performance and reliability booster in conductive bridge RAM," *IEEE IEDM*, pp. 31.5.1 - 31.5.4, 2012.

[37] Memory Strategies International, 2014. [Online]. http://www.memorystrategies.com

[38] Y. De Charentenay, "Emerging NVM enter niche memory markets; expected to reach $ 2B by 2018. Will NVM eventually… => When NVM will replace DRAM and NAND ?," *LETI Memory Workshop*, 2014.

[39] B. Govoreanu, G.S. Kar, Y-Y. Chen, V. Paraschiv, S. Kubicek, A. Fantini et al., "$10x10nm^2$ Hf/HfO_x Crossbar Resistive RAM with Excellent Performance, Reliability and Low-Energy Operation," *IEEE IEDM*, pp. 31.6.1 - 31.6.4, 2011.

[40] E. Vianello, O. Thomas, G. Molas, O. Turkyimaz, N. Jovanovic, D. Garbin et al., "Resistive Memories for Ultra-Low-Power embedded computing design," *IEEE IEDM*, pp. 6.3.1 - 6.3.4, 2014.

[41] L. O. Chua, *IEEE Transa. Circ. Theor.* , vol. 18, no. 5, pp. 507-519, 1971.

[42] J.F. Gibbons and W.E. Beadle , "Switching properties of thin NiO films," *Solid-Stat. Elec.*, vol. 7, pp. 785-797, 1964.

[43] I.G. Baek, M.S. Lee, M.J. Lee, D.H. Seo, D.-S. Suh, J.C. Park et al., "Highly Scalable Non-volatile Resistive Memory using Simple Binary Oxide Driven by Asymmetric Unipolar Voltage Pulses," *IEEE IEDM*, pp. 23.6.1 - 23.6.4, 2004.

[44] H.-S.P. Wong, H.-Y. Lee, S. Yu et al., "Metal–Oxide RRAM," *Proceedings IEEE*, pp. 1951-1970, 2012.

[45] Y Wu, B. Leel and H.S-.P. Wong, "Al_2O_3-based RRAM using atomic layer deposition (ALD) with 1-µA RESET current," *IEEE Elec. Dev. Lett.*, vol. 31, pp. 1449-1451, 2010.

[46] W. Kim, S. Park, Z. Zhang, Y. Yang-Liauw, D. Sekar, H.-S.P. Wong et al., "Forming-free nitrogen-doped AlO_x RRAM with sub-µA programming current," *IEEE VLSI Tech.* , pp. 22-23, 2011.

[47] C. Cagli, D. Ielmini, F. Nardi and A. L. Lacaita, "Evidence for threshold switching in the set process of NiO-based RRAM and physical modeling for set, reset, retention and disturb prediction," *IEEE IEDM*, pp. 1 - 4, 2008.

[48] L. Goux, J.G. Lisoni, X.P. Wang, M. Jurczak and D.J. Wouters, "Optimized Ni Oxidation in 80-nm Contact Holes for Integration of Forming-Free and Low-Power Ni/NiO/Ni Memory Cells," *IEEE Trans. ELec. Dev.*, vol. 56, no. 10, 2009.

[49] F. Nardi, D. Ielmini, C. Cagli, S. Spiga, M. Fanciulli, L. Goux et al., "Sub-10 µA reset in NiO-based resistive switching memory (RRAM) cells," *IEEE IMW*, pp. 1 - 4, 2010.

[50] K.-C. Ryoo, J.-H. Oh, H. Jeong and B.-G. Park, "Irregular resistive switching characteristics and its mechanism based on NiO unipolar resistive random access memory (RRAM)," *Silic. Nanoelec. Work.* , pp. 1-2, 2010.

[51] Z. Wei, Y. Kanzawa, K. Arita, Y. Katoh, K. Kawai, S. Muraoka et al., "Highly Reliable TaO_x ReRAM and Direct Evidence of Redox Reaction Mechanism," *IEEE IEDM*, pp. 1 - 4, 2008.

[52] A. Kawahara, R. Azuma, Y. Ikeda, K. Kawai, Y. Katoh, Y. Hayakawa et al., "An 8 Mb Multi-Layered Cross-Point ReRAM Macro With 443 MB/s Write Throughput," *IEEE Journ. Sold-Stat. Circ.*, vol. 48, no. 1, 2013.

[53] Panasonic corporation, 2013. [Online]. http://news.panasonic.com

[54] M.-J. Lee, C.B. Lee, D. Lee, S.R. Lee, M. Chang, J.Y. Hur et al., "A fast, high-endurance and scalable non-volatile memory device made from asymmteric Ta_2O_{5-x}/Ta_2O_{5-x} bilayer structures," *Nature Mat.*, vol. 10, pp. 625-630, 2011.

[55] A. Prakash, J. Park, J. Song, J. Woo, E.-J. Cha, and H. Hwang, "Demonstration of Low Power 3-bit Multilevel Cell Characteristics in a TaO_x-Based RRAM by Stack Engineering," *IEEE Elec. Dev. Lett.*, vol. 36, no. 1, 2015.

[56] D.-H. Kwon, K. M. Kim, J. H. Jang, J. M. Jeon, M. H. Lee, G. H. Kim, et al., "Atomic structure of conducting nanofilaments in TiO_2 resistive switching memory," *Nat. Nanotechnol.*, vol. 5, p. 148, 2010.

[57] C. Walczyk, C. Wenger, D. Walczyk, M. Lukosius, I. Costina et al., "On the role of Ti adlayers for resistive switching in HfO_2-based metal-insulator-metal structures_ Top versus bottom electrode integration," *J. Vac. Sci. Technol. B*, vol. 29, no. 01AD02, 2011.

[58] Y.S. Chen, H.Y. Lee, P.S. Chen, C.H. Tsai, P.Y. Gu, T.Y. Wu et al., "Challenges and Opportunities for HfO_x Based Resistive Random Access Memory," *IEEE IEDM*, pp. 31.3.1 - 31.3.4, 2011.

[59] L. Zhao, Z.J. Jiang, H.-Y. Chen, J. Sohn, K. Okabe, B. Magyari-Köpe et al., "Ultrathin (~2nm) HfO_x as the Fundamental Resistive Switching Element: Thickness Scaling Limit, Stack Engineering and 3D Integration," *IEEE IEDM*, pp. 6.6.1 - 6.6.4, 2014.

[60] Y.Y. Chen, M. Komura, R. Degraeve, B. Govoreanu, L. Goux, A. Fantini et al., "Improvement of data retention in HfO_2/Hf 1T1R RRAM cell under low operating current," *IEEE IEDM*, pp. 10.1.1 - 10.1.4, 2013.

[61] H. Y. Lee, P. S. Chen, T. Y. Wu, Y. S. Chen, C. C. Wang, P. J. Tzeng et al., "Low Power and High Speed Bipolar Switching with A Thin Reactive Ti Buffer Layer in Robust HfO_2 Based RRAM," *IEEE IEDM*, pp. 1-4, 2008.

[62] C. Cagli, J. Buckley, V. Jousseaume et al., "Experimental and theoretical study of electrode effects in HfO_2 based RRAM," *IEEE IEDM*, pp. 658–661, 2011.

[63] T. Cabout, J. Buckley, C.Cagli et al., "Role of Ti and Pt electrodes on resistance switching variability of HfO_2-based resistive random access memory," *Thin Solid Films*, vol. 533, pp. 19-23, 2013.

[64] F. De Stefano, M. Houssa, J. A. Kittl, M. Jurczak, V. V. Afanas'ev et al., "Semiconducting-like filament formation in TiN/HfO_2/TiN resistive switching random access memories," *Appl. Phys. Lett.*, vol. 100, no. 142102, 2012.

[65] K.-L. Lin, T.-H. Hou, J. Shieh, J.-J. Lin, C.-T. Chou and Y.-J. Lee, "Electrode dependence of filament formation in HfO_2 resistive-switching memory," *Jour. Appl. phys.*, vol. 109, no. 084104, 2011.

[66] Y.Y. Chen, G. Pourtois, C. Adelmann, L. Goux, B. Govoreanu, R. Degreave et al., "Insights into Ni-filament formation in unipolar-switching Ni/HfO_2/TiN resistive random access memory device," *Appl. Phys. Lett.*, vol. 100, no. 113513, 2012.

[67] X. P. Wang, Y. Y. Chen, L. Pantisano, L. Goux, M. Jurczak, G. Groeseneken et al., "Effect of Anodic Interface Layers on the Unipolar Switching of HfO_2-based Resistive RAM," *IEEE VLSI-TSA*, pp. 140 - 141, 2010.

[68] Y. S. Chen, H. Y. Lee, P. S. Chen, P. Y. Gu, C. W. Chen, W. P. Lin et al., "Highly scalable hafnium oxide memory with improvements of resistive distribution and read disturb immunity," *IEEE IEDM*, pp. 1 - 4, 2009.

[69] H.D. Lee, B. Magyari-Köpe and Y. Nishi, "Model of metallic filament formation and rupture in NiO for unipolar switching," *Phys. Rev. B.*, vol. 81, no. 193202, 2010.

[70] U. Russo, D. Jelmini, C. Cagli, A. L. Lacaita, S. Spiga, C. Wiemer et al. , "Conductive-filament switching analysis and self-accelerated thermal dissolution model for reset in NiO-based RRAM," *IEEE IEDM*, pp. 775 - 778, 2007.

[71] A. Fantini, L. Goux, R. Degraeve, D.J. Wouters, N. Raghavan, G. Kar et al., "Intrinsic Switching Variability in HfO_2 RRAM," *IEEE IMW*, pp. 30 - 33, 2013.

[72] D. Garbin, O. Bichler, E. Vianello, Q. Rafhay, C. Gamrat, L. Perniola et al., "Variability-tolerant Convolutional Neural Network for Pattern Recognition Applications based on OxRAM Synapses," *IEEE IEDM*, pp. 28.4.1-28.4.4, 2014.

[73] H. Y. Lee, Y. S. Chen, P. S. Chen, T. Y. Wu, F. Chen, C. C. Wang et al., "Low-Power and Nanosecond Switching in Robust Hafnium Oxide Resistive Memory With a Thin Ti Cap," *IEEE Elec. Dev.Lett*, vol. 31, no. 1, 2010.

[74] T. Cabout, L. Perniola, V. Jousseaume, H. Grampeix, J.F. Nodin, A. Toffoli et al., "Temperature impact (up to 200 °C) on performance and reliability of HfO_2-based RRAMs ," *IEEE IMW*, pp. 116 - 119, 2013.

[75] S. Yu, Y.Y. Chen, X. Guan, H.-S.P. Wong and J. A. Kittl, "A Monte Carlo study of the low resistance state retention of HfO_x based resistive switching memory," *Appl. Phys. Lett.*, vol. 100, no. 043507, 2012.

[76] A. Fantini, L. Goux, S. Clima, R. Degraeve, A. Redolfi, C. Adelmann et al. , "Engineering of $Hf_{1-x}Al_xO_y$ amorphous dielectrics for high-performance RRAM applications ," *IEEE IMW*, pp. 1 - 4 , 2014.

[77] W.G. Kim, J.Y. Kim, J.W. Moon, M.S. Joo, H.J. Choi, S.G. Kim et al., "Effect of Inserting Al_2O_3 Layer and Device Structure in HfO_2-based ReRAM for Low Power Operation," *IEEE IMW*, pp. 1 - 4 , 2012.

[78] H.-L. Chang, H.-C. Li, C.W. Liu, F. Chen and M.-J. Tsai, "Physical Mechanism of HfO_2-based Bipolar Resistive Random Access Memory," *IEEE VLSI-TSA*, pp. 1 - 2, 2011.

[79] Y.Y. Chen, B. Govoreanu, L. Goux, R. Degraeve, A. Fantini, G.S. Kar et al., "Balancing SET/RESET Pulse for > 1010 Endurance in HfO_2/Hf 1T1R Bipolar RRAM," *IEEE Trans. Elec. Dev.*, vol. 59, no. 12, 2012.

[80] Y.Y Chen, R. Degraeve, S. Clima, B. Govoreanu, L. Goux, A. Fantini et al., "Understanding of the Endurance Failure in Scaled HfO_2-based 1T1R RRAM through Vacancy Mobility Degradation," *IEEE IEDM*, pp. 20.3.1 - 20.3.4, 2012.

[81] J.Y. Son and Y.-S. Shin, "Direct observation of conducting filaments on resistive switching of NiO thin films ," *Appl. Phys. Lett.*, vol. 92, no. 222106, 2008.

[82] B.J. Choi, D. S. Jeong, S. K. Kim, C. Rohde, S. Choi, J. H. Oh et al., "Resistive switching mechanism of TiO_2 thin films grown by atomic-layer deposition," *J. Appl. Phys.*, vol. 98, no. 033715, 2005.

[83] G. Bersuker, D. C. Gilmer, D. Veksler, et al., "Metal oxide resistive memory switching mechanism based on conductive filament properties," *J. Appl. Phys.*, vol. 110, p. 124518, 2011.

[84] P. Calka, E. Martinez, V. Delaye et al., "Chemical and structural properties of conducting nanofilaments in TiN/HfO_2-based resistive switching structures," *Nanotech.*, vol. 24, no. 085706, 2013.

[85] A. Sawa, "Resistive switching in transition metal oxides," *Materialstoday*, vol. 11, no. 6, pp. 28 - 36, 2008.

[86] Z. Fang, X. Li, X. Wang and P.G. Lo, "Area Dependent Low Frequency Noise in Metal Oxide Based Resistive Random Access Memory," *Inter. Journ. Infor. Elec. Eng. (IJIEE)*, vol. 2, no. 6, 2012.

[87] G.-H. Buh, I. Hwang and B.H. Park, "Time-dependent electroforming in NiO resistive switching devices ," *Appl. Phys. Lett.*, vol. 95, no. 142101, 2009.

[88] G. Bersuker, D. C. Gilmer, D. Veksler, J. Yum, H. Park, S. Lian et al., "Metal Oxide RRAM Switching Mechanism Based on Conductive Filament Microscopic Properties," *IEEE IEDM*, pp. 19.6.1 - 19.6.4, 2010.

[89] M. Lanza, K. Zhang, M. Porti, M. Nafria, Z.Y. Shen, L.F. Liu et al., "Grain boundaries as preferential sites for resistive switching in the HfO_2 resistive random access memory structures ," *Appl. Phys. Lett.*, vol. 100, pp. 123508 - 123508-4, 2012.

[90] L. Vandelli, A. Padovani, L. Larcher et al., "Comprehensive physical modeling of forming and switching operations in HfO_2 RRAM devices," *IEEE IEDM*, pp. 421–424, 2011.

[91] L. Zhao, J. Zhang, Y. He, X. Guan, H. Qian, Z. Yu et al., "Dynamic Modeling and Atomistic Simulations of SET and RESET Operations in TiO_2-Based Unipolar Resistive Memory," *IEEE Elec. Dev. Lett.*, vol. 32, no. 5, pp. 677 - 679, 2011.

[92] D.S. Jeong, H. Schroeder, U. Breuer and R. Waser, "Characteristic electroforming behavior in Pt/TiO_2/Pt resistive switching cells depending on atmosphere," *J. Appl. Phys.*, vol. 104, no. 123716, 2008.

[93] S. Privitera, G. Bersuker, B. Butcher, A. Kalantarian, S. Lombardo, C. Bongiorno et al., "Microscopy study of the conductive filament in HfO_2 resistive switching memory devices," *Microelec. Eng.*, vol. 109, pp. 75 - 78, 2013.

[94] S.-G. Park, B. Magyari-Köpe and Y. Nishi, "Impact of Oxygen Vacancy Ordering on the Formation of a Conductive Filament in TiO_2 for Resistive Switching

Memory," *IEEE Elec. Dev. Lett.*, vol. 32, no. 2, pp. 197 - 199, 2011.

[95] X. Cartoixà, R. Rurali and J. Suñé, "Transport properties of oxygen vacancy filaments in metal/crystalline or amorphous HfO_2/metal structures," *Phys. Rev. B*, vol. 86, no. 165445, 2012.

[96] K. P. McKenna, "Optimal stoichiometry for nucleation and growth of conductive filaments in HfO_x," *Modelling Simul. Mater. Sci.*, vol. 22, no. 025001, 2014.

[97] C. Walczyk et al., "Pulse-induced low-power resistive switching in HfO_2 metal-insulator-metal diodes for nonvolatile memory applications," *Journ. App.Phys.*, vol. 105, no. 114103, 2009.

[98] Lee et al., "Evidence and solution of over-RESET problem for HfO_x based resistive memory with sub-ns switching speed and high endurance," *IEEE IEDM*, pp. 19.7.1 - 19.7.4, 2010.

[99] S. Yu, X. Guan and H.-S.P Wong, "Conduction mechanism of TiN/HfO_x/Pt resistive switching memory:A trap-assisted-tunneling model," *Appl. Phys.Lett.*, vol. 99, no. 063507, 2011.

[100] C. Walczyk, D. Walczyk, T. Schroeder,T. Bertaud, M. Sowinska, M. Lukosius et al., "Impact of Temperature on the Resistive Switching Behavior of Embedded HfO_2-Based RRAM Devices," *IEEE Trans. Elec. Dev.*, vol. 58, no. 9, 2011.

[101] L.M. Prócel, L. Trojman, J. Moreno, F. crupi, V. Maccaronio, R. Degraeve et al., "Experimental evidence of the quantum point contact theory in the conduction mechanism of bipolar HfO_2-based random access memories," *J. Appl. Phys.*, vol. 114, no. 074509, 2013.

[102] X. L. Jiang, Y. G. Zhao, Y. S. Chen, D. Li, Y. X. Luo, D. Y. Zhao et al., "Characteristics of different types of filaments in resistive switching memories investigated by complex impedance spectroscopy," *Appl. Phys. Lett.*, vol. 102, no. 253507, 2013.

[103] C.-Y. Lin, S.-Y. Wang, D.-Y Lee and T.-Y. Tseng, "Electrical Properties and Fatigue Behaviors of ZrO_2 Resistive Switching Thin Films," *J. Electroch. Societ. (ECS)*, vol. 155, no. 8, pp. H615-H619, 2008.

[104] E. Vianello, O. Thomas, M. Harrand, S. Onkaraiah, T. Cabout, B. Traoré et al., "Back-end 3D integration of HfO_2-based RRAMs for low-voltage advanced IC digital design ," *IC Desig. Tech. (ICIDT)*, pp. 235 - 238, 2013.

[105] Y. Nishi, "Challenges and Opportunities of Nanoelectronic Devices : Resistance Switching Memory," *Nanoscience Foundation Seminar*, April 2014.

[106] ISSCC 2013 : Trends. [Online]. isscc.org/doc/2013/2013_Trends.pdf

Chapter II

Scaling of HfO_2 based RRAM

The possibility of scaling oxide based RRAM in future non-volatile memory applications has raised great interest in the microelectronic industry and research community partly because the conventional floating gate memory technologies FLASH are approaching their scaling limits [1]. The widely accepted working principle of RRAM relying on the reversible change of the oxide layer's resistance through the formation and rupture of localized nanometer-size conductive region [2] [3] makes the technology suitable for aggressive scaling. Of the different types of oxides, various companies [4] and research laboratories [5] have adopted the HfO_2/Ti solution as the active layer responsible for the memory effect because of, among others, its compatibility with conventional CMOS Back-End-Of-Line (BEOL) process. Indeed, scaled devices as small as 10nmx10nm HfO_2 based RRAM have been demonstrated [6]. Very recently, 2nm ultrathin HfO_2 layer sandwiched between Pt and TiN electrodes suitable for 3D integration has also been reported [7]. However, due to the localized nature and smaller dimension (diameter of few to tens of nanometers [8]) of the conductive region responsible for the resistive switching, clear performance assessment study related to devices' switching voltages, thermal stability, endurance and variability need to be addressed. The scalability of the memory cells may be viewed from different perspectives and can be achieved through either the reduction of the oxide thickness, the

reduction of the device active area or the reduction of the Ti top electrode thickness. Each type of scaling may have an impact on RRAM performance and it is therefore important to look at the different possibilities in order to have a more comprehensive understanding of the devices. To this end, in this chapter we investigate the impact of the 3 different scaling types mentioned above namely: oxide thickness scaling, device active area scaling and Ti top electrode scaling on HfO_2 based RRAM performance. Furthermore, we study the impact of the deposition temperature of HfO_2 layer on the devices' characteristics. We then conclude the chapter with the insight gained from the study.

II.1 Fabricated devices for scaling study

1R TiN/HfO_2/Ti and WSi/HfO_2/Ti devices were fabricated in planar mesa process as schematically represented in FigII.1a and FigII.1b respectively. TiN bottom electrodes (BE) were deposited by Physical Vapor Deposition (PVD) and patterned by DUV (Deep Ultra Violet) lithography to obtain device areas ranging from 600nmx600nm to 3µmx3µm. On the other hand, WSi_x plugs were deposited by CVD (Chemical Vapor Deposition) employing the WF_6 and SiH_4 precursors at 400°C and were patterned by hybrid e-beam and DUV lithography to obtain plug diameters from 80 nm to 1 µm. Following these steps, different HfO_2 layer thicknesses (3nm, 5nm, 10nm and 15nm) were deposited by Atomic Layer Deposition (ALD) at 300°C. In samples named HT (High Temperature)-HfO_x, HfO_2 was annealed at 400°C in N_2 ambient for 30min. This annealing process was used to further study the impact of HfO_2 deposition temperature on device performance. Samples named LT (Low Temperature)-HfO_x have undergone a low back-end temperature of less than 250°C during AlCu deposition while this temperature was 450°C for the other samples. Finally, different thicknesses (3nm, 5nm, 10nm and 15nm) of Ti top electrode (TE) were deposited by PVD. We note that the change of Ti thickness was used only in TiN/HfO_2/Ti structure and the active cell area is across the TiN/HfO_2 contact interface which is defined by the TiN area. For, WSi/HfO_2/Ti plug type structure, Ti thickness was fixed at 10nm and the active area of the memory cell is defined by the diameter of the BE WSi electrode. **TableII.1** and **TableII.2** summarize the fabricated along with their naming convention throughout the chapter.

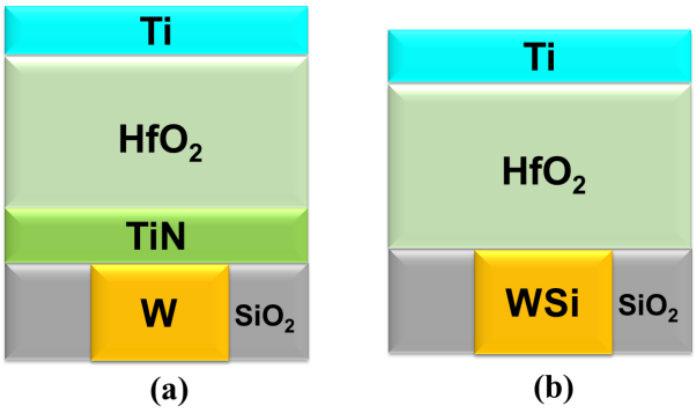

FigII.1. Schematic view of the fabricated devices.

Naming convention	TiN(nm) BE	HfO_2 at 300°C	Ti (nm) TE	T(°C) backend	Area (µm²)
LT-HfO_x	15	10 nm	10	< 250°C	0.36 – 9
HT-HfO_x	15	10 nm + 400°C annealing N2 30 min	10	450°C for 81 s	0.36 – 9
O10/M3	15	10 nm	3	450°C for 81 s	1
O10/M5	15	10 nm	5	450°C for 81 s	1
O10/M10	15	10 nm	10	450°C for 81 s	1
O10/M15	15	10 nm	15	450°C for 81 s	1
O5/M10	15	5 nm	10	450°C for 81 s	1
O15/M10	15	15 nm	10	450°C for 81 s	1

LT-HfO_x → Low Temperature
HT-HfO_x → High Temperature
O → Oxide
M → Ti Top electrode

TableII.1. Fabricated samples for HfO_2 and Ti thickness study.

Naming convention	WSi plug BE	HfO_2 at 300°C	Ti (nm) TE	Plug diameter nm
WSi/HfO_x(3nm)	-	3 nm	10	80 - 1000
WSi/HfO_x(10nm)	-	10 nm	10	80 - 1000

TableII.2. Thin HfO_2 layer used for forming-free operation

Other dedicated devices with a particular architecture named µ-trench structure were fabricated to study the effect of scaling device active area. The structure is shown in FigII.2. Instead of using the whole plug as BE which was the case for WSi/HfO_2/Ti shown in FigII.1b, this structure has only a portion of the TiN BE that is in contact with HfO_2, thus further shrinking the memory cell's active area. For this architecture, 4nm of HfO_2 thickness was deposited by ALD at 300°C and 10 nm Ti TE was deposited by PVD. The BE TiN was also deposited by PVD and patterned by DUV. The width of the trench was 80 nm while its depths ranged from 300 nm to 1µm. Hence the active device areas for this architecture range from 80nmx300nm to 80nmx1000nm (**TableII.3**).

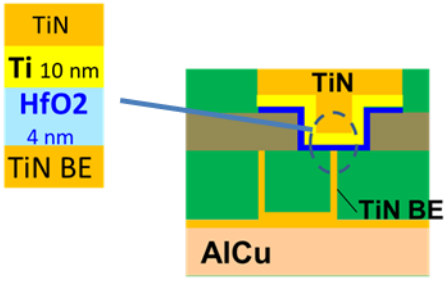

FigII.2. Dedicated µ-trench architecture for the study of active area scaling.

Naming convention	TiN µtrench BE	HfO_2 at 300°C	Ti (nm) TE	Area (µm²)
µ-TiN/HfO2/Ti	-	4 nm	10	0.024 – 0.08

TableII.3. µ-trench structure based fabricated devices for active area scaling

II.2 Electrical characterization

The electrical characterization of the memory cells were performed using Cascade Microtech probing station coupled with either Keithly 4200, Agilent B1500 or HP4156 semiconductor parameter analyzers. The high temperature measurements were carried out with the thermal chuck of Cascade probing station that can be monitored and regulated to a precision of ± 0.2°C around the targeted temperature value. For low temperature measurements reaching 4K, liquid Helium was used to cool the chuck supporting the devices in vacuum.

Most of the devices were tested under quasi-static conditions and will be assumed throughout the chapter unless otherwise stated. The quasi-static tests were carried out by applying a ramp voltage stress of approximately 1V/s to the devices. The devices were subsequently cycled between the two different resistance states whereby the cells were successively SET (change of resistance from R_{off} (HRS) to R_{on} (LRS)) and RESET (change of resistance from R_{on} to R_{off}) in order to extract the corresponding SET and RESET voltages (FigII.3).

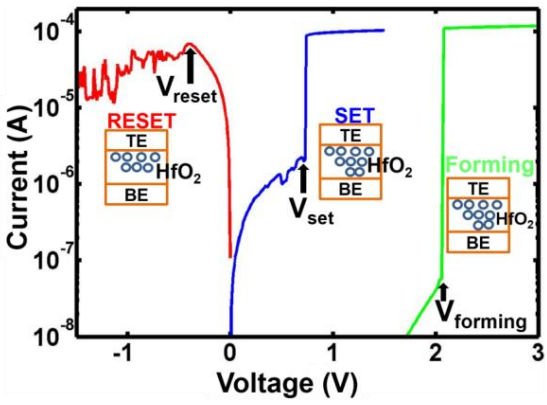

FigII.3. RRAM Switching voltages definition under quasi static operation.

With the switching voltages extracted as well as the resistance values, we can evaluate the variation of these parameters with respect to a particular stack structure such as different electrode materials, changing oxide thickness, device area etc. In order to read the devices' resistance state after a switching operation, a low voltage ramp of

100mV is applied while recording the corresponding current at each voltage step and a linear regression is used following Ohm's law to calculate the resistance. For all the tests, voltage was always applied to the top electrode (TE) keeping the bottom electrode (BE) grounded.

Since the devices are of 1R structures with no access transistors, the compliance current used to limit the maximum current during the forming and SET operations of the devices was controlled by the semiconductor parameter analyzers. This method of limiting current during the devices' switching is not efficient and results in current overshoot during the forming operation. This current overshoot, that makes higher current flow in the device than was targeted, has been attributed to the parasitic capacitance between the semiconductor parameter analyzer and the test samples [9,10,11] and is a major concern in terms of achieving more accurate device performance study. As such, the compliance current that will be shown for the different tests of the 1R devices are only approximate and the conductive paths that are formed will always be at least larger in diameter than what it would be if there was an integrated transistor for more accurate current limitation.

II.3 Forming voltage

Forming operation is a current controlled soft breakdown of the pristine very high resistive HfO_2 layer and induces the formation of conductive filaments (CF) of low resistance value. It is a critical step in RRAM operation and preconditions the devices for resistive switching. In general, high voltages are involved in this operation and as such it is desirable to find ways of reducing it or possibly eliminate it for low voltage operation in high performance new CMOS technologies. In the following sections, we investigate the effects of device fabrication process as well scaling on this forming operation.

II.3.1 Process temperature impact

The two sample types LT-HfO_x (more amorphous sample) and HT-HfO_x (more crystalline sample) are considered. FigII.4a shows the area dependence of forming voltage (V_F) of the two sample types with different thermal budgets during fabrication (V_F extracted from quasi static measurements with a ramp speed of 1V/s). The devices were formed at a compliance current of 1mA. HT-HfO_x presents much lower V_F

compared to LT-HfO_x and we see that for both sample types increasing the device area results in the reduction of the forming voltage. The trends are in agreement with the results of highly scaled HfO_2 RRAM devices from [6]. This indicates that forming voltage does not scale with device area and presents a bottleneck in terms of the scalability of RRAM. Nevertheless, the reduction of the forming voltage with the increasing device area can be fairly reproduced by the probability model of dielectric breakdown which likens the forming operation of the CF to a stochastic process [12]. The larger the area, the higher the probability of finding locations to trigger the forming process which results in the reduction of the forming voltage. It is noteworthy to point out that at larger device areas, the forming voltage seem to saturate and the effect of area scaling becomes less significant.

As mentioned above, despite the reduction of V_F for both sample types, V_F is much lower for HT-HfO_x. This difference in forming voltage for the two samples is more pronounced when plotted with respect to ramp speed as shown in FigII.4b. We attribute this reduction of V_F for HT-HfO_x to the formation of grain boundaries (GB) along which the CF creation is easier [13]. In order to sustain the existence of GB in HT-HfO_x film, we performed the X-Ray Diffraction (XRD) experiment on HfO_2 samples at various temperatures in order to identify its temperature of crystallization. FigII.5 shows the XRD results of HfO_2 at various deposition temperatures by ramping the temperature at 50°C step. We notice that Peaks of crystallization appear between 350°C and 400°C which confirm the existence of poly-crystalline grains in HT-HfO_x. Since LT-HfO_x has seen a maximum back-end temperature of 250°C with HfO_x deposited at 300°C, we believe that that it remains essentially amorphous.

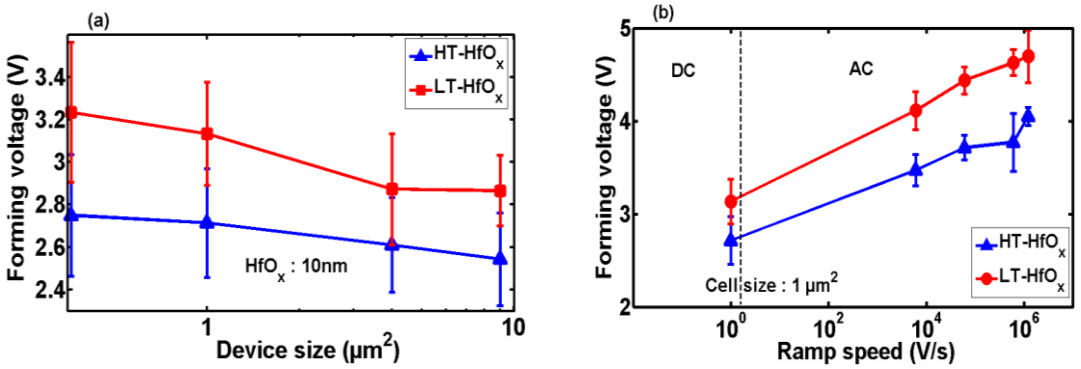

FigII.4 (a) Area dependence of forming voltage of samples with different process temperature conditions. (b) Forming voltage vs. ramp speed highlighting the lower V_F for HT-HfO_x compared to LT-HfO_x.

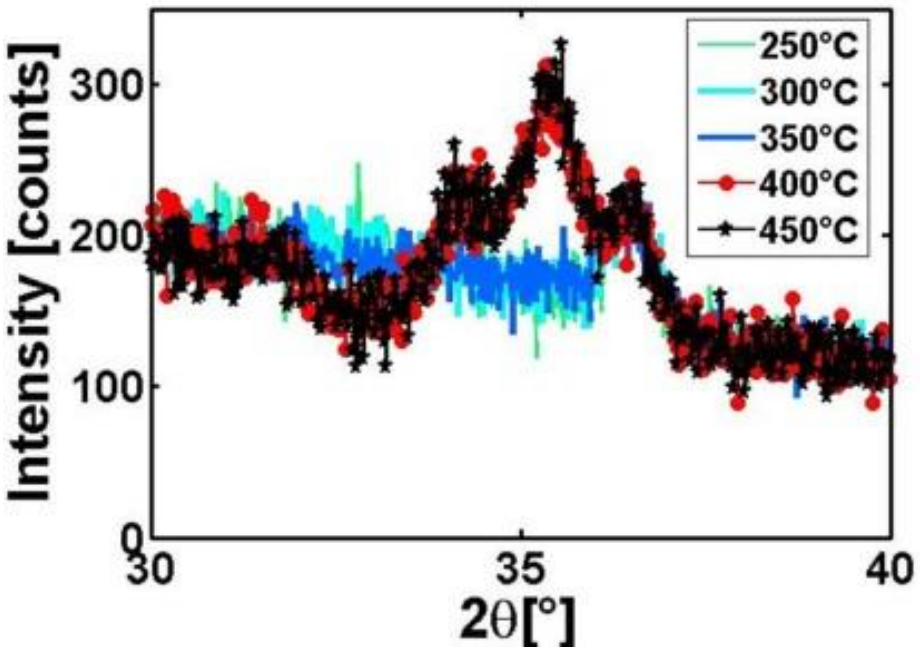

FigII.5. XRD of HfO_x (10nm) at various deposition temperatures. Crystallization starts between 350°C and 400°C. Peaks can be observed at 2*theta=35.6°

Despite the increase of the forming voltage with scaled devices, the results show that an alternative way to counteract the increase of the forming voltage for low voltage operation would be to anneal the devices to a higher temperature with respect to the as-deposited states.

In order to comprehend the role of GB in the creation of the CF and the reduced V_F in HT-HfO_x, we calculated the formation energy of oxygen vacancies (V_o) in the GB and bulk of HfO_2 [14] by employing Density Functional Theory [15] calculations using VASP[1] [16,17] with the GGA-PBE functional for the correlation and exchange. FigII.6a and FigII.6b show the relaxed atomic structure of a Σ5 36.87° (310)/[001] coincidence site lattice (CSL) GB model based on cubic HfO_2 and its schematic ideal geometry, respectively. TableII.4 summarizes the calculated formation energies: a gain of more than 2eV is obtained when oxygen vacancy is generated at GB. This may explain the reduction of V_F in HT-HfO_x compared to LT-HfO_x and corroborates with the findings of Lanza et al. [13] according to which the CF creation is assisted by GB.

[1] VASP stands for Vienna Ab initio Simulation Package. It is a plane wave based DFT code developed in the 90s and is one of the most popular codes being widely used across the world.

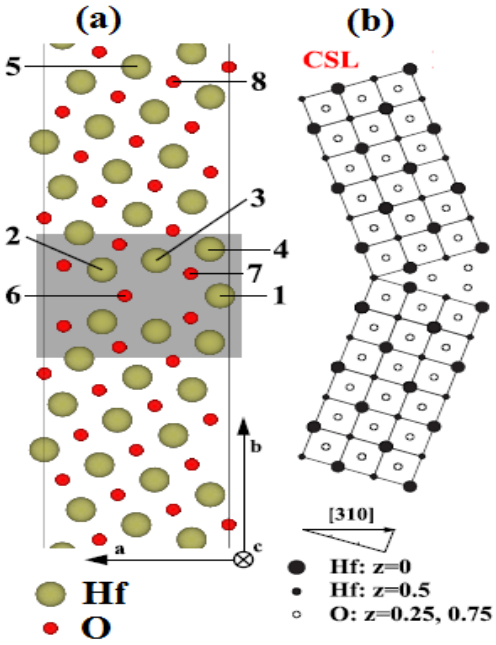

FigII.6 (a) Atomistic representation of the CSL grain boundary in cubic HfO_2, with atomic coordinates optimized and particular sites numbered. Shaded region stands for grain boundary (GB) region. (b) Schematic of the Σ5 36.87° (310)/[001] CSL GB model

	Formation energy of V_o in HfO_2
In the CSL GB region	4.69 eV
In bulk	6.75 eV

TableII.4 The formation of V_o in HfO_2 with and without GB. Notice a gain of more than 2eV when there is GB compared to when there is not. This supports the low V_F in HT-HfO_x.

For a more thorough statistical analysis of the forming voltage for LT-HfO_x and HT-HfO_x, a Weibull distribution analysis of their V_F is conducted. The Weibull cumulative distribution F is defined as:

$$F(x) = 1 - \exp\left\{-\left(\frac{x}{\alpha}\right)^{\beta}\right\} \qquad \textbf{(II. 1)}$$

where x is the independent statistical variable and α is the scale parameter and is defined as the value at which 63% of the samples have failed. β is the shape factor also known as the Weibull slope. Since, forming operation essentially involves the creation of a localized CF with a smaller diameter compared to the device area, according to the weakest-link property of the breakdown (the failure of a small weak point in the device may cause the failure of the entire device) [18], the weibit W=Ln(-Ln(1-F)) of the cumulative distribution F is shifted by $Ln(A_2/A_1)$ when scaling from area A_1 to area A_2 and results in

$$W_2 = W_1 + Ln(A_2/A_1) \qquad \textbf{(II. 2)}$$

Thus the V_F data will form parallel lines with the different areas if the distribution follows the weakest link property as stipulated above. FigII.7 shows the Weibull plot of

the forming voltage for the two sample types. The Weibull slope is small for both samples which corresponds to defect-related breakdown [19], as expected for oxygen-vacancy-rich oxides. The HT treatment of the oxide layer reduces the forming voltage and also further decreases the Weibull slope as shown in FigII.8. Poisson area scaling (The weakest link property of breakdown assumes Poisson distribution and is valid if breakdown is uniform across the device area [18]) holds for LT-HfO_x with the lines being fairly in parallel according to Eq.(II. 2**)** while it fails for HT-HfO_x (0.36µm² overlaps with the 1µm²). This reveals the non-uniformity of the spatial distribution of defects in HT oxide (the slope of V_F vs. area is larger for LT-HfO_x compared to HT-HfO_x as seen in FigII.8). Hence, the Weibull distribution behavior of the forming data indicate that HT-HfO_x are non-uniform after the forming operation and we will shortly see the implications of this non-uniformity on the devices switching resistance distribution.

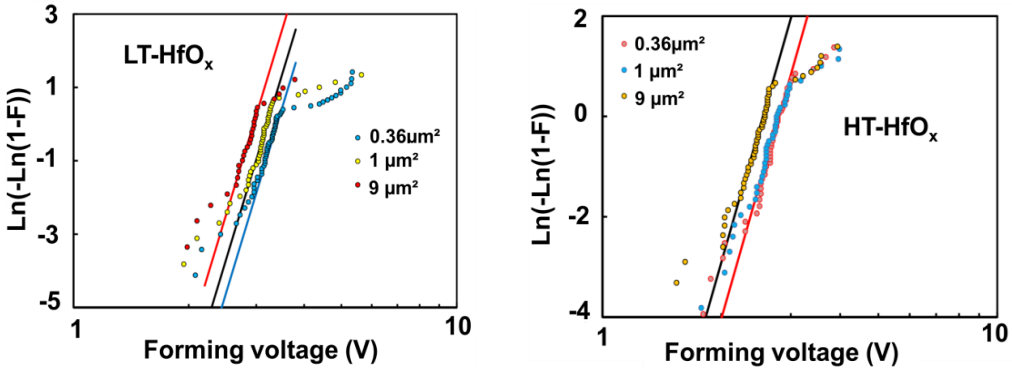

FigII.7. The forming voltage distribution of the two sample types in a Weibull plot. The criteria for V_F extraction were set to when the current reaches 1mA during the forming stage.

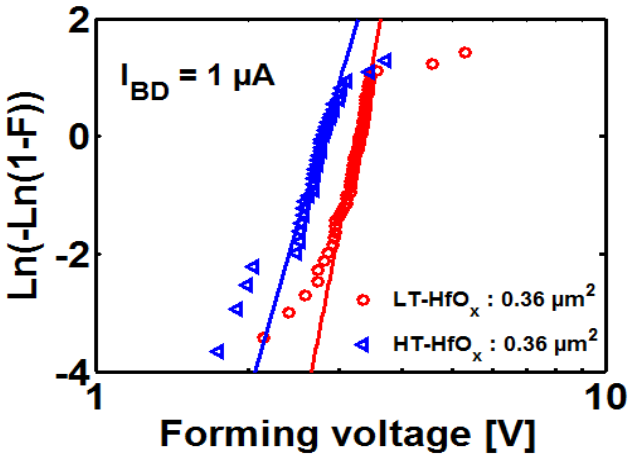

FigII.8. Forming voltage distribution for HT and LT- HfO_x. The slopes of the Weibull fitting are: 19 for LT-HfO_x and 13 for HT-HfO_x.

II.3.2 Influence of the HfO_2/Ti thickness ratio

Forming voltage (V_F) dependence on both HfO_2 and Ti thicknesses is shown in FigII.9. A fairly linear relationship between V_F and HfO_2 thickness is observed (red line in FigII.9), which is consistent with field driven formation of CF and is in agreement with [6,12]. The extracted electric field for forming is ~3MV/cm and agrees well with the 3.5MV/cm obtained in [12]. Therefore, forming voltage scales linearly with the oxide thickness. On the other hand, V_F reduces with increasing Ti thickness (black line in FigII.9), which can be associated with the creation of thicker sub-stoichiometric TiO_x layer at the HfO_2/Ti interface (FigII.10) [20,21]. The reactivity of Ti with oxygen (O) as well as HfO_2/Ti interface is discussed in detail in the chapter dealing with the impact of electrodes on RRAM performance (Chapter III). In FigII.9, we note a saturation of V_F with increasing Ti thickness suggesting that there is a maximum reachable TiO_x region thickness at the HfO_2/Ti interface (i.e. using thicker Ti thickness does not provide a significant reduction of V_F). This saturation phenomenon may be essentially due to the high diffusion barrier of oxygen in Ti (3.5 eV) frustrating further enhancement of the interface thickness (this is detailed in chapter III). As in the previous case, a weibull distribution plot of V_F with different Ti thicknesses by keeping HfO_2 thickness constant at 10nm is plotted in FigII.11. We observe that increasing the Ti thickness deteriorates the dispersion of V_F distribution both because the defect-related tail is enhanced and because the Weibull slope also decreases (probably due to a decrease of the effective oxide thickness to be formed due to the reactivity of Ti with HfO_2 inducing the formation of TiO_x at the interface).

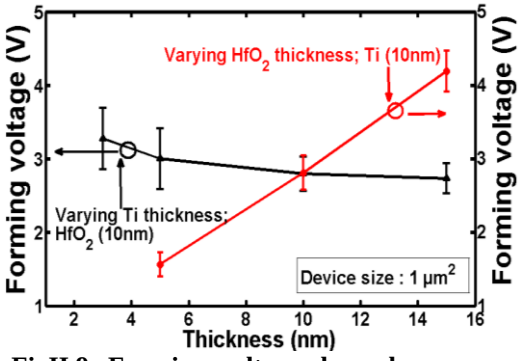

FigII.9. Forming voltage dependence on Ti and HfO2 thickness layers. V_F scales linearly with HfO_2 thickness.

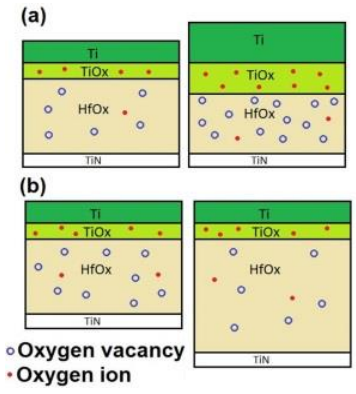

FigII.10. Illustration showing that (a) Thicker Ti induces higher V_o in HfO_2 lowering V_F.(b) Thicker HfO_2 → less V_o for the same Ti layer

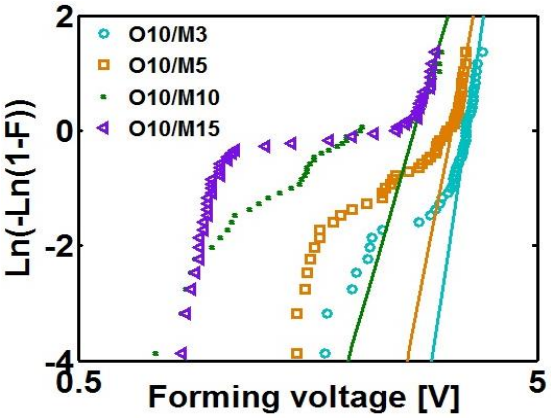

FigII.11. Weibull distribution plot of forming voltage for different Ti thicknesses.

II.4 Switching characteristics

In this part, we will look at the impact of scaling and process temperature on the switching characteristics of the samples studied in the previous section. For the following sections unless otherwise stated, all the devices were programmed at a targeted compliance current of 1 mA. Due to the 1R structure of the devices, current overshoot is generally expected in most of the devices during forming.

II.4.1 LT-HfO_x vs. HT-HfO_x

FigII.12 shows the evolution of SET voltage (V_{set}) and the absolute value of RESET voltage (V_{reset}) with respect to device area ranging from 0.36 µm² to 9 µm² for LT-HfO_x and HT-HfO_x. No clear area dependence of the switching voltages is observed for the range of areas in consideration as opposed to the forming voltage. Also V_{set} is much lower than the forming voltage indicating the SET operation is different from the forming step and that only a portion of CF is essentially involved in the subsequent resistive switching.

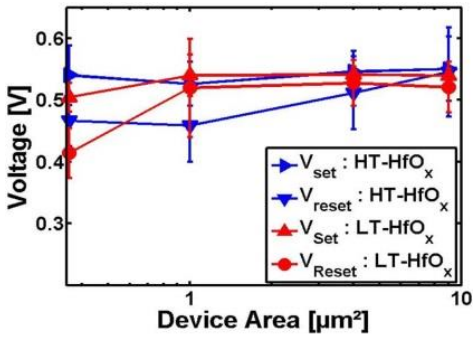

FigII.12. Comparing V_{set} and the absolute value of V_{reset} for HT and LT-HfO_x with different device areas.

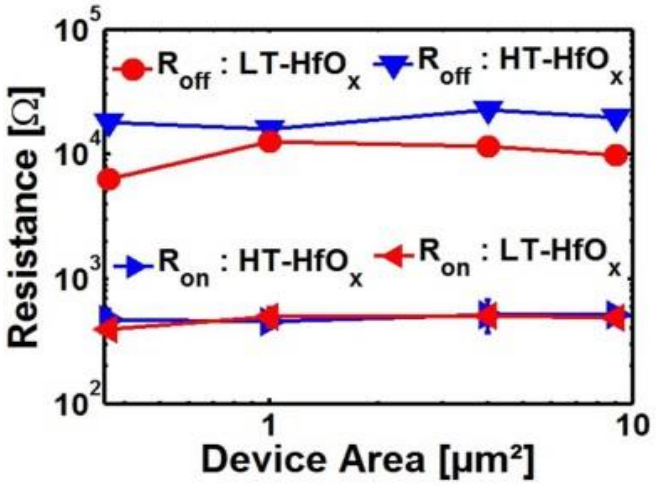

FigII.13. R_{on} and R_{off} vs. device area for HT-HfO_x and LT-HfO_x. R_{off} is higher with HT-HfO_x.

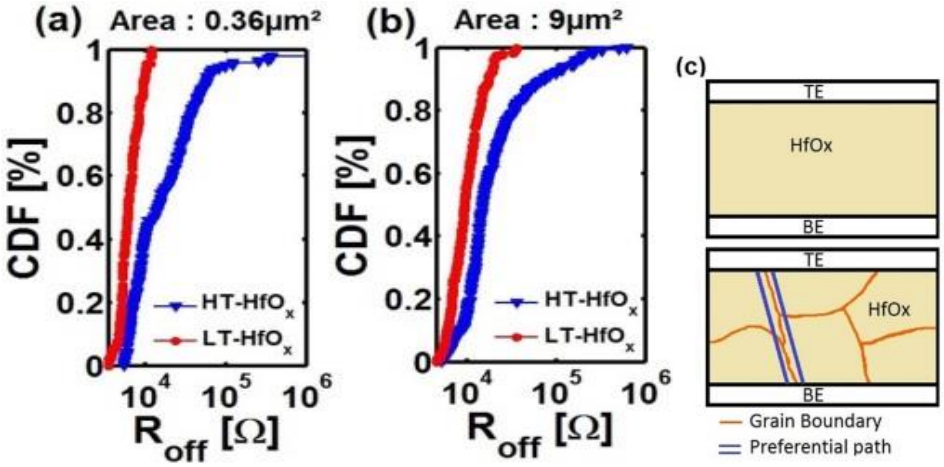

FigII.14. (a,b) Comparing CDF of R_{off} between HT-HfO_x and LT-HfO_x with different device areas. (c) Schematic showing GB as preferential paths for the CF.

Although both samples exhibit similar V_{set} and the absolute value of V_{reset}, R_{off} in HT-HfO_x shows both a higher median value and a larger variability compared to LT-HfO_x in respectively FigII.13 and FigII.14a, b. The improvement of R_{off} dispersion in LT-HfO_x (more amorphous) is in agreement with the improved R_{off} distribution of HfO_2 amorphized with Al_2O_3 inclusion in [22].We have previously seen in the forming voltage section of these devices that the weibull distribution analysis reveals a non-uniform spatial distribution of defects for the HT-HfO_x samples (FigII.7). This non-uniformity induces different switching paths along which the CF may rupture during the RESET process. Therefore, we believe that the larger variability of R_{off} for HT-HfO_x could be related to the leakage paths induced along GBs by the stronger oxygen extraction (FigII.14c) and resulting in possible multiple CF rupture paths during RESET.

II.4.2 Influence of the HfO_x/Ti thickness ratio

Similarly, FigII.15, and FigII.17 respectively show the switching parameters with both different Ti thicknesses (HfO_2 thickness being constant at 10nm) and various HfO_2 thicknesses (with constant Ti layer at 10nm). We observe an increase of R_{off} with thicker Ti layer (FigII.15a) which determines a better R_{off}/R_{on} ratio. This is consistent with the slight increase of V_{set} with Ti layer thickness shown in FigII.15a. Device having thin Ti thickness (3nm) on top of 10 nm HfO_2 showed very poor resistive yield after forming and had very poor R_{off}/R_{on} ratio. These results agree well with the improvement of HfO_2 based RRAM devices' performance with increasing Ti top electrode thickness in [23]. However, we observe that thicker Ti seems to increase the R_{off} variability. The increases of both R_{off} and its variability are consistent with a larger amount of oxygen interstitial ions (O_i) and vacancies V_o generated during the device processing (as a consequence of the oxygen reactivity with the Ti layer) and during the initial forming operation. During the RESET process, more O_i are available in thicker Ti for recombination with V_o and hence increasing R_{off}. To the best of our knowledge, we have not yet seen in the literature experimental data showing both an increase of R_{off} and its variability with increasing Ti layer. We believe that the used compliance current (1 mA) plays a major role in the observed trend. Indeed, the morphology and diameter of CF strongly depend on the forming/SET conditions and the compliance current used [24]. Higher compliance current results in lower R_{on} values (thicker CF region) as shown in FigII.16. It is probable that with an integrated transistor with the devices in a 1T1R causing better compliance current control, this R_{off} increase with Ti layer may not be observed.

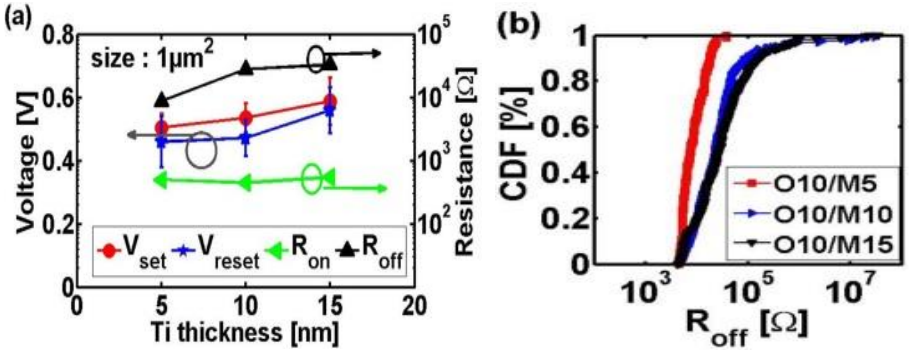

FigII.15(a). $V_{set/reset}$, $R_{on/off}$ vs. increasing Ti layer. Higher Ti layer induces an increase of R_{off}. (b) R_{off} distribution of Fig.13a with increasing Ti layer. O10 for 10 nm HfO_2 and M# with # indicating Ti thickness.

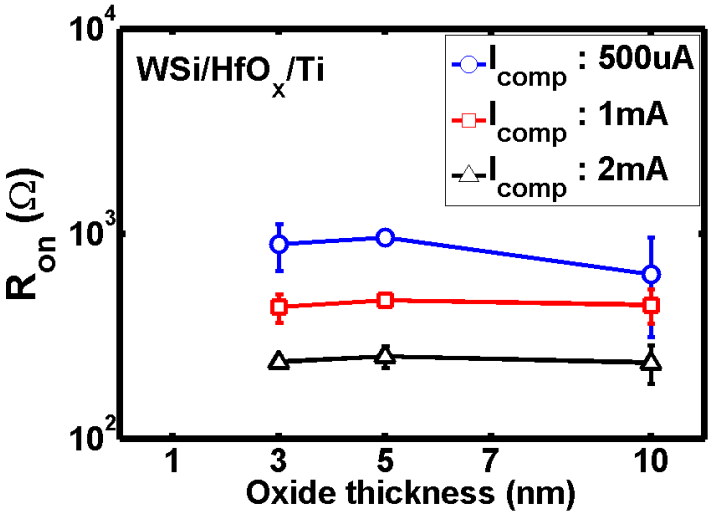

FigII.16. Dependence of R_{on} on the compliance current I_{comp}. Higher I_{comp} results in lower R_{on}.

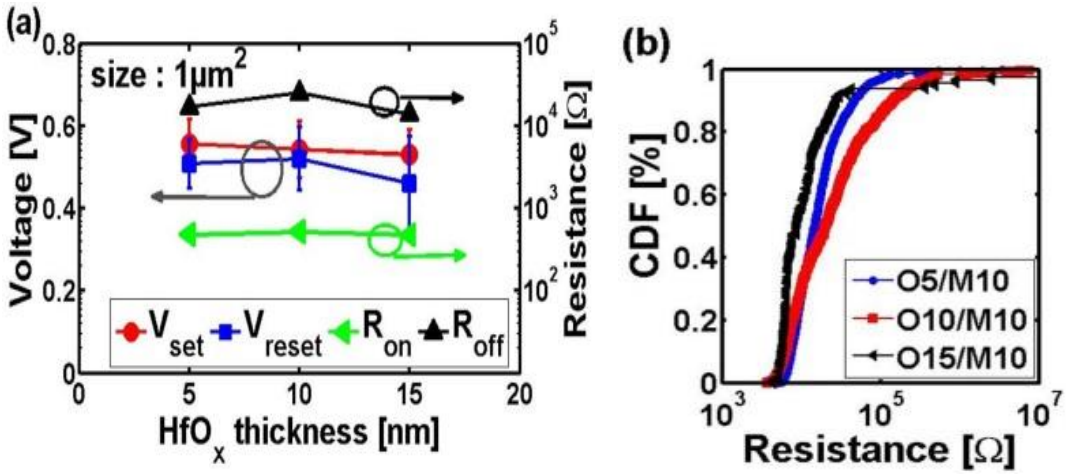

FigII.17. (a) $V_{set/reset}$, $R_{on/off}$ vs. increasing HfO_x layer (b) R_{off} distribution of fig.16a with increasing HfO_2 layer.

On the other hand in FigII.17a, neither R_{on} nor R_{off} exhibits any clear dependence on HfO_2 thickness while Ti thickness is kept constant (10nm) which can be explained by the fact that a similar TiO_x layer is created with constant Ti thickness. Finally as performance assessment criteria, FigII.18 shows that increasing Ti/HfO_2 ratio results in higher device yield in terms of switching. We observe an optimized ratio corresponding to the stack Ti(10nm)/HfO_2(5nm) showing the highest yield (this is based on the switching efficiency of an average of 10 to 20 dc sweep cycles for a statistics of 150 devices per sample). This can be a figure of merit in terms of device specification and tuning metal/oxide ratio for high performance RRAM.

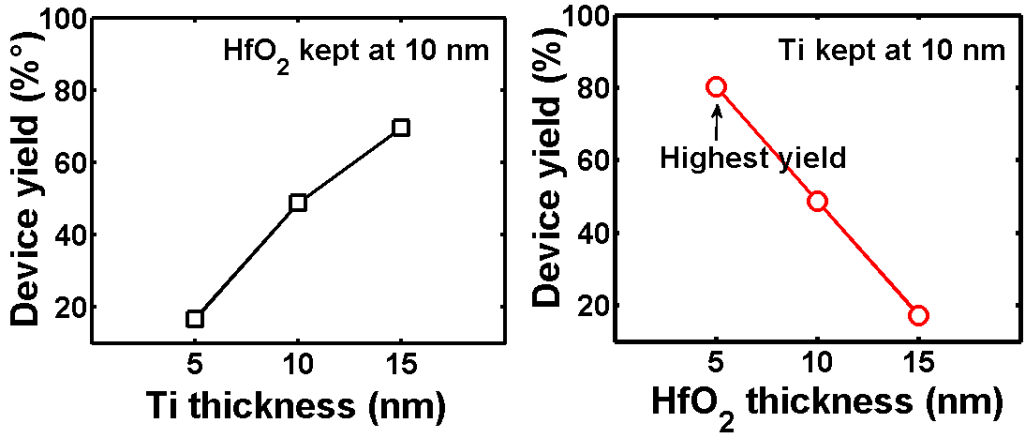

FigII.18. Device yield with increasing Ti and HfO_x layers. Less switching failure is observed with thicker Ti layers and highest switching yield is obtained with HfO_2(5nm)/Ti(10nm).

II.5 High temperature (HT) thermal stress

Depending on the applications, scaled devices should not only have good electrical and switching performance, but also should comply with thermal stability requirements. For the purpose of investigating the thermal stability of the devices, we formed them at 1mA and cycled them for few cycles. We subsequently programmed them to either R_{on} for low resistance thermal stability or R_{off} for high resistance thermal stability. The devices were put in oven and their resistance states were monitored. We subjected them to high temperature stress at 300°C since they were stable at lower temperatures with 1mA programming current. FigII.19 below shows their stability at 250°C thermal stress. One could ask why we did not program the devices at lower compliance current. This is because the poor limitation of the compliance current in 1R structure causing overshoot during forming makes the low programming condition inefficient because the devices would have already seen higher current. In the following, we look at the thermal stability behaviour of the different samples.

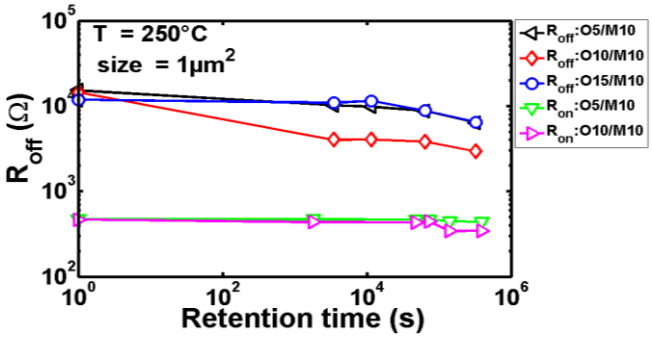

FigII.19. Devices showing good thermal stability at 250°C stress. O# refers to oxide with thickness#. M# refers to metal Ti electrode with thickness #.

II.5.1LT-HfO_x vs. HT-HfO_x

FigII.20 shows the evolution of R_{off} and R_{on} with stress time for HT-HfO_x and LT-HfO_x. Both samples show a significant decrease of R_{off} with stress time while R_{on} remains approximately constant (a slight decrease is observed). Similar trends were observed with different device areas and the range of scaling under consideration does not have an impact on the devices thermal stability. Both R_{on} and R_{off} trends obtained in this experiment are very dependent on the high (1mA) compliance current used to program the devices. Indeed, opposite trends for R_{on} (R_{on} failing towards R_{off} with retention time) and R_{off} (R_{off} increasing towards pristine high resistance values) were obtained by Chen et al. [25] using low compliance currents (10µA and 40 µA). In fact we will see in the chapter dealing with impact of doping on RRAM performance that the trend of R_{on} with retention time does fail towards high resistance states at low compliance currents [26]. Nevertheless, with our test conditions, R_{on} remains very stable and it is R_{off} that is relatively unstable at very high temperature (300°C). Under normal conditions, we expect all the devices to be very stable.

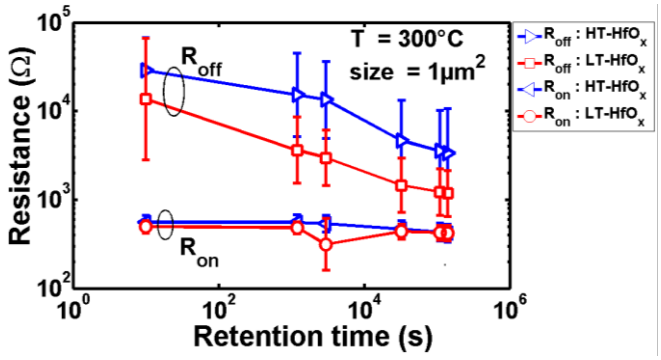

FigII.20. Thermal stress of R_{off} and R_{on} at 300°C for HT-HfO_x and LT-HfO_x. No area dependence of failure rate was observed.

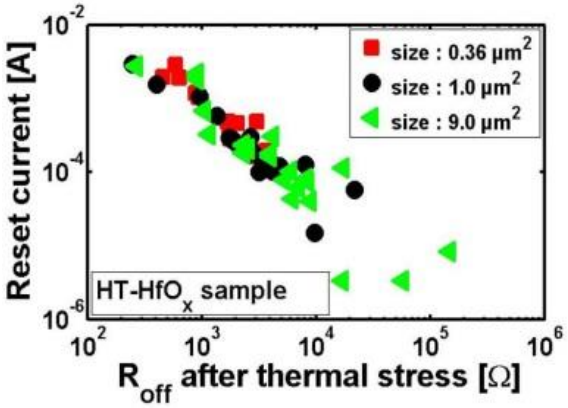

FigII.21. Reset current vs. Resistance after thermal stress of devices from FigII.20 for sample HT-HfO_x. No clear area dependence of reset current is observed.

In order to have a better picture of the devices' thermal stability and whether this extreme data retention test is still filamentary or not , we investigated the RESET current of the devices with different areas after the thermal stress. FigII.21 shows the reset current as a function of the resistance after thermal stress for devices from FigII.20. We observe that the reset current does not exhibit any clear area dependence (the different data overlap) which means that the devices' failure is not due to a uniform Ti or V_o/O_i diffusion in active area. A further support to the previous statement comes from FigII.22 where an assessment of the forming characteristics on pristine cells is performed on the wafer before and after the 300°C stress. FigII.22 does not show significant change in the forming characteristics and this HT stress has negligible impact on the HT-HfO_x devices' pristine states. Therefore, the filament "recreation" during the failure of the devices from R_{off} towards R_{on} is predominantly carried over the CF region in the bulk of the oxide.

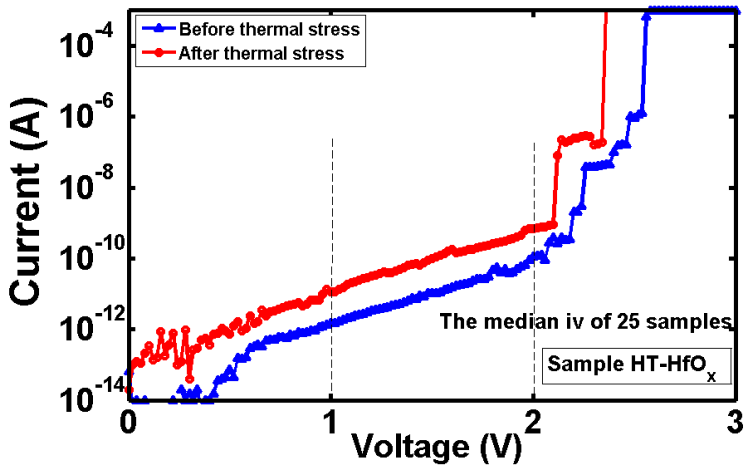

FigII.22 .Median IV curve of HT-HfO_x samples before and after thermal stress. The stress time was $13.98x10^4$s.

II.5.2 Influence of the HfO_x/Ti thickness ratio

Similar thermal stress was performed with devices having different HfO_2 thicknesses with a constant 10nm Ti layer and different Ti thicknesses with a constant 10nm HfO_2 layer as shown in FigII.23b and FigII.24 respectively. For all the devices, R_{on} is stable. However, R_{off} fails towards R_{on} with similar failure profile and no significant Ti or HfO_2 thickness dependence on this failure is observed. Nevertheless, FigII.24 suggests that thin HfO_2 (O5/M10) seems to fail a bit faster towards the end compared to thick HfO_2.

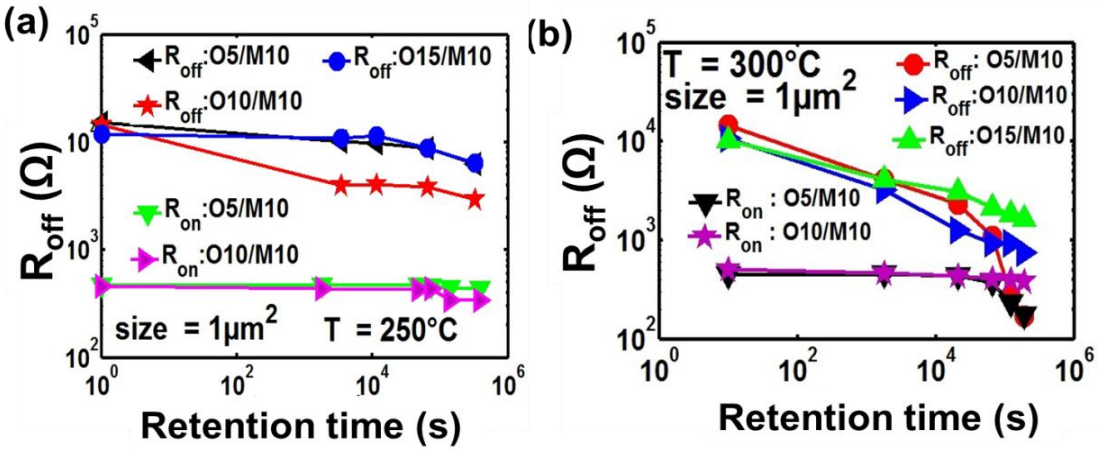

FigII.23. Thermal stress of R_{off} and R_{on} for devices with different HfO_x layer thickness (a) at T = 250°C and (b) at T = 300°C. O# for oxide thickness of #nm and M# for Ti thickness of #nm.

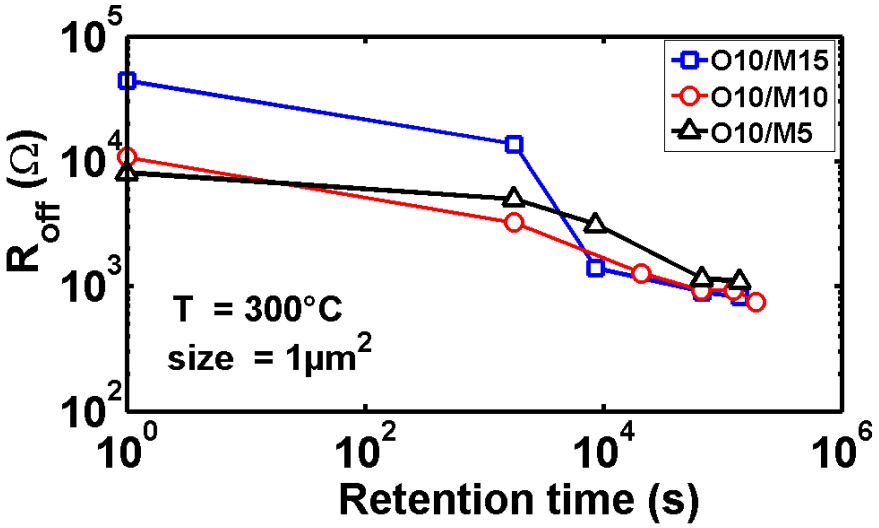

FigII.24. Thermal stress of R_{off} for devices having different Ti layer thickness at T = 300°C.

To understand these failure trends, both lateral and vertical diffusion of ionic species may be present. We saw in the section dealing with HT-HfO_x devices that the failure mode is globally filamentary and that there seems to be no uniform diffusion over the device surface which makes the possibility of vertical diffusion of the species not predominant. Under this HT stress, we believe that the generation of V_o is mostly enhanced by lateral diffusion of O_i in the HfO_x matrix causing either the reinforcement of R_{on} or the failure of R_{off} towards R_{on} as shown in the pictorial model of FigII.25. A possible scenario could be the diffusion of some Ti atoms from the Ti layer towards the CF region inside HfO_x. This hypothesis could be envisaged due to the slight decrease of R_{on} during the thermal stress for all the samples. The conduction mechanism of the devices at low resistance state could give some hints. To that end, FigII.26 shows the activation energy of charge transport extracted from R_{on} after SET (devices programmed with bias application) and after thermal stress (devices failed

towards R_{on} because of the thermal stress) of sample type HfO_2(5nm)/Ti(10nm) [O5/M10] represented in FigII.23b. Similar values are obtained for the two cases and this suggests that the nature of the CF is the same whether it has been recreated by thermal stress or after SET which indicates O_i/V_o remain essentially the main defects in the process rather than Ti (although the presence of Ti cannot be completely excluded).

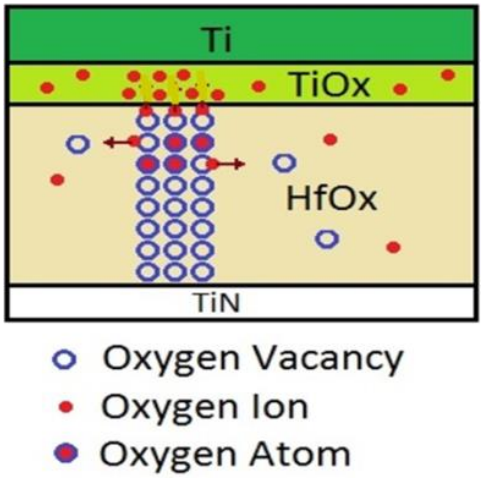

FigII.25. Illustration showing the lateral diffusion of O_i at HT stress causing the recreation of the CF during the thermal stress. This is enhanced in thin HfO_x (fixed Ti layer) and thick Ti (fixed HfO_x layer) because of more V_o/O_i in their matrices.

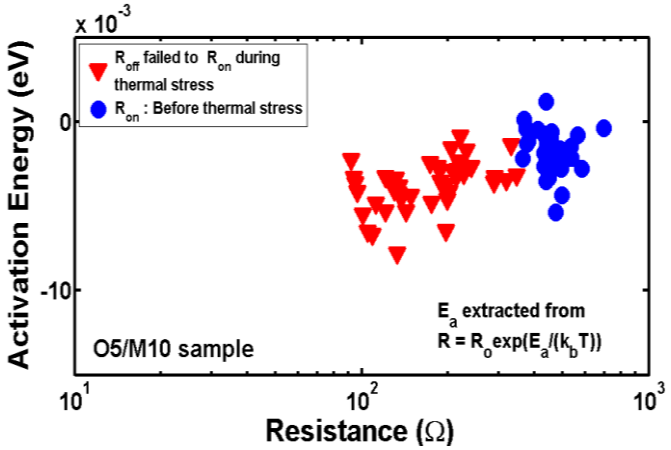

FigII.26. Activation energy of conduction extracted from the Arrhenius plot of R_{on} vs. rising temperature of sample O5/M10 before and after thermal stress.

In this part of the study, we have compared LT/HT HfO_x and HfO_2/Ti thickness ratios and provided more insight on the influence of the defect density in the active layer. HT-HfO_x devices exhibited lower V_F as was the case of samples with smaller HfO_2/Ti thickness ratio: this could be a benefit for low-power operation. Concerning switching parameters, HT-HfO_x samples as well as devices with thicker Ti layer exhibited higher R_{off} at the cost of degraded uniformity. All the sample types showed good thermal stability at the 1 mA programming current. In terms of the devices'

physical mechanisms, filamentary switching seems to be at the basis of the explanation of extremely high temperature (i.e. 300°C) stress that provokes a thermally assisted filament recreation. TableII.5 provides a summary of the key points discussed above and their influence on HfO_2 based RRAM characteristics.

	V_F	R_{off}/R_{on} ratio	Thermal stress	R_{off} uniformity	Comments
Increasing BEOL max T	✓	✓	--	~x	More GB → easier creation of V_o (→ lower V_F and higher variability)
Increasing Ti thickness	✓	✓		~x	more V_o in HfO_2 (→ lower V_F and higher variability) and thicker TiO_y(→ higher R_{off})
Increasing HfO_x thickness	x	--	~✓	ss	lower V_o in HfO_2 (→ higher V_F) and similar variability → same TiO_y (→ same R_{off})

TableII.5: Summary of the key points with respect to samples considered.
✓ : Improvement ~✓: Slight improvement
x : Degradation ~x : Slight degradation
-- : No impact ss : same

II.6 Horizontal/Area scaling of HfO_2 RRAM with the µ-trench architecture

As mentioned earlier in the chapter, a dedicated µtrench structure based RRAM was fabricated in Leti for the scaling study of the devices. The structure is again shown below (FigII.27).

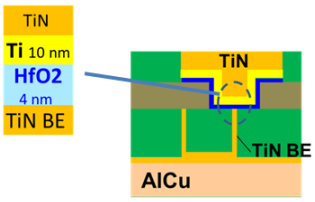

FigII.27. Dedicated µ-trench architecture for the study of active area scaling

The trench width was 80 nm while its depths were 300 nm, 500 nm, 750 nm and 1µm. Hence the active device areas for this architecture range from 80nmx300nm to 80nmx1000nm. HfO_2 thickness was 4 nm.

II.6.1 Switching characteristics

The devices for this section were programmed at 100µA compliance current with minor overshoot despite their 1R structure as shown in FigII.28. Hence, all the switching characteristics were obtained with the 100 µA test conditions. It remains somehow unclear why 100 µA worked fine with these devices with minor current overshoot compared to the devices of the previous section. Probably, because of the thin HfO_2 (4nm) coupled with 10 nm Ti which is more leaky (more defects in the oxide bulk) that made the forming operation more easy. This agrees with low current overshoot measured by Gilmer et al. [27] with leaky HfO_2 oxides.

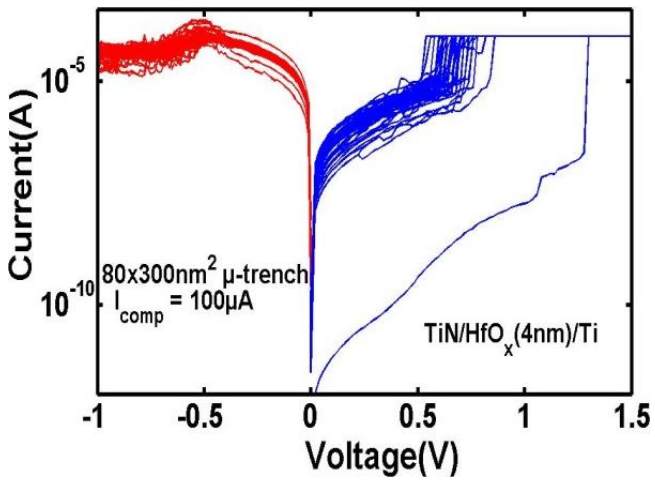

FigII.28. Current voltage IV switching characteristics of the 80nmx300nm µtrench structure. Very low overshoot was observed during the forming operation. This can be seen in the RESET current which is very close to the compliance current.

FigII.29 shows the evolution of the forming voltage with respect to the device area. Similar to the forming data of HT/LT-HfO_x, V_F increases with the device area scaling and we observe that as the area increases the mean values approach each other which could lead to a saturation of V_F for very large devices as mentioned in section II.3.1. The experimental data were fitted to the area scaling model of forming voltage proposed by Chen in [12]. The model relies on the stochastic nature of the breakdown process and is developed using a probability model which ends up with an expression given by

$$V_F = C_1 + C_2 \mathrm{Ln}(A/a^2) \qquad \textbf{(II. 3)}$$

where V_F is the forming voltage, C_1 and C_2 are constants, A the device area and a unit cubic cell that divides the oxide into small cubes. The fitting agrees well with the experimental data (R^2 = 0.98) and corroborates the statistical nature of the CF formation during the forming operation.

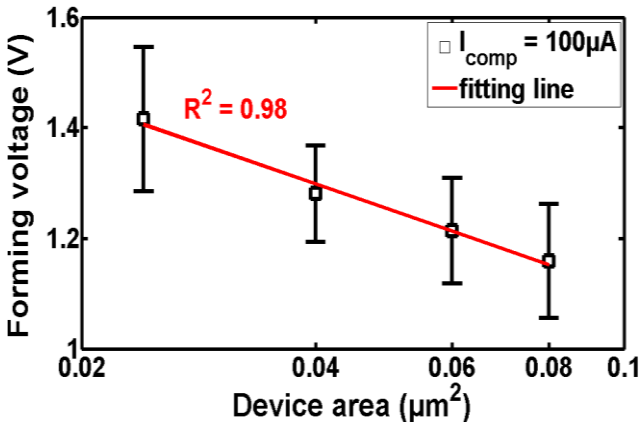

FigII.29. The evolution of the forming voltage with respect to the device area. Data fitted to the area scaling model of forming voltage from [12]**.**

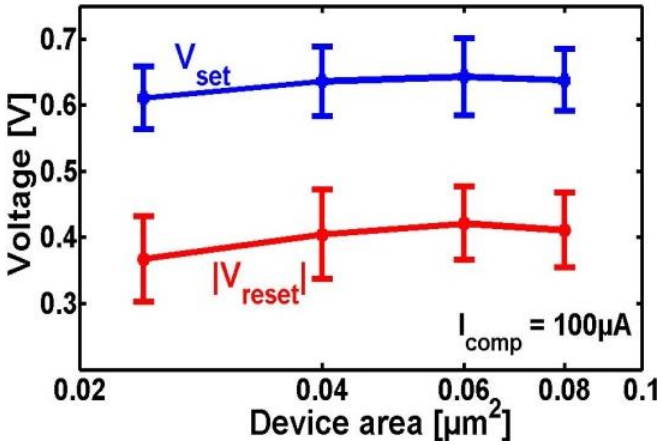

FigII.30. Area scaling of SET and absolute value of RESET voltages. No significant dependence of the switching voltages on device area is observed.

FigII.30 shows the SET and the absolute value of RESET voltages for the devices with respect to the device area. Both voltages show no significant dependence on the device area. The low SET and RESET voltages may be interesting in terms of integrating the devices in high density applications requiring low voltage operation. FigII.31 also shows that a minor decrease of RESET current is observed with smaller device areas which essentially translate into the suitability of the devices for low power operation.

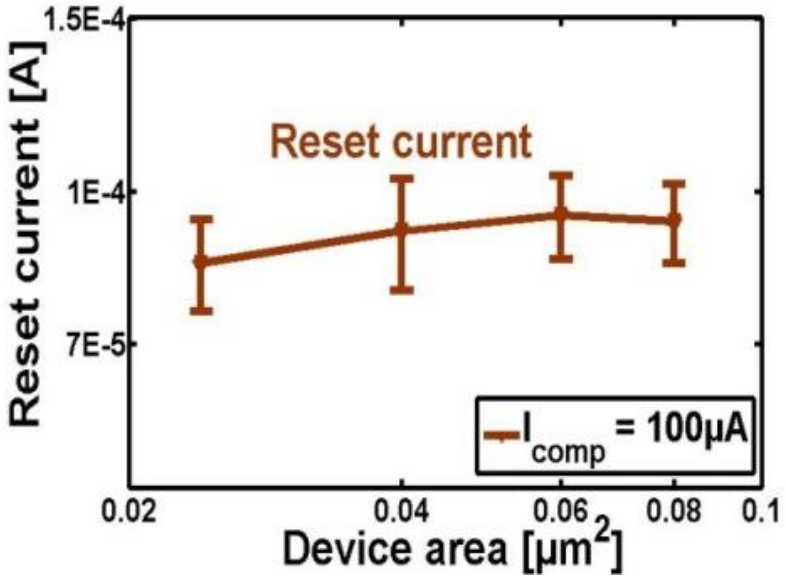

FigII.31. Area scaling of the RESET current for the µtrench structure devices.

The cumulative distribution of the devices' resistance is shown in FigII.32. All the different device sizes exhibit similar distribution and variability. Another major interest in RRAM scaling is to find solutions for improving the variability of R_{off} from cycle to cycle and device to device. The area reduction does not seem to solve the problem. These results are consistent with the variability results of Garbin et al. [28] where a plateau was observed for R_{off} distribution irrespective of the RESET conditions. Hence, variability issues in RRAM seem to be intrinsically related to how the devices are fabricated. Novel device fabrication techniques via doping, alloying or control of defects would be necessary to improve the uniformity of R_{off}.

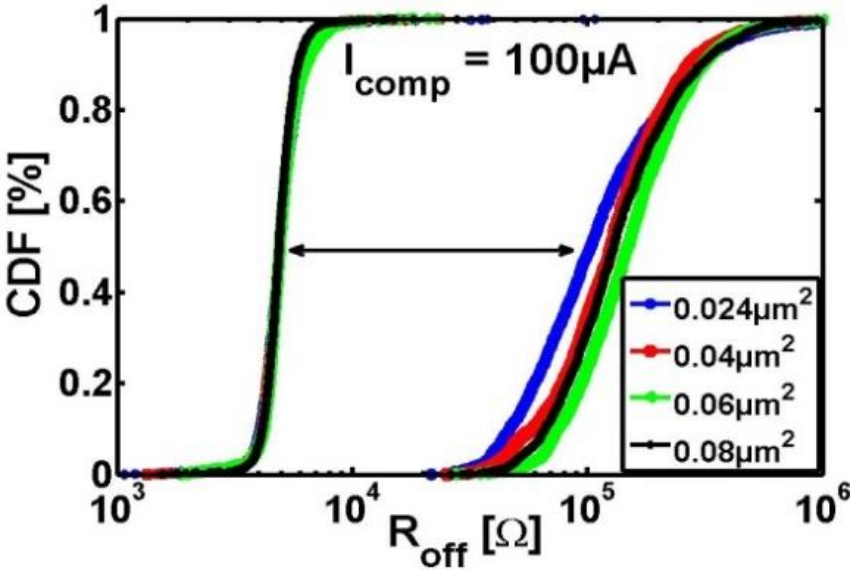

FigII.32. Resistance distribution of µ-trench structure devices. Similar distribution is observed for the different device sizes.

II.7 Pushing the scaling of HfO_2 thickness

We saw in the previous sections the impact of scaling active device area, oxide thickness and Ti top electrode on RRAM performance. One of the major points that we observed is that forming voltage does not scale with device area and its value remains high for thick oxides which is a bottleneck for novel low power CMOS technologies. However, if we plot again the dependence of forming voltage on HfO_2 thickness (FigII.33), we see that by further reducing the oxide thickness below 3nm, forming-free operation may be achieved. Indeed, we fabricated both thin and thick WSi/HfO_x/Ti devices (introduced earlier) in 1R structures in order to investigate the aggressive scaling of the oxide thickness and the results are presented in the following sections.

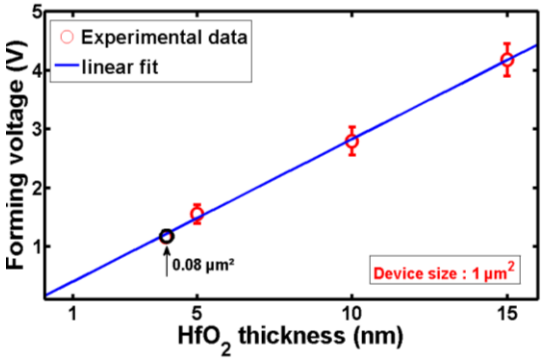

FigII.33. Linear dependence of forming voltage on HfO_2 thickness. By pushing oxide thickness scaling below 3nm, forming-free operation may be achieved.

II.7.1 Forming-free operation of HfO_2 based RRAM

As highlighted above, the forming operation of RRAM devices involve relatively high-voltage values which place considerable electrical stress on the memory cells affecting their expected behavior [9]. Indeed, it has been pointed out that the switching characteristics of the devices are mostly determined during the forming step [10]. To limit the impact of the forming operation, possible solutions have been proposed: hot forming [10], constant voltage stress forming [9] and thin HfO_x based forming-free devices [29]. The latter solution is of particular interest since Chen et al. [5] showed high-performance forming-free devices with very good characteristics. However, their analysis did not provide sufficient information about the devices' initial properties. Furthermore, a deeper understanding of the atomistic structure of these devices is still lacking. In this part, we study the forming-free operation of the devices by combining experimental data and ab initio calculations. We propose a possible microstructure for forming-free devices based on Hf-oxide.

II.7.2 Test samples

The samples are already described earlier above. However, for simplicity we recall them again. The samples of concern are the WSi/HfO_2/Ti samples. The HfO_2 thickness is either 3nm or 10 nm. Ti thickness is always 10 nm. WSi plug diameters ranges from 80 nm to 1µm.

II.7.3 Simulation

All simulations were based on density functional theory (DFT) [6]. For this part, we used the VASP code [16,17], with the GGA-PBE technique to describe the exchange-correlation term, and PAW pseudopotentials to account for the core electrons [30,31]. To describe the wave functions, the plane wave basis cutoff energy was 500 eV, while for the optimization of supercell geometry and atomic positions, the maximum residual force was 0.04 eV/Å. The formation energies of various oxygen vacancies were calculated in the oxygen-rich limit, where the chemical potential of oxygen is set as a half of that of O_2. More details about the formation energy calculations are provided in chapter 5.

II.7.4 Results and discussion

FigII.34 shows the IV plots of the pristine 10 nm HfO_x sample after a necessary electroforming step due to the initial high resistance of the devices. The high first RESET current of the 10 nm HfO_x is caused by the current overshoot in 1R devices during electroforming because of the limited control of the compliance current by the

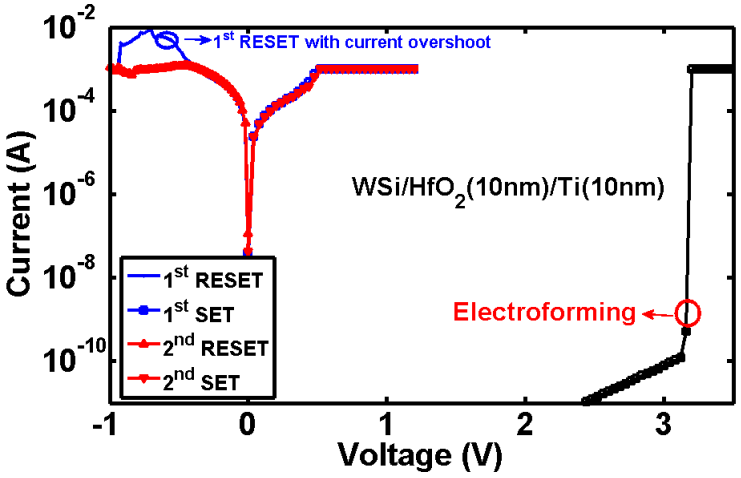

FigII.34. I-V curves of several SET/RESET cycles of the 10 nm *Hf*O_x sample

measuring instruments. This current overshoot reflected during the RESET operation, has been attributed to the parasitic capacitance between the instrument and the samples [9,10,11] as pointed out earlier. FigII.35 shows the IV plots of the 3 nm HfO_x layer where the devices start from an initial low resistance state, thus requiring no forming operation. FigII.35 also shows that, similar to the 10 nm case, the first RESET current is much higher than the subsequent RESET operations. However, this high first RESET current is not related to the current overshoot during forming because the 3 nm devices were not submitted to a forming operation. To comprehend this behavior, the first RESET current is plotted as function of the device area in FigII.36 for both 3nm and 10 nm HfO_x. Contrary to the 3 nm HfO_x, the 10 nm HfO_x does not exhibit any area dependence for the first RESET current since a forming operation was carried out creating conductive paths. It is worth to note that the 3nm HfO_x devices with cell diameter larger than 200nm could not be RESET to R_{off} for subsequent switching.

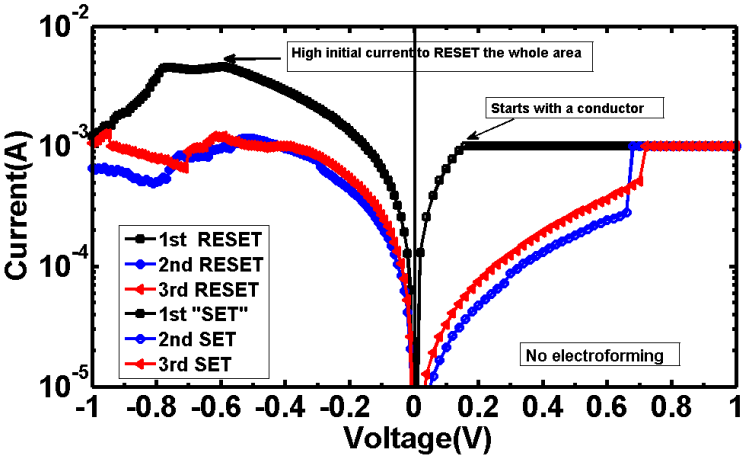

FigII.35. I-V curves for several SET/RESET cycles of the 3 nm HfO_x sample.

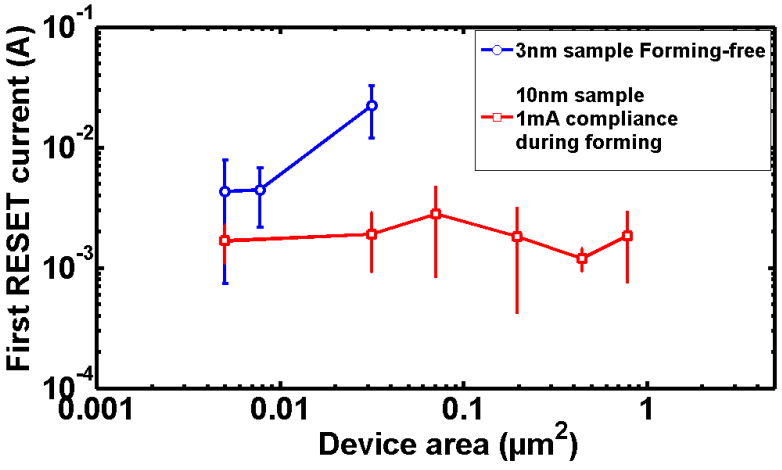

FigII.36. The first "RESET current" (maximum current during a RESET sweep) for the 3 nm and 10 nm samples with various areas.

Both devices show bipolar switching characteristics. Since Ti is known as a strong oxygen-reactive material, the 3 nm film is likely to be oxygen-deficient, but not like pure Hf metal since the devices can be successfully RESET (the fuse-antifuse mechanism [32] only applies to filament patches rather than the whole cell area). On the other hand, after the initial SET/RESET cycle, the following RESET currents were almost area-independent as shown in FigII.37, suggesting that conductive filaments are responsible for carrying current. Indeed, the ON-state resistances of both the 10 nm cell and the 3 nm cell (except for the first RESET operation), exhibit strong dependence on the compliance current during the previous SET, rather than on the device area (FigII.38).

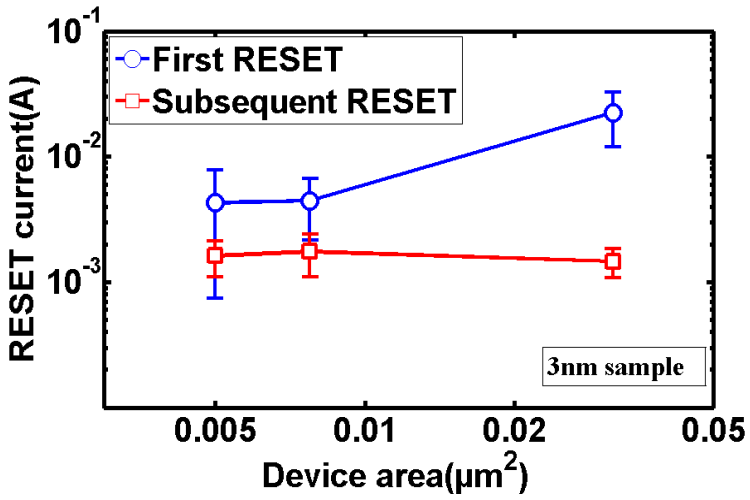

FigII.37. Area dependence of the first and subsequent RESET currents for a 3 nm forming-free cell. The first RESET was performed over the whole device area.

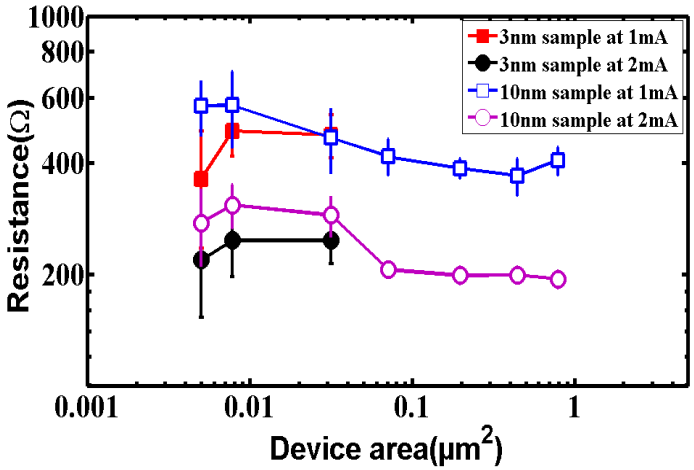

FigII.38. ON-state resistance dependence on the SET compliance current for the 3 nm and 10 nm samples with different areas.

These results suggest that the initial state of the 3nm forming-free cell consists of some low-resistive sub-oxides of hafnia, whose conductance is relatively homogeneous across the device area. However, the first RESET step (FigII.35) oxidizes

the sub-oxides, rendering them insulating/semiconducting. It is the first SET operation (2nd SET in FigII.35) in the 3 nm cell, or the electroforming in the 10 nm cell, that creates filamentary paths. Hence, hafnia sub-oxides may be related to an initial low resistive state, just as in the case of the Ti_4O_7 Magnéli phase in TiO_2 RRAM [33].

To gain insight into the initial state of the 3 nm hafnia cell, we monitored the initial resistances (R_{init}) of the devices while varying the temperature. Both low and high temperature measurements are conducted. FigII.39 and FigII.40 show an extremely weak inverse proportionality between R_{init} and temperature (from 4K to 473K) which indicates a behavior that is not typical of a semiconductor. The temperature response of the forming-free devices may be related to a combination of many conductive HfO_x sub-oxides and a poor semiconducting region surrounding them. The conductivity of the latter region is weakly activated when temperature is raised which does not support the presence of any dominant thermal assisted phenomenon.

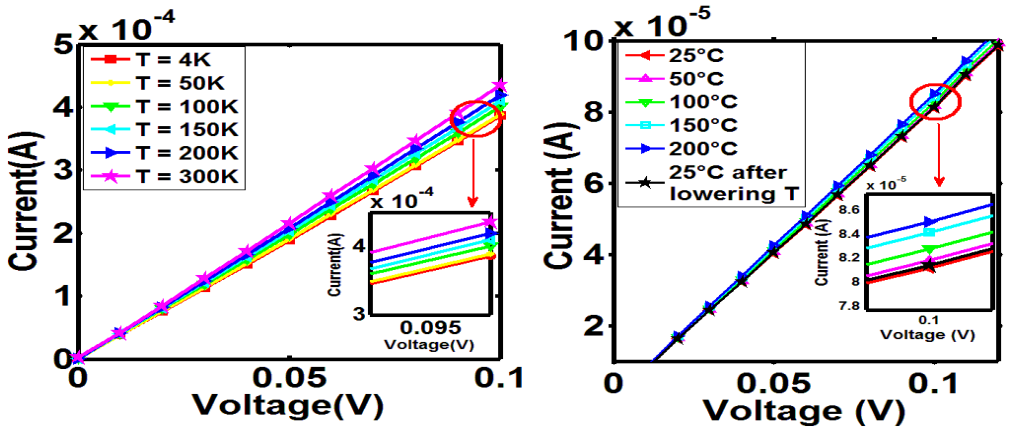

FigII.39. IV-plots of the initial resistance (R_{init}) measurement at different temperatures. The inset shows zoomed IV-plots around 0.1 V.

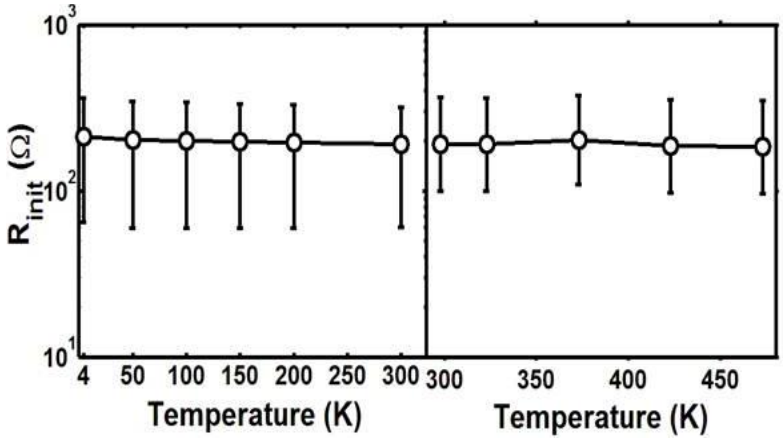

FigII.40. Dependence of R_{init} on temperature for the forming-free 3 nm HfO_x. A slight decrease of resistance with rising temperature is observed.

II.7.5 First-Principles calculations: Insight on the atomic structure of the forming-free devices

In order to further investigate the low-resistive state of the forming-free devices, we performed first-principles calculations on different hafnia sub-oxides with the aim of understanding the microscopic nature of the oxide layer. For the generic HfO_x formula, two limiting cases exist: metal Hf (x=0) and the insulator monoclinic HfO_2 (x=2). At a threshold x=x0, the material is supposed to experience a metal-insulator transition. In our theoretical approach, some strong off-stoichiometric HfO_x models were considered. Their crystal structures are shown in FigII.41 while their densities of states (DOS) are shown in FigII.42.

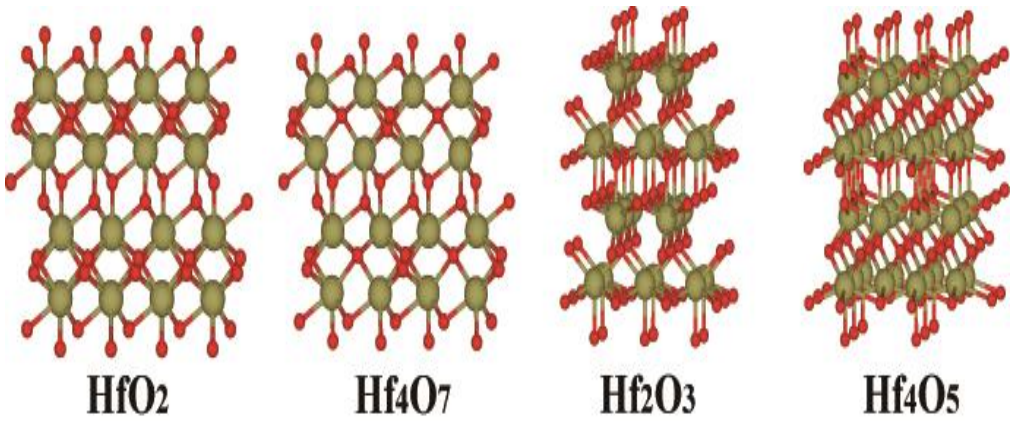

FigII.41. Atomic models for the ground state configurations of HfO_2, Hf_4O_7, Hf_2O_3 and Hf_4O_5.

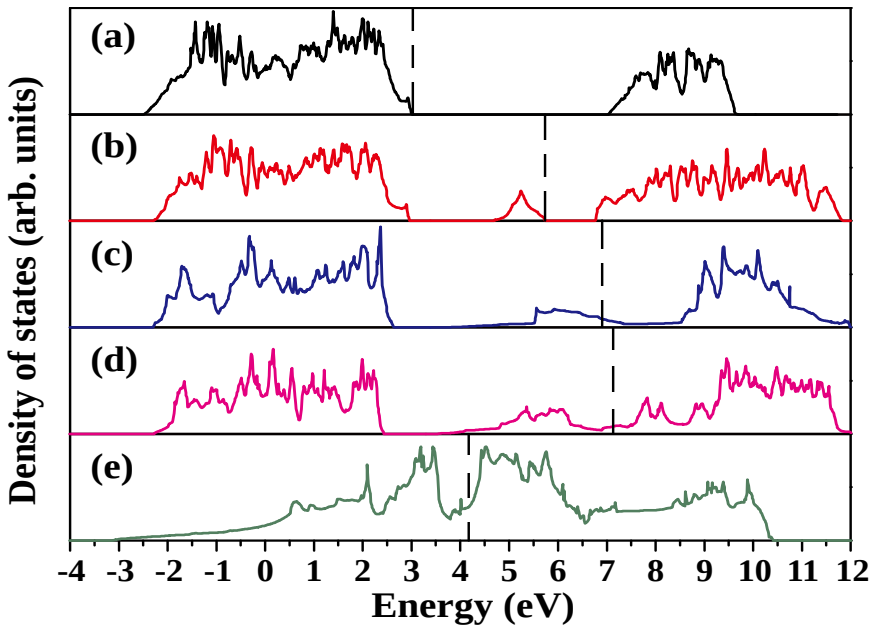

FigII.42. DOS of various HfO_x models: (a) monoclinic HfO_2; (b) Hf_4O_7; (c) tetragonal Hf_2O_3; (d) Hf_4O_5; (e) hcp Hf. The highest occupied molecular orbital (HOMO) level and the Fermi level are marked with a vertical dashed line for insulators/semiconductors and for metals/semi-metals, respectively.

The Hf_4O_7 model, obtained through the introduction of one oxygen vacancy per 12-atom monoclinic HfO_2 unit cell followed by full optimization of atomic positions, is a semiconductor with a reduced band gap compared with the stoichiometric HfO_2.The ground state Hf_2O_3 model, possessing a tetragonal rather than monoclinic structure as recently predicted, is semi-metallic [34]. The Hf_4O_5 model was obtained through the introduction of one oxygen vacancy in the tetragonal Hf_2O_3 primitive cell. Compared to Hf_2O_3, Hf_4O_5 shows a higher DOS at the Fermi level. Finally, the hcp metal Hf possesses a much higher DOS near the Fermi level compared with all the above sub-oxides. These results indicate that the initial conductive phase may be related to some HfO_x sub-oxide where x is close to or below 1.5 [35]. The initial conductive phase is not expected to be pure Hf metal since a cylindrical metal covering the whole device area cannot be easily affected by a RESET operation; only a narrow filament can. The reason for sub-oxide formation can be attributed to the strong oxygen-reactivity characteristics of Ti electrodes. In Reference [14] (also in the chapter dealing with CF formation, Chapter V) we have shown that the formation energy of an oxygen vacancy in monoclinic HfO_2 is 7.00 eV if the oxygen is released in O_2 molecular form. However, its formation energy is drastically reduced to 0.76 eV if the missing oxygen atom migrates to Ti, becoming an interstitial in the Ti electrode. Therefore, the Ti electrode may have been oxidized to a sub-stoichiometric TiO_x layer near the Ti/HfO_2 interface during device fabrication as experimentally demonstrated in [20], leaving HfO_x sub-oxide patches in the dielectric. The thick Ti (10 nm) to thin HfO_2 (3 nm) ratio used in our experiments may enhance the reduction of the hafnia initial state resulting in the measured forming-free operation.

As a selection rule of Ti/HfO_2 thickness ratio, our study reveals that the maximum ratio of Ti layer thickness to HfO_2 thickness should not exceed 3 to allow initial forming or SET operation. A higher ratio (> 3) results in low resistance pristine devices. The initial resistance and IV plot of TiN/HfO_2(3nm)/Ti(5nm) samples are shown in FigII.43. The Ti/HfO_2 thickness ratio is less than 3 (5/3). Therefore, the devices' initial resistance after fabrication are relatively low but an initial forming or 1st SET operation is required to precondition the cells for resistive switching unlike the initial conductive state of the HfO_2(3nm)/Ti(10nm) forming-free samples. We note that the forming-free operation that we observed in our samples is achieved only with small device areas (between 80nm to 200nm cell diameters). Higher device areas could not be

RESET to R_{off} for subsequent switching. Therefore, forming-free operation of devices having important Ti/HfO_2 thickness ratio (> 3) and initial conductive states should be targeted only to highly scaled RRAM memory cells.

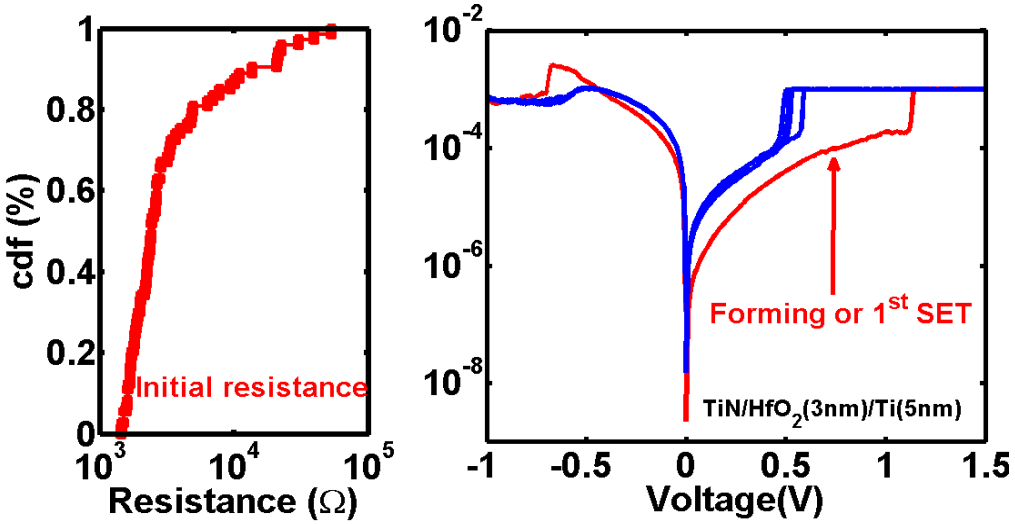

FigII.43. Initial resistance distribution and IV plot of the HfO_2 (3nm)/Ti (5nm) sample. Despite the reduction of the forming or 1st SET voltage, an initial formation of CF is required for resistive switching unlike the forming-free operation of the HfO_2 (3nm)/Ti (10nm) sample.

II.8Conclusions

HfO_2 RRAM devices have interesting scaling potentials for high density applications. The biggest bottleneck for RRAM scaling is the forming voltage which increases with smaller device areas. There are alternative solutions to reduce this forming voltage increase with scaled devices through high temperature annealing of the devices or oxide thickness reduction. High temperature annealing may be easier to implement depending on the maximum thermal budget allowed for the devices at the cost of possible degradation of the devices' R_{off} uniformity. The reduction of the oxide thickness may be a better solution. However too thin an oxide may arise other issues such as the degradation of the devices' thermal stability.

The area dependence of the forming voltage can be easily reproduced by the stochastic nature of breakdown which is based on a probability model. Thus, the larger the device area, the higher the probability of finding locations to trigger the forming process which results in the reduction of the forming voltage. It is noteworthy to point out that at larger device areas, the forming voltage seem to saturate and the effect of area scaling becomes less significant.

Low temperature deposited HfO_2 are essentially amorphous and present higher forming voltage but their weibull distribution suggest that their spatial distribution of

defects are more uniform than those of the high temperature deposited HfO_2. High temperature deposited HfO_2 have more degraded R_{off} distribution compared to low temperature deposited oxides. In both cases, low weibull slopes were extracted, thus reinforcing defect related breakdown phenomenon as is the case in oxygen vacancy rich devices.

The major impact of reducing HfO_2 thickness is the reduction of the forming voltage which comes at the expense of degraded thermal stability at high temperatures. It does not change much on the other switching parameters such as SET and RESET voltages and resistance distributions. On the other hand, increasing the Ti thickness not only results in the decrease of the forming voltage but also the increase of R_{off}/R_{on} ratio. However, it induces a degraded R_{off} uniformity. By combining the different results, our study points out that the optimal stack composition would be HfO_2(5nm)/Ti(10nm) because it has better yield, good switching characteristics, good thermal stability and a good compromise between R_{off}/R_{on} ratio and R_{off} variability.

The scaling study with the dedicated µtrench architecture showed very promising results in terms of both low voltage and low power applications. The only limiting point is the similar R_{off} variability for all the device areas. Engineering the HfO_2 layer with other materials will probably be necessary for improved uniformity.

We saw that aggressive scaling of the HfO_2 layer thickness results in forming-free operation if the thickness of the Ti electrode is kept high (ratio > 3). Our results indicate that the initial conductive phase of these devices may be related to some HfO_x sub-oxide where x is close to or below 1.5. The experimental data show that the maximum ratio of Ti layer thickness to HfO_2 thickness should not exceed 3 to allow initial forming or SET operation.

There is probably not one magic solution that could meet all the requirements of the different applications. However, we saw that there are many ways to optimize the scaling potential of RRAM in high density applications. With a specific application in mind, HfO_2 based memory devices can be surely tuned and engineered for novel non-volatile applications.

References

[1] J. S. Meena, S. M. Sze, U. Chand and T. -Y. Tseng, "Overview of emerging nonvolatile memory technologies," *Nanosc. Resear. Lett.*, vol. 9, p. 526, 2014.

[2] H.-S.P. Wong, H.-Y. Lee, S. Yu et al., "Metal–Oxide RRAM," *Proceedings IEEE,*

pp. 1951-1970, 2012.

[3] G. Bersuker, D. C. Gilmer, D. Veksler, et al., "Metal oxide resistive memory switching mechanism based on conductive filament properties," *J. Appl. Phys.*, vol. 110, p. 124518, 2011.

[4] C. Walczyk, C. Wenger, D. Walczyk, M. Lukosius, I. Costina et al., "On the role of Ti adlayers for resistive switching in HfO_2-based metal-insulator-metal structures_ Top versus bottom electrode integration," *J. Vac. Sci. Technol. B*, vol. 29, no. 01AD02, 2011.

[5] Y.S. Chen, H.Y. Lee, P.S. Chen, C.H. Tsai, P.Y. Gu, T.Y. Wu et al., "Challenges and Opportunities for HfO_x Based Resistive Random Access Memory," *IEEE IEDM*, pp. 31.3.1 - 31.3.4, 2011.

[6] B. Govoreanu, G.S. Kar, Y-Y. Chen, V. Paraschiv, S. Kubicek, A. Fantini et al., "$10x10nm^2$ Hf/HfO_x Crossbar Resistive RAM with Excellent Performance, Reliability and Low-Energy Operation," *IEEE IEDM*, pp. 31.6.1 - 31.6.4, 2011.

[7] L. Zhao, Z.J. Jiang, H.-Y. Chen, J. Sohn, K. Okabe, B. Magyari-Köpe et al., "Ultrathin (~2nm) HfO_x as the Fundamental Resistive Switching Element: Thickness Scaling Limit, Stack Engineering and 3D Integration," *IEEE IEDM*, pp. 6.6.1 - 6.6.4, 2014.

[8] U. Celano, Y. Y. Chen, D. J. Wouters, G. Groeseneken, M. Jurczak, and W. Vandervorst, "Filament observation in metal-oxide resistive switching devices," *Appl. Phys. Lett.*, vol. 102, no. 12, pp. 121602-1–121602-3, 2013.

[9] A. Kalantarian, G. Bersuker, D. C. Gilmer, D. Veksler, B. Butcher, A. Padovani, O. Pirrotta, L. Larcher, R. Geer, Y. Nishi, and P. Kirsch, "Controlling uniformity of RRAM characteristics through the forming process," *IEEE IRPS*, p. 6C.4.1, 2012.

[10] B. Butcher, G. Bersuker, K. G. Young-Fisher, D. C. Gilmer, A. Kalantarian, Y. Nishi et al., "Hot forming to improve memory window and uniformity of low-power HfO_x-based RRAMs," *IEEE IMW*, pp. 1-4, 2012.

[11] H. J. Wan, P. Zhou, L. Ye, Y. Y. Lin, T. A. Tang, H. M. Wu, and M. H. Chi, "In Situ observation of compliance-current overshoot and its effect on resistive switching," *IEEE Elect. Dev. Lett.*, vol. 31, p. 246, 2010.

[12] A. Chen, "Area and Thickness Scaling of Forming Voltage of Resistive Switching Memories," *IEEE Elec. Dev. Lett.* , vol. 35, pp. 57-59, 2014.

[13] M. Lanza, K. Zhang, M. Porti, M. Nafria, Z.Y. Shen, L.F. Liu et al., "Grain boundaries as preferential sites for resistive switching in the HfO_2 resistive random access memory structures ," *Appl. Phys. Lett.*, vol. 100, pp. 123508 - 123508-4, 2012.

[14] K.-H. Xue, P. Blaise, L.R.C. Fonseca, G. Molas, E. Vianello, B. Traoré et al., "Grain-boundary composition and conduction in HfO_2: An ab-initio study," *Appl. Phys. Lett.*, vol. 102, p. 201908, 2013.

[15] P. Hohenberg and W. Kohn, “Inhomogeneous electron gas” Phys. Rev., vol. 136, p. B864, 1964;W. Kohn and L. J. Sham, “Self-consistent equations including exchange and correlation effects”, Phys. Rev., vol. 140, p. A1133, 1965,.

[16] G. Kresse and J. Furthmüller, "Efficiency of ab-initio total energy calculations for metals and semiconductors using a plane-wave basis set," *Comput. Mater. Sci.*, vol. 6, p. 15, 1996.

[17] G. Kresse and J. Furthmüller, "Efficient iterative schemes for ab initio total-energy calculations using a plane-wave basis set," *Phys. Rev. B*, vol. 54, p. 11169, 1996.

[18] D.M. Fleetwood, R.D Schrimpf, *Defects in Microelectronic Materials and Devices: chapter 16*, CRC Press, Ed. Boca Raton, FL, 2008.

[19] J.F. Verweij and J.H. Klootwijk, "Dielectric breakdown I: A review of oxide breakdown," *Microelec. Journ.* , vol. 27, pp. 611-622, 1996.

[20] M. Sowinska, T. Bertaud, D. Walczyk, et al., "Hard x-ray photoelectron spectroscopy study of the electroforming in Ti/HfO_2-based resistive switching structures," *Appl. Phys. Lett.*, vol. 100, p. 233509, 2012.

[21] A. Padovani, L. Larcher , P. Padovani, C. Cagli, and B. De Salvo, "Understanding the Role of the Ti Metal Electrode on the Forming of HfO_2-Based RRAMs," *IEEE IMW*, pp. 1-4, 2012.

[22] C.-H. Huang, J.-H. Jieng, W.-Y. Jang, C.-H. Lin, T.-Y Tseng, "Improved Resistive Switching Characteristics by Al2O3 Layers Inclusion in HfO_2-Based RRAM Devices," *ECS Solid Stat. Lett.*, vol. 2, pp. 63-65, 2013.

[23] B.B. Weng, Z. Fang, Z.X. Chen, X.P. Wang, G.Q. Lo, and D.L. Kwong, "ALD HfO_2 based RRAM with Ti capping," *WASET*, vol. 7, no. 9, 2013.

[24] T.-H Hou, K.-L. Lin, J. Shieh, J.-H. Lin,C.-T. Chou, and Y.-J. Lee, "Evolution of RESET current and filament morphology in low-power HfO_2 unipolar resistive switching memory," *Appl. Phys. Lett.*, vol. 98, 103511, 2011.

[25] Y.Y. Chen, M. Komura, R. Degraeve, B. Govoreanu, L. Goux, A. Fantini et al., "Improvement of data retention in HfO_2/Hf 1T1R RRAM cell under low operating current," *IEEE IEDM*, pp. 10.1.1 - 10.1.4, 2013.

[26] B. Traoré, P. Blaise, E. Vianello, H. Grampeix, A. Bonnevialle, E. Jalaguier et al., "Microscopic understanding of the low resistance retention in HfO_2 and HfAlO based RRAM," *IEEE IEDM*, pp. 21.5.1 - 21.5.4, 2014.

[27] D.C. Gilmer, G. Bersuker, H.-Y. Park, C. Park, B. Butcher, W. Wang et al., "Effects of RRAM stack configuration on forming voltage and current overshoot," *IEEE IMW*, pp. 1-4, 2013.

[28] D. Garbin, O. Bichler, E. Vianello, Q. Rafhay, C. Gamrat, L. Perniola et al., "Variability-tolerant Convolutional Neural Network for Pattern Recognition Applications based on OxRAM Synapses," *IEEE IEDM*, pp. 28.4.1-28.4.4, 2014.

[29] Y.-S. Chen, T-Y. Wu, P.-J. Tzeng, P.-S. Chen, H.-Y. Lee, C.-H. Lin, et al., "Forming-free HfO_2 bipolar RRAM device with improved endurance and high speed operation," *VLSI Techn. Syst. Appl.*, p. 37, 2009.

[30] P. E. Blöchl, "Projector augmented-wave method," *Phys. Rev. B.*, vol. 50, p. 17953, 1994.

[31] G. Kresse and D. Joubert, "From ultrasoft pseudopotentials to the projector augmented-wave method," *Phys. Rev. B.*, vol. 59, p. 1758, 1999.

[32] R. Waser, R. Dittmann, G. Staikov, and K. Szot, "Redox-based resistive switching memories – nanoionic mechanisms, prospects, and challenges," *Adv. Mater.*, vol. 21, pp. 2632–2663, 2009.

[33] D.-H. Kwon, K. M. Kim, J. H. Jang, J. M. Jeon, M. H. Lee, G. H. Kim, et al., "Atomic structure of conducting nanofilaments in TiO_2 resistive switching memory," *Nat. Nanotechnol.*, vol. 5, p. 148, 2010.

[34] K.-H. Xue, P. Blaise, L. R. C. Fonseca, and Y. Nishi, "Prediction of semi-metallic tetragonal Hf_2O_3 and Zr_2O_3 from first-principles," *Phys. Rev. Lett.*, vol. 110, no. 065502, 2013.

[35] K.-H. Xue, B. Traoré, P. Blaise, et al., "A combined ab initio and experimental study on the nature of conductive filaments in Pt/HfO_2/Pt resistive random access memory," *IEEE Trans. Electron Dev.*, vol. 61, p. 1394, 2014.

Chapter III

Role of electrode material on HfO_2 based RRAM performance

The Metal-Insulator-Metal (MIM) structure of HfO_2 based RRAM presents two interfaces which are respectively the bottom electrode/oxide interface and the top electrode/ oxide interface. As stated in Chapter I, RRAM devices may operate in two different switching modes: unipolar/non-polar mode and bipolar mode; the prevalence of one switching mode or the other being solely dependent on the oxide/ electrode interface and not only on the properties of the oxide alone. Hence, in this chapter we investigate the fundamental role played by the electrode/oxide interface on HfO_2 based RRAM operation.

III.1 Samples description

1R BE/HfO_2/TE devices in either planar mesa or BE plug structures were fabricated as schematically represented in FigIII.1a and FigIII.1b respectively. Different bottom electrode (BE) and top electrode (TE) combinations were used as summarized in TableIII.1 and TableIII.2. The fabrication process for the W BE plug was the following: DUV (Deep Ultra Violet) lithography, SiN/SiO_2 etching, W deposition by Physical Vapor Deposition (PVD) and polished through Chemical-mechanical Planarization (CMP), yielding in device areas ranging from 300nmx300nm to 1.8µmx1.8µm.

TiN, Ti and Pt electrodes were also deposited by PVD and their respective thicknesses are shown in the summary tables. On the other hand, TaCN electrodes were deposited by Plasma-enhanced atomic layer deposition (PE-ALD) at 325°C. For the planar structures, the devices were patterned by DUV and the respective areas range from 400nmx400nm to 1.8µmx1.8µm. In all the devices, HfO_2 was deposited by ALD at either 300°C or 350°C (corresponding to two different ALD tools) as shown in the summary tables. The impact of area and HfO_2 deposition temperature on RRAM performance was studied in chapter II and their effect was mainly significant on the forming voltage. Forming voltage was reduced with larger devices or with high temperature deposited films. As such, the impact of area and HfO_2 deposition temperature will not be stretched upon in this chapter. For the electrical characterization, voltage was always applied to the TE keeping the BE grounded and the compliance current was enforced by the semiconductor parameter analyzer.

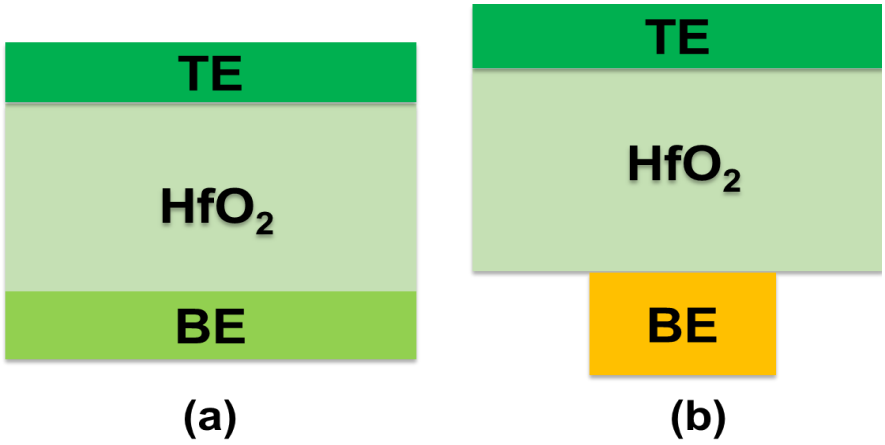

FigIII.1. Schematic view of the fabricated planar mesa (a) and BE plug (b) devices.

Stack	Naming (BE/TE)	HfO_2 deposition T	structure
W / HfO_2(10nm)/Ti(20nm)	W/Ti(20nm)	300°C	Plug
W/HfO_2(10nm)/TiN(25nm)	W/TiN	300°C	Plug
W/HfO_2(10nm)TaCN(25nm)	W/TaCN	300°C	Plug
TaCN(25nm)/HfO_2(10nm)/Ti(10nm)	TaCN/Ti(10nm)	300°C	Planar
TiN(25nm)/HfO_2(10nm)/Ti(10nm)	TiN/Ti(10nm)	300°C	Planar

TableIII.1. Fabricated device samples with HfO_2 deposited at 300°C corresponding to a specific batch of wafers

Stack	Naming (BE/TE)	HfO_2 deposition T	structure
Pt(25nm)/HfO_2(10nm)/Pt(25nm)	Pt/Pt	350°C	Planar
TiN(25nm)/HfO_2(10nm)/TiN(25nm)	TiN/TiN	350°C	Planar
Pt(25nm)/HfO_2(10nm)Ti(5nm)	Pt/Ti(5nm)	350°C	Planar
TiN(25nm)/HfO_2(10nm)/Ti(10nm)	TiN/Ti(10nm)	350°C	Planar

TableIII.2. Fabricated device samples with HfO_2 deposited at 350°C corresponding to a specific batch of wafers.

III.2 Switching performance: HfO_2 at 300°C

TableIII.3 summarizes the quasi-static (DC) switching performance of these devices along with their switching modes. In our study, W/Ti(20nm) devices were tested in bipolar mode although Chen et al. reported the use of the similar W/HfO_2/Ti stack in unipolar mode with better performance in the bipolar mode [1]. Similarly W/TiN and TiN/Ti (10nm) were only tested in bipolar mode with superior performance since a similar previous study conducted in our group showed that TiN/Ti devices were efficiently switched only in the bipolar mode [2] [3]. For W/TaCN and TaCN/Ti, we performed both unipolar and bipolar modes. W/TaCN did not show resistive switching in either mode while TaCN/Ti showed very poor switching effect in the bipolar mode with positive voltage applied to Ti (TE) during the forming/SET operations. W/Ti, W/TiN and TiN/Ti sample types have all exhibited good resistive switching yield. The switching characteristic of the different samples are presented in the next section.

	W/Ti(20 nm)	W/TiN	W/TaCN	TaCN/Ti(10nm)	TiN/Ti(10nm)
Switching polarity	Bipolar	Bipolar	Bipolar	Bipolar	Bipolar
Forming voltage (V)	3.8 ± 0.5	3.8 ± 0.4	6.2 ± 0.7	3.2 ± 0.1	3.0 ± 0.4
Set voltage (V)	0.7 ± 0.1	0.6 ± 0.1	-	-	0.7± 0.1
Reset voltage (V)	0.6 ± 0.1	0.6 ± 0.1	-	-	0.7 ± 0.1
R_{on}(Ohm) (median)	~ 700	~500	-	-	~700
R_{off} (Ohm) (median)	20 k	57 k	-	-	~9 k
I_{reset}	~ 1mA	~ 1mA	-	-	~1mA
Switching Yield	**Good**	**Good**	**No switching**	**Very poor /no switching**	**Good**
comments	We did not test the devices in unipolar mode but unipolar behavior was reported by [1].		The devices were tested in unipolar mode as well but did not switch	The devices were tested in unipolar mode as well but did not switch.	

TableIII.3. Summary of the quasi-static switching performance of the HfO_2 samples fabricated at 300°C.

III.2.1 Comparing the switching characteristics

FigIII.2 compares the forming voltage (V_F) of the different RRAM devices with different electrode materials. This forming step is a current controlled breakdown of the pristine very highly-resistive HfO_2 layer. It has been documented [4], [5] that it induces the formation of conductive filaments (CF) of low resistance value. TiN/Ti(10nm) RRAM devices present the lowest V_F compared to the other electrode combinations. This may be explained by the reactivity of Ti with the HfO_2 layer creating a TiO_y layer at the Ti/HfO_2 interface [6] [7]. This Ti/HfO_2 interface will be investigated in detail later in the chapter.

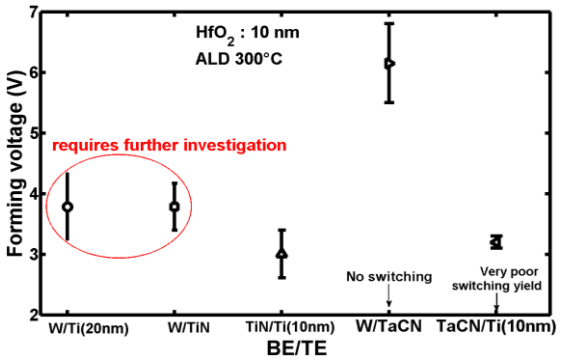

FigIII.2. Comparing the forming voltage of the different electrode combinations with HfO_2 fabricated at 300°C.

We observe that W/Ti(20nm) and W/TiN have similar V_F. This is counterintuitive because the introduction of Ti at the top electrode was supposed to have more important impact on V_F and potentially reduce it to lower values reaching those of TiN/Ti(10nm). At this stage, we do not have clear picture to explain this phenomenon and will require further investigations. A further anomaly or complexity of these W/Ti (20nm) devices may be seen in the comparison of the median forming IV plots of the W/Ti(20nm) and W/TiN shown in FigIII.3 where W/TiN present higher pre-forming current. A possible explanation may be an important oxidation of the interfacial TiN/HfO_2 layer where more Ti dangling bonds in the TiN matrix get oxidized at the interface [8] inducing more defects in the oxide layer. Nevertheless pure Ti is more oxygen reactive than TiN and hence lower V_F was expected for W/Ti (20nm) which is not measured. More refined physical/chemical characterizations of these devices, which are missing, could help understand some of these phenomena.

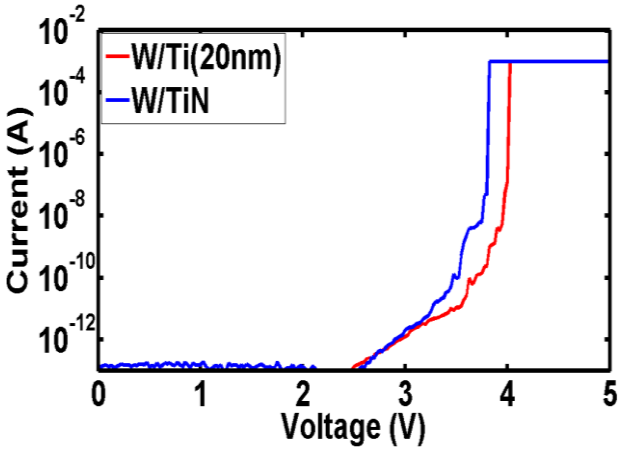

FigIII.3. Comparing the median IV plot of W/Ti (20nm) and W/TiN devices[2].

[2] The statistics is based on more than 20 devices per sample type.

W/HfO_2/TaCN devices present much higher V_F compared to W/HfO_2/Ti or W/HfO_2/TiN. This high V_F for W/TaCN is possibly due to both the oxidation of W/HfO_2 interface creating WO_y layer at the bottom electrode/oxide interface and the less reactivity of TaCN with oxygen when deposited on HfO_2. However, we observe that V_F gets reduced with TaCN/HfO_2/Ti(10nm) devices with the introduction of Ti as top electrode.

SET and absolute value of RESET voltages (V_{set} and V_{reset}) for the different samples are shown in FigIII.4. The different samples present similar switching voltages for both SET and RESET. Likewise, the different samples also have similar RESET current that is almost equal to the 1 mA compliance current during the forming/SET operations. Hence, the main impact of these electrode materials is on the forming voltage of the devices and show less effect on the rest of the switching voltages and currents.

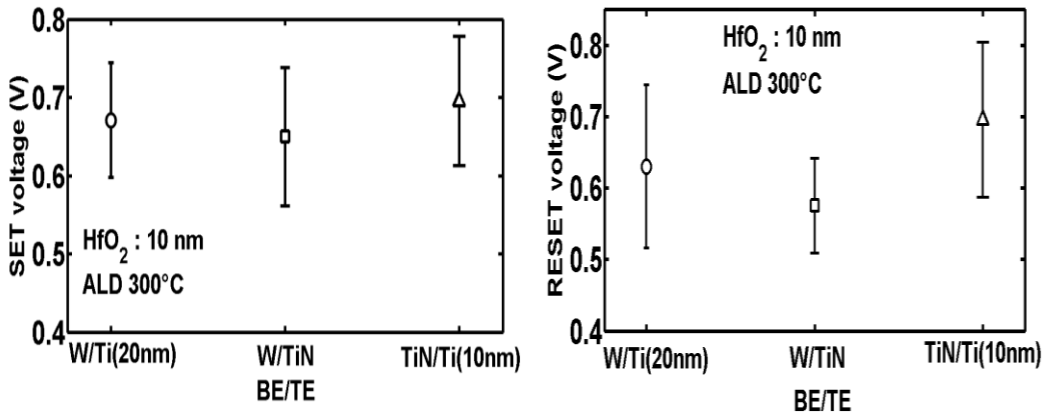

FigIII.4. Comparing SET and the absolute value of RESET voltages for the different samples.

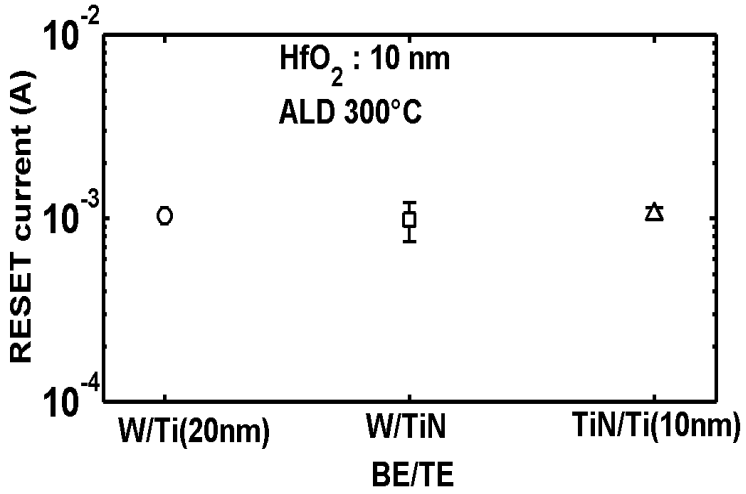

FigIII.5. RESET current comparison of the different samples.

The resistance distributions of the respective sample types are shown in FigIII.6. All the sample types exhibit similar R_{on} values which is consistent with the fact that R_{on} is mostly determined by the compliance current used during the conductive filament (CF) formation [9]. W/TiN devices present larger median switching resistance window. However, the different sample types present similar tail of the R_{off} distribution. This higher median R_{off} for W/TiN may be explained by the less reactivity of O ions with the TiN top electrode during forming/SET operations and hence more O ions are available (at TiN/HfO_2 interface or around CF close to the interface) for recombination with the conductive filament (CF) region during the RESET operations.

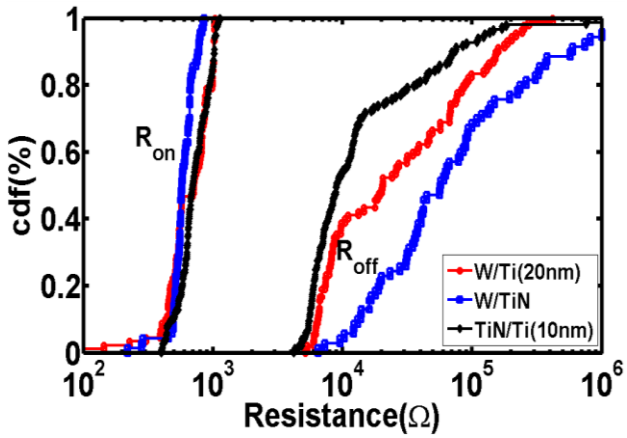

FigIII.6. Resistance distributions of the different samples with HfO_2 deposited at 300°C.

III.2.2 No and/or poor resistive switching with the presence of TaCN electrode

When TaCN was used as top electrode, no resistive switching phenomenon was observed and the devices were stuck to the low resistance and failed to RESET. On the other hand, when TaCN was used as bottom electrode and Ti as top electrode, poor resistive switching yield was obtained but in general when the devices fail, they get ultimately stuck to the low resistance state as shown in FigIII.7. Since W/Ti and W/TiN devices have shown good switching yield, this indicates that the failure of W/HfO_2/TaCN or the poor switching of TaCN/HfO_2/Ti is probably mainly due to the presence of TaCN electrode. FigIII.8 shows a possible explanation for this problem of TaCN as electrode in HfO_2. When TaCN is used as top electrode, the O ions migrate towards it with the applied positive bias during the forming operation and get stuck there failing to migrate back to the oxide layer during the RESET operation. It is possible that the migrated O ions react with the carbon in the TaCN layer forming some

stable TaCON that make the O ions unrecoverable (FigIII.8 left). Indeed, Piallat et al. studied the PEALD deposited TaCN on HfO_2 and observed the oxidation of TaCN/HfO_2 interface [10]. The oxygen content was increased at top and bottom interfaces of TaCN layer [10]. Adelmann et al. also studied MOCVD (metal-organic chemical-vapor deposition)-TaCN electrodes for thin film metal gate applications and suggested the presence of C-O bonds from their photoemission spectra [11]. Hence the presence of O in TaCN is possible. Similarly, when TaCN is used as bottom electrode, we observe some resistive switching cycles because the O ions can migrate back and forth between the Ti top electrode and the CF region in the HfO_2 oxide layer. However, during the switching operations, it is likely that some of the O ions get trapped at the TaCN bottom electrode and affecting proper cycling of the devices. This ultimately leads to their switching failure towards R_{on}.

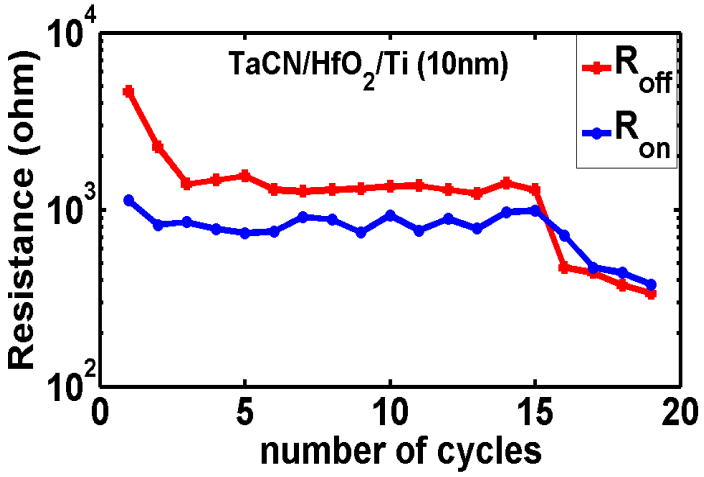

FigIII.7. Cycling of TaCN/HfO_2/Ti(10nm) showing the devices failure to R_{on}.

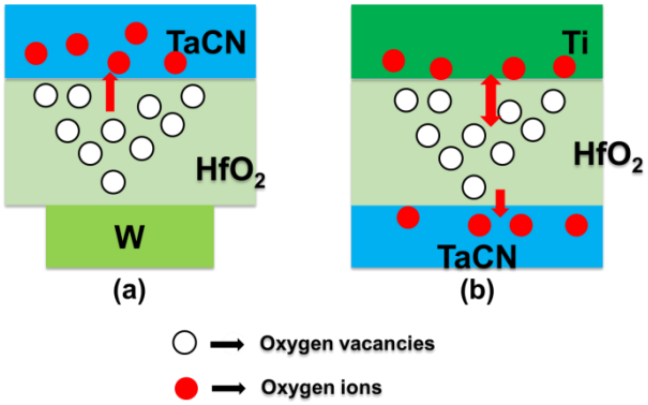

FigIII.8. Pictorial models showing possible switching failure or poor switching yield when TaCN is used as electrode (a) failure to switch to R_{off} after the forming operation where the O ions get stuck inside the TaCN or TaCN/HfO_2 interface (b) Devices perform some resistive switching cycles and the O ions ultimately get immobilized inside the TaCN bottom electrode.

III.3 Switching performance: HfO_2 at 350°C

The samples discussed are shown in **TableIII.2**. For simplicity, TiN/Ti will refer to TiN/HfO_2/Ti stack as above, Pt/Pt for Pt/HfO_2/Pt and Pt/Ti for Pt/HfO_2/Ti.

III.3.1 Switching characteristics

FigIII.9 shows the typical current voltage (IV) switching characteristics for the different samples. Pt/Pt samples display unipolar behavior while Pt/Ti and TiN/Ti display bipolar characteristics. FigIII.10 compares the switching voltages of the respective sample types. Pt/Pt samples present much higher forming voltage (V_F) compared to both Pt/Ti and TiN/Ti samples with the latter two showing similar V_F values.

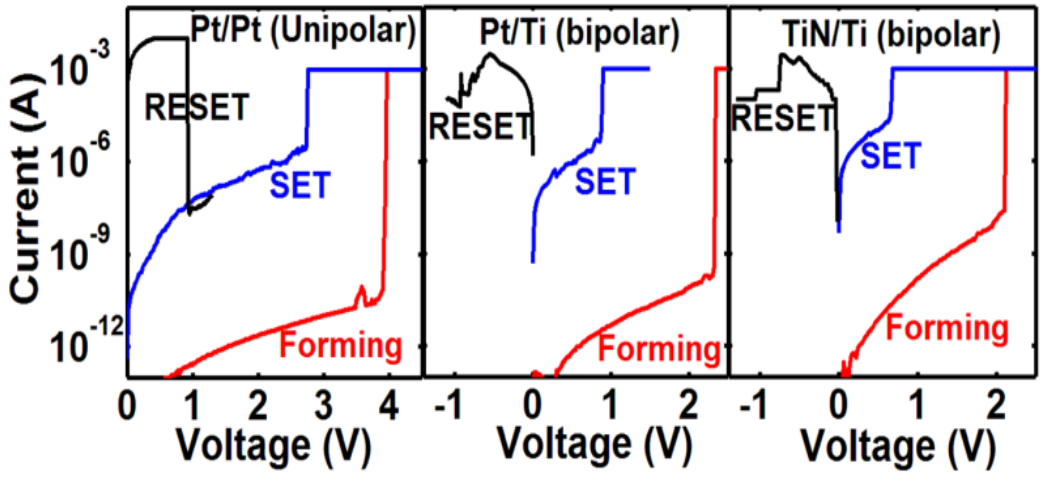

FigIII.9. Typical IV plot of unipolar Pt/Pt and bipolar Pt/Ti and TiN/Ti RRAM.

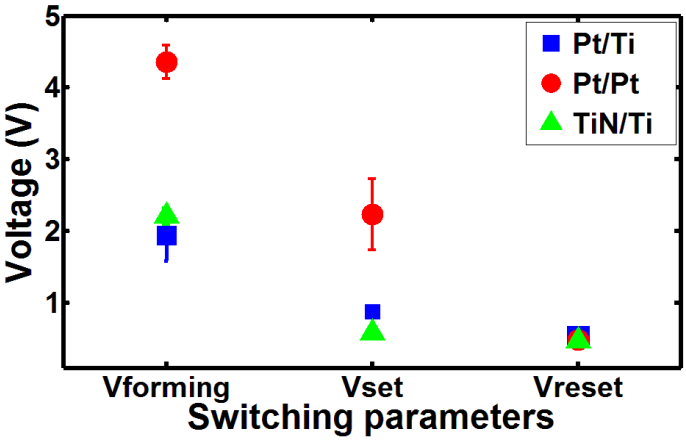

FigIII.10. Comparison of the switching voltages for the respective samples. Pt/Pt has a higher V_F while V_F for Pt/Ti and TiN/Ti are similar. We note similar $|V_{reset}|$ for all the sample types.

TiN/Ti and Pt/Ti devices exhibit a lower V_F. As mentioned earlier, this may be partly explained by the sub-stoichiometric region created at the Ti/HfO_2 interface

caused by the reactivity of the overlying Ti metal with oxygen (O) during the device fabrication [6], [7].

SET voltages (V_{set}) and RESET voltages (V_{reset}) for the different samples are also compared in FigIII.10. V_{set} is much higher for Pt/Pt while this value is lower than 1V for samples having Ti as TE. V_{set} is much lower than V_F for all the samples which is a strong indication that after the forming process, only a portion of the CF is involved in the reconstruction and rupture of the CF during SET and RESET respectively. Interestingly, the absolute V_{reset} value is similar for all the sample types as observed in the devices of the previous section and is defined as the voltage at which current is maximum during the RESET process. This may suggest similar field dependent and/or voltage dependent processes triggering RESET for all the devices irrespective of the electrode material used in RRAM stack.

The RESET curves for the different samples are further investigated in FigIII.11 and FigIII.12. Two different RESET profiles are observed: abrupt and progressive (FigIII.11**a** and FigIII.11**b** respectively). *In the abrupt RESET a sharp current drop of more than one order of magnitude takes place at V_{reset}*. On the other hand, for the progressive RESET, increasing the voltage beyond V_{reset}, the current exhibits a more gradual decrease, thereby making the RESET procedure a multi-step process. For Pt/Pt samples, we observe both abrupt and progressive RESET phenomenon with the abrupt process being the most frequent scenario: more than 70% of devices out of a statistics of 31 samples showed abrupt RESET (FigIII.11).

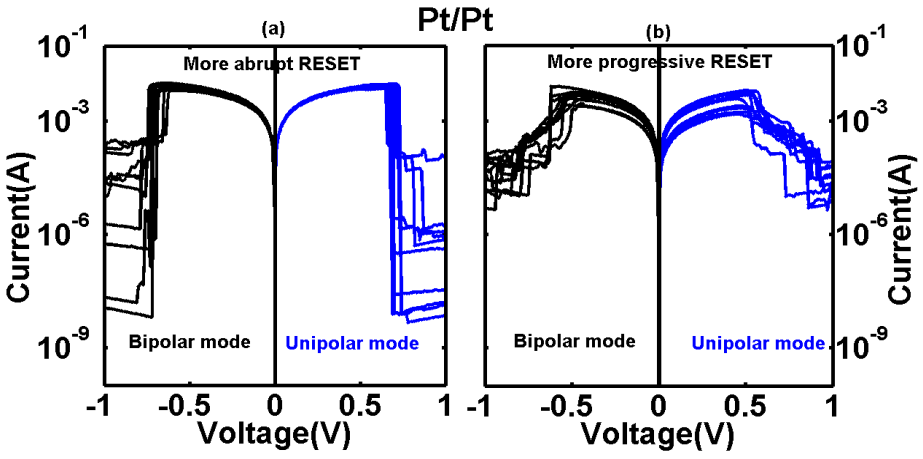

FigIII.11. Abrupt and progressive RESET profiles for Pt/Pt samples. The abrupt scenario being the predominant profile.

The abrupt process is a signature of a more affected CF during RESET with much higher R_{off} values compared to progressive ones (FigIII.11**a** vs FigIII.11**b**).

Furthermore, we observe that the IV plots are nearly symmetrical whether the RESET is performed in positive or negative polarities. This may suggest that oxygen defects responsible for resistive switching do not have preferential sites for accumulation on either electrode in Pt/Pt stack and that they may probably be randomly distributed on either oxide-electrode interface. On the other hand, for Pt/Ti and TiN/Ti samples, the RESET process is progressive (FigIII.12) exhibiting more uniform R_{off} distributions as shown in FigIII.13 [2]. Higher R_{off} values are reached after continuous application of voltage beyond V_{reset} suggesting that O ions are gradually moved towards CF to recombine with it. Hence, CF rupture for Ti/Ti and Pt/Ti devices seems to be more difficult during RESET compared with Pt/Pt. The introduction of Ti electrode seems to have introduced this improvement in the switching characteristics. We will return to this part later in the chapter for possible physical interpretations behind these different RESET profiles.

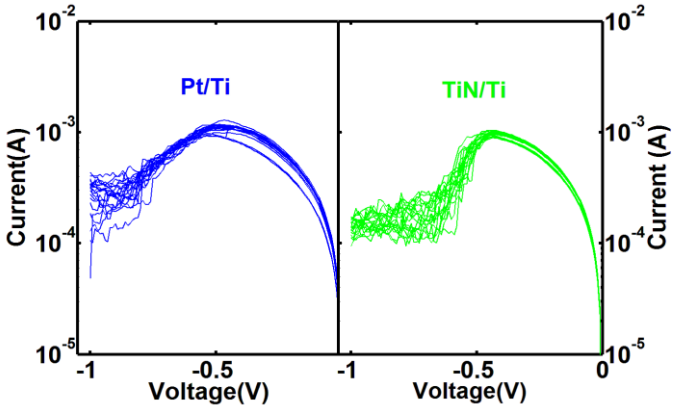

FigIII.12. Progressive RESET profiles for Pt/Ti and TiN/Ti samples.

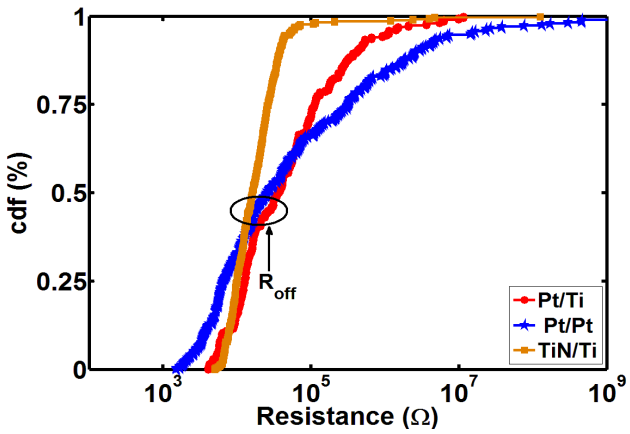

FigIII.13. CDF plot of resistance for all samples. Huge variability of R_{off} is present in Pt/Pt sample. An improved variability for TiN/Ti samples is seen with Pt/Ti being in an intermediate state.

III.3.2 Resistance behaviour with temperature

As an attempt to understand the temperature behavior of R_{off} for the different samples, the devices were programmed to high resistive state at room temperature and their R_{off} states were monitored while increasing temperature as seen in FigIII.14. FigIII.14 and FigIII.15a show that R_{off} for Pt/Pt increases with rising T and does not restore its initial state after cycling back to room temperature while for Pt/Ti and TiN/Ti (FigIII.14) samples R_{off} decreases with temperature exhibiting a semiconductor-like behavior, [12], [13] and CF is not very affected, i.e; they restore their initial state after cycling back to room temperature (shown for TiN/Ti in FigIII.15b). These results show the poor thermal stability of the Pt/Pt sample with respect to the Ti/TiN sample. Possible physical phenomena behind these different trends of R_{off} temperature profile depending on the electrode material are provided later.

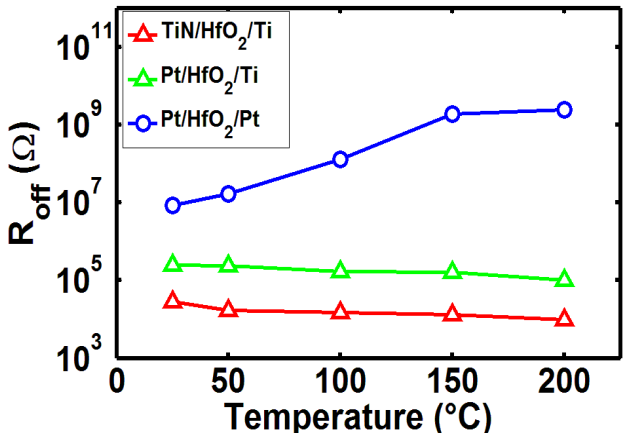

FigIII.14. Monitoring R_{off} at different temperatures for all the samples. R_{off} increases with temperature for Pt/Pt while it decreases with T for Pt/Ti and TiN/Ti.

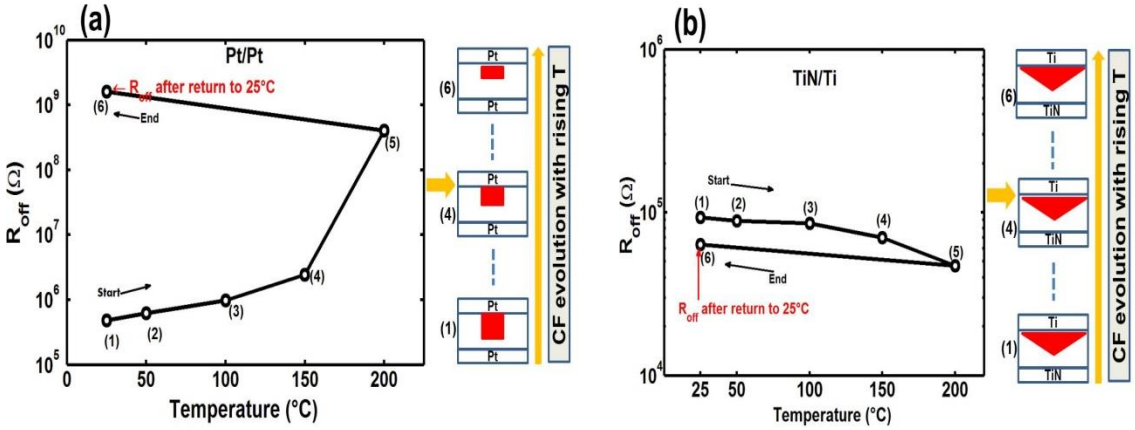

FigIII.15. Reading of R_{off} at different temperatures: a) R_{off} vs. T for Pt/Pt. Note the complete change of state, i.e., devices do not recover their initial R_{off} value; b) R_{off} vs. T for TiN/Ti. Devices recover their initial R_{off}.

III.4 Electrode material and switching mode

Having studied the switching characteristics of the different electrode materials with HfO_2, we observe a general trend: unipolar/non-polar mode of switching is observed with electrodes non-reactive with oxygen and symmetrical on either side of the HfO_2 layer like the Pt/HfO_2/Pt memory stack. While bipolar mode is observed with oxygen reactive electrodes and not symmetrical on either side of HfO_2 layer like TiN/HfO_2/Ti. However this general trend is not conclusive. Chen et al. reported unipolar switching of W/HfO_2/Ti devices [1] despite the presence of Ti at the top electrode with the bipolar mode being, though, more performant in terms of switching characteristics. De Stefano et al. reported unipolar switching with TiN/HfO_2/TiN devices [14] as we would expect due to the symmetry of the electrodes. Indeed, we have fabricated similar TiN/HfO_2/TiN devices and observed unipolar switching with very poor switching yield and the devices were properly switched in the bipolar mode with negative voltage applied to the top electrode as shown in FigIII.16. Despite the presence of TiN at top and bottom electrodes, the devices do not seem to be symmetrical due to the ALD deposition of HfO_2 on the TiN bottom electrode. ALD deposition process involves water (H_2O) and it is probable that the TiN BE gets more oxidized compared to the TiN TE and hence creating an interfacial TiON layer at the BE/oxide interface which breaks the symmetry of the electrodes (FigIII.16 right).

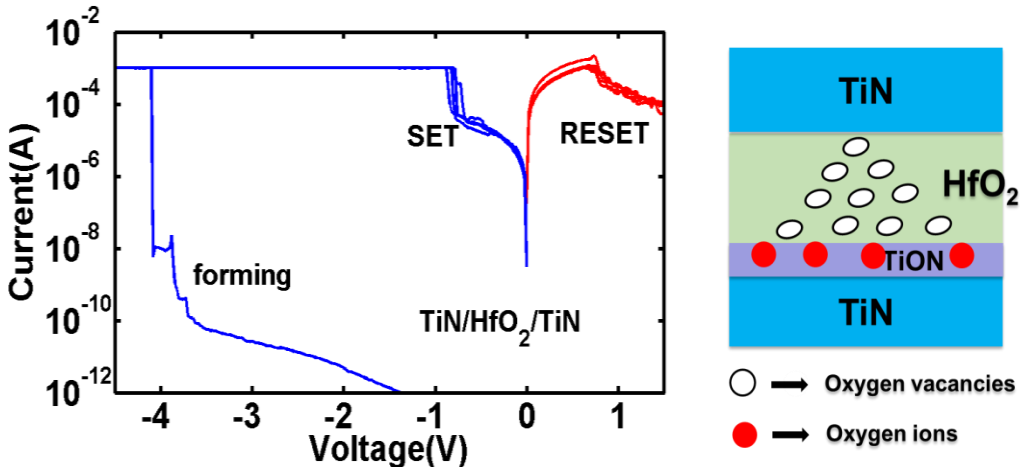

FigIII.16. (left) Current-voltage plot of TiN/HfO_2/TiN in bipolar mode with negative voltage applied to the top TiN electrode (right) pictorial model showing the bipolar mode of the devices with negative electrode applied to TE. The number of defects in the illustration is for qualitative view only and has no special meaning.

The symmetry rule of the electrodes for unipolar/non-polar switching may be really true only if the electrodes are purely inert and non-reactive with oxygen like Pt.

The presence of TiN or other related electrodes that are susceptible to oxidation, the symmetry rule may no longer hold.

III.5 Ab initio calculations/Simulations

III.5.1 Calculation methods

In order to have more understanding about the impact of the electrode materials on the devices' performance and some of the physical mechanisms involved in the switching operations, we carried out some first principles calculations. All simulations were based on density functional theory [15]. We used SIESTA[3] code [16], with the GGA-PBE functional to describe the exchange-correlation term, and Troullier-Martins pseudopotentials were used for each atomic species to account for the core electrons [17]. Polarized Double-Zeta (DZP) basis set with an energy shift of 50 meV and a Mesh cut-off of 300 Rydberg were used for the calculations. We occasionally used LDA functional to complete some results when necessary. A 2x2x2 monoclinic HfO_2 supercell with 96 atoms was set up for the point defects formation and FigIII.17 shows the supercell with the Frenkel-Pair (FP). A 4-fold coordinated oxygen site was considered for the oxygen vacancy during FP formation. For the optimization of the supercell geometry and atomic positions, the maximum residual force was 0.02eV/Å. The formation energies of neutral/charged FP and point defects were calculated using:

$$\Delta \boldsymbol{H^{FP}} = \boldsymbol{E_{tot}^{FP}} - \boldsymbol{E_{tot}^{HfO_2}} + \boldsymbol{q}(\boldsymbol{E_{VB}} + \boldsymbol{E_F}) \quad \textit{(III.1)}$$

$$\Delta H^{Vo/Oi} = E_{tot}^{Vo/oi} - E_{tot}^{HfO_2} \pm \mu_o \pm q(E_{VB} + E_F) \quad (III.2)$$

Where E_{tot}^{FP} is the energy of the supercell with FP, $E_{tot}^{HfO_2}$ the energy of HfO_2 supercell, E_{VB} the top of the valence band (VB), E_F the Fermi level measured from the top of the VB, $E_{tot}^{Vo/oi}$ the energy of the supercell with V_o or O_i, μ_o oxygen (O) chemical potential (plus for oxygen vacancy V_o and minus for oxygen interstitial O_i). For O chemical potential, we assumed an O_2 rich atmosphere (1.36 eV per O_2 correction was used [18]). Note that in the case of an insulator encapsulated in a Metal-Insulator-Metal (MIM) structure, the E_F level we use in (1) and (2) has to be interpreted as an electron injection level coming from the electrodes.

[3] SIESTA (Spanish Initiative for Electronic Simulations with Thousands of Atoms) is another popular DFT code that uses atomic orbitals as basis set. It is the code that is extensively used in this thesis.

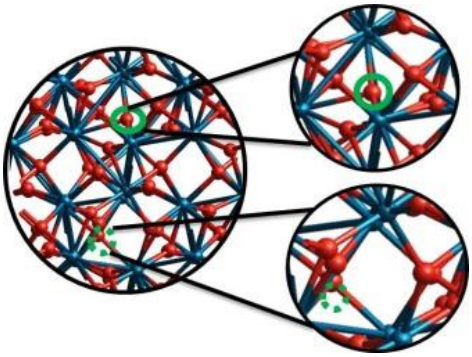

FigIII.17. 2x2x2 HfO_2 supercell with FP. O_i and V_o are respectively shown in solid and dashed circles. Hf atoms are represented blue and red for O atoms.

The activation energies or diffusion barriers (E_a) of defects were calculated using the climbing image Nudged Elastic Band (CI-NEB) technique [19] as implemented in Atomistic Simulation Environment (ASE) [20]. E_a corresponds to the height of the barrier when a diffusing species migrates from an initial state (IS) to a final state (FS) through a point of high potential energy called Transition State (TS). For the NEB calculations, at least 5 intermediate images were used and a maximum force of 0.05 eV/A was used as convergence criteria.

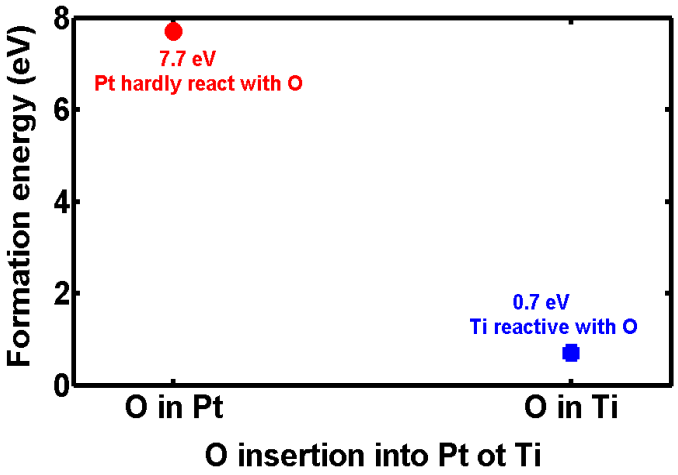

FigIII.18. Formation energy of O_i incorporation in Pt or Ti with O_i leaving behind an oxygen vacancy in the HfO_2 layer.

III.5.2 Ti/HfO_2 interface

In our study, different electrode material types were used but Pt and Ti represent the extremes of non-reactive and reactive electrodes with oxygen respectively. Both Pt and Ti are used as top electrodes. Although, Pt has been used as a catalyst in oxygen reduction reactions in fuel cell applications [21], it remains an inert metal and hardly

reacts with O as shown in FigIII.18 [22]. Nevertheless, Nagata et al. reported possible Pt-O formation using hard x-ray spectroscopy under bias [23]. On the other hand, Ti is known as an O reactive metal (FigIII.18) [22] and its reactivity with the HfO_2 layer is important in the memory device performance. Therefore, we have looked at the possible Ti/HfO_2 interface that may be formed as well as the diffusion of O across it. We investigated this scenario by studying the thermodynamic stability of the combination of Ti and Hf sub-oxides when Ti is deposited on HfO_2. A number of studies were conducted on Hf and Ti sub-oxides by different groups even though those studied were in general not oriented towards RRAM applications. Of these studies, αTiO_y ($0 \leq y \leq 0.5$) and HfO_y ($0 \leq y \leq 0.5$) phase diagram calculations were respectively performed in [24] and [25] by Burton and van De Walle. Puchala and Van der Ven investigated the thermodynamics of ZrO system [26] which share many similarities with HfO system. Ti_2O_3 and Ti_4O_7 Magnéli phases were recently investigated in [27] which followed upon the work of Marezio and Dernier [28]. These works allowed us to construct the stable TiO_y and HfO_y crystal structures for our interface calculations. The following chemical reaction was used to reflect the thermodynamic ensemble involving Ti deposition on HfO_2 and has to be interpreted as a reaction occurring at the Ti/HfO_2 interface:

$$HfO_2 + Ti \rightarrow TiO_y + HfO_{2-y}$$

FigIII.19 shows the formation enthalpy (ΔH) of $TiO_y + HfO_{2-y}$ by varying y and the results obtained with two different functionals, namely GGA and LDA, are also compared. We note that the surface energies of the different interfaces were not considered. The calculated energies using LDA are lower than those obtained with GGA and the average value between LDA and GGA may be more representative of the experimental values if they were available. Nevertheless, we see that for both functionals, ΔH corresponding to y = 0.5 has the lowest energy. This is an interesting point: *It indicates that the most probable composition of the Ti/HfO_2 interface when Ti is deposited on HfO_2 during device fabrication would be $TiO_{0.5}/HfO_{1.5}$ or Ti_2O/Hf_2O_3 written differently*. Therefore, we propose that when $Ti/HfO_2/TiN$ RRAM device is fabricated, the composition of the stack would most probably look like $Ti/Ti_2O/Hf_2O_3/HfO_2/TiN$ before the forming operation. This is pictorially shown below (FigIII.20). The formation of TiO_y layer on HfO_2 after Ti deposition was experimentally

validated by Sowinska et al. [6] and their results support our findings about Hf-Ti suboxides formation at the Ti/HfO_2 interface. The sub-oxide layers (Ti_2O and Hf_2O_3) making up the interface are both metallic/semi-metallic. The semi-metallic behavior of Hf_2O_3 has already been published by Xue et al. [29,30]. Ti_2O belongs to the Pbcn (No. 60) space group as calculated by Burton and van de Walle while Hf_2O_3 belongs to the $P\bar{4}m2$ (No. 115) space group as calculated by Xue et al.

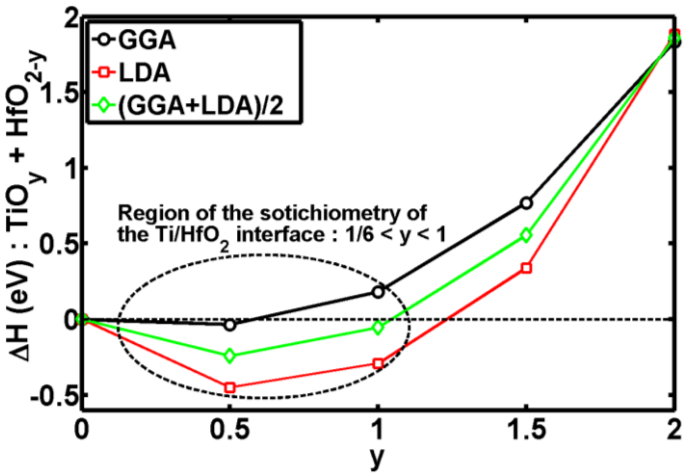

FigIII.19. Thermodynamic stability of the possible *Ti/HfO₂* interface. The calculations indicate a region of 1/6 ≤ *y* ≤ 1 for the interface with *Ti₂O/Hf₂O₃* being the most favorable composition.

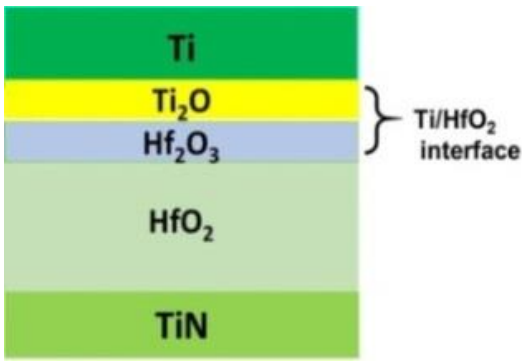

FigIII.20. Pictorial model showing probable Ti/HfO_2 interface after Ti deposition on HfO_2 from thermodynamic perspective.

Although our calculations do not provide any information about the thickness of this interface, we have shown in chapter II that 10 nm of Ti on 3nm of HfO_2 resulted in forming-free operation and that the initial states of the devices were conductive. Therefore, we hypothesize that the thickness of the interface should be thin probably below few nanometers (≤ 3 nm) because the diffusion of O in Ti would be kinetically limited. Indeed, we calculated the diffusion of O in hcp-Ti (FigIII.21) by considering O in octahedral sites (lowest energy position of O_i in hcp-Ti) and obtained a barrier of

3.5 eV in agreement with the 3.25 eV calculated by Wu et al. [31]. However, Wu et al. performed more comprehensive calculations of O diffusion in Ti by looking at all its possible diffusion paths and found that the migration of O may be lower via some other directions with average activation energy of about 2.1 eV. Therefore, O may still diffuse in Ti via high energy sites. Despite our calculated E_a for O diffusion being higher, 2.1 eV calculated by Wu et al. still suggest that continuous O diffusion to Ti will be kinetically limited at some point.

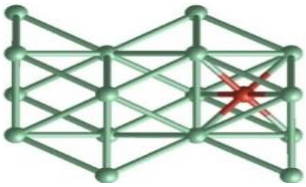

	E_a (eV)
O_i in hcp-Ti	3.5

FigIII.21. Atomistic model showing O_i in hcp-Ti considered for diffusion. The table shows the calculated diffusion barrier.

To provide a more thorough picture about Ti reactivity with HfO_2 at the interface, we constructed a Ti/HfO_2 interface model by inspiring from the work of Prodhomme et al. [32] on TiN/HfO_2 interface in matching our interface Ti and Hf atoms. We placed the interface Ti atoms on HfO_2 by coinciding the lattice direction of Ti with those of interface Hf in HfO_2. We then added layers of hcp-Ti on top of the interface followed by a vacuum and allowed the system to relax (minimize the total forces and stresses). Since constructing the full interface as shown in FigIII.20 would be very challenging in terms of matching the different structures and computationally very prohibitive, the stoichiometry of our interface model is not exactly like the one obtained with the thermodynamic study (FigIII.19). However, our constructed model has the merit of providing some useful information about RRAM operation. FigIII.22 shows the constructed interface and the considered O atom that was allowed to migrate from HfO_2 to Ti. We note that the migrating O atom that is considered is right at the interface and the calculated barrier could change depending on the way the interface was constructed and whether the moving atom was near the interface or not. Nevertheless, the calculated 1.5 eV (TableIII.4) for oxygen diffusion through the interface indicates that oxygen may migrate across Ti/HfO_2 interface if sufficient energy is present during device fabrication to allow for its slight oxidation. In our devices, Ti was deposited at 350 °C (623.15 K) and subsequent top contact pad (AlCu) deposition was carried out at 450 °C (723.15 K). For a semi-quantitative estimation and using the Arrhenius equation

$$\tau = \tau_o \exp(-E_a/(k_b T)) \qquad \text{(III. 3)}$$

with $\tau_o = 10^{13}$Hz, T = 700K and E_a = 1.5 eV, we calculate a migration time t = $1/\tau$ = 6.3 ms. Hence, we believe that these thermal budgets supply enough energy to the O atoms at the Ti/HfO_2 interface and allow them to overcome the calculated 1.5 eV barrier or slightly higher. Further O enhanced diffusion into the bulk of Ti would be kinetically limited as previously mentioned. These results support the pictorial interface model of FigIII.20**.**

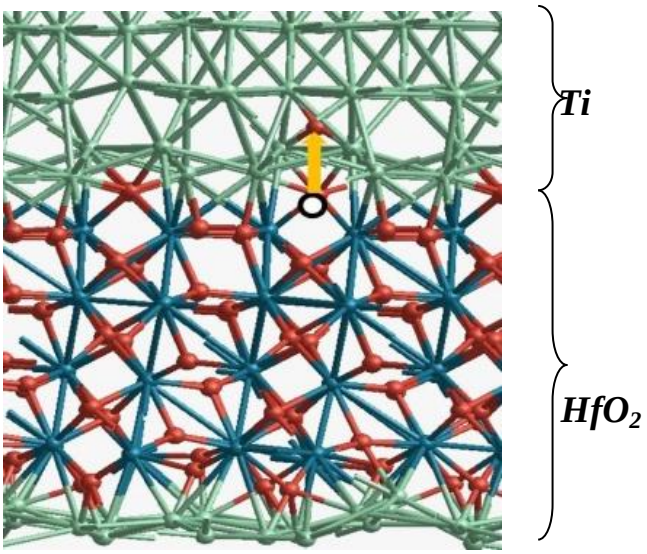

FigIII.22. Ti/HfO_2 interface model and O migration across it. The open circle indicates the initial position of the O atom before diffusion.

TableIII.4. Diffusion barrier of O at the Ti/HfO_2 interface.

Defect	E_a (eV)
O at Ti/HfO_2 interface	1.5

III.5.3 Frenkel-Pair defect formation : prototype defect for CF formation in HfO_2 RRAM

Frenkel pair (FP) defect is an oxygen atom that leaves behind an oxygen vacancy and sits in an interstitial position resulting in an oxygen vacancy/oxygen interstitial (O_i + V_o) pair. Hence, in our approach, we consider FP as prototype defects that may lead to the conductive filament formation during the forming operation in RRAM. We investigated FP formation in both neutral and charged states. FigIII.23 shows their formation energies with respect to the Fermi level which corresponds to the electron injection level into the system. In the following $\boldsymbol{O_i^{+/-q}}$ and $\boldsymbol{V_o^{+/-q}}$ respectively

stand for oxygen interstitial and oxygen vacancy in charge state +/-q. The formation energy (ΔH^{FP}) of the neutral FP (O_i^{2-} + V_o^{2+}) calculated as 5.2 eV, in agreement with [33], is energetically high. However, depending on the Fermi level ΔH^{FP} may become lower by introducing charges into the system. FP formation with e^- injection becomes more favorable at -2,-3 and -4 charge states close to CB (FigIII.23) with the injected electrons transiting at the oxygen vacancy sites (V_o) below the CB as shown in the FP defect energy levels of FigIII.24. This is an important point: It indicates that in order to break Hf-O bonds thereby creating (V_o, O_i) pairs which ultimately leads to CF formation, charge injection is required. The consequence of this result is that oxide degradation may be initiated by electron injection. FP formation in HfO_2 will be more thoroughly discussed in chapter V.

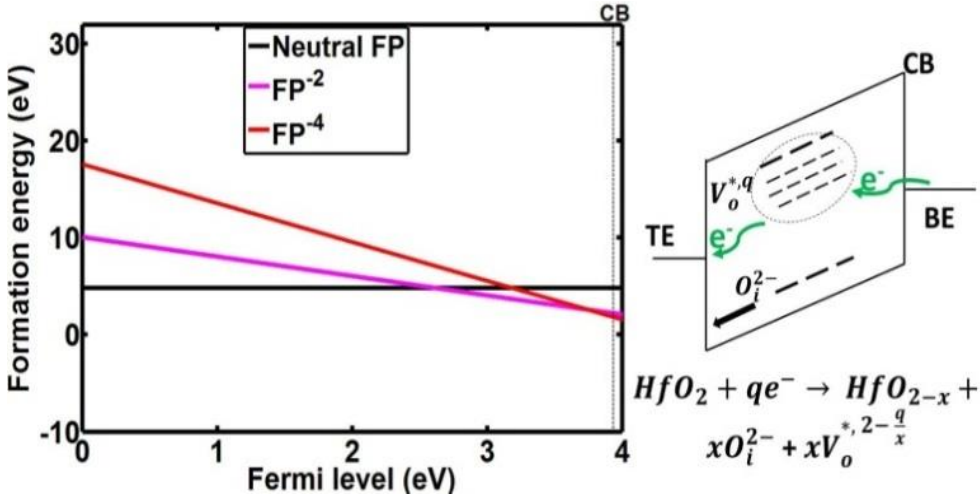

FigIII.23. Formation energy of neutral and charged FP with respect to the Fermi level measured from the VB.

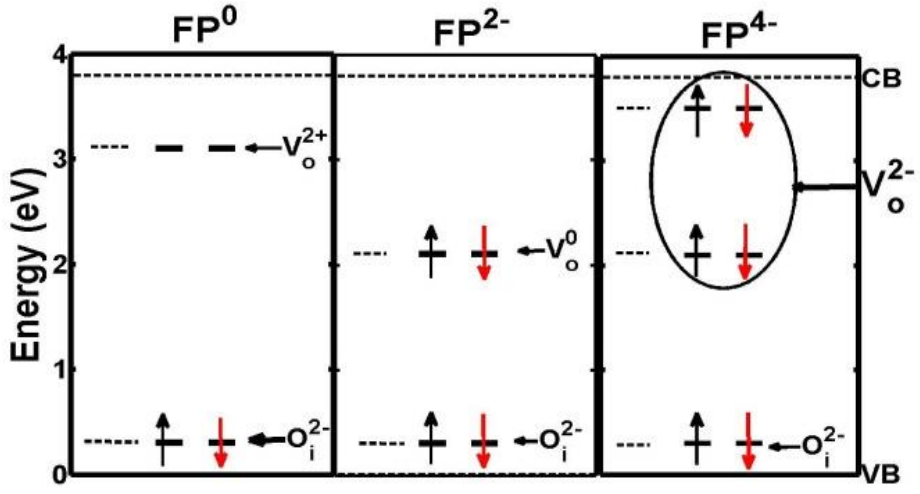

FigIII.24. Defect energy levels of FP formation with e^- injection extracted from the projected density of states on the defects. O_i remains at O_i^{2-} state while V_o changes from V_o^{2+} to V_o^{2-}.

III.5.4 A quick view of CF formation in HfO_2 via electron injection

Having considered FP formation in HfO_2, in this section we briefly look at some of the stages that lead to the CF formation through the electron injection process. CF formation will be discussed more extensively in chapter V. Details about e^- transition, emission and/or capture rates are beyond the scope of this study. FigIII.25 shows the stability of point defects (V_o, O_i) with respect to the Fermi level (electron injection level) in HfO_2 which is in good agreement with [33]. The graph is suitable for describing pre-defects that may be present in HfO_2 after its deposition on BE during fabrication. We note that no band gap correction scheme has been used and the underestimation of the gap by DFT is a well know problem with standard functionals like LDA and GGA [33]. V_o^{2+} defect is the favorable vacancy charge state from VB to close to mid-gap, V_o^{+1} becomes favorable at around mid-gap and then changes to neutral V_o. Based on the defect stability graph (FigIII.25) and if there exist pre-defects like (V_o, O_i) in HfO_2 after device fabrication, we propose the band diagrams of FigIII.26 for FP formation in HfO_2 via e^- injection. The energy levels used for the defects are consistent with the obtained energies from [34] and [35]. At finite temperature, pre-defects (V_o, O_i) exist because of thermodynamic principles of entropy [36]. However, we expect less O_i in TiN/Ti due to the reactivity of O_i with Ti compared with Pt/Pt. This leads to higher V_o concentration in TiN/Ti which is in line with its higher initial current during the forming stage.. Three cases are respectively considered in FigIII.26a, b, c and are described as follows.

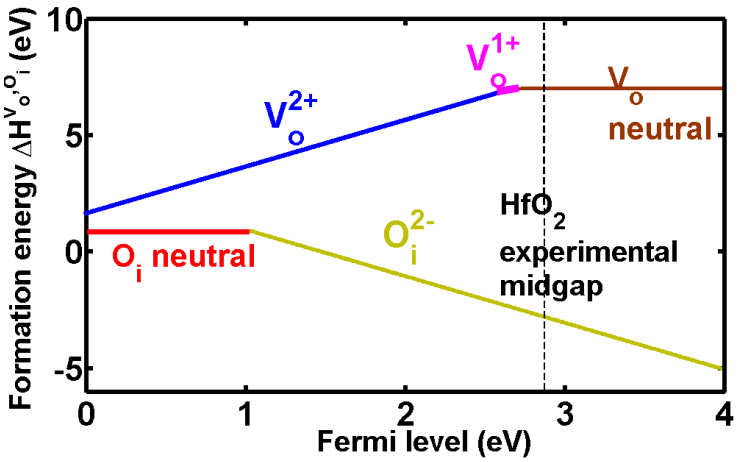

FigIII.25. V_o and O_i stability in HfO_2 with respect to the Fermi level measured from VB.

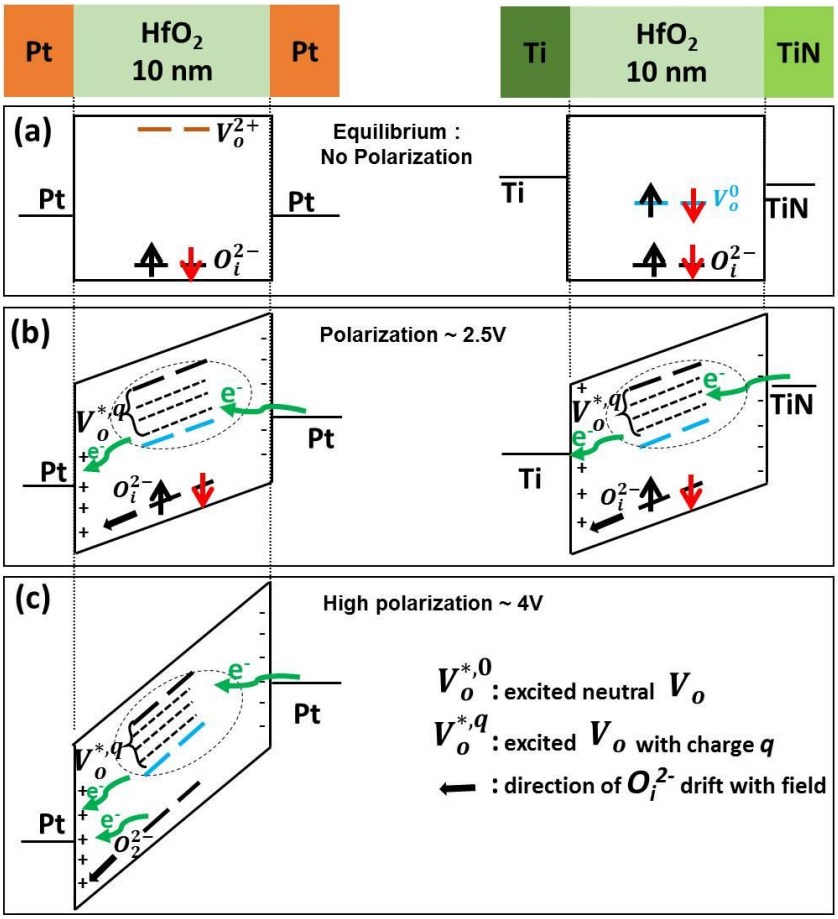

FigIII.26. Energy band diagrams of Pt/HfO_2/Pt and TiN/HfO_2/Ti stacks during e^- injection.

(a) Equilibrium/No polarization: This corresponds to the case where no voltage is applied. Based on the alignment of the electrodes with HfO_2 (FigIII.26) and the previous defects stability graph with the Fermi level (FigIII.25), the most stable defects under equilibrium in TiN/Ti devices are neutral V_o^0 and O_i^{2-} while they are V_o^{2+} and O_i^{2-} for Pt/Pt. It is noteworthy to note that the low energy state of FP when it is formed in HfO_2 is composed of V_o^{2+} and O_i^{2-} pair (see above) for at least temporarily. It is the electrode alignment level with HfO_2 that may change the resulting stable V_o charge state when the entire MIM RRAM structure is in equilibrium.

(b) Polarization at ~ 2.5V: In this case (FigIII.26b), the applied voltage to TE with BE grounded is greater than or equals to the forming voltage of TiN/Ti devices (FigIII.9) but less than that for Pt/Pt.

Possible FP states for TiN/Ti:

When FP formation is initiated with voltage application via electron injection, the resulting excited FP states can accept one or two electrons to respectively become $FP^{1-}(V_o^{*,1+}, O_i^{2-})$ or $FP^{2-}(V_o^{*,0}, O_i^{2-})$ or lose one (two) electron(s) to TE from FP close to the BE and become $FP^{1+}(V_o^{*,2+}, O_i^{1-})$, $FP^{2+}(V_o^{*,2+}, O_i^{0})$ (see Chapter V: section

V.4.2). In Chapter V, we show that FP^{+q} in TiN/HfO_2/Ti RRAM are unstable and rarely formed/expected during CF formation. Nevertheless, all the mentioned charge states with regards to V_o fall in the ellipse region (FigIII.26). Due to the positive polarity on Ti, the O_i^{2-} ions drift towards it and accumulate over there enhancing the formation of TiO_y at the Ti/HfO_2 interface in agreement with the increase of the interface TiO_y layer after forming according to the experimental results of Sowinska et al. [6].

Possible FP states for Pt/Pt:

With voltage application that initiates FP formation via electron injection, the resulting V_o states can accept 1 or more electrons to become $FP^{1-}(V_o^{*,1+}, O_i^{2-})$, $FP^{2-}(V_o^{*,0}, O_i^{2-})$ or lose electrons and become $FP^{1+}(V_o^{*,2+}, O_i^{1-})$ or $FP^{2+}(V_o^{*,2+}, O_i^{0})$. As for TiN/Ti, The O_i^{2-} ions drift towards the top Pt electrode due to the applied field. However, since the considered voltage (~2.5V) is not sufficient to form Pt/Pt devices, we suspect that at this voltage the O_i^{2-} would recombine with the created V_o at that instant due to the low O_i^{2-} diffusion barrier (shown later) and further voltage application is required to stabilize the CF.

c) High polarization ≥ 4V: TiN/Ti is not considered in this scenario because of its lower forming voltage. FP transitions considered for Pt/Pt in the previous case are applicable. However, one more important scenario occurs with O_i^{2-} as a result of FP^{4+} formation and we believe that it could be described as follows:

$$O_i^{2-} + O_o^{2-} \rightarrow O_2 + 4e^- \ (TE)$$

The O_i^{2-} reacts with its neighbor lattice oxygen (O_o^{2-}) thereby forming the molecular O_2 (FigIII.27) at the interface Pt/HfO_2 with the release of $4e^-$ to anode Pt [37], [38]. The formation of O_2 in HfO_2 RRAM has been experimentally proposed by Calka et al. [37]. Since the system is out equilibrium during the forming operation, another possibility could be the formation of O_2^{2-} according to:

$$O_i^{2-} + O_o^{2-} \rightarrow O_2^{2-} + 2e^- \ (TE)$$

The O_i^{2-} reacts with its neighbor lattice oxygen (O_o^{2-}) causing the formation of peroxide O_2^{2-} ion by injecting $2e^-$ into the TE. We postulate that it is the formation and accumulation of these O_2 or peroxide ions at the Pt/HfO_2 interface on the anode side that stabilize the CF in Pt/Pt devices. The low barrier of O_i^{2-} would make it difficult to

stabilize the CF if it did not lose some of its electrons to form neutral O_2 or peroxideO_2^{2-} (This part is more developed in Chapter V: section V.4.2).

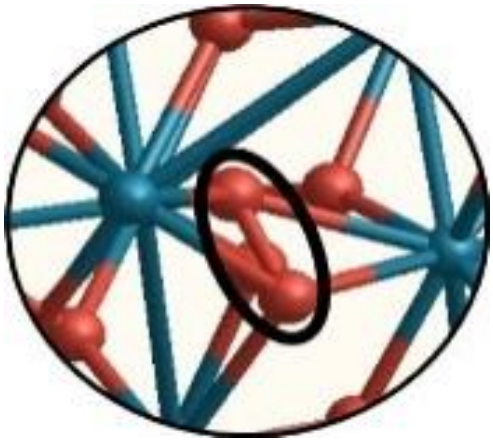

FigIII.27. The O_i^{2-}reacts with a lattice O_o^{2-} atom to form molecularO_2 .

III.5.5 Defect diffusion

Knowing defects' energy levels and their formation energy information provide indications about their stability and possible predominance or not under thermodynamic equilibrium. However, they do not provide any information about defects kinetics and which process may be thermodynamically favorable but kinetically limited. Since movement of defects (oxygen vacancies V_o and oxygen interstitials O_i) is at the heart of RRAM operation, oxygen vacancy diffusion was investigated in Al_2O_3 based RRAM [39]. In the case of HfO_2, V_o migration was thoroughly studied by Capron et al. for CMOS applications [40]. In our study, we also investigated the diffusion barriers of both O_i and V_o in their neutral and charged states in HfO_2 for more understanding on RRAM operation. V_o diffusion barriers were calculated by considering its migration from an initial position to a neighboring atomic position (FigIII.28). As for O_i, the diffusion was performed by exchange that is the starting atom takes the position of a substituting atom which continues to the final position as shown in the pictorial model of FigIII.29. Both V_o and O_i migrations are associated with activation energies (E_a) that are summarized in TableIII.5. The activation energy calculated for V_o^0 (2.16 eV) and V_o^{2+} (0.81) are in agreement with respectively 2.19 eV and 0.49 eV calculated by Capron et al. [40] for V_o^0 and V_o^{2+}. Similarly, the calculated barriers for O_i are in agreement with 0.7 eV for O_i^0 and 0.2 for O_i^{2-} obtained by Hou et al. [41]. The calculated diffusion barriers will help explain some of the phenomena in the next sections.

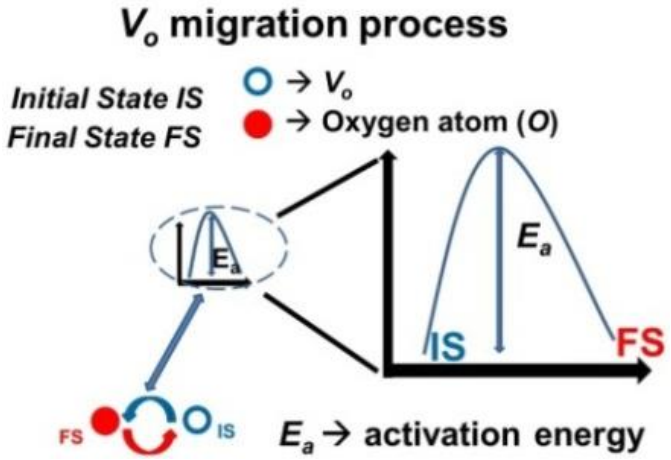

FigIII.28. Pictorial model showing V_o migration process with a near atom. This migration is associated with an E_a that is calculated by the NEB technique.

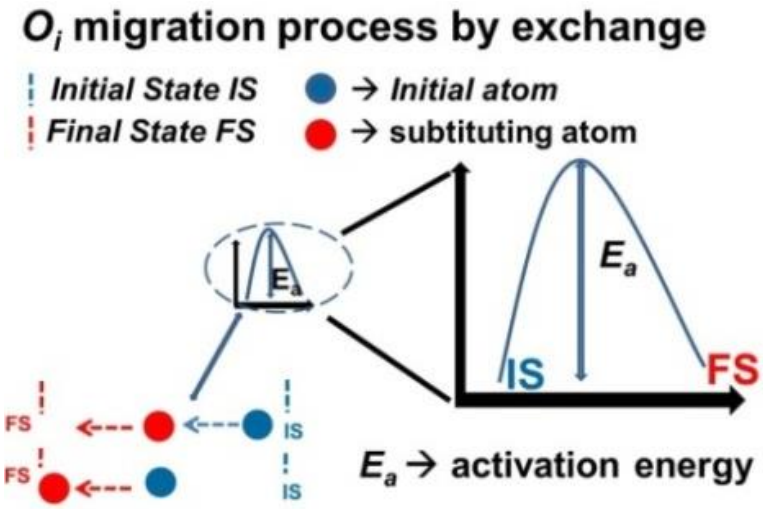

FigIII.29. Pictorial model showing O_i migration process by exchange. This migration is associated by an Ea that is calculated by the NEB technique.

TableIII.5. Defects activation energy calculations.

Defect type	E_a (eV): this work	E_a (eV): literature
V_o^0	2.2	2.19 [40]
V_o^{2+} [IS to FS]	0.9	0.49 [40]
V_o^{2+}[FS to IS]	0.1	0.05 [40]
O_i^0	0.6	0.7 [41]
O_i^{2-}	0.2	0.2 [41]

III.5.6 Thermal stability

In order to understand the poor thermal stability of Pt/Pt samples and the increase of R_{off} values with the temperature rise (FigIII.14), we refer to the calculated diffusion barriers for neutral and charged oxygen interstitials (O_i, O_i^{2-}) in HfO_2 as shown in TableIII.5**.** Since Pt is hardly reactive with O, we propose the models of

FigIII.30 as possible distribution of O_2^{2-}/O_i (O_2) and V_o in HfO_2 layer when CF is formed. When temperature is raised in Pt/Pt sample, the O_2^{2-}/O_i distributed around V_o rich CF region recombine with the latter resulting in CF re-oxidation, thus explaining R_{off} increase with T. This O_2^{2-}/O_i recombination with V_o in Pt/Pt sample is further reinforced with T rise due to the low migration barrier of O_i as shown in TableIII.5. This is not the case in TiN/Ti or Pt/Ti samples because of the low concentration of O_i in HfO_2 layer due to the reactivity of Ti with oxygen.

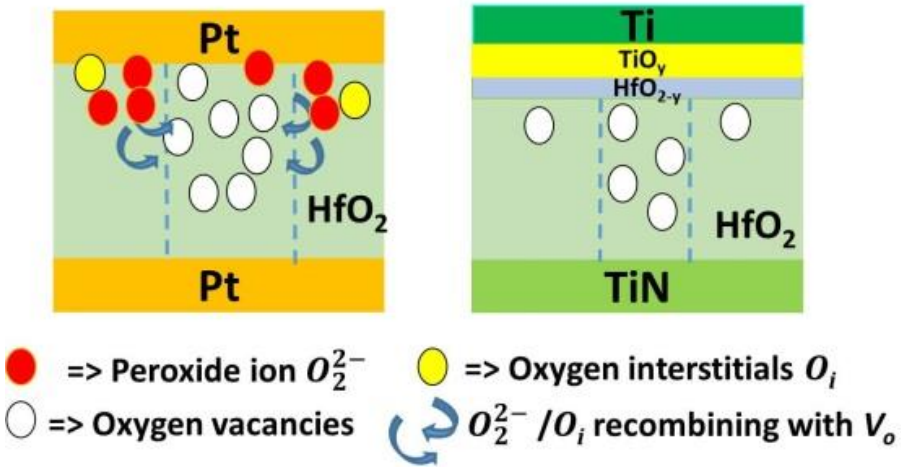

FigIII.30. Illustration showing the resistance increase with temperature in Pt/Pt which is explained by the re-oxidation of the CF region by O_2^{2-}/O_i at Pt/oxide interface. For Pt/Ti and TiN/Ti, R_{off} slightly decreases with T and the CF is not very affected.

III.5.7 RESET profiles

Using the O_i/V_o profile shown in FigIII.31, we associate the progressiveness or abruptness of RESET as a direct consequence of the distribution of oxygen ions in HfO_2 layer when CF is formed. We attribute the abrupt RESET to the scenario where the O_2^{2-}/O_i surrounding the CF region at the interface recombine abruptly with the latter resulting in much higher R_{off} levels (more ruptured CF) as shown in FigIII.31 due to the low migration barrier of O_i^{2-} (0.24 eV). The progressive RESET occurs when O_i mostly present at the oxide/electrode interface recombine gradually with CF region. The fact that both RESET types occur with Pt/Pt samples with more predominant abrupt scenario could be attributed to the stochastic nature of RRAM switching with some interfacial O_2^{2-}/O_i causing more progressive RESET by rupturing CF at its tip. The absence of much abrupt RESET in TiN/Ti and Pt/Ti samples is mostly due to the reactivity of O_i with Ti layer which hinders the abrupt recombination of O_i with CF region (FigIII.32).

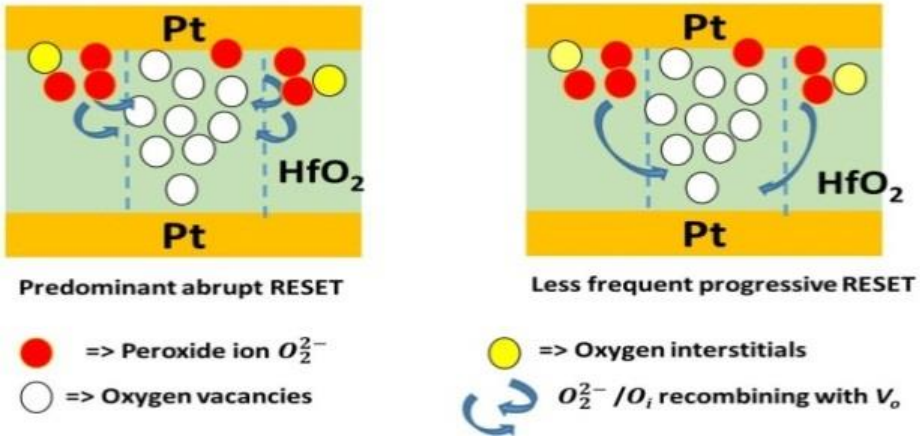

FigIII.31. Illustration showing possible O_i/V_o recombination scenario during abrupt and progressive RESET in Pt/Pt.

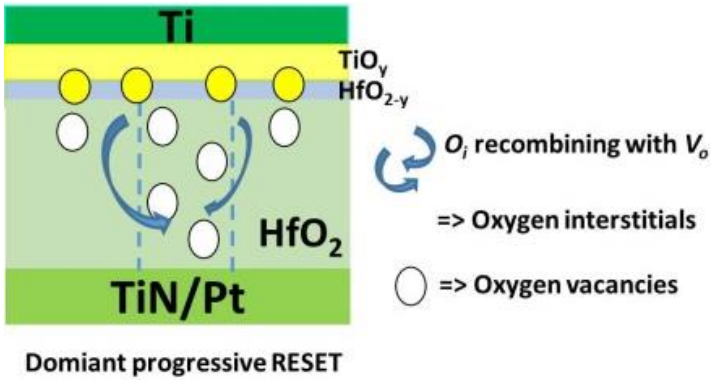

FigIII.32. Illustration showing possible O_i/V_o recombination scenario during progressive RESET in TiN/Ti and Pt/Ti devices.

III.6 Conclusions

We have provided a comprehensive analysis of RRAM switching characteristics by using a variety of electrode materials. The performance of HfO_2 based memory cells and their switching modes are largely dependent on the electrode/oxide interface rather than on the properties of the oxide layer alone. Devices showing unipolar switching mode generally have symmetrical electrodes at the bottom and top electrodes and are non-reactive with oxygen like Pt. Bipolar devices generally have non-symmetrical electrodes with one of the electrodes being oxygen reactive like Ti.

In our devices having TaCN as electrodes, we either did not observe resistive switching when TaCN was used as top electrode or measured very poor switching yield when TaCN was used as BE with Ti being the top electrode. W/HfO_2/Ti and W/HfO_2/TiN devices present good switching yield with larger switching window. However they have larger forming voltage compared to TiN/HfO_2/Ti devices. Similarly, Pt/HfO_2/Pt devices also exhibit larger forming voltage compared to TiN/HfO_2/Ti

memory cells. Both W/HfO_2/TiN and Pt/HfO_2/Pt devices have larger median R_{off} values with more important variability.

The introduction of Ti not only induced the reduction of the forming voltage but also resulted in the improvement of the uniformity of the devices. This is mainly attributed to the reactivity of Ti with oxygen resulting in the formation of subs-stoichiometric TiO_y layer at the Ti/HfO_2 interface. Our study of the thermodynamics of this interface reveals that its optimal stoichiometry and composition after device fabrication would be Ti_2O/Hf_2O_3**.**

The conductive filament formation for resistive switching involves Hf-O bonds breakage. This scenario was investigated through the Frenkel-pair (FP) defects formation in both neutral and charged states. The results show that the formation energy of the FP may be strongly reduced by charge injection and that oxide degradation may be initiated by electron injection.

For the devices' thermal stability and variability, the combined experimental and calculations results show that the concentration of oxygen interstitial (Oi) ions in the oxide after CF formation is larger for RRAM devices with inert electrodes (like Pt) compared with O reactive electrodes (like Ti) which results in degraded device performance. The lower O_i concentration in HfO_2 layer with Ti electrodes results in improved thermal stability and device variability.

As a closing note, the choice of the electrode material is very crucial in the search of optimized switching properties of HfO_2 based memory cells. Depending on the target applications, the metal electrode selection process may be addressed. It is very likely that the final RRAM material stack will be composed of a doped/alloyed HfO_2 or bilayer HfO_2 with some other oxides to cater for larger window and at the same time keep lower switching voltages and improved reliability.

References

[1] P.-S. Chen, Y.-S. Chen, K.-H. Tsai and H.-Y. Lee, "Polarity dependence of forming step on improved performance in Ti/HfO_x/W with dual resistive switching mode," Microelec. eng., vol. 112, pp. 157 - 162, 2013.

[2] T. Cabout, J. Buckley, C.Cagli et al., "Role of Ti and Pt electrodes on resistance switching variability of HfO_2-based resistive random access memory," Thin Solid Films, vol. 533, pp. 19-23, 2013.

[3] C. Cagli, J. Buckley, V. Jousseaume et al., "Experimental and theoretical study of electrode effects in HfO_2 based RRAM," IEEE IEDM, pp. 658–661, 2011.

[4] G. Bersuker, D. C. Gilmer, D. Veksler, et al., "Metal oxide resistive memory

switching mechanism based on conductive filament properties," J. Appl. Phys., vol. 110, p. 124518, 2011.

[5] S. B. Lee, H. K. Yoo, S. H. Chang, et al., "Time-dependent current-voltage curves during the forming process in unipolar resistance switching," Appl. Phys. Lett., vol. 98, no. 053503, 2011.

[6] M. Sowinska, T. Bertaud, D. Walczyk, et al., "Hard x-ray photoelectron spectroscopy study of the electroforming in Ti/HfO_2-based resistive switching structures," Appl. Phys. Lett., vol. 100, p. 233509, 2012.

[7] A. Padovani, L. Larcher , P. Padovani, C. Cagli, and B. De Salvo, "Understanding the Role of the Ti Metal Electrode on the Forming of HfO_2-Based RRAMs," IEEE IMW, pp. 1-4, 2012.

[8] C.Y. Chen, L. Goux, A. Fantini, A. Redolfi, S. Clima, R. Degraeve et al., "Understanding the Impact of Programming Pulses and Electrode Materials on the Endurance Properties of Scaled Ta_2O_5 RRAM Cells," IEEE IEDM, pp. 14.2.1 - 14.2.4, 2014.

[9] A. Fantini, L. Goux, R. Degraeve, D.J. Wouters, N. Raghavan, G. Kar et al., "Intrinsic Switching Variability in HfO_2 RRAM," IEEE IMW, pp. 30 - 33, 2013.

[10] F. Piallat, V. Beugin, R. Gassilloud, L. Dussault, B. Pelissier, C. Leroux et al., "Interface and plasma damage analysis of PEALD TaCN deposited on HfO_2 for advanced CMOS studied by angle resolved XPS and C–V," Appl. Surf. Scienc., vol. 303, pp. 388–392, 2014.

[11] C. Adelmann, J. Meersschaut, L.-Å. Ragnarsson, T. Conard, A. Franquet, N. Sengoku et al., "Thermally stable high effective work function TaCN thin films for metal gate electrode applications," Jour. Appl. Phys., vol. 105, 053516, 2009.

[12] B. Gao, J. F. Kang, Y. S. Chen, et al., "Oxide-based RRAM: unified microscopic principle for both unipolar and bipolar switching," IEEE IEDM, pp. 417–420, 2011.

[13] Z. Fang, H. Y. Yu, W. J. Liu, et al., "Temperature instability of resistive switching on HfO_x-based RRAM devices," IEEE Elec. Dev. Lett., vol. 31, pp. 476–478, 2010.

[14] F. De Stefano, M. Houssa, J. A. Kittl, M. Jurczak, V. V. Afanas'ev et al., "Semiconducting-like filament formation in TiN/HfO_2/TiN resistive switching random access memories," Appl. Phys. Lett., vol. 100, no. 142102, 2012.

[15] P. Hohenberg and W. Kohn, "Inhomogeneous electron gas" Phys. Rev., vol. 136, p. B864, 1964;W. Kohn and L. J. Sham, "Self-consistent equations including exchange and correlation effects", Phys. Rev., vol. 140, p. A1133, 1965,.

[16] J. Soler et al., "The SIESTA method for ab-initio order-N materials simulation," J. Phys.: Condens. Matter, vol. 14, pp. 2745-2779, 2002.

[17] N. Troullier and J. L. Martins, "Efficient pseudopotentials for plane-wave calculations," Phys. Rev. B., vol. 43, pp. 1993-2006 , 1991.

[18] L. Wang, T. Maxisch and G. Ceder, "Oxidation energies of transition metal oxides within the GGA+U framework," Phy. Rev. B., vol. 73, no. 195107, 2006.

[19] G. Henkelman, B. P. Uberuaga, and H. Jónsson, "A climbing image nudged elastic band method for finding saddle points and minimum energy paths," J. Chem. Phys., vol. 113, p. 9901, 2001.

[20] S. R. Bahn and K. W. Jacobsen, "An Object-Oriented Scripting Interface to a Legacy Electronic Structure Code," Comput. Sci. Eng., vol. 4, pp. 56-66, 2002.

[21] S. Mukerjee and S. Srinivasan , "Enhanced electrocatalysis of oxygen reduction on platinum alloys in proton exchange membrane fuel cells," J. Electroanal. Chem.,

vol. 357, pp. 201-224, 1993.

[22] K.-H. Xue, P. Blaise, L.R.C. Fonseca, G. Molas, E. Vianello, B. Traoré et al., "Grain-boundary composition and conduction in HfO_2: An ab-initio study," Appl. Phys. Lett., vol. 102, p. 201908, 2013.

[23] T. Nagata, M. Haemori, Y. Yamashita, H. Yoshikawa, Y. Iwashita, K. Kobayashi et al., "Oxygen migration at $Pt/HfO_2/Pt$ interface under bias operation," Appl. Phys. Lett., vol. 97, 082902, 2010.

[24] B.P. Burton, A. Van de Walle, "First principles phase diagram calculations for the octahedral-interstitial system αTiO_x, $0 \leq x \leq 0.5$," CALPAD, vol. 39, pp. 97-103 , 2012.

[25] B.P. Burton, A. Van de Walle, "First principles phase diagram calculations for the octahedral-interstitial system HfO_x, $0 \leq x \leq 0.5$," CALPAD, vol. 37, pp. 151-157, 2012.

[26] B. Puchala, A. Van der Ven, "Thermodynamics of the Zr-O system from first-principles calculations," Phys.Rev.B., vol. 88, no. 094108, 2013.

[27] A.C.M. Padilha et al., "Ti_nO_{2n-1} Magnéli phases studied using density functional theory," Phys. Rev. B., vol. 90, no. 035213, 2014.

[28] M. Marezio, P.D. Dernier, "The crystal structure of Ti_4O_7, a Member of the Homogenous series Ti_nO_{2n-1}," Journ. Sol. Stat. Chem., vol. 3, pp. 340-348, 1971.

[29] K.-H. Xue, P. Blaise, L. R. C. Fonseca, and Y. Nishi, "Prediction of semi-metallic tetragonal Hf_2O_3 and Zr_2O_3 from first-principles," Phys. Rev. Lett., vol. 110, no. 065502, 2013.

[30] K.-H. Xue, B. Traoré, P. Blaise, et al., "A combined ab initio and experimental study on the nature of conductive filaments in $Pt/HfO_2/Pt$ resistive random access memory," IEEE Trans. Electron Dev., vol. 61, p. 1394, 2014.

[31] H.H. Wu and D.R. Trinkle, "Direct Diffusion through Interpenetrating Networks: Oxygen in Titanium," Phys. Rev. Lett., vol. 107, 045504, 2011.

[32] P.-Y. Proddhomme, F. Fontaine-Vive, A. Van der Geest, P. Blaise, J. Even , "Ab initio calculation of effective work functions for a $TiN/HfO_2/SiO_2/Si$ transistor stack," Appl. Phys. Lett., vol. 99, no. 022101, 2011.

[33] J. X. Zheng et al., "First-principles study of native point defects in hafnia and zirconia," Phys. Rev. B., vol. 75, pp. 104112-1–104112-7 , 2007.

[34] P. Broqvist and A. Pasquarello, "Oxygen vacancy in monoclinic HfO_2: A consistent interpretation of trap assisted conduction, direct electron injection, and optical absorption experiments," Appl. Phys.Lett., vol. 89, no. 262904, 2006.

[35] K. Xiong, J. Robertson, M. C. Gibson, and S. J. Clark, "Defect energy levels in HfO_2 high-dielectric-constant gate oxide," Appl. Phys. Lett., vol. 87, no. 183505, 2005.

[36] N. W. Ashcroft and N. D. Mermin, Solid state physics, chapter 30. Philadelphia, USA: Saunders College, 1976.

[37] P. Calka, E. Martinez, V. Delaye et al., "Chemical and structural properties of conducting nanofilaments in TiN/HfO_2-based resistive switching structures," Nanotech., vol. 24, no. 085706, 2013.

[38] B. Traoré, P. Blaise, E. Vianello et al., "Impact of electrode nature on the filament formation and variability in HfO_2 RRAM," IEEE IRPS, pp. 5E.2.1 - 5E.2.5, 2014.

[39] M.Y. Yang, K. Kamiya, B. Magyari-Kope, M. Niwa, Y. Nishi and K. Shiraishi, "Charge-dependent oxygen vacancy diffusion in Al_2O_3-based resistive-random-

access-memories," Appl. Phys. Lett. , pp. 103, 093504, 2013.

[40] N. Capron et al., "Migration of oxygen vacancy in HfO_2 and across the HfO_2/SiO_2 interface: A first-principles investigation," Appl. Phys. Lett., vol. 91, no. 192905, 2007.

[41] Z.F. Hou, X.G. Gong, Q. Li, "Al-induced reduction of the oxygen diffusion in HfO_2 : an ab initio study," J. Phys.Cond. Matter, vol. 20, no. 135206, 2008.

Chapter IV

Impact of doping/alloying on HfO_2 based RRAM

In this chapter, we investigate the impact of engineering the HfO_2 layer by alloying it with other materials such as aluminum oxide (Al_2O_3) and titanium oxide (TiO_2). Alloying HfO_2 with Al_2O_3 will be viewed both from experimental and theoretical perspectives with particular attention given to the microscopic understanding of the low resistance state retention. The effect of alloying with TiO_2 will be mainly studied through the theoretical approach and the results will be assessed with regards to the available experimental data in the literature.

IV.1 Hafnium aluminum oxide alloy ($Hf_{1-x}Al_{2x}O_{2+x}$)

In the following sections, we study the impact of alloying HfO_2 with Al_2O_3 resulting in $Hf_{1-x}Al_{2x}O_{2+x}$ stoichiometry on RRAM electrical performance and reliability with more focus on the low resistance state retention.

IV.1.1 Samples description and fabrication for electrical characterization

5nm of HfO_2 and $Hf_{1-x}Al_{2x}O_{2+x}$ (9:1) were deposited by the atomic layer deposition (ALD*)* technique at 300°C in which $Hf_{1-x}Al_{2x}O_{2+x}$ (9:1) stands for the following : In each 10 cycles of ALD supercyle, 9 cycles was devoted to HfO_2 deposition followed by 1 cycle of that of Al_2O_3. For the rest of the chapter, HfAlO shall refer to $Hf_{1-x}Al_{2x}O_{2+x}$. The oxide layers (HfO_2 and HfAlO) were sandwiched between 35 nm TiN bottom electrode (BE) and 10 nm Ti top electrode (TE). Both BE and TE were deposited by physical vapour deposition (*PVD)* and the memory cell was fabricated in a mesa process as schematically represented in FigIV.1. The devices were integrated with an access transistor in 1T1R structure and the transistors were fabricated in 65-nm *CMOS* technology process. In the case of 1T1R structure, the compliance current during forming and SET operations is controlled by the access transistor and the devices do not suffer from the current overshoot problem that was highlighted in chapters I and II.

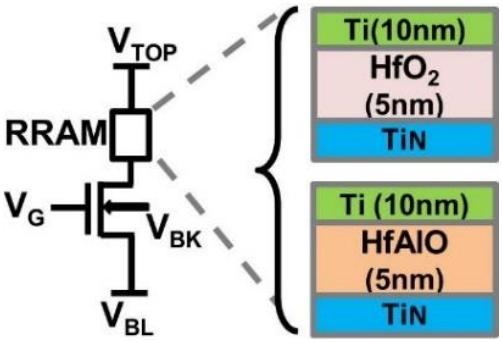

FigIV.1. 1T1R structure showing the HfO_2 and HfAlO oxide layers sandwiched between TiN (BE) and Ti (TE).

IV.1.2 Material properties

TableIV.1 highlights some of the material properties of both HfO_2 and HfAlO sample types as well as their available counterparts from ab initio calculations. We note

that for the two sample types, an annealing at 400°C for 1 hour in N_2 ambient was performed to simulate the back end temperature (T) seen by the devices used for electrical characterization. The ab initio data were calculated using structures that will be detailed later in the chapter. We observe that densities obtained from ab initio are slightly higher than the experimental values because of the more crystalline structures used for the ab initio models (as-deposited samples have lower density compared to annealed ones due to the crystallization process). Furthermore, HfAlO have a higher atomic concentration compared to HfO_2 resulting in shorter Hf-O and Al-O bond lengths. We shall see the implications of this bond shrinking later on the diffusion process.

	HfO_2			HfAlO (9:1)		
	Experiment		Ab initio (DFT)	Experiment		Ab initio (DFT)
	as-dep.	Annealed		as-dep.	Annealed	
Density (g/cm^3) [XRR]	9.56	9.63	9.78	8.76	8.79	8.83
Ratio Hf/(Hf+Al) (%) [RBS]	100	-	100	86	-	82
Dielectric constant	22.2	-	-	18.9	-	-
Atomic density ($atoms/cm^3$)	-	-	$8.39x10^{22}$	-	-	$8.53x10^{22}$

TableIV.1. Table showing the extracted physical parameters of the two sample types from physical characterization and ab-initio calculations. Red names in square bracket correspond to the technique used for the physical characterization. XRR stands for X-ray Reflectometry and RBS for Rutherford BackScattering.

IV.1.3 Switching characteristics

FigIV.2a, and b compare the IV switching voltages of HfO_2 and HfAlO. SET and RESET voltages are similar for both oxide types. The main difference between the two sample types being the higher forming voltage (V_F) for HfAlO as is further evidenced in FigIV.3. This in agreement with the experimental data of Fantini et al. [1].The Low V_F for HfO_2 may be related to two phenomena: its lower band gap which was measured by ellipsometry (5.6 eV for HfO_2 vs. 5.7 eV for HfAlO) and its higher dielectric constant (TableIV.1). The lower band gap of HfO_2 may favour more electron injection into it thereby giving an explanation to its higher pre-forming current (FigIV.3). Moreover, using Lorentz-Mossoti relation [2]:

$$E_{loc} = \frac{k+2}{3} E \qquad \text{(IV.1)}$$

where E_{loc} is the local electric field, k the dielectric constant and E the external field. We note that E_{loc} is higher for the higher dielectric constant (high-k) oxide (HfO_2) compared to HfAlO. According to the thermochemical description of dielectric breakdown proposed by McPherson et al. [2], this local electric field essentially reduces the barrier of HfO bond breakage process in HfO_2 during the forming operation compared to HfAlO as seen in the following:

$$\Delta H = \Delta H^* - p_0 E_{loc} \qquad \text{(IV.2)}$$

Where (ΔH) is the activation energy of bond breakage, ΔH^* the zero-field activation energy, p_0 the molecular dipole moment.

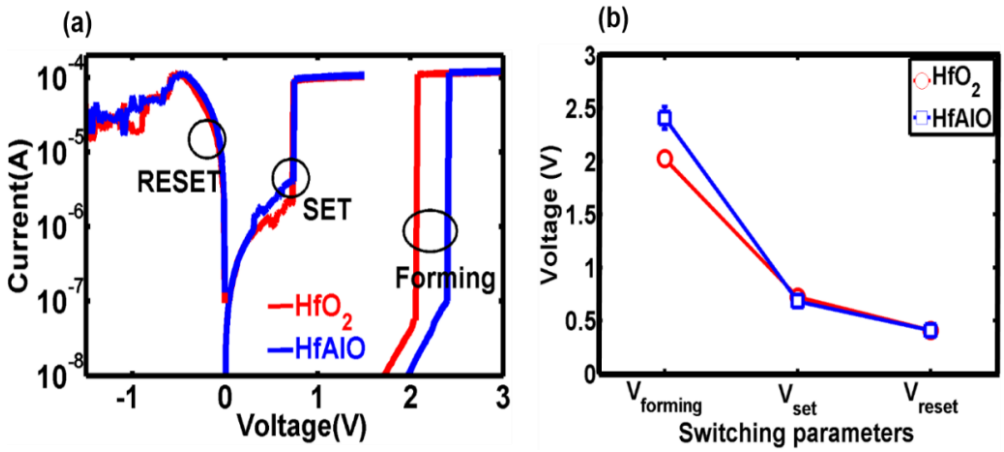

FigIV.2. Comparison of the IV switching parameters of HfO_2 and HfAlO sample types. (a) IV curves and (b) extracted geometric mean switching voltages. The main difference is the higher forming voltage (V_F) for HfAlO.

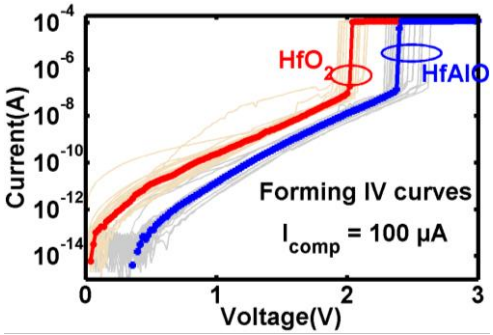

FigIV.3. Forming IV for both HfO_2 and HfAlO. Thick curves represent median of over 25 devices for each sample type. The lower V_F for HfO_2 is related to its lower band gap (more injection) and the increase of its local electric field due to its higher dielectric constant following Lorentz-Mossoti relation [2].

R_{on} and R_{off} distributions are also compared in FigIV.4 with an enforced compliance current of 100 µA and no significant difference is noted. Fig.6 shows the 10^6 cycling endurance for both samples (FigIV.5). Hence, in terms of switching characteristics, HfO_2 and HfAlO based RRAM devices have similar performance with the main difference being the lower forming voltage for HfO_2.

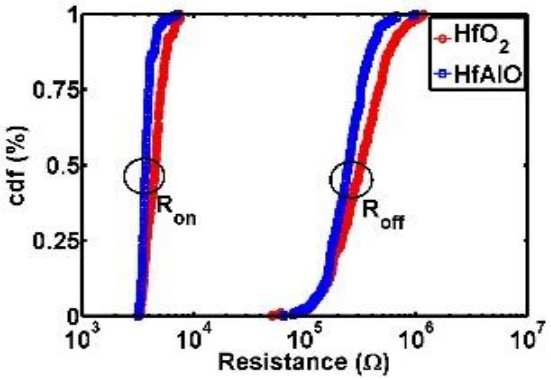

FigIV.4. Cdf plot of R_{on} and R_{off} for both samples. No significant difference is noted.

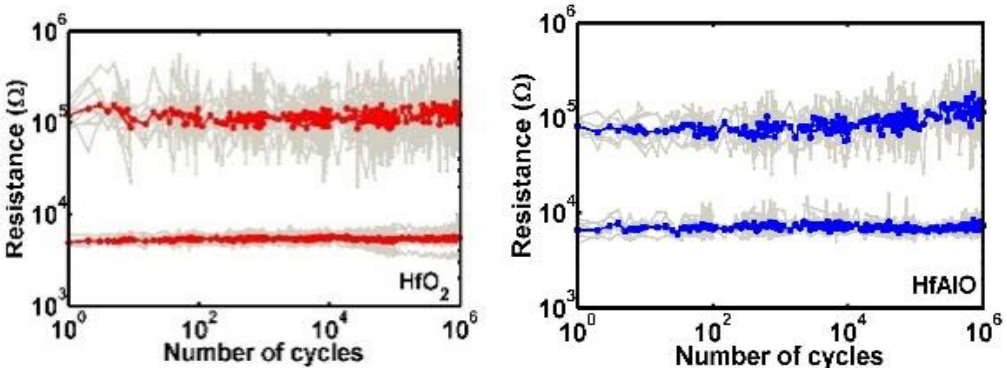

FigIV.5. Cycling endurance for both HfO_2 and HfAlO RRAM samples. As in Fig.5, no significant difference is noted. Both samples exhibit good cycling endurance.

IV.1.4 Low resistance (R_{on}) data retention

The data retention measurements were performed by programming the devices to the low resistance state with an enforced compliance current of ~ 100 µA that was set by applying proper voltage to the gate of the select transistor. The devices were put into the oven at the test temperature and their states were monitored. FigIV.6 shows R_{on} retention evolution of HfO_2 with time at 200°C and fails towards high resistance values as the retention time increases which we associate to the diffusion of V_o at the tip (constriction) of the conductive filament (CF) as shown in the pictorial model (inset FigIV.6). FigIV.7 compares the mean (geometric mean) R_{on} of HfO_2 at different

temperatures (T) and we observe that as T increases R_{on} fails faster towards R_{off} which indicates that R_{on} retention is a highly T activated process.

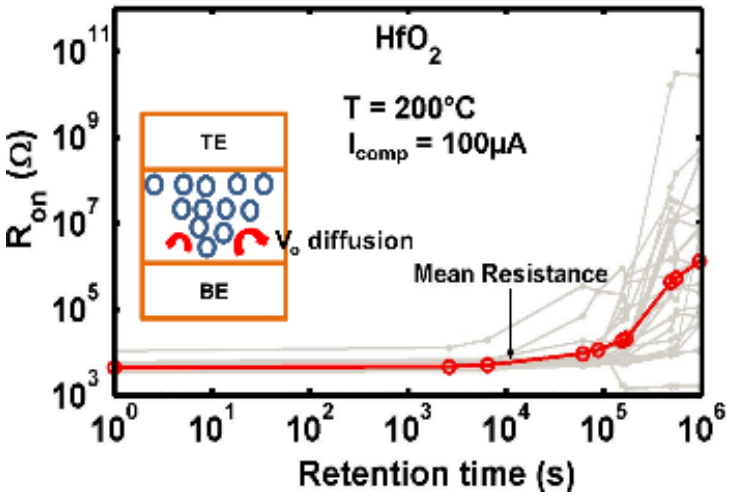

FigIV.6. R_{on} retention behaviour of HfO_2 at 200°C. The red curve shows the geometric mean trend of the devices. The pictorial model attributes the R_{on} failure to V_o diffusion at the *CF* tip (constriction) that is investigated later.

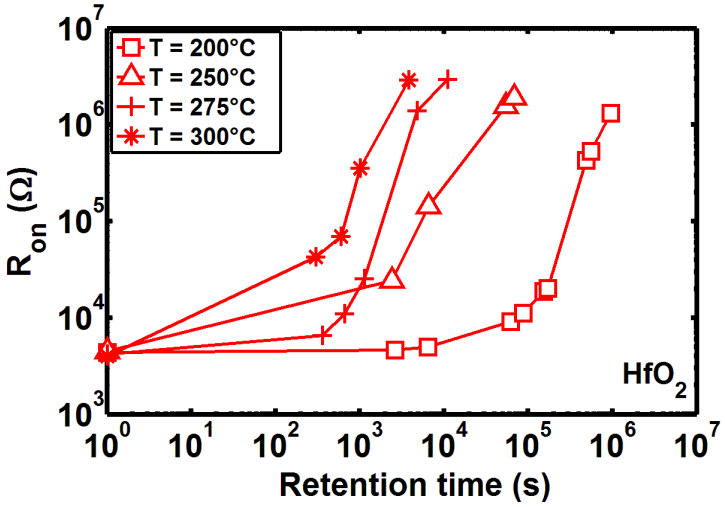

FigIV.7. Mean (geometric mean) R_{on} retention of HfO_2 at 4 different temperatures T. As expected, R_{on} failure is accelerated as T is raised. This is attributed to increased V_o diffusion at high T.

Similarly, FigIV.8 and FigIV.9 respectively show R_{on} retention of HfAlO at 200°C and the comparison of the mean R_{on} at different T. As in the case of HfO_2, R_{on} retention is a T activated process and fails faster towards high resistance level as T is raised. FigIV.10 compares the evolution of the mean R_{on} retention profile for HfO_2 and HfAlO. It can be clearly seen that HfAlO has a better R_{on} stability at all the investigated T. The improvement of R_{on} retention with Al incorporation is in agreement with the results of Fantini et al. [1] and Chen et al. [3].

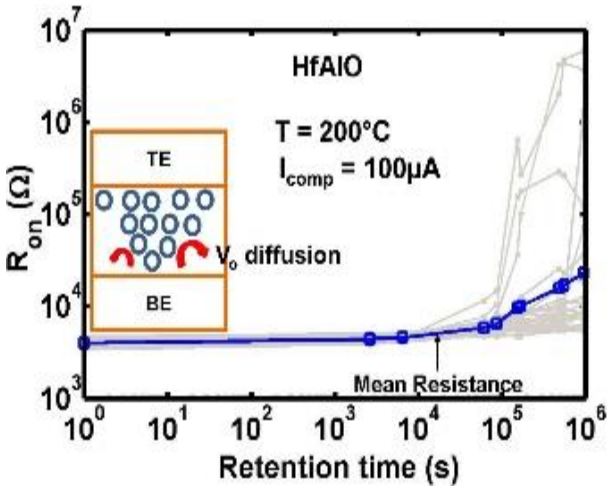

FigIV.8. R_{on} retention behaviour of HAfO at 200°C. The blue curve shows the geometric mean trend of the devices. As for HfO_2, the pictorial model attributes the R_{on} failure to V_o diffusion that is further investigated later.

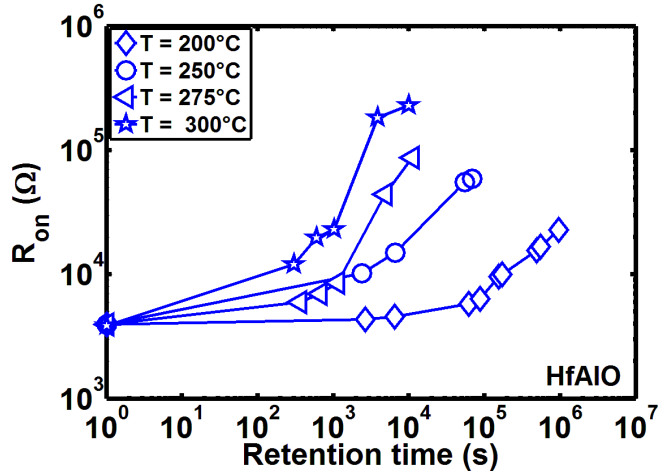

FigIV.9. Geometric mean R_{on} retention of HfAlO at 4 different temperatures T. As for HfO_2, R_{on} failure is accelerated as T is raised.

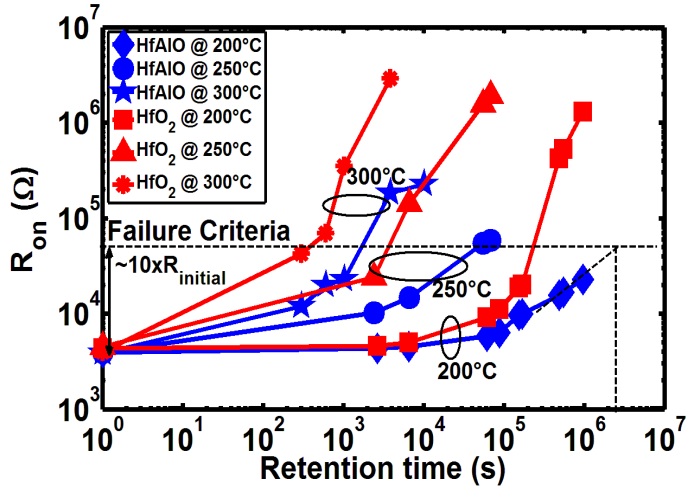

FigIV.10. Comparing R_{on} retention behaviour for HfO_2 and HfAlO. HfAlO has a better R_{on} stability. HfO_2 shows a more abrupt failure while it is more gradual for HfAlO.

IV.1.5 Arrhenius plot for activation energy extraction

Both HfO_2 and HfAlO devices being activated in T during R_{on} retention, it is then possible to extract some activation energy using the Arrhenius type of equation by plotting the devices' fail time during the retention with respect to T. This becomes possible by choosing an acceptable failure criterion for R_{on} evolution with the retention time. For our devices, the ratio between R_{off} and R_{on} corresponding to the switching window is around one order of magnitude or a little bit higher (FigIV.4). Therefore, we chose a failure criterion of 10 whereby we extracted the failure time at the point where the initial R_{on} has drifted towards R_{off} by one order of magnitude. The extracted failure times based on the above criteria, shown in FigIV.10**,** are plotted in an Arrhenius plot (FigIV.11**)** using the Arrhenius equation:

$$\tau = \tau_0 exp(-\frac{E_a}{k_b T}) \qquad \text{(IV.3)}$$

where τ is the rate of reaction, τ_0 the pre-exponential factor (~ 10^{12} – 10^{13} Hz), E_a the activation energy, $k_b$the Boltzmann constant and T the temperature. The linear trend of the failure time with respect to the inverse of temperature shows that the R_{on} retention failure process in HfO_2 based RRAM follows an Arrhenius type of law. Higher E_a is extracted for HfAlO consistent with its better thermal stability as shown in the previous figures and more than 10 years of retention of at least 125°C is extrapolated for both sample types.

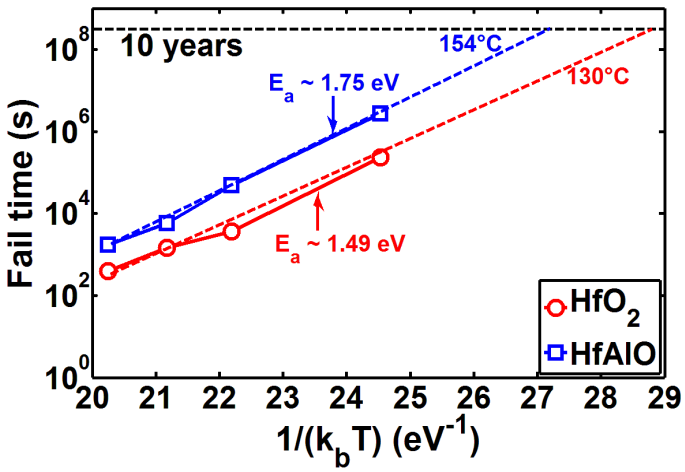

FigIV.11. Extracted failure time based on the criteria shown in Fig.11. A higher activation energy (E_a) is extracted for HfAlO (using Arrhenius). Both samples present more than 125°C retention of 10 years.

We have seen that in the above low resistance retention tests that the failure profile of R_{on} is a drift towards R_{off} values with the programming current of 100 µA and is in agreement with the failure profiles reported by Chen et al [4]. This profile is in contrast with the low resistance retention of the 1R devices that we have seen in Chapter II where their states were very stable at all the investigated temperatures with the programming current of 1mA and possible overshoot during forming. This indicates that R_{on} retention profile is highly dependent on the programming current as seen in the different experimental data and consistent with the Monte Carlo simulations of Yu et al [5]. One may be tempted to improve R_{on} thermal stability of RRAM by enforcing higher programming current. However, this occurs at the cost of high power operation and degraded R_{off} stability (Chapter II). Hence, using higher programming current for improved R_{on} retention profile may not be an efficient approach.

In the following sections, we will attempt to provide a microscopic understanding to the R_{on} retention failure towards R_{off} with low compliance current used.

IV.1.6 Ab initio calculations

All simulations were based on density functional theory (DFT) [6] using SIESTA code [7], with the GGA-PBE functional to describe the exchange-correlation term, and Troullier-Martins pseudopotentials were used for each atomic species to account for the core electrons [8]. Polarized Double-Zeta (DZP) basis set with an energy shift of 50 meV and a Mesh cut-off of 300 Rydberg were used for the calculations. A 2x2x2 monoclinic HfO_2 ($mHfO_2$) supercell with 96 atoms was set up for V_o formation energy and diffusion barriers calculations. For HfAlO supercell optimization, all the atomic coordinates and cell geometry were relaxed until the maximum residual forces were less than 0.02 eV/A. The activation energies (E_a) for V_o diffusion were calculated using the Climbing Image Nudged Elastic Band (CI-NEB) technique [9] as implemented in the Atomistic Simulation Environment (ASE) [10]. For the NEB calculations, at least 5 intermediate images were used and a maximum force of 0.05 eV/A was used as the convergence criteria.

IV.1.7 HfAlO model construction

In order to study the kinetics of V_o in HfAlO and relate the experimental data to the ab initio calculations results, an HfAlO model for the calculations had to be constructed. We proceeded with the model construction by inspiring from the HfAlO film deposition during the ALD process. In each 10 cycles of ALD, 9 cycles were devoted to HfO_2 deposition followed by 1 cycle of Al_2O_3 giving a 9:1 ratio. Hence, we used the following chemical equation to calculate the atomic proportions of Al, Hf and O in the HfAlO model:

$$(1-x)HfO_2 + xAl_2O_3 \rightarrow Hf_{1-x}Al_{2x}O_{2+x} \quad \text{(IV. 4)}$$

where x being 0.1 corresponds to the proportion of Al_2O_3 deposition during the ALD cycle. With the atomic proportions calculated from the above reaction, we took a 96 $mHfO_2$ supercell, replaced a number of Hf atoms of a layer by Al respecting the $Hf_{1-x}Al_{2x}O_{2+x}$ stoichiometry and allowed the system to fully relax (minimize forces and stresses). We tried different distributions of Al atoms inside the supercell and the low energy configuration was the one where an AlO_x layer is formed instead of distributed Al atoms inside the matrix. FigIV.12 shows the supercell used for HfO_2 and the constructed model for HfAlO. With constructed HfAlO model, the atomic proportions of Al, Hf and O in the supercell were in good agreement with the RBS data shown in TableIV.1.

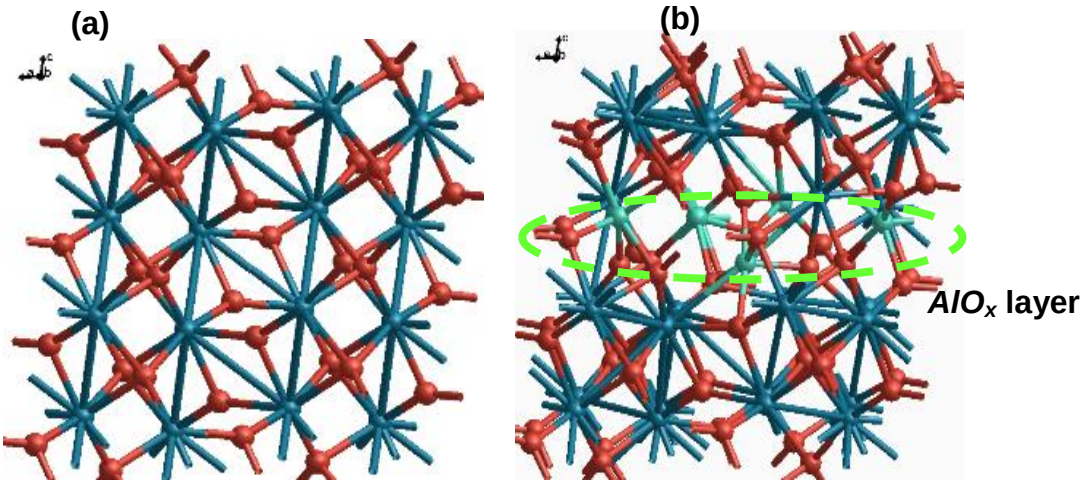

FigIV.12. HfO_2 monoclinic structure used for ab-initio calculations. Blue spheres for *Hf* atoms and Red for *O* (b) HfAlO structure used and constructed based on RBS data of TableIV.1 for the different atomic proportions. Blue spheres for *Hf*, Red for *O* and Green for *Al*.

IV.1.8 Diffusing species in HfO_2 or HfAlO during R_{on} retention

The retention profile of R_{on} towards R_{off} in TiN/oxide/Ti RRAM could be related to two different processes as shown FigIV.13: (a) the vertical diffusion of interfacial oxygen (O_i) from the Ti/oxide interface to the oxygen vacancy (V_o) rich conductive filament (CF) thereby recombining with it or (b) the lateral diffusion of V_o at the CF constriction (tip). We note that the exact location of the tip or constriction of the CF is not known but we suspect that it would be closer to the bottom electrode rather than the reactive top electrode (see Chapter V: section V.6). In process (a), O ions would either need to diffuse from the interfacial TiO_y layer to the CF and recombine with the entire interface contact area or diffuse through the CF to recombine with it at its constriction. In process (b) V_o would need to diffuse away from the CF.

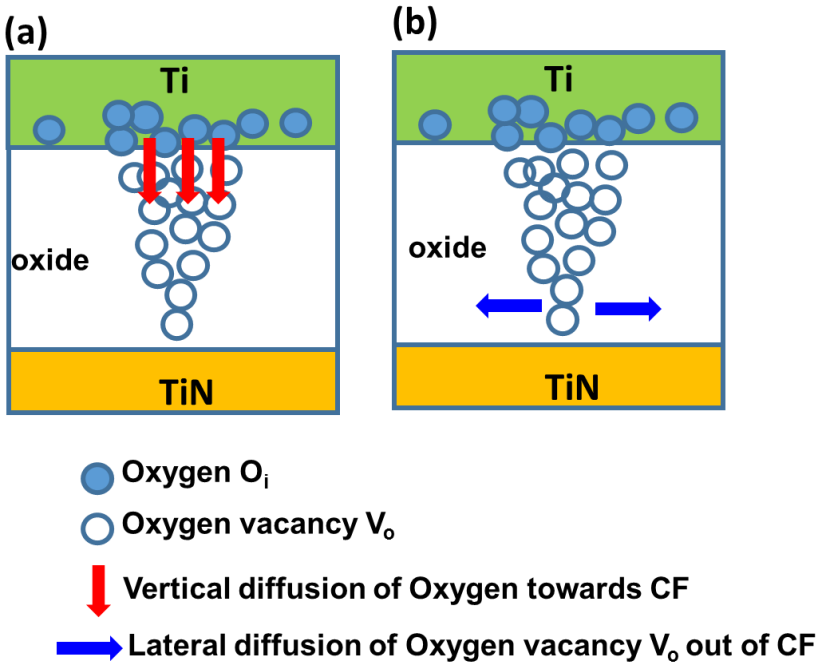

FigIV.13. Possible retention failure mechanism in HfO_2 or HfAlO RRAM (a) O stored at the interfacial Ti/oxide layer diffuses back into the oxide and recombine with V_o (b) R_{on} failure to R_{off} due to lateral diffusion of V_o.

Hence, knowledge of the diffusion of O inside hafnia suboxides may help understand if process (a) is predominant. Therefore, we have perfomed some O diffusion calculations in hafnia suboxides and the results are shown in FigIV.14. Our calculations are not exhaustive and depending on the diffusion paths, the calculated barriers may be lower or higher. However, the general trend that we see from these results is that when HfO_x becomes more metallic (O deficient), the O diffusion barrier inside it becomes higher. For process (a) to be predominant, the entire CF contact area

with the interface would need to be recombined by O involving more recombination events. We, therefore, made the assumption that R_{on} retention failure would be mainly dominated by the lateral diffusion of V_o out of the CF region following process (b). Nevertheless, O diffusion barriers in HfO_x (> 2.4 eV for $0 \leq x \leq 1$) that we have calculated in this work are not sufficient/conclusive to completely exclude process (a).

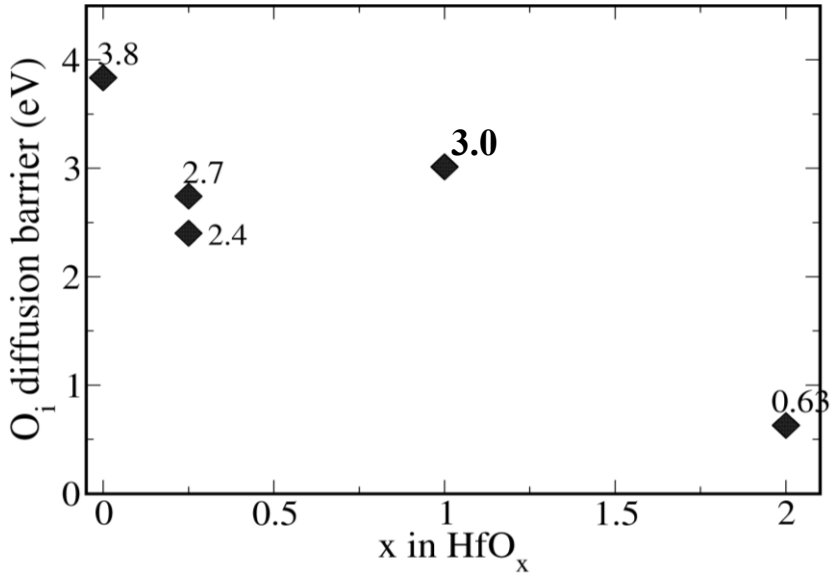

FigIV.14. O_i diffusion barriers in HfO_x.

Having considered V_o as the dominant diffusing species in R_{on} retention, we needed to make an educated assumption about the V_o charge state during the diffusion process. In order to answer this question we studied the stability of neutral and positively charged V_o in HfO_2 when no electric field is applied to the sample. This stability of $\boldsymbol{V_o^{+/-q}}$, *+/-q* being the charge state, was looked at through their formation energy using the following:

$$\Delta \boldsymbol{H^{Vo}} = \boldsymbol{E_{tot}^{Vo}} - \boldsymbol{E_{tot}^{HfO_2}} + \boldsymbol{\mu_o} \pm \boldsymbol{q}(\boldsymbol{E_{VB}} + \boldsymbol{E_F}) \quad \textbf{(IV.5)}$$

Where $E_{tot}^{HfO_2}$ is the total energy of defect free HfO_2 supercell, E_{VB} the top of the valence band (*VB*), E_F the Fermi level measured from the top of the *VB*. E_{tot}^{Vo} is the energy of the supercell with V_o and μ_o oxygen (*O*) chemical potential. For O chemical potential, we assumed an O_2 rich atmosphere (1.36 eV per O_2 correction was used [6]). One could also use the O chemical potential in Ti by assuming the removed O atom was inserted in Ti. What would change is the value of the formation energy which would be lowered because of the reactivity of Ti with O but the trend of V_o stability would not be affected.

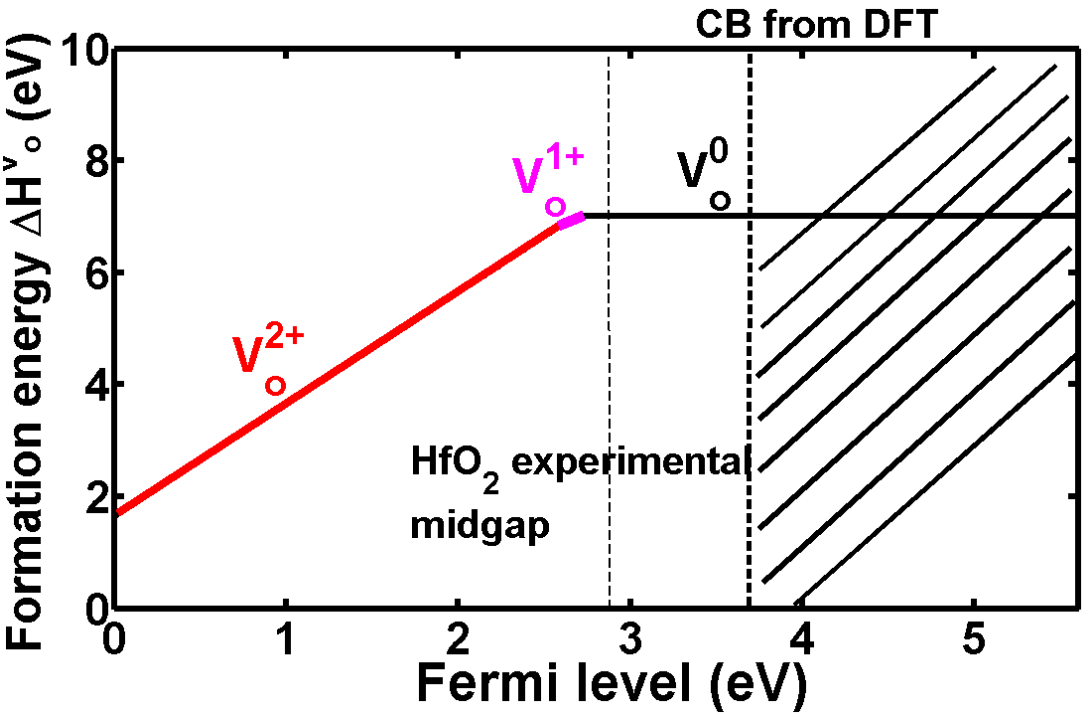

FigIV.15. V_o formation energy in HfO_2 with respect to Fermi level. Neutral V_o becomes thermodynamically favourable from close to experimental mid-gap condition. The dashed region would correspond to the gap opening region if a band gap correction scheme was used. It is possible that the gap also opens slightly from the valence band with band gap correction [11].

FigIV.15 shows the most favorable V_o states with respect to the Fermi level (electron injection level). The figure shows that neutral V_o becomes thermodynamically more favorable from close to mid-gap. Due to the underestimation of band gaps in DFT calculations [12], the dashed region would correspond to the gap opening region if a band gap correction scheme was used. It is possible that the gap also opens slightly from the valence band with band gap correction as calculated by more accurate GW formalism [11]. FigIV.16a, b respectively show V_o energy level and the band diagram of HfO_2 when no voltage is applied which corresponds to the zero bias case of data retention test. We observe that the BE level is above the V_o level which corresponds to the favorable zone of neutral V_o formation. The aggregation of charged vacancies (V_o^{2+}) in the filament region is very unlikely due to repulsive coulombic forces and the electron injection from the cathode into V_o essentially neutralize them [13]. Therefore, FigIV.15 and FigIV.16 provide strong indications that *neutral* V_o *are essentially the dominant diffusing species during* R_{on} *retention from thermodynamic perspective*.

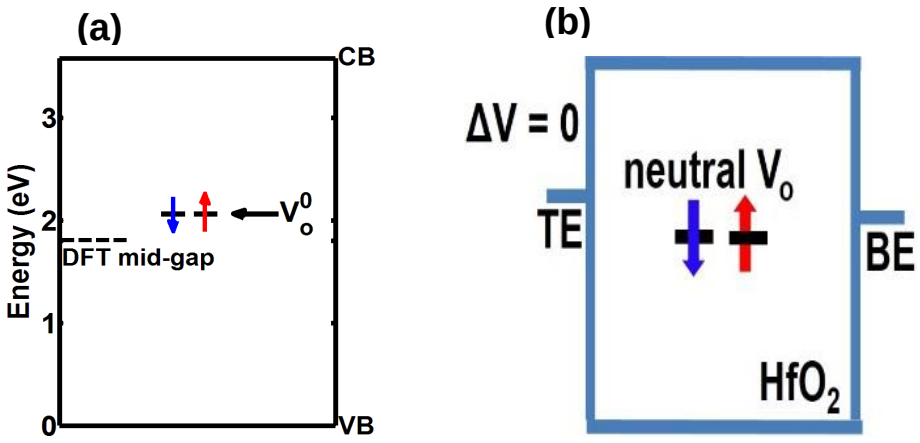

FigIV.16. (a) Neutral V_o level in HfO_2. This energy level is above midgap from DFT calculations. (b) Band diagram showing neutral V_o level in HfO_2 at mid-gap. This corresponds to the case when no bias is applied which is the scenario of data retention. TiN (BE) and Ti (TE).

IV.1.9 V_o diffusion process

Under thermodynamic equilibrium atoms vibrate around their equilibrium positions with an average thermal energy ½ k_bT in each degree of freedom [14] (FigIV.17a). However, through thermal excitations or other processes, atoms may gain energy and jump over a barrier when the gained energy is higher than activation energy Ea (FigIV.17b). E_a corresponds to the height of the barrier when a diffusing species migrates from an initial state (*IS*) to a final state (*FS*) through a point of high potential energy called Transition State (*TS*).

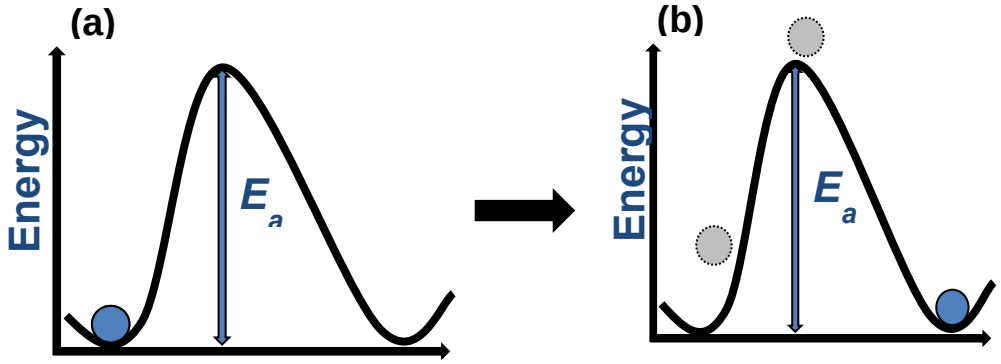

FigIV.17. (a) Atom vibrating around its equilibrium position (b) atom having gained enough energy, jump over a barrier to another position.

E_a is an important quantity in harmonic Transition State Theory (H*TST*) which states that the reaction rate (τ) from *IS* to *FS* is given by $\tau = \tau_o exp(-E_a/k_bT)$ following the

Arrhenius type of equation [14]. Therefore, since the fail time from the retention test shown in FigIV.11 also follows Arrhenius expression, V_o diffusion barriers (FigIV.18) that are calculated using the NEB technique can in principle, be related to E_a extracted from R_{on} retention experiment.

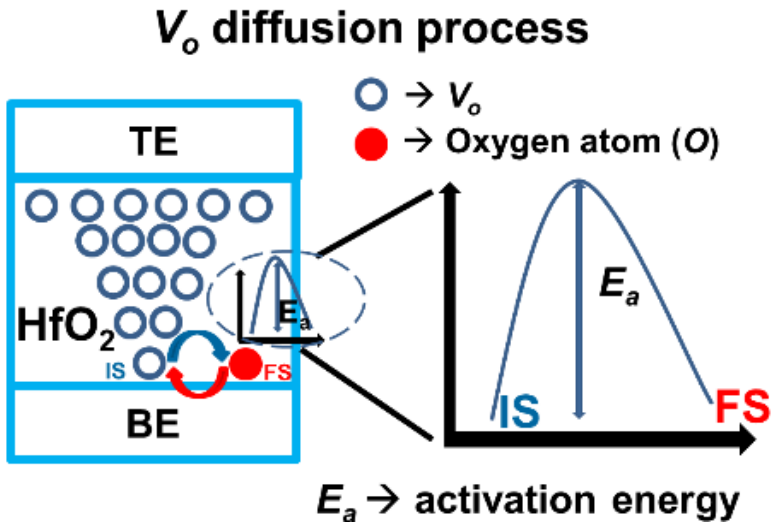

FigIV.18. Model showing V_o diffusion process during R_{on} retention where the *CF* ruptures at the tip (constriction). The diffusion process is associated with an E_a that is calculated with the NEB technique.

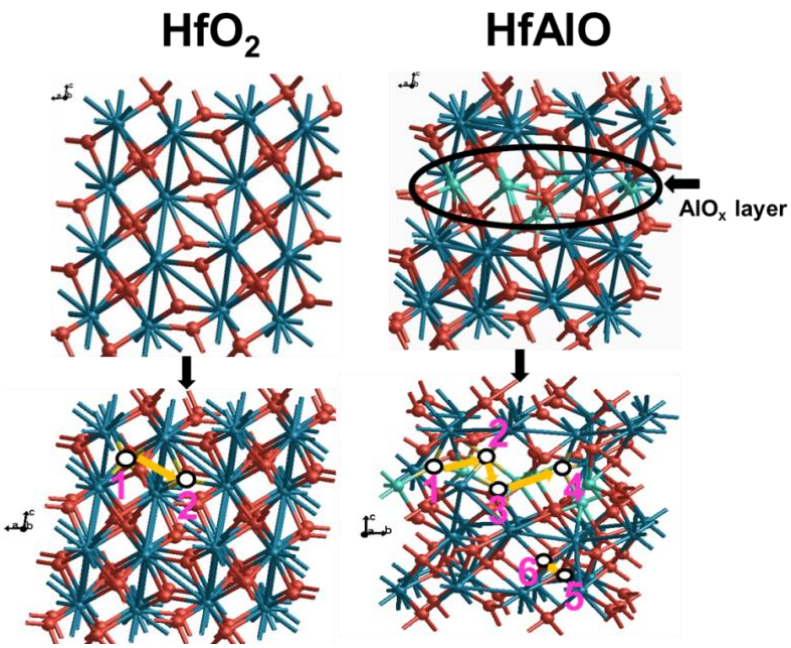

FigIV.19. (left) $mHfO_2$ structure with the atomic positions numbered 1 and 2 considered for the initial and final states of V_o diffusion inside HfO_2. (right) HfAlO model and atomic positions numbered 1, 2, 3, 4, 5 and 6 considered for V_o diffusion in HfAlO.

Having established the fact that R_{on} retention test is mainly dominated by neutral V_o diffusion process in the bulk of the oxide and that the activation energies from the

experiment and theory could be related, we calculated the diffusion barriers of V_o by considering different paths in HfAlO and HfO_2. FigIV.19 shows the diffusion paths considered in HfO_2 and HfAlO and are numbered from 1 to 4. FigIV.20 shows the diffusion profile of V_o in HfO_2 and an E_a of 2.16 eV (TableIV.2) is calculated consistent with the 2.19 eV obtained by Capron et al. [15]. Capron et al. further state that V_o diffusion in HfO_2 is isotropic with an average activation energy of 2.4 eV. The atomistic models of FigIV.20 show V_o migration corresponding to different states during the diffusion process.

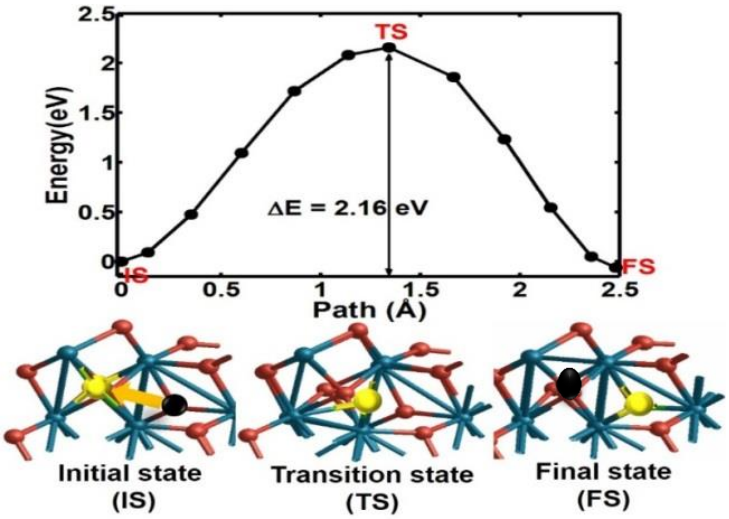

FigIV.20. V_o diffusion in HfO_2 corresponding to atomic positions 1 to 2 in FigIV.19. An E_a of 2.16 eV is calculated in agreement with [15]. [15] gives an average E_a of 2.4 eV with different long range V_o diffusion paths investigated. Black sphere represents the initial V_o position while yellow sphere represents the moving O.

Defect	Atomic positions	E_a (eV)	Distance (Å)
V_o^0	1 to 2	2.16	2.48
	2 to 1	2.22	2.48
*4*V_o *as predefects* + V_o^0	1 to 2	1.76	2.48

TableIV.2. Calculated V_o difusion barriers and distance between the considered atomic positions in HfO_2.

In order to compare this calculated E_a (2.16 eV) to that of V_o diffusion in HfAlO, different atomic positions were considered and are summarized in TableIV.3. FigIV.21 shows typical V_o diffusion profile in HfAlO and corresponds to the migration from 1 to 2. Depending on the initial states, the calculated E_a varies from 2.08 eV (3 to 4 in TableIV.3) to 2.69 eV (6 to 5 in TableIV.3). Since diffusion is a statistical process with different paths involved, the activation energy is determined by the energy of the

highest transition state during long range diffusion. By comparing V_o diffusion barrier in HfO_2 to those obtained in HfAlO, one can see that *Al* incorporation increased V_o diffusion barrier which is consistent with the high E_a for HfAlO extracted from the experiment.

V_o defect	Atomic positions	E_a (eV)	Distance (Å)
V_o^0	1 to 2	2.53	2.85
	2 to 1	2.27	2.85
	2 to 3	2.23	2.80
	3 to 2	2.45	2.80
	3 to 4	2.08	2.86
	4 to 3	2.42	2.86
	5 to 6	2.33	2.56
	6 to 5	2.69	2.56

TableIV.3. Calculated V_o difusion barriers and distance between the considered atomic positions in HfAlO.

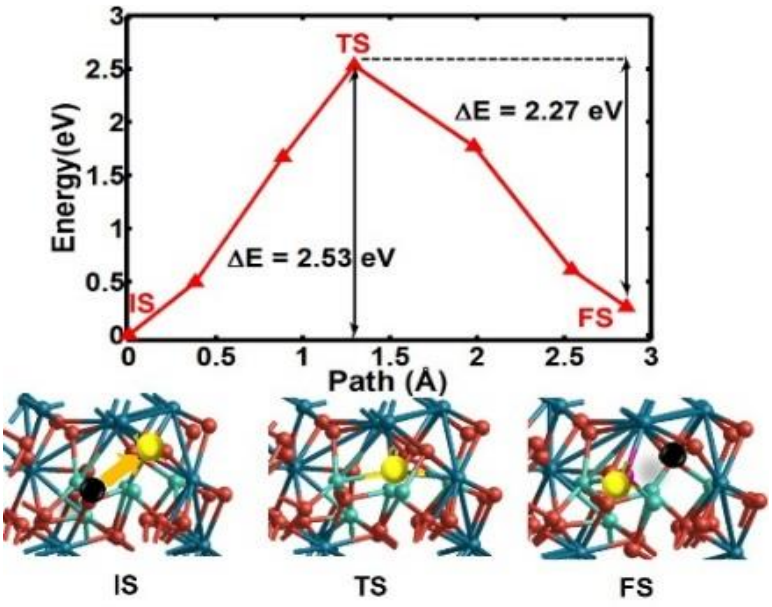

FigIV.21. V_o diffusion path corresponding to atomic positions 1 to 2 in HfAlO. E_a of 2.27 eV and 2.53 eV are calculated which are still higher than in HfO_2. Black sphere represents the initial V_o position while yellow sphere represents the moving O.

However, we observe that the experimental activation energies are lower compared with ab initio based calculated E_a. Since, the thin films used for the electrical

characterization are likely to be defective with probably some amorphous spots in their matrices, calculations performed with defective cells may be desired. We investigated this effect by inducing $4V_o$ in HfO_2 as pre-defects and re-calculated the diffusion of V_o in HfO_2 (1 to 2 from FigIV.19 left) as shown in FigIV.22. We notice that the introduction of $4V_o$ as pre-defects resulted in E_a lowering by ~0.4 eV which becomes close to the experimental data. Indeed, HfO_2 becomes slightly defective when Ti is deposited on top of it due to the reactivity of Ti with O_i as we have thoroughly investigated it in Chapter III and the fact that CF creation during the forming operation also affects HfO_2 surrounding it. Another legitimate point would be considering V_o diffusion profile in an amorphous system. Our constructed HfAlO model is already slightly amorphous because of the introduction of Al and the structural relaxation resulted in a symmetry that deviated from that of pure monoclinic HfO_2. As for HfO_2, the considered model is crystalline. However, V_o migration in amorphous HfO_2 was investigated by Tang [16] and the obtained barriers for both neutral and charged oxygen vacancies are very similar to the calculated values in this work. Hence, our theoretical calculations remain valid despite the more crystalline structure of our models.

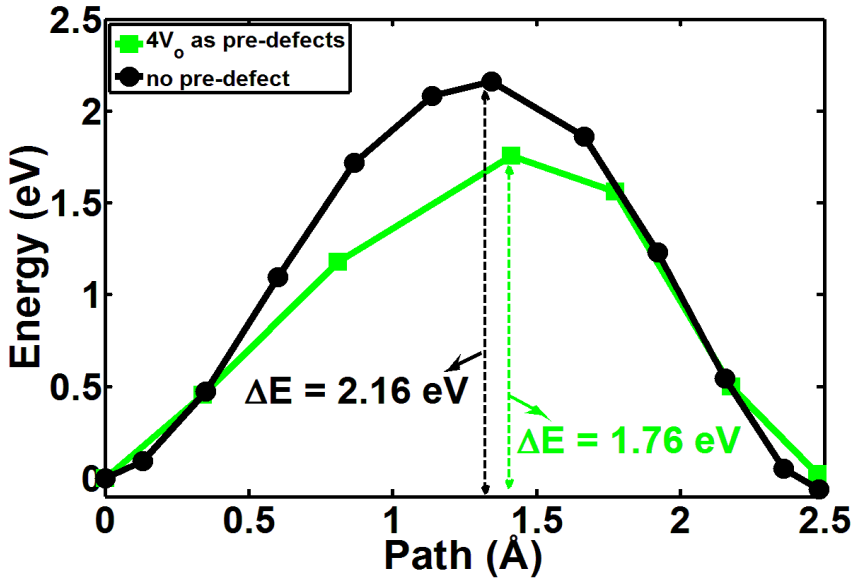

FigIV.22. Decrease of E_a by ~0.4 eV with $4V_o$ as pre-defects in HfO_2 compared to the case with no-pre-defect (Fig17). This may explain why the experimental E_a are lower than the calculated ones with ab-initio where the structures are crystalline while the devices are polycrystalline/amorphous with defects.

IV.2 Hafnium titanium oxide alloy ($Hf_{1-x}Ti_xO_2$)

In addition to alloying HfO_2 with Al, few studies on alloying HfO_2 with Ti have been reported [3] [17] with the aim of understanding and correlating the switching

performance and retention behavior of the devices with the properties of materials. We saw in Chapter II that the problem of R_{off} variability in RRAM seems to be intrinsically related to the properties of HfO_2 based RRAM despite the scaling of the devices and varying the programming conditions [18]. Thus, engineering the HfO_2 layer through alloying or doping with other materials seems to be a necessity for further improvement. Since, we do not have fabricated HfTiO devices, our study is limited to only theoretical calculations and we use the literature experimental data when they are available to sustain or infirm our calculations. In the previous section on HfAlO, we looked at the V_o diffusion barrier calculations and related them to microscopic nature of R_{on} retention. Similarly in this section our theoretical calculations are focused on V_o diffusion in HfTiO and this will provide more comprehensive view on R_{on} retention using other materials.

IV.2.1 HfTiO model construction

We proceeded with the HfTiO model construction as we did with HfAlO. We assumed an ALD process in which every 4 cycles of HfO_2 is followed by 1 cycle of TiO_2 using this chemical reaction:

$$(1-x)HfO_2 + xTiO_2 \rightarrow Hf_{1-x}Ti_xO_2 \quad \text{(IV. 6)}$$

where *x* being 0.2 corresponds to the proportion of TiO_2 deposition during this assumed ALD deposition process. As in the case of HfAlO and with the atomic proportions calculated from the above reaction, we took a 96 $mHfO_2$ supercell, replaced a number of Hf atoms of a layer by Ti respecting the $Hf_{1-x}Ti_xO_2$ stoichiometry and allowed the system to fully relax (minimize forces and stresses). FigIV.23 shows the constructed HfTiO model along with the $mHfO_2$ supercell. In this model, 6 Ti atoms are used in the TiO layer which results in an exact proportion of 18.75% of Ti.

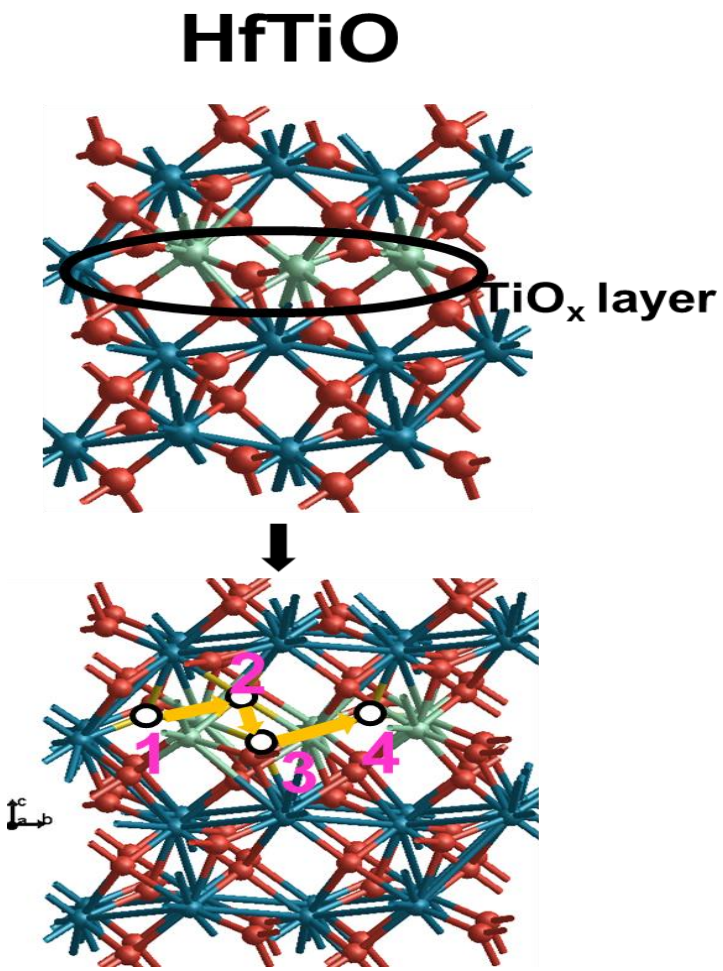

FigIV.23. Constructed HfTiO model along with atomic position 1 to 4 considered for V_o diffusion.

TableIV.4 summarizes the V_o diffusion barriers calculated in the constructed HfTiO model. Three cases of V_o diffusion in the TiO_x layer of HfTiO were considered and all have much lower diffusion barriers compared with the 2.16 eV calculated in HfO_2.

V_o defect	Atom positions	E_a (eV)	Distance (Å)
V_o^0	1 to 2	1.37	2.89
	2 to 1	1.38	2.89
	2 to 3	1.07	2.72
	3 to 2	1.45	2.72
	3 to 4	0.68	2.56
	4 to 3	0.81	2.56

TableIV.4. Calculated V_o difusion barriers and distance between the considered atomic positions in HfTiO.

Based on our understanding of R_{on} retention that we developed throughout the chapter, the low diffusion of V_o in HfTiO indicates that HfTiO should present degraded R_{on} retention profile compared with HfO_2. Indeed, Chen et al investigated the retention performance of HfO_2 by alloying it with Al, Ti and Si in ALD cycles and targeted 18% of each alloying material in HfO_2 [3]. Interestingly, their targeted 18% of the alloying species compare very well with the 18.75% that we used for Ti and 18.2 % for Al in HfAlO (9:1) for our different constructed models. They found that R_{on} retention performance was improved with Al and Si doping into HfO_2 while Ti incorporation degraded the retention profile of the devices. These results are in excellent agreement with both our available experimental results on HfAlO and the predicted calculations on HfTiO. Therefore, our understanding about R_{on} retention is so far validated by both experiment and theory and it seems that the microscopic nature of R_{on} retention is intrinsically related to the lateral diffusion process of V_o out of the CF.

IV.2.2 Insight on V_o diffusion barriers

FigIV.24 shows the formation energy of some of the V_o states that were considered during the diffusion barrier calculations in HfO_2 and HfAlO. Each ellipse corresponds to the formation energies of the initial and final states for the considered V_o. We observe that V_o formation energy is only slightly lowered by Al incorporation when the removed O atom shared a bond with Al in HfAlO. This difference is not very significant given the range of variation of the calculated formation energies. Therefore, with the similar V_o formation energy in HfO_2 and HfAlO, it is difficult to explain the high V_o diffusion barrier in HfAlO. In order to have more insight on this high V_o diffusion barrier in HfAlO, we calculated Hf-O bond lengths in both HfO_2 and HfAlO supercells as well as that of Al-O as shown in FigIV.25. Al incorporation induced the shrinkage of the different bonds (1.93 Å for Al-O; 2.16 Å for Hf-O) with some relative dispersion (slightly amorphised structure) while Hf-O bonds in HfO_2 are very peaked around 2.17 Å (FigIV.25) and TableIV.5. This bond shrinkage in HfAlO as well as its higher atomic concentration (TableIV.1) reduces the atomic mobility due to probable higher coulomb interaction which results in an increase of V_o diffusion barrier.

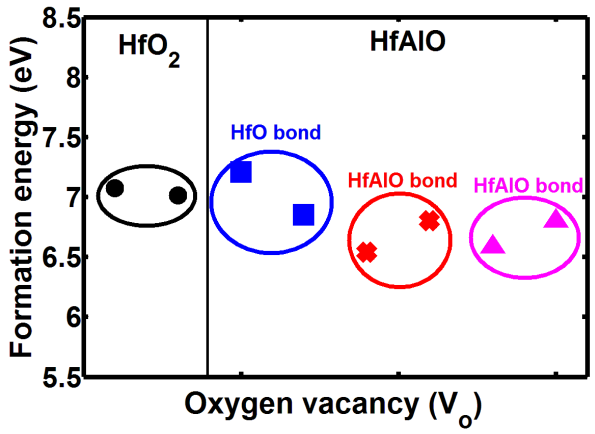

FigIV.24. Formation energy (ΔHV_o) of V_o in HfO_2 and HfAlO from the models shown in FigIV.12. ΔHV_o is slightly lower for HfAlO. The 4 different ellipses with different colours correspond *to* V_o diffusion paths that are investigated.

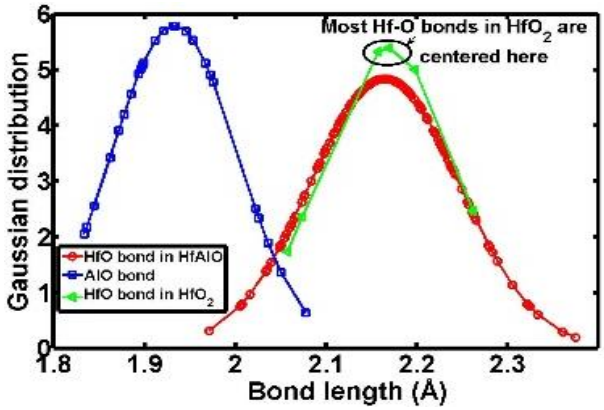

FigIV.25. Comparing bond lengths in HfO_2 and HfAlO. Al-O has the shortest bond length. *HfO* bond length in HfAlO also reduced with *Al* incorporation. This bond shrinkage associated with higher atomic concentration may be the main effects related to a higher V_o diffusion barrier in HfAlO.

bond	Mean length (Å)
AlO	1.93
HfO in HfAlO	2.16
HfO in HfO_2	2.17

TableIV.5. Summary of bond lengths in HfO_2 and HfAlO.

Similarly, FigIV.26 shows the formation energy of V_o in both HfTiO and HfO_2. The considered O atoms for V_o formation energy shared bonds with Ti in TiO_x layer (FigIV.23). This formation energy is lowered by more than 1eV for HfTiO compared with HfO_2 and hence anion-cations bonds became much weaker with Ti incorporation. FigIV.27 compares the bond lengths of Hf-O and Ti-O in HfTiO. One can see that the

mean length of Hf-O bond (2.16 Å) remained the same as in HfAlO while that of Ti-O was calculated to be 2.06 Å. In rutile TiO_2 crystal structure, the mean length of Ti-O bond varies between (1.95 Å to 1.98 Å) [19] which is lower than the calculated Ti-O bond length when Ti is introduced in HfO_2. Nevertheless, Ti-O bond length still remains shorter than Hf-O bond. As such, the shorter Ti-O bond in HfTiO cannot explain the low V_o diffusion barrier in HfTiO. Therefore, we attribute the low V_o diffusion barrier in HfTiO to the weakened anion-cation bonds because of their lower V_o formation energies compared to HfO_2.

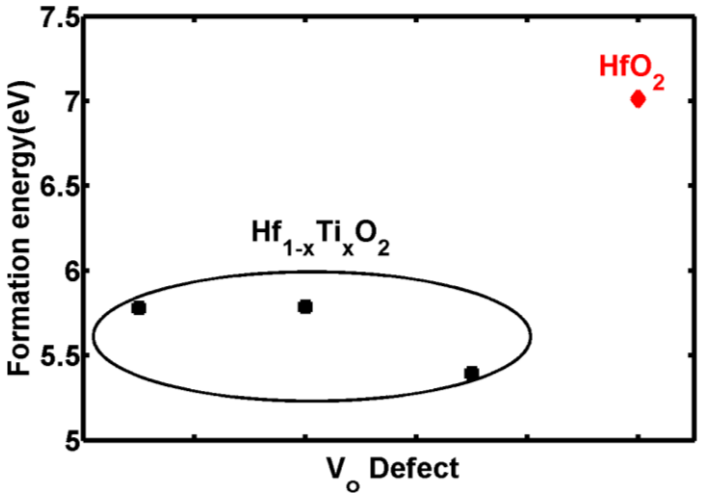

FigIV.26. Formation energy of V_o in HfTiO and HfO_2.

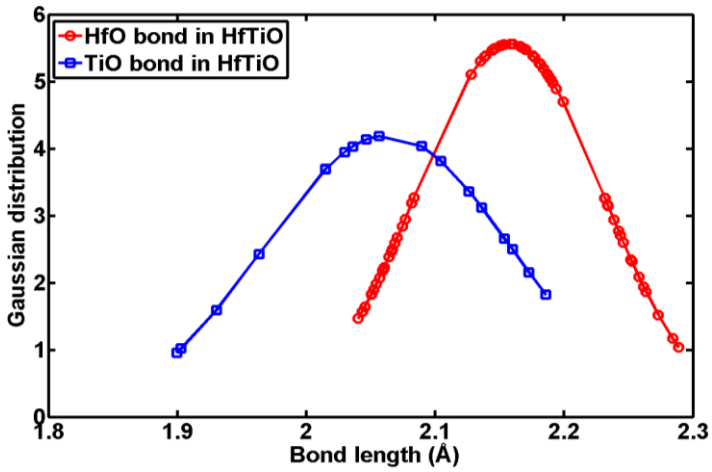

FigIV.27. Comparing TiO and HfO bond lengths in *HfTiO*.

From this study, one can see that it is not easy to draw a simple rule allowing for the alloying/doping material selection for thermal stability prediction in HfO_2 based RRAM. For more rigorous prediction about devices' thermal stability, one should perform V_o diffusion barrier calculations. Although not general or universal, our study

brings about some hints about the alloying/doping material selection process in order to improve R_{on} thermal stability in RRAM. If the alloying material (M) tends to form much shorter bond lengths with O in HfO_2 compared to Hf-O while inducing similar V_o formation energy compared to HfO_2, it may be likely that the devices' low resistance state thermal stability will be improved as shown with HfAlO in this work and HfSiO as reported by Chen et al. [3]. The improvement of R_{on} thermal stability with Si incorporation could be imagined due to its much shorter bond length that varies between 1.604 Å and 1.627 Å as reported by Dove et al. [20]. On the other hand, M-O bonds that tend to get stretched when incorporated in HfO_2 (as in the case of Ti-O bond in HfO_2) or closer to Hf-O bond length while causing much lower V_o formation energy compared to HfO_2 (weak bonds), it may be likely that R_{on} retention will be degraded. Similar study would need to be performed with other alloying materials in HfO_2 for better projection/prediction. We hope that our findings will help facilitate the material selection process in the optimization of HfO_2 based RRAM devices.

IV.3 Conclusions

The impact of alloying HfO_2 with Al has been studied from both experimental and theoretical perspectives. The study points out the impact of the atomic composition and structure on the resistive switching layer's thermal stability. As far as the switching characteristics are concerned, Al incorporation into HfO_2 did not have significant impact on the switching voltages and resistances except for the forming voltage which was lower for HfO_2 based devices compared with HfAlO. The lower forming voltage for HfO_2 was attributed to both its lower band gap as well as its higher dielectric constant enhancing Hf-O bond breakage process.

Low resistance state (R_{on}) retention behaviors of both HfO_2 and HfAlO were comprehensively investigated. R_{on} retention failure has shown to be highly temperature activated and Al incorporation into HfO_2 improved the thermal stability of devices. The device failure during the retention was attributed to the lateral diffusion of V_o out of the conductive filament. Ab initio based V_o diffusion barriers in HfO_2 and HfAlO were calculated in order to understand the microscopic picture of R_{on} retention. The calculations showed high barriers for HfAlO which were in agreement with the experimental results. The high V_o diffusion barrier for HfAlO was explained by the shorter Al-O bond lengths associated with its higher atomic concentration which

hindered V_o diffusion. Our study shows that alloying HfO_2 with a proper dopant (Al in this study) is an efficient methodology to improve devices' thermal stability.

A further step towards understanding the impact of doping on HfO_2 based RRAM thermal stability was carried out by alloying HfO_2 with Ti within the framework of theoretical calculations. Our calculations showed that V_o barriers diffusion in HfTiO were lower compared with HfO_2 which suggested their poor R_{on} retention behaviours. Our theoretical predictions were validated by experimental data which provided more insight on the microscopic understanding of the low resistance state retention.

References

[1] A. Fantini, L. Goux, S. Clima, R. Degraeve, A. Redolfi, C. Adelmann et al. , "Engineering of $Hf_{1-x}Al_xO_y$ amorphous dielectrics for high-performance RRAM applications ," *IEEE IMW*, pp. 1 - 4 , 2014.

[2] J. McPherson, J.-Y. Lim, A. Shanware and H. Mogul, "Thermochemical description of dielectric breakdown in high dielectric constant materials," *Appl. Phys. Lett.*, vol. 82, 2121, 2003.

[3] Y.Y. Chen, R. Roelof, A. Redolf, R. Degraeve, D. Crotti, A. Fantini et al., "Tailoring switching and endurance / retention reliability characteristics of HfO_2/Hf RRAM with Ti, Al, Si dopants," *VLSI Tech.*, pp. 1 - 2, 2014.

[4] Y.Y. Chen, M. Komura, R. Degraeve, B. Govoreanu, L. Goux, A. Fantini et al., "Improvement of data retention in HfO_2/Hf 1T1R RRAM cell under low operating current," *IEEE IEDM*, pp. 10.1.1 - 10.1.4, 2013.

[5] S. Yu, Y.Y. Chen, X. Guan, H.-S.P. Wong and J. A. Kittl, "A Monte Carlo study of the low resistance state retention of HfO_x based resistive switching memory," *Appl. Phys. Lett.*, vol. 100, no. 043507, 2012.

[6] P. Hohenberg and W. Kohn, "Inhomogeneous electron gas" Phys. Rev., vol. 136, p. B864, 1964;W. Kohn and L. J. Sham, "Self-consistent equations including exchange and correlation effects", Phys. Rev., vol. 140, p. A1133, 1965,.

[7] J. Soler et al., "The SIESTA method for ab-initio order-N materials simulation," *J. Phys.: Condens. Matter*, vol. 14, pp. 2745-2779, 2002.

[8] N. Troullier and J. L. Martins, "Efficient pseudopotentials for plane-wave calculations," *Phys. Rev. B.*, vol. 43, pp. 1993-2006 , 1991.

[9] G. Henkelman, B. P. Uberuaga, and H. Jónsson, "A climbing image nudged elastic band method for finding saddle points and minimum energy paths," *J. Chem. Phys.*, vol. 113, p. 9901, 2001.

[10] S. R. Bahn and K. W. Jacobsen, "An Object-Oriented Scripting Interface to a Legacy Electronic Structure Code," *Comput. Sci. Eng.*, vol. 4, pp. 56-66, 2002.

[11] M. Jain, J.R. Chelikowsky and S. Louie, "Quasiparticle Excitations and Charge Transition Levels of Oxygen Vacancies in Hafnia," *Phys. Rev. Lett.* , vol. 107, 216803, 2011.

[12] J. X. Zheng et al., "First-principles study of native point defects in hafnia and zirconia," *Phys. Rev. B.*, vol. 75, pp. 104112-1–104112-7 , 2007.

[13] K.-H. Xue, B. Traoré, P. Blaise, et al., "A combined ab initio and experimental study

on the nature of conductive filaments in Pt/HfO_2/Pt resistive random access memory," *IEEE Trans. Electron Dev.*, vol. 61, p. 1394, 2014.

[14] D. Sholl and J. A. Steckel, *Density Functional Theory: A Practical Introduction*, John Wiley & Sons, Ed., 2009.

[15] N. Capron et al., "Migration of oxygen vacancy in HfO_2 and across the HfO_2/SiO_2 interface: A first-principles investigation," *Appl. Phys. Lett.*, vol. 91, no. 192905, 2007.

[16] C. Tang, "First principles studies of point defects in HfO_2 and Si-HfO_2 interfaces," University of Connecticut, PhD thesis 2009.

[17] B. Chakrabarti, R.V. Galatage and E.M. Vogel, "Multilevel Switching in Forming-Free Resistive Memory Devices With Atomic Layer Deposited $HfTiO_x$ Nanolaminate," *IEEE Elec. Dev. Lett.*, vol. 34, no. 7, 2013.

[18] D. Garbin, O. Bichler, E. Vianello, Q. Rafhay, C. Gamrat, L. Perniola et al., "Variability-tolerant Convolutional Neural Network for Pattern Recognition Applications based on OxRAM Synapses," *IEEE IEDM*, pp. 28.4.1-28.4.4, 2014.

[19] J. Muscat, V. Swamy and N.M. Harrison, "First-principles calculations of the phase stability of TiO_2," *Phys. Rev. B*, vol. 65, 224112, 2002.

[20] M. T. Dove, D. A. Keen, A. C. Hannon and I. P. Swainson, "Direct measurement of the Si–O bond length and orientational disorder in the high-temperature phase of cristobalite," *Phys. Chem. Minerals*, vol. 24, pp. 311–317, 1997.

Chapter V

Filament formation, composition and stability

Throughout the different chapters, we have seen several interesting switching features of HfO_2 based RRAM in terms of low voltage operation, thermal stability and high cycling endurance. Oxide material engineering and the choice of electrode material allowed the fabrication of such performing RRAM devices. However, there remain some challenging points regarding the composition and nature of the conductive filament as well as a consistent microscopic understanding of the resistive switching. The missing detailed picture of the resistive switching is among others a blocking point for the adoption of the technology by the industrials. Therefore, in this chapter, we will attempt to provide our understanding about the possible composition and nature of the conductive filament as well as the microscopic picture behind its formation.

V.1 Introduction

HfO_2 is an insulator with a large band gap (~5.6 eV [1] or 5.7 eV [2]) and high dielectric constant of around (22-25) [1] [3]. Its film is generally deposited by the atomic layer deposition (ALD) technique which gives it a higher quality with low leakage current and better thickness conformity. It usually crystallizes in monoclinic structure under low pressure and temperature conditions [4] [5]. However, HfO_2 thin films are mostly amorphous with a transition towards crystallinity depending on the thickness and deposition temperature [6]. The high quality of HfO_2 as a good insulator in CMOS gate oxides contrasts its use as a switchable layer in RRAM applications. In RRAM, charge transport, involving larger currents (from microamperes µA to few milliamperes mA), occurs inside the oxide layer during the different switching operations. This transport can only be possible if HfO_2 layer has defects. Among the possible defects that are encountered in oxides are oxygen vacancies (V_o), oxygen interstitials (O_i), Frenkel-pairs (FP). In polycrystalline HfO_2 films, grain boundaries (GB) also contribute as defect spots. Understanding the role of these defects in pristine HfO_2 or their formation during the forming step is essential in RRAM operation. V_o, O_i and FP were already mentioned in some of the previous chapters. They are revisited in this chapter for more coherent and comprehensive view of hafnia based memory devices operations.

V.2 Calculations methods

The majority of the results of this chapter are based on first principles calculations performed within the density functional theory (DFT) formalism [7] as implemented in SIESTA [8]. We used the GGA-PBE functional to describe the exchange-correlation term, and Troullier-Martins pseudopotentials were used for each atomic species to account for the core electrons [9]. Polarized Double-Zeta (DZP) basis set with an energy shift of 50 meV and a Mesh cut-off of 300 or 350 Rydberg were used for the calculations. A 2x2x2 monoclinic HfO_2 supercell with 96 atoms was considered for all the calculations except for the grain boundary model in which the supercell contained 360 atoms. For the optimization of the supercells' geometry and atomic positions, the maximum residual force was 0.02eV/Å. Defects diffusion barriers were calculated using the climbing image nudged elastic band (CI-NEB) technique [10] as implemented in ASE package [11]. For the NEB calculations, at least 5 intermediate images were used and a maximum force of 0.05 eV/A was used as convergence criteria. Charge analysis was carried out within the Bader charge decomposition method [12].

Details about the calculations of the energetics of a specific system will be provided in the respective section.

PART I: Towards the conductive filament formation

V.3 Study of Defects from device fabrication process

In this section, we investigate potential defects that may be formed in HfO_2 during its ALD deposition process with hafnium tetrachloride (HfCl4) precursor as is the case in our fabricated RRAM devices studied in the previous chapters (Eq. V.1). We are not interested in H or Cl defects that should normally be taken away from HfO_2 in the form of Hydrochloride (HCl). Hence, in our study, we will only look at oxygen (O) related defects. During the ALD process, HfO_2 is deposited on top of the bottom electrode (BE) that can be TiN, Pt or any other conducting material that may serve as electrode. For more clarity, we will consider TiN or Pt as bottom electrodes.

$$\boldsymbol{HfCl_4 + 2H_2O \rightarrow HfO_2 + 4HCl} \quad \textbf{(V.1)}$$

V.3.1 HfO_2 deposition on BE electrode TiN or Pt

FigV.1 shows a schematic representation of HfO_2 being deposited on BE during RRAM device fabrication process. The figure allows the definition of a suitable thermodynamic ensemble for defects formation. When HfO_2 is deposited on BE, the Fermi level of the system is fixed by the metal BE. Moreover and by virtue of simplification, we assume the ALD deposition process to occur in an oxygen rich ambient. Under this assumption which is reasonable, the chemical potential of oxygen (μ_o) may be safely assumed to be that of O from molecular O_2 for O defects formation investigated in the next following sections.

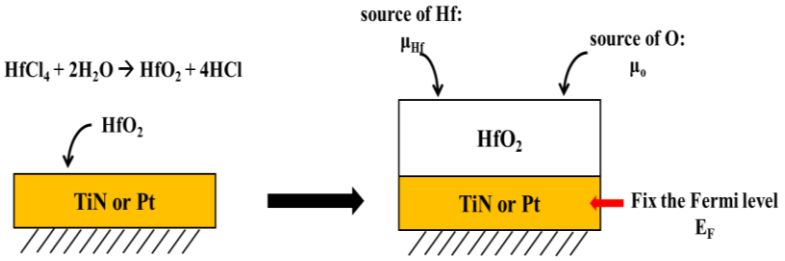

FigV.1. HfO_2 deposition on BE during the film fabrication process. At this stage, the Fermi level of the system is fixed by the BE.

V.3.1.1 Oxygen interstitials O_i

Oxygen interstitial defect can be created when an extra oxygen atom is added to the oxide structure and placed in a non-lattice position. Several non-lattice O_i sites are possible in HfO_2 and some of the non-equivalent positions with their optimized structures obtained by calculations are represented in FigV.2.

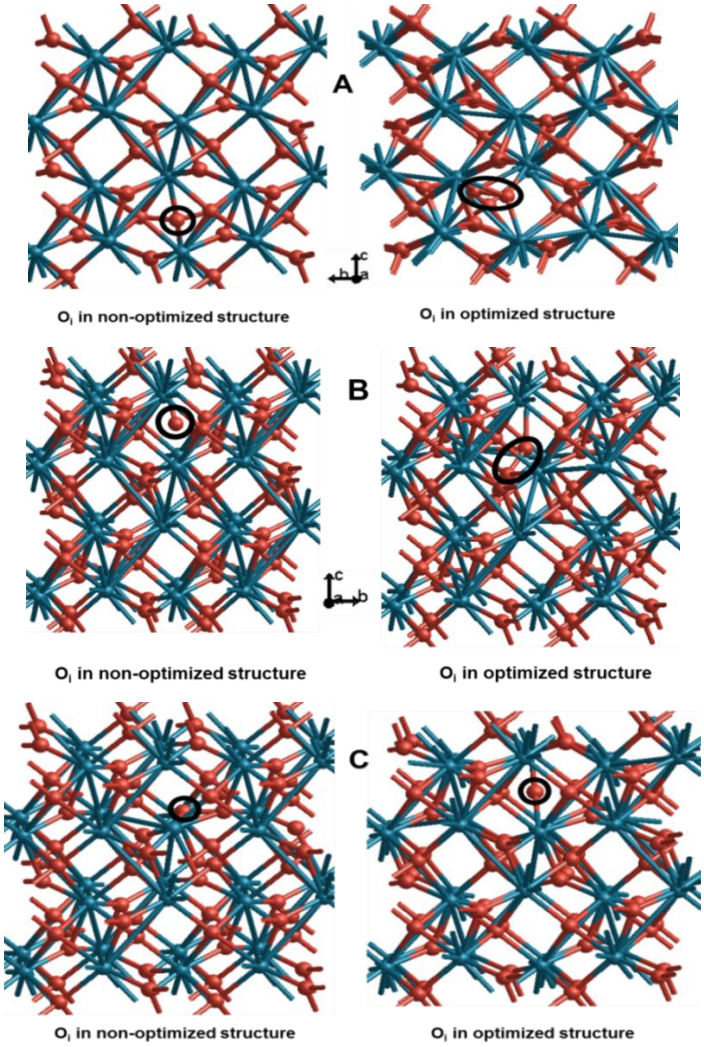

FigV.2. Atomistic structures of different O_i positions in monoclinic HfO_2 with their optimized structures.

FigV.3 shows the assumed thermodynamic ensemble for O_i formation in HfO_2 and their formation energies with the different structures (FigV.2) summarized in TableV.1 are calculated using the following:

$$\Delta H^{Oi,\pm q} = E_{tot}^{oi,\pm q} - E_{tot}^{HfO_2} - \mu_o \pm q(E_{VB} + E_F) \quad \text{(V.2)}$$

where $E_{tot}^{HfO_2}$ is the energy of the defect-free HfO_2 supercell, E_{VB} the top of the valence band (VB), E_F the Fermi level measured from the top of the VB, q the charge of the

system, $E_{tot}^{oi,\pm q}$ the energy of the supercell with O_i at charge $\pm q$, and μ_o oxygen (O) chemical potential. In our SIESTA calculations, $\boldsymbol{E_{VB}}$ was relatively constant (very little change) between neutral and charged states. As such, $\boldsymbol{E_{VB}}$ remains as a good reference for our study of defects stability. For calculations in which $\boldsymbol{E_{VB}}$ is floating with changing value between neutral and charged states, a correction term should be added to the formation enthalpy equation (V.2). For O chemical potential, we assumed an O_2 rich atmosphere as discussed above. Since we used GGA functional for our calculations, Wang et al. have identified some errors in the GGA oxidation energies [13]. They found that these errors were mainly originating from the overbinding of GGA in the O_2 molecule when the oxidant is O_2. This constant error from O_2 was estimated to -1.36 eV per O_2 molecule and was extracted from the shift of the experimental formation enthalpy of some metal oxides (MeO_x) compared with their calculated GGA energies [13]. Hence, in our calculations, we also used the -1.36 eV corrections per O_2.

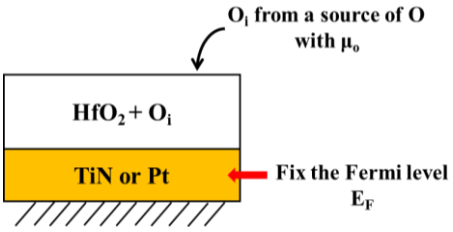

FigV.3. **The thermodynamic ensemble assumed for the formation of O_i in HfO_2 during HfO_2 deposition on BE.**

Neutral O_i type	Formation energy ΔH^{Oi} (eV)	Bader charge on O_i in (C) or complex O_2 in (A and B)
A	0.9	-1.45 e^-
B	0.8	-1.46 e-
C	1.5	-0.63 e^-

TableV.1. Formation energies of O_i in HfO_2

The O_i interstitial in cases A and B have similar formation energies and are in agreement with the calculated values obtained by Zheng et al. [14]. In the optimized structures of A and B, the O_i forms a bond with a nearest lattice (O_o) atom thereby forming a kind of O_2 molecule/ion in the HfO_2 matrix (FigV.2 A and B) whereas structure C does not bond with any O atom and remains attached to two neighbour Hf

atoms. FigV.4 shows the density of states (DOS) of the different systems with their HOMO (Highest Occupied Molecular Orbital) levels aligned to that of HfO_2. The DOS reveals that the O_i atom in structures A and B forms a kind of peroxide O_2^{2-} ion. Indeed the Bader charge analysis of the complex O_2 in A and B reveals that the net charge on O_i and its neighbour O_o are -1.45 et -1.46 for A and B respectively (TableV.1). Structure C is peculiar and presents the highest formation energy (1.5 eV) which makes it unfavourable. It has a net charge of -0.63 e^- which indicates that it captured some of the charges of its nearest Hf atoms. However, its DOS reveals two states in the gap of HfO_2 corresponding to the two empty states of its $2p^4$ orbitals. These results show *that the most favourable position of O_i in* HfO_2 *is to form a bond with a lattice O atom resulting in peroxide type* O_2^{2-} *ion under the assumption of* O_2 *rich environment in equilibrium.*

In our DFT calculations the band gap is underestimated (3.7 eV vs. 5.6 eV from experiment [1]) which is a known issue [14]. Several band gap correction schemes exist such as the many body perturbation theory in the GW approach [15] or hybrid functionals based on HSE (Heyd, Scuseria and Ernzerhof) implementation [16]. These correction schemes are heavy and computationally prohibitive especially with large systems that we are interested in our study. Therefore, we did not consider these band gap correction methods in our calculations which induce errors in our calculated defect energy levels and the offset of electrodes' alignment with HfO_2.

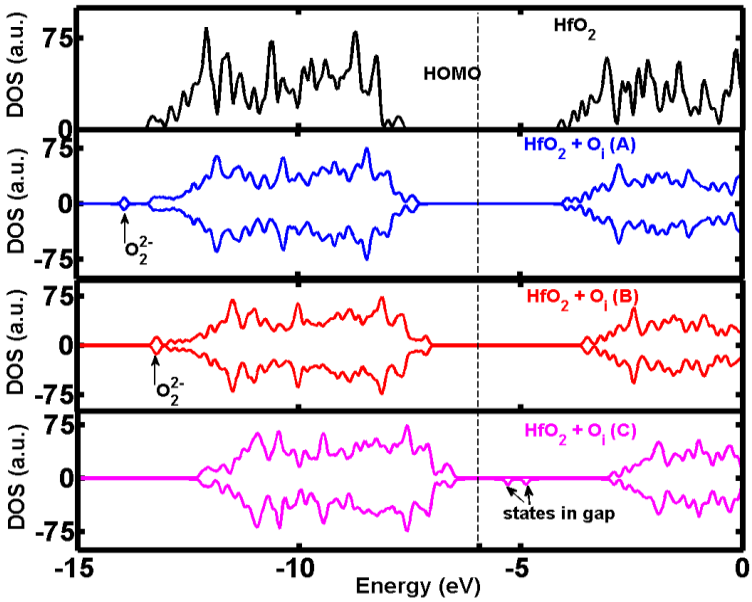

FigV.4. Density of states of HfO_2 with different O_i interstitial positions. The topmost DOS corresponds to the total DOS of defect-free HfO_2. For the cases A, B and C: positive DOS corresponds to spin up and negative DOS correspond to spin down.

With regards to O_i formation in RRAM, our ensemble (FigV.3) assumes HfO_2 on top of the BE which imposes the Fermi level (electron injection level into the oxide) of the system. This makes defects formation dependent on the Fermi level. FigV.5 shows the stability of O_i respect to the Fermi level and indicates that the formation of neutral O_i becomes favorable only when the electron injection level is close to VB which is possible with only very high work function electrodes. Using the standard electrodes in microelectronics such as Ti, TiN, Pt (FigV.5) the most favorable O_i state is O_i^{2-} when HfO_2 is deposited on TiN or Pt during RRAM fabrication process. Furthermore, formation of O_i of structure C is not expected in HfO_2 during device fabrication. Due to the underestimation of the band gap, the dashed region in FigV.5 artificially corresponds to the gap opening region if a band gap correction scheme was used. However, it is possible that the gap also opens slightly from the valence band with band gap correction [17].

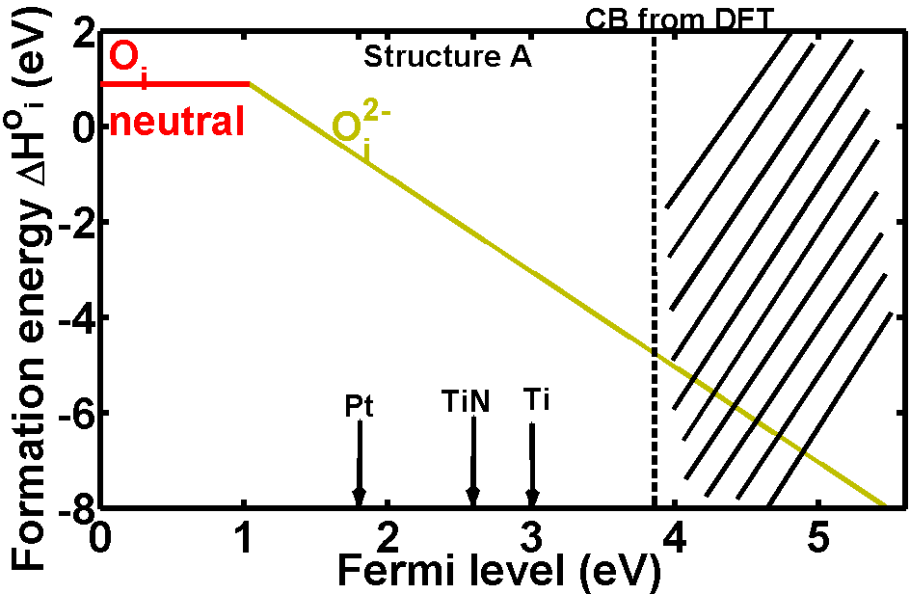

FigV.5. Thermodynamic stability of O_i in HfO_2 with the Fermi level (electron injection level).

FigV.5 also shows the alignment levels of Ti, TiN and Pt with HfO_2 and were estimated as follows. From the Ti/HfO_2 interface model that we developed in Chapter III, the conduction band offset (CBO) between Ti and HfO_2 was about 0.7 eV. Therefore, we chose Ti level to be 0.7 eV below the conduction band. Fonseca et al. studied the valence band offset (VBO) of TiN/HfO_2 interface with different stoichiometries within the GGA approximation using the technique of density of states projected on planes of atoms (PDOS) [18]. They calculated the VBO to be about 2.4 – 2.7 eV when the interface was a mixture of Ti-N-Hf or Ti-O-Hf bonds while VBO was

3.4 eV when the interface was purely Hf and Ti atoms. Since an interface TiN/HfO_2 that is purely Hf-Ti bonds without any O or N is unlikely, we chose a VBO of 2.6 eV for TiN/HfO_2 which is consistent with the VBO of 2.5 – 2.7 eV calculated by Prodhomme et al. within the Local Density Approximation [19]. For Pt/HfO_2, VBO of about 1.3 – 2.0 eV was calculated by Gavrikov et al. when the interface was slightly reduced using the GGA approximation [20]. 1.3 eV was obtained when Pt-Hf bonds disappeared completely at the interface and the number of Pt-O bonds was increased while 2 eV was calculated for two cases: (a) when there was one O atom at the interface for every two Hf atoms and did not lead to the formation of Pt-O bonds or (b) when there were two O atoms per two Hf atoms and some Pt-O bonds were formed with some other Pt-Hf bonds remaining. Since completely reduced Pt/HfO_2 interface leading to 1.0 eV of VBO is very unlikely, we chose VBO of 1.8 eV for Pt by assuming a slightly reduced Pt/HfO_2 interface. The alignment levels obtained for Ti, TiN and Pt with HfO_2 in this section will be assumed for the rest of the chapter.

V.3.1.2 Oxygen vacancies V_o

Oxygen vacancy (V_o) defect is a vacant oxygen lattice site in the oxide layer. In monoclinic HfO_2 (m-HfO_2), two different O atoms exist presenting different numbers of coordination: 3-fold coordinated (three neighbor Hf atoms) and 4-fold coordinated (four neighbor Hf atoms) O atoms. FigV.6 shows the two possible vacancy types in m-HfO_2 depending on the coordination of the O atom.

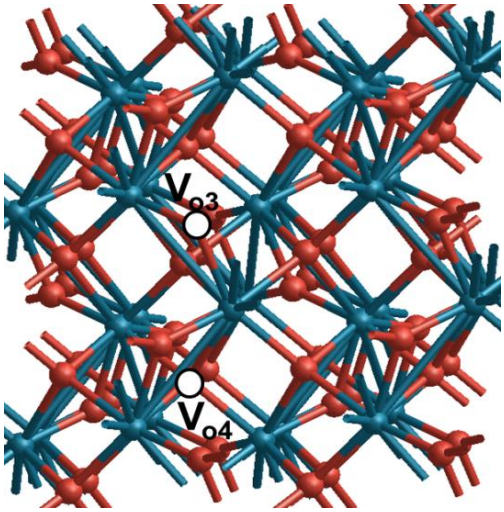

FigV.6. Atomistic structure of m-HfO_2 showing 4-fold coordinated oxygen vacancy (V_{o4}) and 3-fold coordinated (V_{o3}).

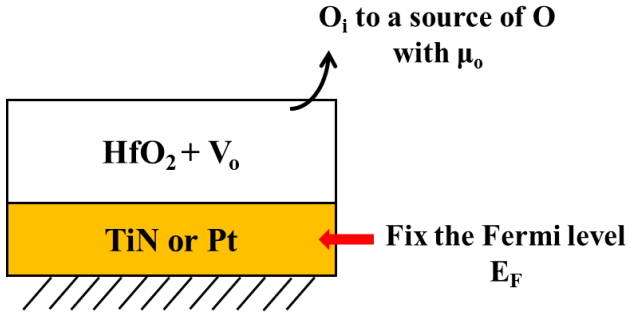

FigV.7. The thermodynamic ensemble assumed for the formation of V_o in HfO_2 during HfO_2 deposition on BE.

FigV.7 shows the assumed thermodynamic ensemble for V_o formation in HfO_2 and their formation energies, summarized in TableV.2, are calculated using:

$$\Delta H^{Vo,\pm q} = E_{tot}^{Vo,\pm q} - E_{tot}^{HfO_2} + \mu_o \pm q(E_{VB} + E_F) \quad \text{(V.3)}$$

Where $E_{tot}^{HfO_2}$ is the energy of the defect-free HfO_2 supercell, E_{VB} and E_F are defined as in the case of O_i. $E_{tot}^{Vo,\pm q}$ is the energy of the supercell with V_o at charge $\pm q$, and μ_o oxygen (O) chemical potential as above and q the charge of the system.

Neutral V_o type	Formation energy ΔH^{Vo} (eV)
V_{o4}	7.0
V_{o3}	7.1

TableV.2. Formation energies of V_o in HfO_2

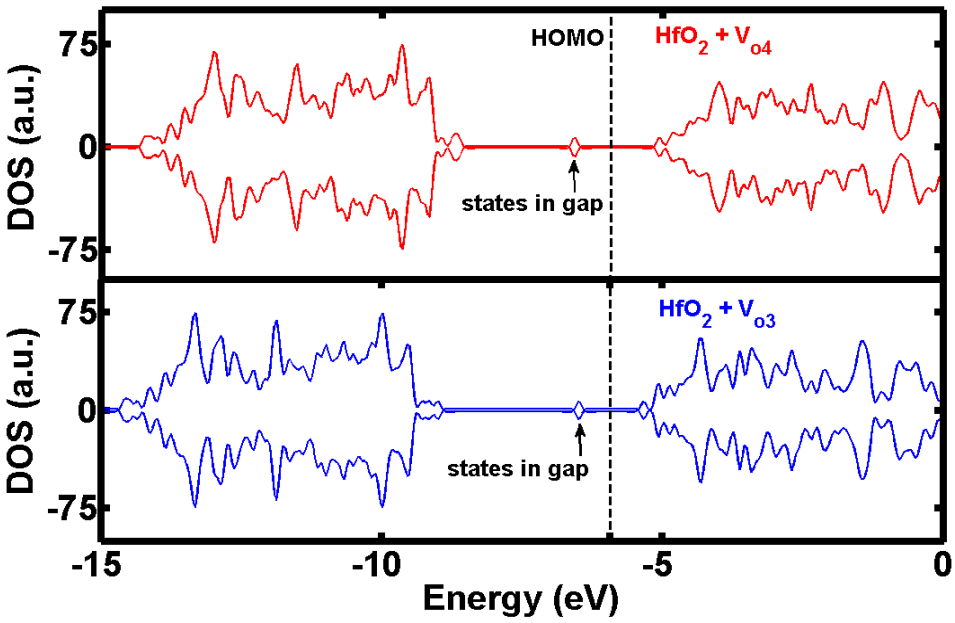

FigV.8. DOS of HfO_2 with V_o defect.

V_{o4} formation is more favorable than V_{o3} by approximately 0.1 eV which is very close to the 0.13 eV difference calculated by Zheng et al. [14]. The optimization of the two V_o types does not induce any significant structural change in the HfO_2 matrix. FigV.8 shows the DOS of the two V_o types with their HOMO levels aligned: both show filled states inside the gap sitting a little above the calculated DFT mid-gap. These V_o states inside the gap may act as charge trapping centers during RRAM switching operations. Nevertheless, the formation energy of V_o remains very high in its neutral state (~7 eV). This formation energy depends on the choice of oxygen chemical potential and whether the removed O atom goes to an electrode or to molecular O_2 form as is assumed in this section. FigV.9 shows the formation energy of V_o with respect to the Fermi level and indicates that charge injection can favor V_o formation and the most favorable V_o states are further shown in FigV.10. V_o^{2+} formation is favorable from VB up to close to mid-gap and is probably the predominant vacancy type when Pt is used as BE (Pt) under equilibrium. Close to mid-gap, among the different charge states of V_o, neutral V_o becomes more stable with low work function electrodes like TiN or Ti. The uncertainty in TiN alignment level may tend to make V_o^{+1} also favorable at this stage. FigV.10 further shows that if very low work function electrodes are used as BE, V_o^{2-} formation may become favorable (for example Li or Mg as BE).

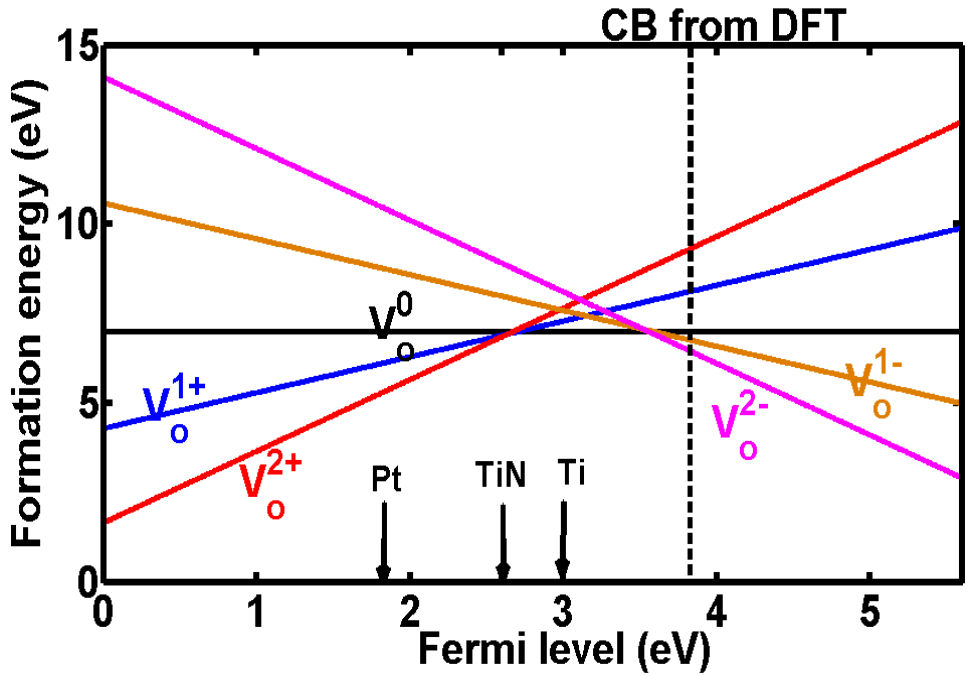

FigV.9. Formation energy of V_o with respect to the Fermi level.

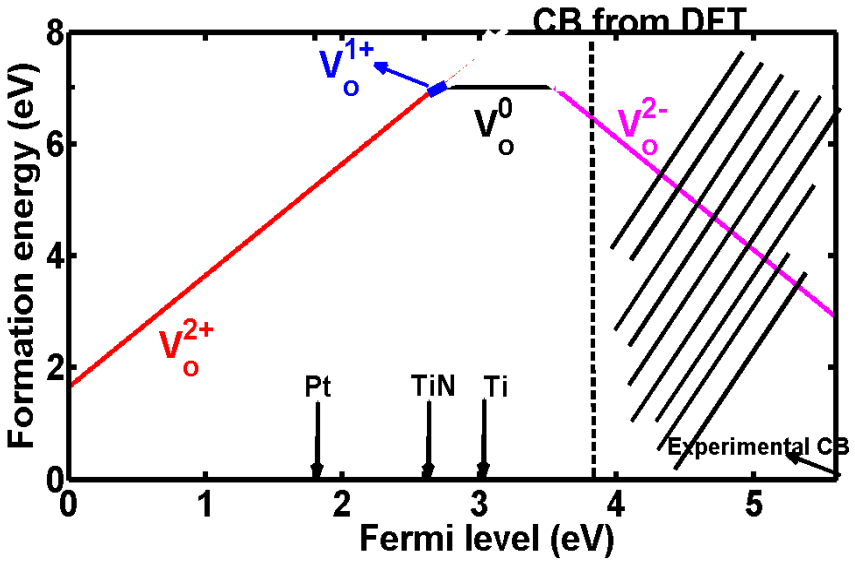

FigV.10. Most favorable V_o states with respect to the Fermi level. The dashed region would artificially correspond to the gap opening region if a band gap correction was used.

In terms of point defects kinetics, TableV.3 summarizes calculated V_o and O_i diffusion barriers. Neutral and negatively charged V_o have high diffusion barriers and as such are generally immobile at low temperature without external field. V_o diffusion barrier is reduced in its 2+ charge state. On the other hand, O_i have low diffusion barriers and very mobile especially in their 2- charge state. The low diffusion barrier of O_i^{2-} may make them diffuse from HfO_2 when in contact with a more reactive electrode.

Defect type	E_a (eV): this work	Ea (eV): literature
V_o^0	2.2	2.19 [21]
V_o^{2+} [IS to FS]	0.9	0.49 [21]
V_o^{2+}[FS to IS]	0.1	0.05 [21]
V_o^{2-}	2.1	2.45 [22]
O_i^0	0.6	0.7 [23]
O_i^{2-}	0.2	0.2 [23]

TableV.3. Calculated V_o and O_i diffusion barriers in HfO_2. IS stands for Initial State and FS for Final State.

V.3.1.3 Extended Frenkel-pair (FP) defects

Frenkel pair (FP) defect is oxygen atom that leaves behind an oxygen vacancy and sits in an interstitial position resulting in an oxygen vacancy/oxygen interstitial (O_i + V_o) pair. Hence, in our approach, we will later consider FP as prototype defects that may lead to the dielectric degradation and thus the conductive filament formation during the forming operation in RRAM. As discussed in the oxygen interstitial defect section, several O_i positions are possible in HfO_2 which induces the possibility of

having different FP configurations. FigV.11 shows 2 different FP configurations with the 4-fold coordinated oxygen atom considered as the vacancy.

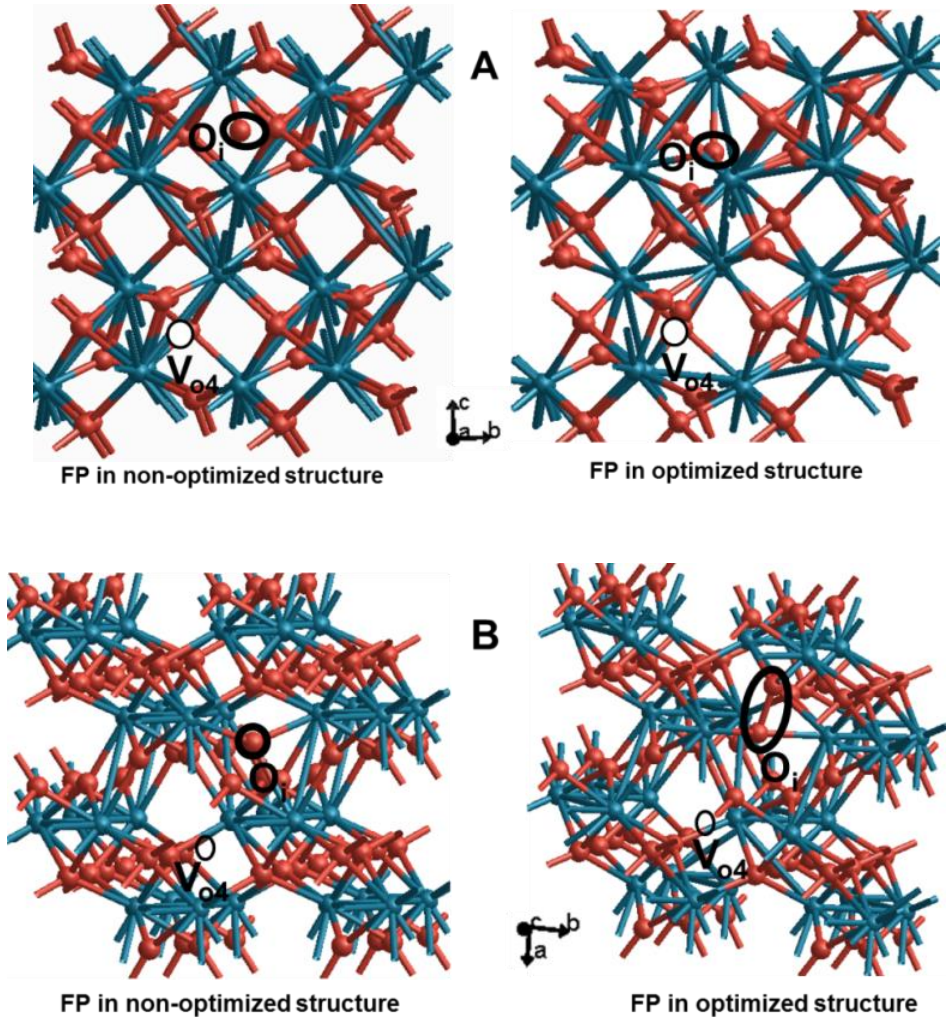

FigV.11. Two different configurations of FP in $mHfO_2$ together with their optimized positions.

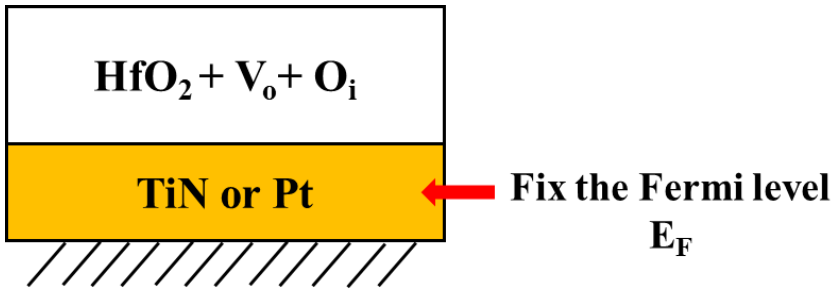

FigV.12. The thermodynamic ensemble assumed for the formation of FP in HfO_2 during HfO_2 deposition on BE. Both O_i and V_o are assumed to remain in HfO_2.

FigV.12 shows the assumed thermodynamic ensemble for FP formation in HfO_2 and their formation energies in neutral/charged states summarized in TableV.4 were calculated using:

$$\Delta H^{FP,\pm q} = E_{tot}^{FP,\pm q} - E_{tot}^{HfO_2} \pm q(E_{VB} + E_F) \quad \textbf{(V.4)}$$

where $E_{tot}^{FP,\pm q}$ is the energy of the supercell with FP at charge $\pm q$, $E_{tot}^{HfO_2}$ the energy of HfO_2 supercell, E_{VB} the top of the valence band (VB), E_F the Fermi level measured from the top of the VB and q the charge. The formation energy of FP for both cases is high with case B involving even much higher energy (8.5 eV). From the Bader charge analysis of TableV.4, we notice that locally O_i and V_o have more formal charges (-1.26 and +1.76) for case A than for case B (-0.65 and +1.59) indicating that despite the system being globally neutral O_i behaves like O_i^{2-} and V_o like V_o^{2+} for case A. For case B, it is as if O_i behaves like neutral O_i and V_o like neutral V_o as can be seen from its high formation energy of 8.5 eV (approximately equal to the formation energy of isolated V_o + the formation energy of neutral O_i case C above). The DOS of the two FP cases is shown in FigV.13 and the HOMO levels of the different cases are aligned to that of HfO_2. The DOS of case A shows empty V_o and filled O_i states inside the gap which respectively correspond to V_o^{2+} and O_i^{2-} in agreement with the Bader charge analysis. For case B, V_o states are filled (V_o^0) and O_i form a complex O_2 deep inside the valence band showing that there is barely any charge exchange between the O_i and V_o forming the FP. When FP is formed with a 3-fold coordinated oxygen atom considered for the vacancy, we calculated a formation energy of 4.9 eV which indicates that FP formation energy is slightly lower with V_{o3} compared with V_{o4}. Hence, the most favourable FP defect in HfO_2 is V_o^{2+} and O_i^{2-} pair when HfO_2 is isolated.

Neutral FP type	Formation energy ΔH^{FP} (eV)	Bader charge on O_i	Bader charge on Hf atoms near V_o
Case A	5.2	-1.26	1.76
Case B	8.5	-0.65 (-1.5 for complex O_2)	1.59

TableV.4. Formation energies of FP for cases A and B in HfO_2.

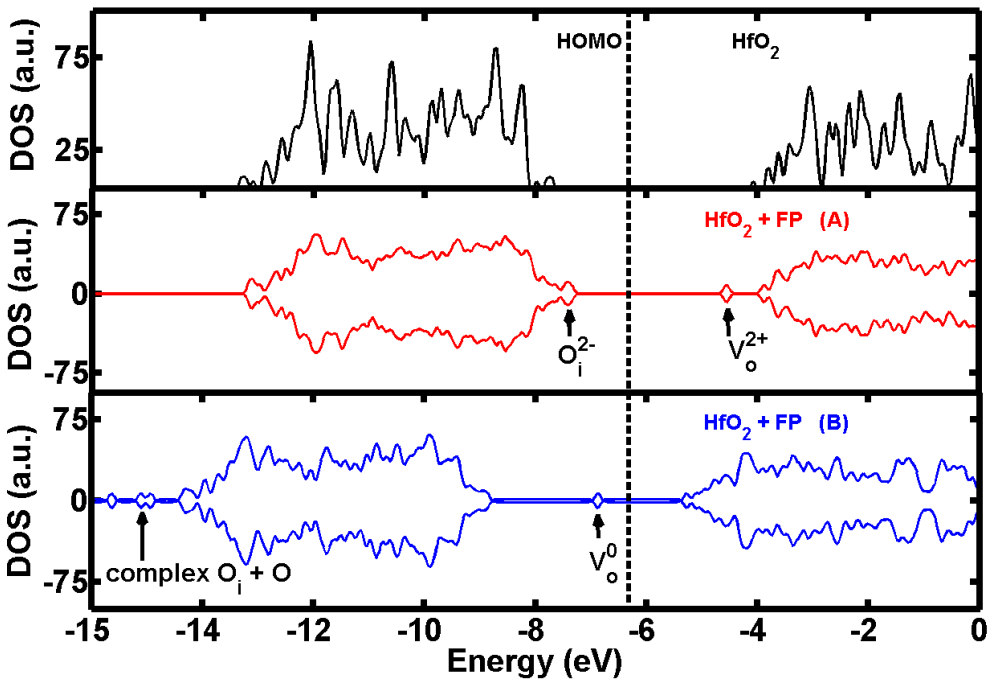

FigV.13. DOS of HfO_2 with Frenkel pair defects.

Nevertheless, the formation energy of neutral FP remains very high and Hf-O bond breakage is then very unlikely under equilibrium. This formation energy may be lower by introducing charges into the system as shown in FigV.14. FigV.14 indicates that the stable FP state is FP^{2-} [$V_o^0 + O_i^{2-}$] for TiN electrode while it is FP^0($V_o^{2+} + O_i^{2-}$) that is stable when HfO_2 is deposited on Pt. From the charge analysis, FP^{2-} is indeed $V_o^0 + O_i^{2-}$, FP^0 remains $V_o^{2+} + O_i^{2-}$ and FP^{2+} is $V_o^{2+} + O_i^0$. The high formation energy of FP suggests that it will only form in small concentrations in HfO_2 under equilibrium.

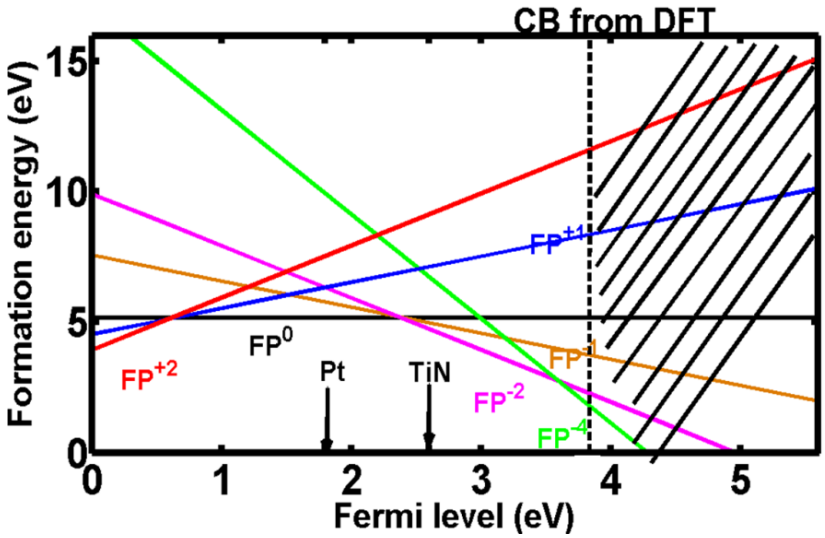

FigV.14. Formation energy of FP with respect to the Fermi level.
$FP^{\pm q} = HfO_2 : (O_i^{2-} + V_o^{2+} \mp qe^-)$

The thermodynamic view of the FP stability that we have provided is very useful and allows us to comprehend different phenomena on their formation. During the degradation of oxides or the formation of CF for RRAM, the kinetics of defects and other non-equilibrium phenomena occur. Our DFT calculations are not suitable for systems out of equilibrium or other excited cases. However, they may provide us kinetic information through defects diffusion barriers. As far as FP or the other defects (V_o or O_i) are concerned, their diffusion barrier information is very important in order to understand how Hf-O bonds may actually break in RRAM. Hence, an attempt to understand FP diffusion is discussed in the next section.

V.3.1.4 FP diffusion process

For the diffusion barrier calculation of FP, we considered the O_i and V_o defects positions shown in FigV.15. Unlike the previous section, we used the 3-fold oxygen atom for the vacancy since it had a slightly lower formation energy compared with FP formed with a 4-fold coordinated O atom. We suspect that the two cases would be similar had we performed similar calculations with the 4-fold coordinated O atom for the vacancy (probably a difference of less than a few tenth of eV). The extended FP diffusion calculations were performed by considering the exchange mechanism. This is achieved by allowing an intermediate O_o to replace the starting O_i for migration to the final position as shown in FigV.15. The motivation to proceed with the exchange mechanism was that the direct diffusion of O_i was unlikely and a barrier of more than 8 eV for the direct process was estimated. Both neutral and charged FP were considered for the diffusion process.

FigV.16 shows the diffusion profile of the extended FP with calculated barriers of 6.5 eV and 4.5 eV for FP^0 and FP^{2-} respectively. Similar to its formation energy, FP also presents very high diffusion barrier which is lowered by 2 eV with e^- injection. In order to understand if few pre-defects coupled with electron injection have an impact on FP diffusion, we introduced one and two oxygen vacancies in the supercell of FigV.15 and considered the same FP migration mechanism. TableV.5 summarizes the different calculated barriers. We notice that the introduction of the pre-defects did not change much in the calculated energy barriers. However, we observe a reduction of the barriers by around 2 eV with electron injection for all the cases except for the $4e^-$ injection scenario. More electron injection (over 2) did not bring significant reduction in the computed barriers. As pointed out above, the high formation energy and diffusion

barrier of FP support the fact that it will only in exist in low concentration inside the oxide layer after HfO_2 deposition on BE. We will later use FP diffusion information for more understanding on CF formation in RRAM.

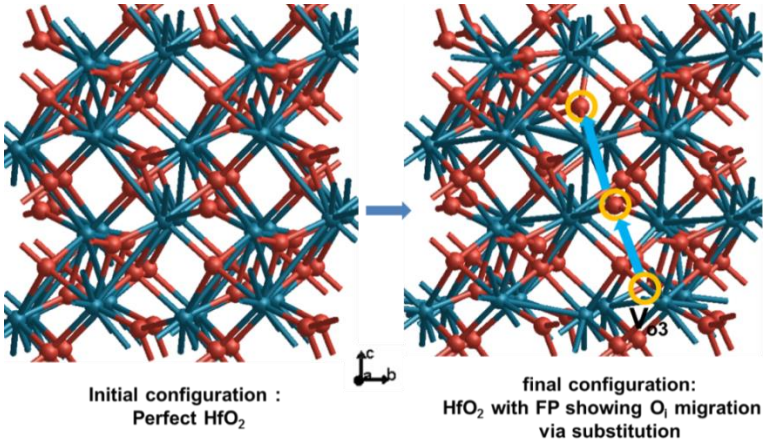

FigV.15. Extended FP defect considered for the diffusion in HfO_2. The diffusion is performed by exchange where an intermediate O_o substitutes the starting O_i to migrate to the final position.

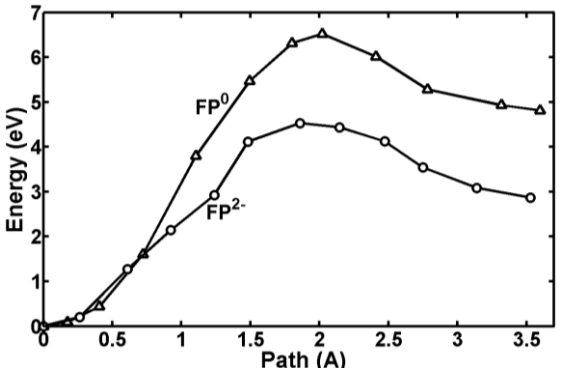

FigV.16. Diffusion profile of neutral and charged extended FP in HfO_2.

Defect type	Diffusion barrier (eV)
FP^0	6.5
FP^{2-}	4.5
$1V_o + FP^0$	6.4
$1V_o + FP^{2-}$	4.4
$2V_o + FP^0$	6.3
$2V_o + FP^{2-}$	4.8
$2V_o + FP^{4-}$	5.0

TableV.5. Calculated diffusion barriers of the extended FP considered.

V.3.2 TE deposition on HfO_2 during the process

FigV.17 shows a schematic representation of TE (Ti or Pt) being deposited on HfO_2 during device fabrication process. In this scenario we assume the Fermi level of the system to be fixed by TE. Furthermore, the assumption of O_2 rich atmosphere is no longer valid because the deposition of TE does not occur in an O_2 rich environment. Therefore, the chemical potential of oxygen (μ_o) for this section may be safely assumed to be that of O inside the TE for O defects formation. Therefore, O chemical potential is evaluated using the following equation:

$$\boldsymbol{\mu_{o,TE}} = \boldsymbol{E_{TE}^{Oi}} - \boldsymbol{E_{TE}} \quad \text{(V.5)}$$

where E_{TE}^{Oi} is the energy of metal TE supercell with an oxygen atom and E_{TE} the energy of TE.

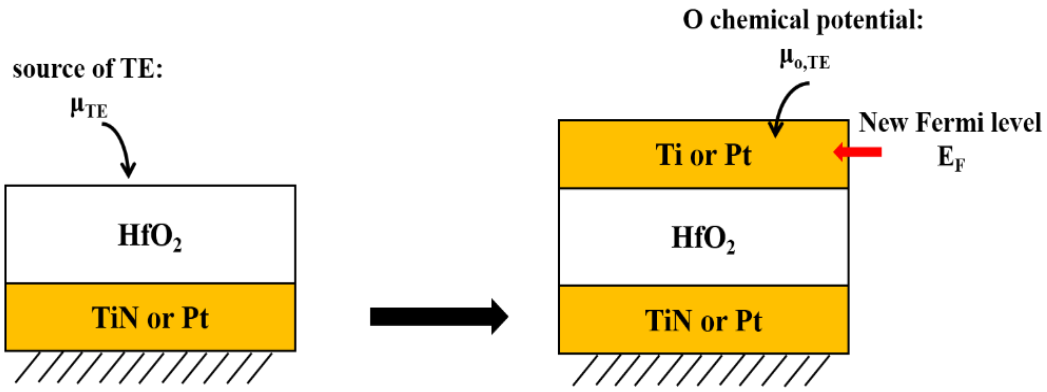

FigV.17. Thermodynamic ensemble showing TE deposition on HfO_2

V.3.2.1 V_o/O_i defect

FigV.18 shows the stability of O_i in HfO_2 when the chemical potential of oxygen is assumed to be that of O in TE Ti. The formation energy is computed as before except that the O chemical potential is calculated as shown in equation (V.5). We observe that both neutral and negatively charged O_i have high formation energy indicating that it is very unlikely that O_i remain in HfO_2 after Ti deposition. When O chemical potential is assumed to be that of O in TE Pt, FigV.19 shows that the formation energy of O_i^{2-} in HfO_2 is negative at the Pt alignment level indicating that O_i preferentially remain in HfO_2 rather than going to Pt.

On the other hand, FigV.20 shows that neutral V_o formation energy in HfO_2 gets drastically lowered when the missing O atom goes to the Ti layer instead of the O_2 form (0.70 eV vs. 7.01 eV). This V_o formation is essentially equivalent to the formation

of extended FP with V_o in HfO_2 and O_i in Ti. For Pt, V_o^{2+} is the stable state at its alignment level (FigV.21). The combined information from FigV.18 to FigV.21 indicates two things: Firstly, the alignment level of Ti with HfO_2 band gap indicates that neutral V_o are the dominant defect states after device fabrication while it is V_o^{2+} that are dominant when Pt is used as TE. Secondly, O_i preferentially react with Ti leaving behind V_o in HfO_2 for TiN/HfO_2/Ti stack while both O_i and V_o preferentially remain in HfO_2 for Pt/HfO_2/Pt cell.

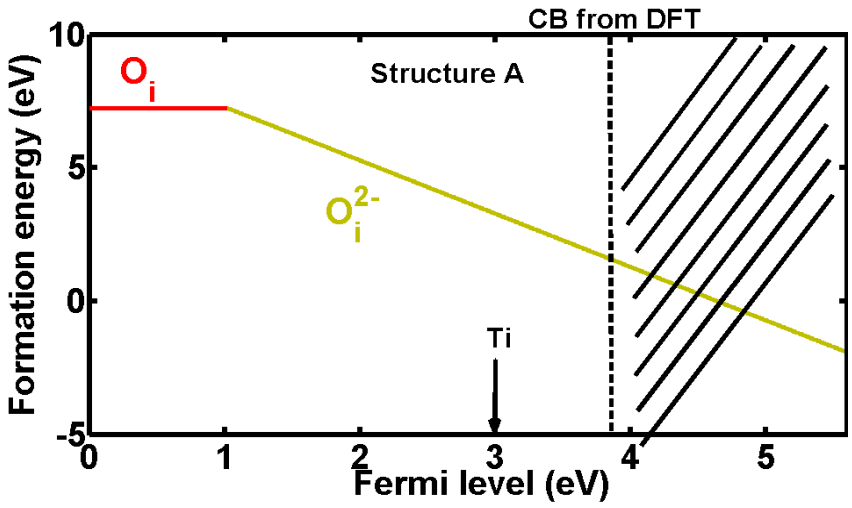

FigV.18. Thermodynamic stability of O_i in HfO_2 in contact with Ti TE as a function of the Fermi level (electron injection level).

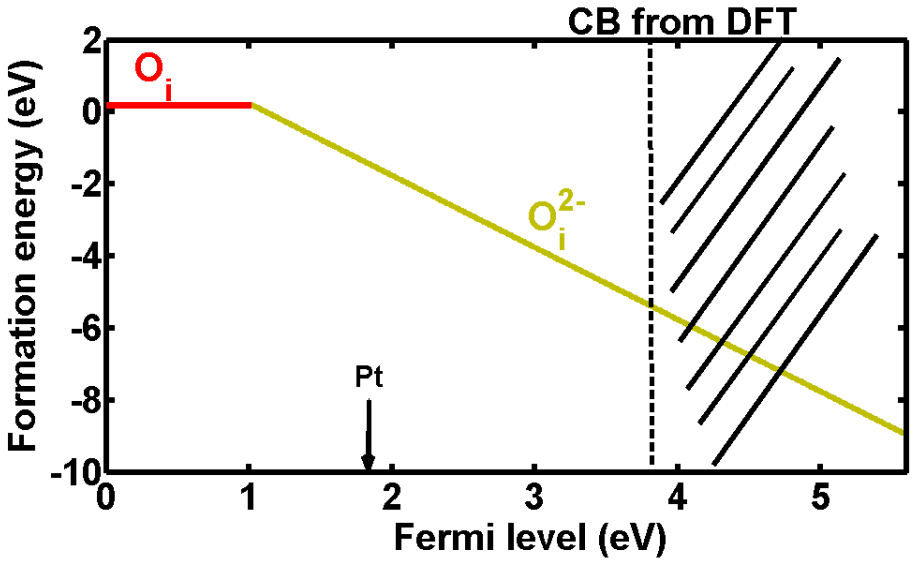

FigV.19. Thermodynamic stability of O_i in HfO_2 in contact with Pt TE as a function of the Fermi level.

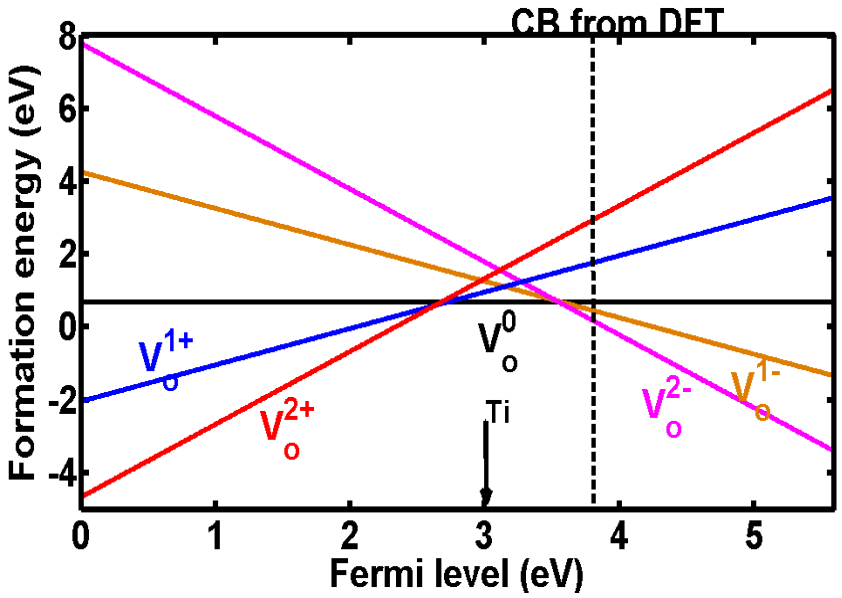

FigV.20. Thermodynamic stability of V_o in HfO_2 with O_i going to Ti. This is equivalent to extended FP formation with V_o in HfO_2 and O_i in Ti.

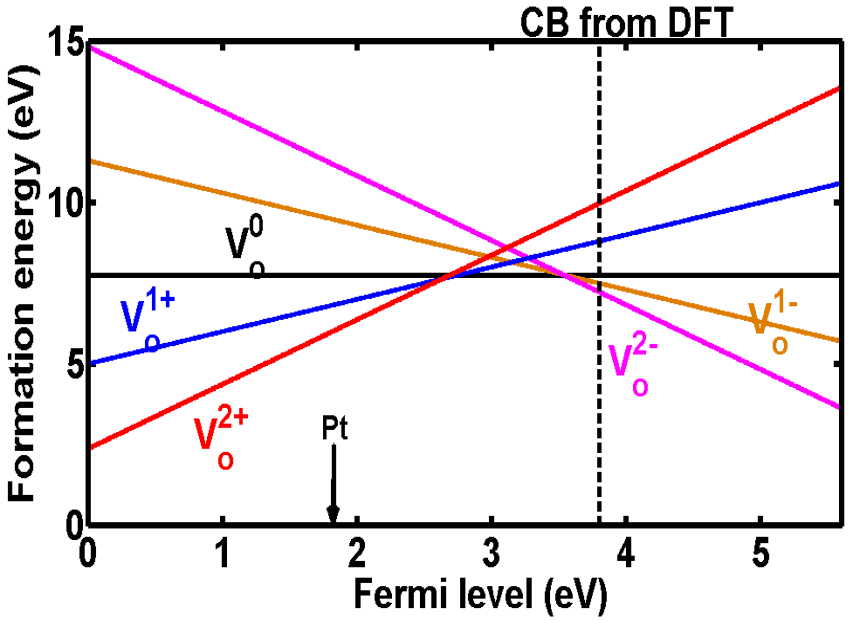

FigV.21. Thermodynamic stability of V_o in HfO_2 with O_i going to Pt. This is equivalent to extended FP formation with V_o in HfO_2 and O_i in Pt.

V.4 CF formation

Having considered most of the predominant defect types that may be present in HfO_2 after device fabrication and their kinetic information through diffusion barriers calculations, we propose in this section our understanding about CF formation in HfO_2 based RRAM. The model couples the thermodynamic of defects and their diffusion barriers to explain how the filament potentially grows and ultimately creates a conduction path between the top and bottom electrodes of RRAM.

V.4.1 RRAM device at V = 0

The actual RRAM devices are fabricated in a metal-insulator-metal (MIM) structure similar to a capacitor. The presence of two metal electrodes, which are assumed to be thick enough, impose their Fermi levels on either side of HfO_2 layer. These Fermi levels may be defined by the work functions of the two metals with respect to HfO_2 affinity although the alignment of the metal electrodes with the dielectric is better defined by the band offset concept. If the two metals have different work functions, a built-in potential is created in the dielectric when the two metal electrodes are short-circuited (V = 0V) as shown in FigV.22. The built-in potential is expressed as:

$$V_{bi} = E_F^{TE} - E_F^{BE} \qquad \textbf{(V. 6)}$$

Point defects (V_o or O_i) in HfO_2 may exchange electrons by tunneling effects with the electrodes and the electrodes may act as electron reservoirs with a Fermi level. We would like to evaluate if this charge exchange is permanent at V= 0 V by assuming the following conditions: low defect concentration compared to the total atomic concentration which in essence ensures the integrity of the dielectric layer, the dielectric layer is thin enough to allow for charge exchange and no charge image effect is present. From our treatment of point defects formation, we saw that after the device fabrication, it is possible that fewer defects (V_o, O_i or FP) be formed in HfO_2 layer. Therefore we assume that pre-defects exist in HfO_2 and that these pre-defects may exchange charge with one of the electrodes. A defect (D) along the lateral dimension of the dielectric is assumed at a position x where x = 0 corresponds to the TE and x =1 corresponds to the BE. We then assume the following definitions: $D^{\pm q,BE}(x)$ corresponds to a defect (V_o, O_i or FP) with charge $\pm q$ at a position x that exchanges charge with BE. $D^{\pm q,TE}(x)$is defined in a similar manner for defect D at position x that exchanges charge with TE.

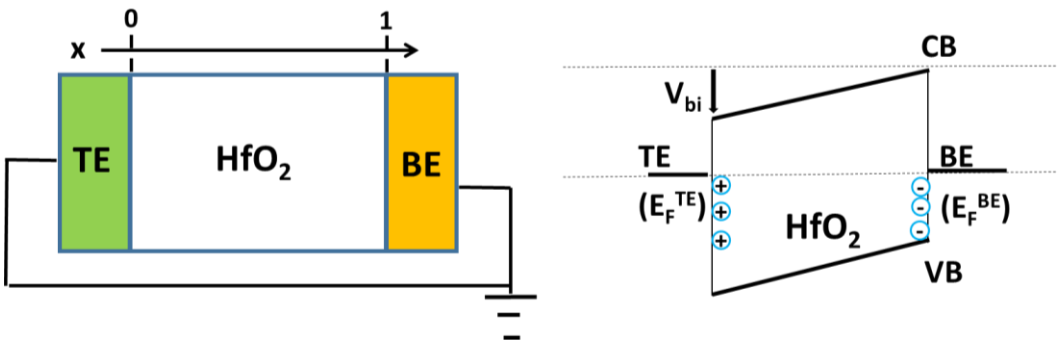

FigV.22. HfO_2 sandwiched between TE and BE with electrodes short-circuited.

If we consider the internal polarization of the dielectric layer (FigV.22) due to the work function difference of the two electrodes and the charge exchange with one of the electrodes, one can formulate the following reactions and the corresponding energies:

At BE: q electrons from $BE + D^0(x) \rightarrow D^{-q,BE}(x)$

where $D^0(x)$ is the neutral defect at position x, $D^{-q,BE}(x)$ the defect with charge –q injected from BE. The formation enthalpy for this reaction can be written as:

$$\Delta \boldsymbol{H_{BE}(-q)} = \boldsymbol{E(D^{-q,BE})} - \boldsymbol{E(D^0)} - \boldsymbol{q.E_F^{BE}} - \boldsymbol{q.(1-x).V_{bi}} \qquad \textbf{(V. 7)}$$

Where $E(D^{-q,BE})$ is the total energy of defect D with charge –q from BE and $E(D^0)$ the total energy of defect D in its neutral state. We assumed a linear voltage drop over the dielectric layer which holds as long as the defect concentration inside the dielectric is not important so as not to affect its integrity.

Similarly we may write $D^0(x) \rightarrow D^{+q,TE}(x) + q$ electrons into TE

The corresponding formation enthalpy is given by:

$$\Delta \boldsymbol{H_{TE}(+q)} = \boldsymbol{E(D^{+q,TE})} - \boldsymbol{E(D^0)} + \boldsymbol{q.E_F^{TE}} - \boldsymbol{q.x.V_{bi}} \qquad \textbf{(V. 8)}$$

The above two formation enthalpy equations are symmetric and results in:

$$\Delta H_{BE}(q) = \Delta H_{TE}(q); \quad \text{at V = 0 V}$$

This allows the definition of a unique Fermi level. With the above development, defects formation energies can be evaluated in a situation that is more realistic and closer to RRAM operation. The use of the above equations necessitates the knowledge of the Fermi levels of the metal electrodes and we used a CBO of 0.7 eV for Ti, VBO of 2.6 eV for TiN and VBO of 1.8 eV for Pt as explained at the end of section V.3.1.1. Since our calculations underestimate the band gap of HfO_2 and as such we do not have precise electrode alignment levels with HfO_2.

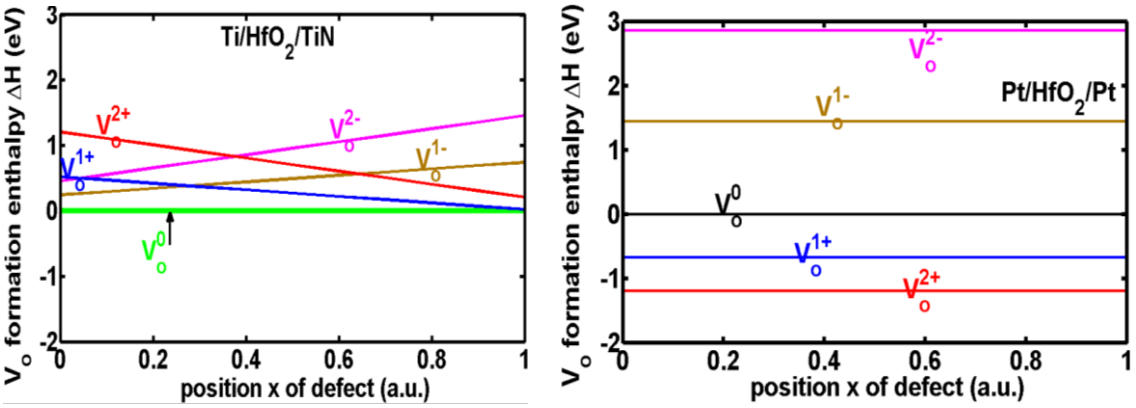

FigV.23. V_o stability at 0V bias in (left) TiN/HfO_2/Ti MIM and (right) Pt/HfO_2/Pt.

FigV.23 shows the stability of V_o in HfO_2 sandwiched between different metal electrodes at 0V. For both figures, the neutral V_o state was taken as the reference which essentially assumes that after the fabrication process few pre-defects were already formed inside the dielectric as mentioned earlier. For TiN/HfO_2/Ti RRAM, neutral V_o state is the most favorable defect at equilibrium. Due to the uncertainty in the electrodes alignment levels with HfO_2, V_o may become V_o^{2+} close to TiN by losing its electrons to it. For Pt/HfO_2/Pt, V_o^{2+} is the most favorable defect state. We get horizontal lines for all the charge states of V_o because of the symmetry of the electrodes: the built-in potential V_{bi} is null. Similarly, the stability of O_i is plotted in FigV.24 for both RRAM stacks and O_i^{2-} is the most favorable oxygen interstitial defect.

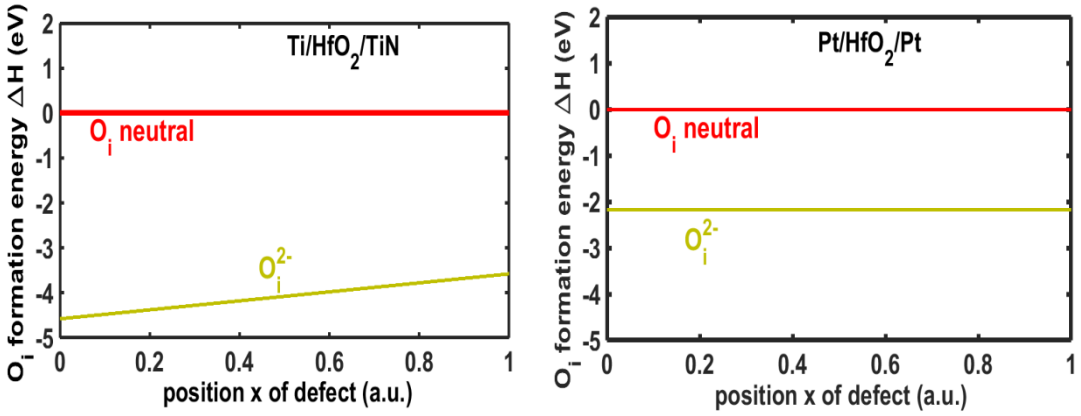

FigV.24. O_i stability at 0V bias in (left) TiN/HfO_2/Ti MIM and (right) Pt/HfO_2/Pt.

V.4.2 RRAM device at V > 0

We look at the case of external polarization with an applied voltage V of few volts as shown in FigV.25. The equations developed for the zero bias case are still valid except that an applied voltage V is added to V_{bi}:

At BE: q electrons from $BE + D^0(x) \rightarrow D^{-q,BE}(x)$

The formation enthalpy for this reaction is transformed into:

$$\Delta H_{BE}(-q) = E(D^{-q,BE}) - E(D^0) - q.E_F^{BE} - q.(1-x).(V_{bi}+V) \qquad \textbf{(V. 9)}$$

where V is the applied voltage. As long as the integrity of the dielectric is ensured, we may assume a linear voltage drop across it.

Similarly we may write $D^0(x) \rightarrow D^{+q,TE}(x) + q$ electrons into TE

The corresponding formation enthalpy is given by:

$$\Delta H_{TE}(+q) = E(D^{+q,TE}) - E(D^0) + q.E_F^{TE} - q.x.(V_{bi} + V) \qquad \textbf{(V. 10)}$$

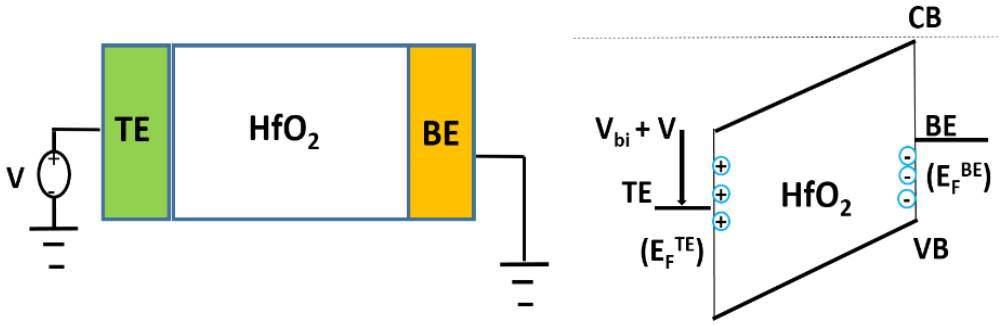

FigV.25. RRAM MIM structure and its simplified band diagram with an external voltage V.

The two enthalpy formulas differ by qV, that is

$$\Delta H_{BE}(q) = \Delta H_{TE}(q) + qV.$$

The applied external voltage leads to a permanent non-equilibrium situation. This means that the formation enthalpy equations with the external voltage cannot describe a permanent equilibrium scenario and should be interpreted differently compared to the zero bias case. The following graphs with the external voltage attempt to investigate the possible defects' charge states out of equilibrium and as such which defect states would often occur with respect to both electrodes should be considered simultaneously. Normally, one would associate a lifetime for a specific defect with a charge state q at a position x between the electrodes. That is, a probability needs to be associated to a specific defect state in its charging/discharging reactions. These considerations are out of the scope of what our DFT calculations can do.

FigV.26 shows the possible V_o states in TiN/HfO_2/Ti and Pt/HfO_2/Pt devices under an external applied voltage of 2V. For clarity, we only included few charge states (more interesting) of V_o in the respective graphs. Since the system is out of equilibrium with the applied voltage, we need to consider simultaneously the possibility of charge exchange between V_o and both electrodes. In FigV.26, we observe that for each V_o state, we have $V_o^{+/-q}$ (BE) that may exchange charge with BE or $V_o^{+/-q}$(TE) that may exchange charge with TE. To understand the process as schematically represented in FigV.27, let us consider V_o for TiN/HfO_2/Ti:

a) Close to the top electrode Ti(x=0), neutral V_o can accept electrons from the BE TiN and temporarily becomes V_o^{2-}(BE) as is shown in the figure.

b) However, since the system is out of equilibrium, this V_o^{2-}(BE) can give its 2 electrons to the top Ti electrode and hence becomes neutral V_o. This can be seen by the fact that V_o^{2-}(TE) is higher in energy than neutral V_o^0.

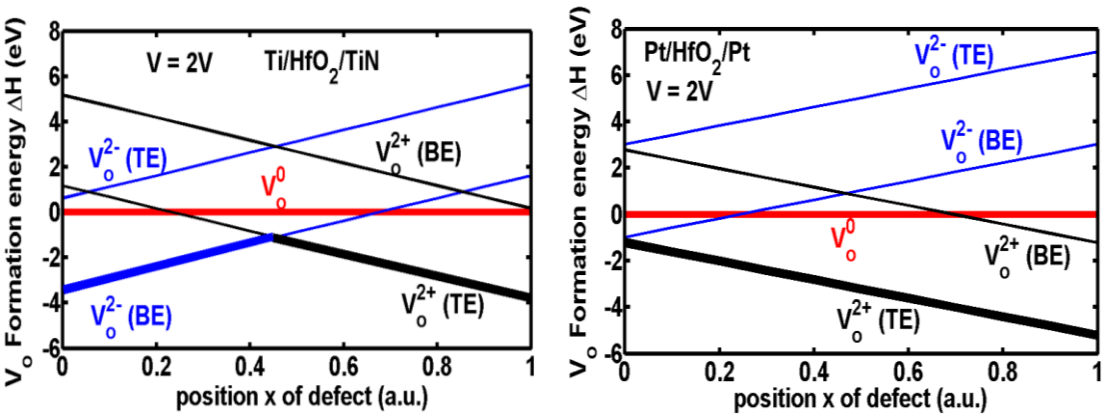

FigV.26. V_o charge states under an external polarization of 2V in (left) TiN/HfO_2/Ti and (right) Pt/HfO_2/Pt.

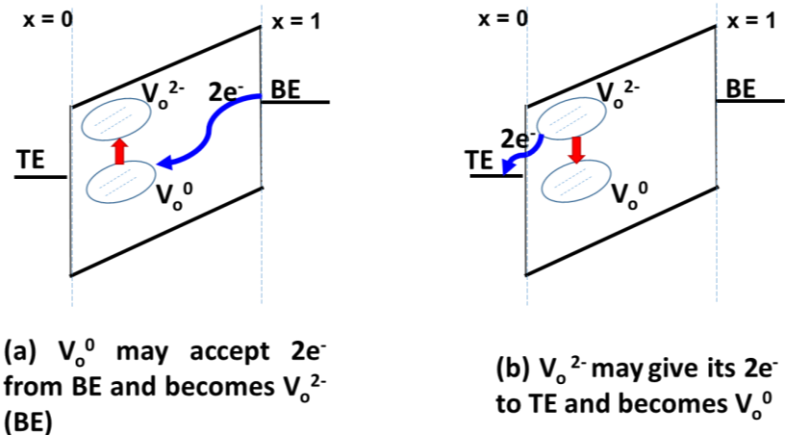

FigV.27. Schematic representation of charge exchange between V_o close to TE and electrodes Ti/TiN.

Interestingly, close to the BE (TiN), it is V_o^{2+} state that appears to be more pronounced as represented by V_o^{2+}(TE). This is achieved by the following as represented schematically in FigV.28:

a) Neutral V_o close to TiN and in higher energy state than Ti Fermi level can give its electrons to top electrode Ti and become V_o^{2+}(TE).

b) However, those V_o^{2+}(TE) in the proximity of TiN, can accept electrons from TiN and become neutral as can be seen by the higher formation energy of V_o^{2+}(BE) with respect to neutral V_o^0 (FigV.26).

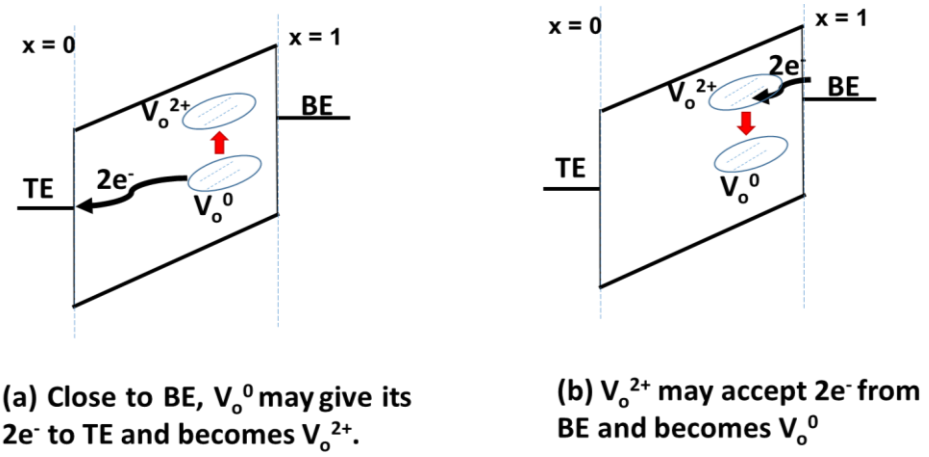

FigV.28. Schematic representation of charge exchange between V_o close to BE and electrodes Ti/TiN.

Combining the possible V_o transitions schematically shown in FigV.27 and FigV.28, TAT like transitions involving $2e^-$ transfer in TiN/HfO_2/Ti based RRAM could be tentatively described. Our results indicate that electron transfer in a process like TAT is very complex and may involve more than one electron.

$$\boldsymbol{V_o + 2e^- \rightarrow V_o^{2-} \rightarrow V_o + 2e^-} \qquad \textbf{(V. 11)}$$

$$\boldsymbol{V_o \rightarrow V_o^{2+} + 2e^- \rightarrow V_o} \qquad \textbf{(V. 12)}$$

From the V_o transitions in TiN/HfO_2/Ti, it appears that, during the electron injection process before the filament is formed, negatively charged V_o (V_o^{2-}) start to form close to Ti and positively charged V_o (V_o^{2+}) close to BE and these charged V_o states tend to neutralize somewhere between the electrodes. V_o^{2+}(TE) transitions in TiN/HfO_2/Ti seems to occur often up to close to midway between BE and TE. However if V_o tends to accumulate near BE, transition from V_o^0 to V_o^{2+} near BE may probably

not be too pronounced during the switching operation because localized electron tunneling from neutral V_o to TE, and hence becoming V_o^{2+}, may be limited as the distance from TE becomes important.

Similarly FigV.26 (right) shows the transitions of V_o in Pt/HfO_2/Pt with an external voltage applied. From BE to TE, V_o seems to essentially transit in its V_o^{2+}(TE) state by giving its e^- to Pt TE. Since, Pt/HfO_2/Pt devices form at higher voltage (>4V) than the 2V considered, one may expect that V_o^{2-} becomes more pronounced close to TE (Pt) at higher applied voltages and this is shown in FigV.29.

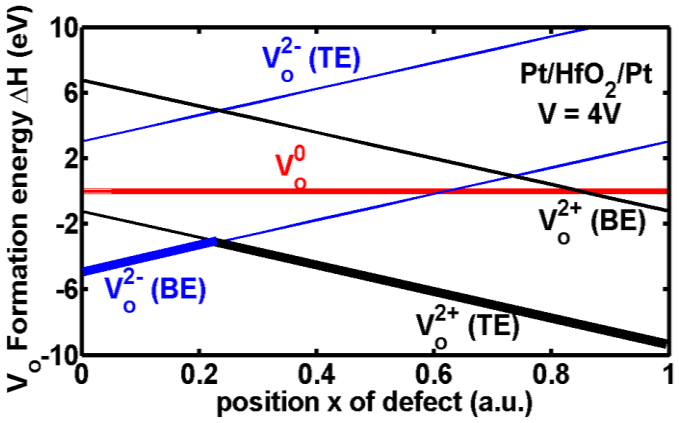

FigV.29. V_o charge states under an external polarization of 4 V in Pt/HfO_2/Pt.

So far we have looked at V_o transitions under an applied field which provides information about possible electron transport mechanism in RRAM via a process like trap assisted tunneling (TAT). We did not investigate V_o^{+q} to $V_o^{+q'}$ (trap to trap) transitions which could also be interesting [24]. However, Hf-O bond breakage is necessary during the forming operation and FP formation was assumed as an important ingredient (prototype) for this process. Therefore treatment of FP out of equilibrium as we have thus far done with V_o can be very useful in deepening our insight on the CF formation. FigV.30 shows extended FP formation in TiN/HfO_2/Ti RRAM (see FigV.20 section V.3.2.1) under an applied voltage of 2V. In this process, FP (V_o^{2+} + O_i^{2-}) is first formed in HfO_2 and we assume that the formed O_i^{2-} further reacts with Ti involving some energy gain (Ti being reactive with O) by leaving the oxygen vacancy in HfO_2 as shown in FigV.20. The results show that FP^{2-}(BE) (V_o^0 + O_i^{2-}) is favorably more pronounced over the entire range between BE and TE with the scenario being most favorable close to Ti TE. Nevertheless, the energy of probable FP^{2-}(BE) formation is positive from BE up to very close to TE. This energy may become negative if the formed O_i^{2-} reacts with Ti (O reactivity with Ti induces an energy gain of around 6 eV).

As for FP^{2+}(TE) (V_o^{2+} + O_i^0), its formation in TiN/HfO_2/Ti during the CF formation seems very unlikely due to its high energy.

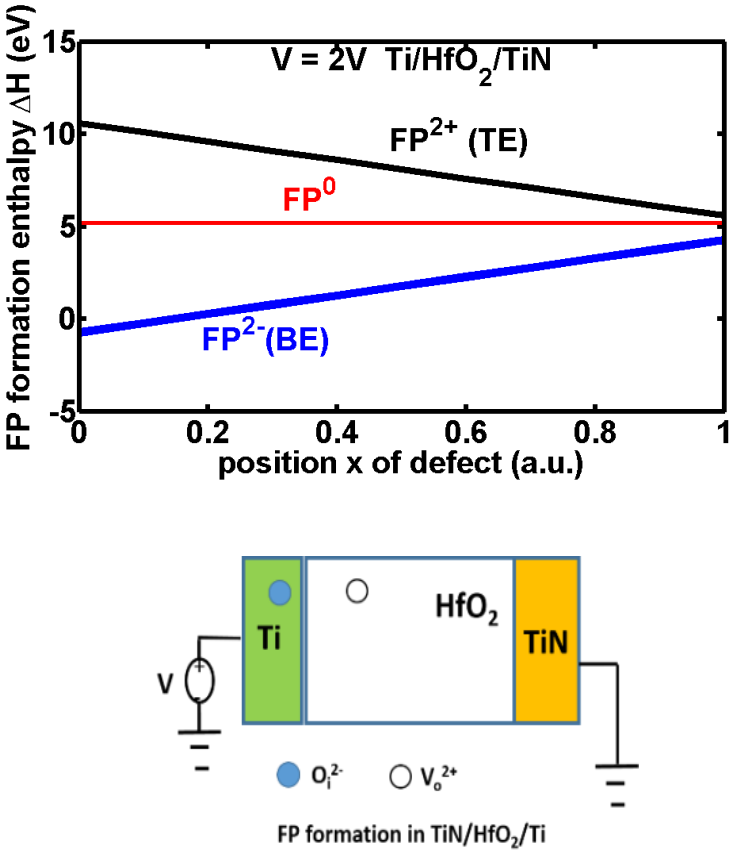

FigV.30. FP states in TiN/HfO_2/Ti under an external applied voltage of 2 V.

With regards to the forming process, the Hf-O bonds breakage probably formed via electron injection can be summarized as follows:

At TiN (BE):

$$\boldsymbol{HfO_2 - 2e_{TE}^- \rightarrow HfO_2\{FP = O_i^0 + V_o^{2+}\}} \qquad \textbf{(V.13)}$$

where $HfO_2\{FP\}$ is HfO_2 with FP formed inside it and e_{TE}^- electrons injected into TE.

At Ti (TE):

$$\boldsymbol{HfO_2 + 2e_{BE}^- \rightarrow HfO_2\{FP^{2-} = O_i^{2-} + V_o^0\}} \qquad \textbf{(V.14)}$$

$$\boldsymbol{HfO_2\{FP^{2-}\} + Ti \rightarrow Ti{:}O + HfO_2\{V_o^0\} + 2e_{TE}^-} \qquad \textbf{(V.15)}$$

With O incorporation into Ti involving some energy gain[4] (of approximately > 5 eV) and e_{BE}^{-} electrons being injected from BE.

$\boldsymbol{Ti:O}$ are the $\boldsymbol{O_i^{2-}}$ ions that migrated to Ti forming some TiO_x interface with the $2e^-$ injected into TE leaving behind neutral oxygen vacancies as shown in FigV.31a. The neutral V_o are immobile due to their high diffusion barrier (2.2 eV) and form a virtual anode that essentially shrink the effective oxide layer thickness. This stage corresponds to the initial phase of the forming operation and the first Hf-O bonds start breaking at Ti/HfO_2 interface due to low O diffusion barrier at that interface (~1.5 eV). By keeping the voltage application, new V_o and O_i pairs are formed under increasing electric field due to the oxide shrinking with the widening of the virtual anode following the same process as described in equations (V.12 to V.15) as shown in FigV.31b. The CF keeps growing from the new virtual anode until it connects the Ti and TiN through the creation of a conductive path (FigV.31c, d). In FigV.30, we observe that FP^{2+} are rarely expected/formed in $TiN/HfO_2/Ti$ due to their higher formation enthalpy and as such they do not contribute significantly in CF formation.

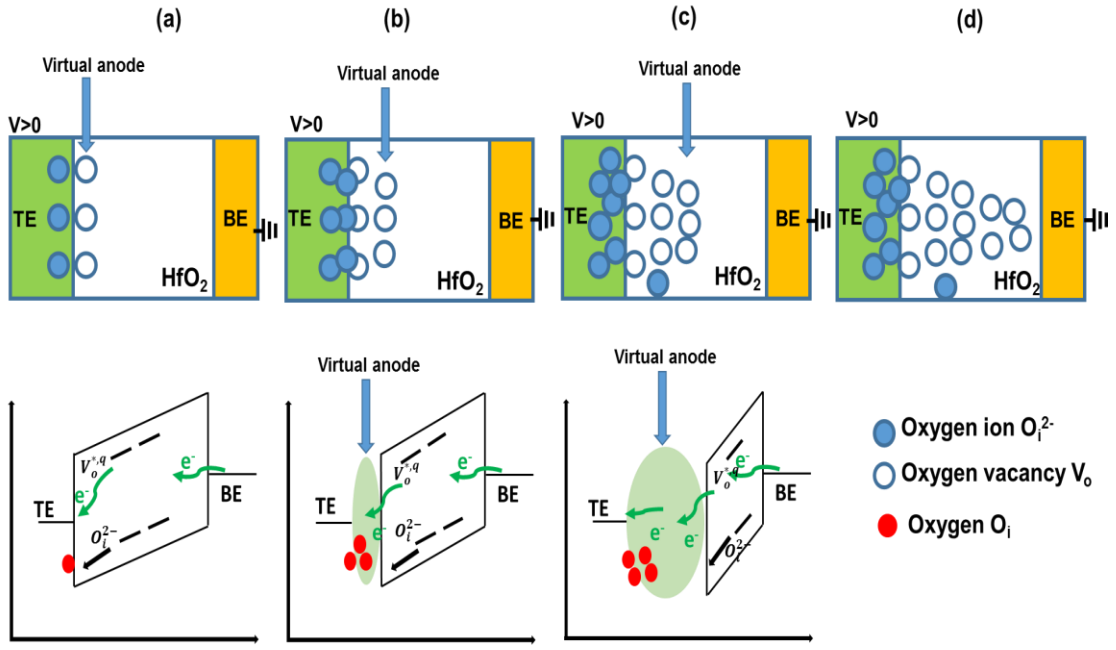

FigV.31. CF formation model for $TiN/HfO_2/Ti$ RRAM. (a) First bonds start to break at the TE/oxide interface leaving behind a V_o rich region forming a virtual anode. The O ions migrate to the interface Ti TE region (b) new Hf-O bonds are broken close the virtual anode due to increasing electric field (c) The moving virtual anode gets closer to BE and new bonds are broken due more intense field. (d) The CF is finally formed connecting TE and BE.

[4] There is an energy gain of 6.3 eV for removing oxygen from HfO_2 leaving behind a vacancy and inserting the removed O into Ti instead of going into molecular O_2. A more rigorous treatment would involve calculating the energy cost of inserting O_i^{2-} into Ti. Since Ti is a metal, this latter case is difficult to evaluate within DFT.

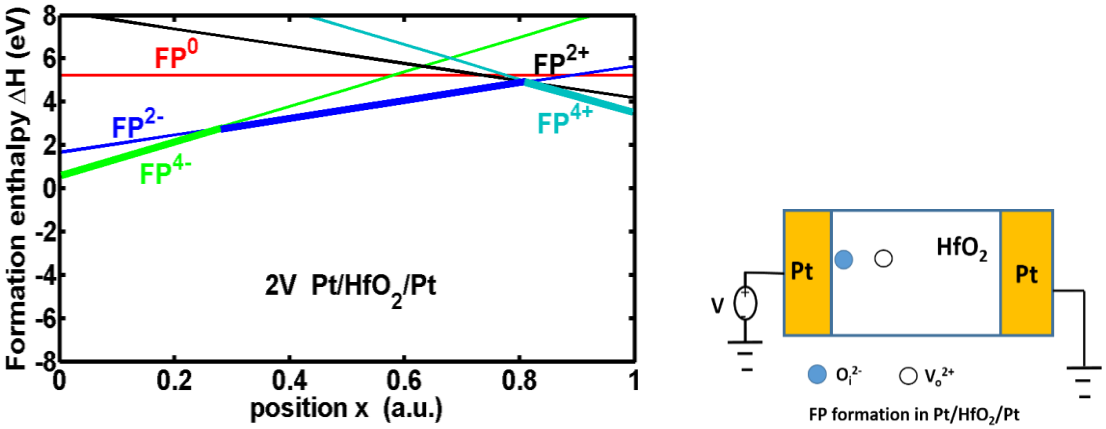

FigV.32. FP states in Pt/HfO_2/Pt under an external applied voltage of 2V.

FigV.32 shows the transitions of FP states in Pt/HfO_2/Pt stack under an applied voltage of 2 V. Since Pt is an inert metal and non-reactive with O, we assumed both O_i and V_o forming FP to remain inside the HfO_2 layer or eventually some O_i going to Pt/HfO_2 interface. Despite the positive energy for all the FP states, we observe that close to TE (x=0), $FP^{4-}(V_o^{2-} + O_i^{2-})$ is more pronounced with probably longer transition time. This changes to $FP^{2-}(V_o^{0} + O_i^{2-})$ midway and finally becomes $FP^{4+}(V_o^{2+},O_2)$ close to BE (see below for O_2 formation). We did not include other transitions in the graph in order to keep it clearer. But we should keep in mind that FP^{4-} close to TE may lose its e^- and become FP^0 $(V_o^{2+} + O_i^{2-})$. The same is true for FP^{2-}. Contrary to TiN/HfO_2/Ti, 2V was not sufficient to form 10 nm Pt/HfO_2/Pt devices and higher voltage (>4V) was necessary. FigV.33 shows FP transition states in Pt/HfO_2/Pt at 4V and we observe that the transient stability regions of both FP^{4-} and FP^{4+} have increased compared to FigV.32 and FP^{2-} disappeared midway at 4V. It seems that transient FP^{2-} $(V_o^{0} + O_i^{2-})$ or FP^{4-} $(V_o^{2-} + O_i^{2-})$ did not allow the stability of CF formation at TE due to the recombination of O_i^{2-} and V_o^{2+} after injecting electrons to TE. However, by the continuous application of voltage up to 4V and more, FP^{4+} becomes more pronounced over a larger part of the dielectric layer (from BE to close to midway) which may result in the formation of O_2 following [25] [26] [27]:

At Pt (TE):

$$\boldsymbol{HfO_2 + 4e^-_{BE} \rightarrow HfO_2\{FP^{4+} = O_i^{2-} + V_o^{2+} + 4e^-_{BE} = O_i^{2-} + V_o^{2-}\}} \quad \textbf{(V. 16)}$$

At Pt (BE):

$$\boldsymbol{HfO_2 - 4e^-_{TE} \rightarrow HfO_2\{FP^{4+} = O_o^{2-} + O_i^{2-} - 4e^-_{TE} + V_o^{2+} = O_2 + V_o^{2+}\}} \quad \textbf{(V. 17)}$$

Since the system is out of equilibrium, the eventual formation of FP^{2+} could also lead to peroxide O_2^{2-} formation following:

$$HfO_2 - 2e_{TE}^- \rightarrow HfO_2 \left\{ FP^{2+} = O_o^{2-} + O_i^{2-} + V_o^{2+} = O_2^{2-} + V_o^{2+} \right\} \quad \textbf{(V. 18)}$$

From our understanding, it is the formation of these O_2 or O_2^{2-} that stabilize the CF formation in Pt/HfO_2/Pt devices. Therefore, this indicates that CF formation in Pt/HfO_2/Pt probably starts at the bottom electrode Pt with the first temporary formation of complex O_2^{2-} or O_2 allowing for CF stability (FigV.34) while V_o^{2+} migrate towards BE. Due to the applied field the temporary O_2^{2-}/O_2 may gain electrons from BE to make them migrate in the form of O_i^{2-} ions towards the TE. By reaching the TE, the O_i^{2-} ions probably accumulate over that interface in the form of O_2^{2-}/O_2 after injecting their e^- to TE.

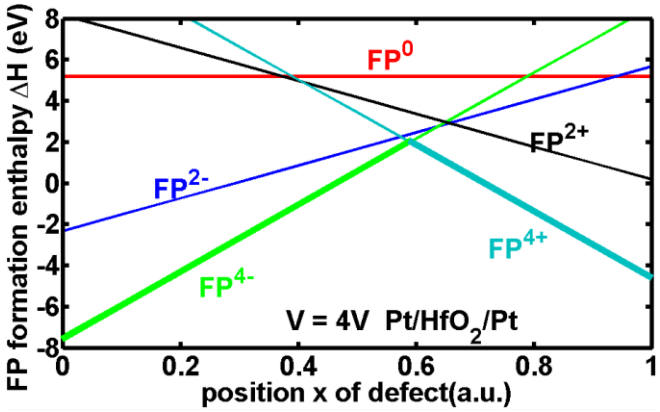

FigV.33. Stability of FP in Pt/HfO_2/Pt under an external applied voltage of 4V.

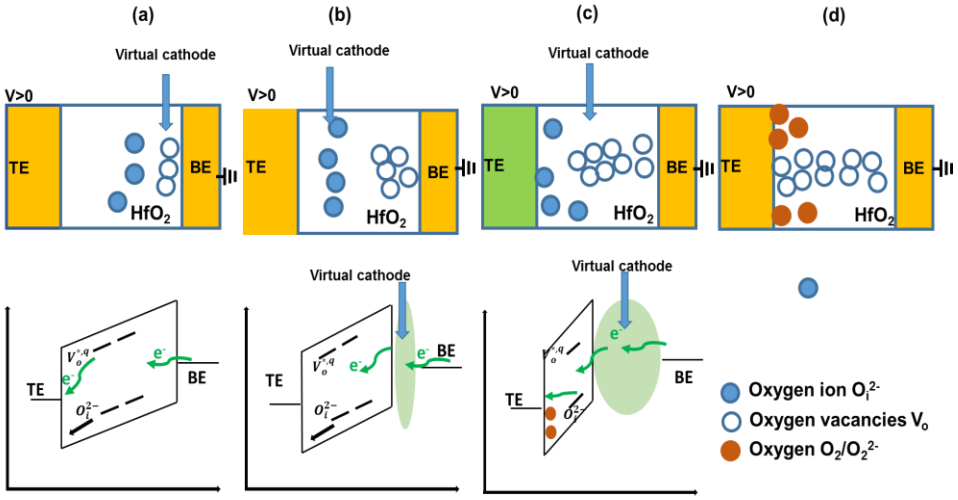

FigV.34. CF formation model for Pt/HfO_2/Pt RRAM. (a) First bonds start to break at the BE/oxide interface leaving behind a V_o rich region forming a virtual cathode. The O ions migrate to the interface Pt TE region (b) new Hf-O bonds are broken close to the virtual cathode due to increasing electric field (c) The moving virtual cathode gets closer to TE and new bonds are broken due more intense field. O_i^{2-} close to TE lose their e^- and become complex O_2^{2-} complex or O_2 (d) The CF is finally formed connecting BE and TE.

PART II: GB, Hf suboxides and CF composition

V.5 Role of grain boundaries (GB)

Since GBs correspond to spots in the oxide where different lattices mismatch in especially polycrystalline films, one may suspect that those spots are potential weak points in the oxide where bond breakage may start or be enhanced. We studied coincident lattice site (CSL) type of GB in a joint work with Xue et al. [28] by assuming cubic HfO_2 and was shown in Chapter II. In most HfO_2 thin films used in RRAM, HfO_2 phases that are identified are monoclinic or orthorhombic [29] under normal ALD deposited HfO_2 at 300°C to 350°C. In order to approach these real experimental phases, we used the same CSL structure of [28] and allowed it to fully relax in all the direction (minimize forces and stresses). The obtained HfO_2 structure after full relaxation is shown in FigV.35. The supercell contains 360 atoms and the GB region has only 3-fold and most interestingly 2-fold coordinated O atoms. The atomic configurations in the bulk of the supercell have orthorhombic/monoclinic like structure which makes the model more realistic. FigV.36 compares the DOS of m-HfO_2 to HfO_2 with GB and shows that the GB model remains an insulator and its band gap is slightly reduced due to under-coordination consistent with the results of Xue et al. [28]. To consider defects formation in HfO_2 with GB, we considered the 2-fold oxygen vacancy (V_{o2}) in GB, the 3-fold coordinated O vacancy (V_{o3}) in GB and V_{o3} inside the bulk. Their formation energies summarized in TableV.6 are calculated using the following:

$$\Delta \boldsymbol{H^{Vo}} = \boldsymbol{E^{Vo}_{tot\_GB}} - \boldsymbol{E^{HfO_2}_{tot\_GB}} + \boldsymbol{\mu_o} \quad \textbf{(V.19)}$$

where $\boldsymbol{E^{Vo}_{tot\_GB}}$ is the energy of the HfO_2 supercell with GB containing V_o, $\boldsymbol{E^{HfO_2}_{tot\_GB}}$ the energy of the HfO_2 supercell with GB and μ_o oxygen (O) chemical potential defined as half of O_2 molecule and 1.36 eV per O_2 correction was used [13]. The formation energy of V_{o3} at GB and in bulk of HfO_2 are similar in this model (7.0 eV). The fact that V_{o3} formation energy in bulk of the GB model is very similar to what we have previously calculated for m-HfO_2 (7.1 eV) support our finding that our HfO_2 model with GB have more orthorhombic/monoclinic configuration in its bulk. For V_{o2}, the formation energy

is almost 2 eV lower than for V_{o3} or V_{o4} formation energy. This indicates that low coordinated O atoms in GB of HfO_2 or at interfaces may be precursors for the CF formation in RRAM. This is in agreement with the results of Lanza et al. [30] and Bersuker et al. [31] concerning the ease of CF formation along GBs.

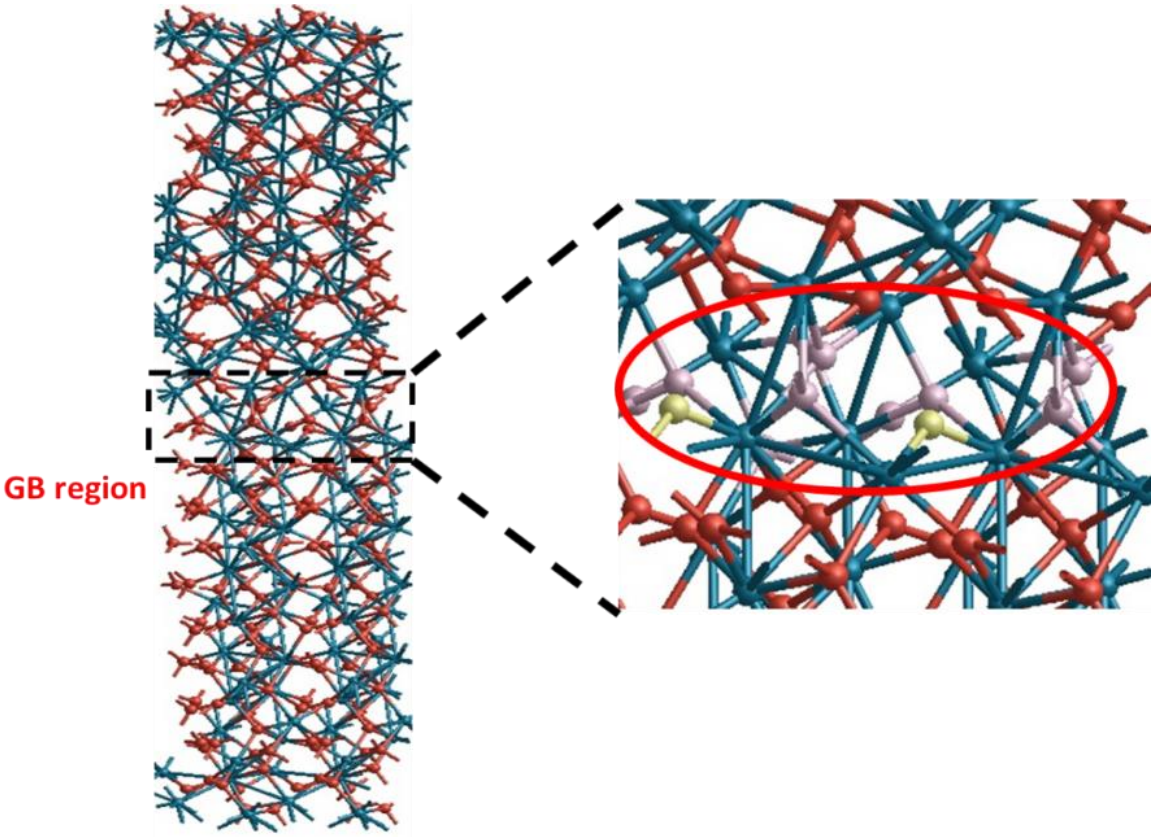

FigV.35. HfO_2 with GB derived from the CSL model of [28]**. The colored atoms in the red circle highlight the low O coordination in GB.**

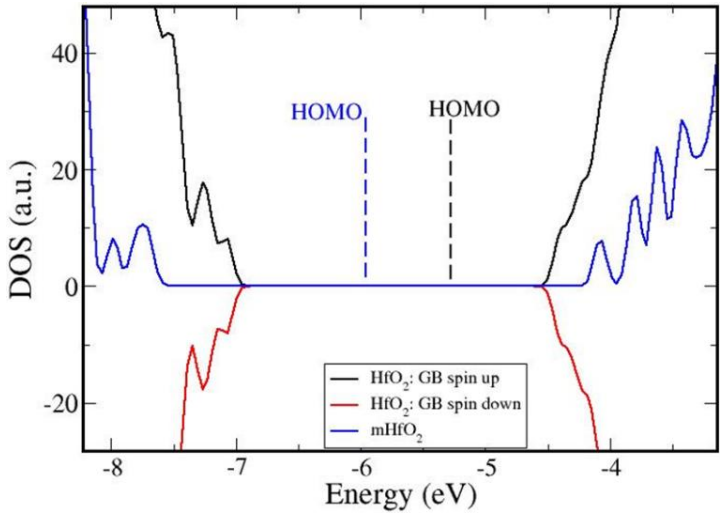

FigV.36. DOS of HfO_2 with and without GB. HfO_2 with GB presents a reduced gap.

Neutral V_o with GB model	Formation energy ΔH^{Vo} (eV)
V_{o2} in GB	5.6
V_{o3} in GB	7.0
V_{o3} in bulk	7.0

TableV.6. Formation energies of V_o in HfO_2 model with GB.

V.6 CF rupture: RESET

The RESET operation involves the rupture of CF by bringing the devices to high resistance state. FigV.37 shows the model we propose for bipolar RESET operation which attributes the CF rupture to a two-step process: (1) the migration of O_i from TiO_x layer to V_o rich HfO_y region (2) the recombination of oxygen ions (O_i^{2-}) and oxygen vacancies (V_o^{2+}).

With the negative voltage applied to TE cathode, we have:

$$\boldsymbol{TiO_x + HfO_y \rightarrow TiO_x\{V_o\} + HfO_y{:}O_i} \qquad \textbf{(V.20)}$$

Where $\boldsymbol{TiO_x\{V_o\}}$ represents O_i that migrated from $\boldsymbol{TiO_x}$ by leaving behind a vacancy and $\boldsymbol{HfO_y{:}O_i}$ is the V_o rich HfO_y CF with the O_i that migrated from TiO_x. At the beginning of the RESET stage, HfO_y is a conducting medium which imposes its local Fermi level and is less sensitive to the field. One can also observe from the RESET curves that globally current increases linearly with voltage during the initial RESET stage (FigV.38). As the voltage increases, O_i move from TiO_x to HfO_y and HfO_y becomes more and more O rich until the concentration of V_o in HfO_y becomes lower than a certain threshold. At this point, HfO_y becomes more sensitive to the field.

At BE anode with V_o near it:

$$\boldsymbol{V_o^0 \rightarrow V_o^{2+} + 2e_{BE}^-} \qquad \textbf{(V.21)}$$

And

$$\boldsymbol{HfO_y + V_o^{2+} + O_i^{2-} \rightarrow HfO_z\,;\ y < z} \qquad \textbf{(V.22)}$$

With negative bias applied to TE which is acting as cathode during RESET, neutral oxygen vacancies near the anode (BE) inject their electrons to it and become charged (V_o^{2+}). These V_o^{2+} are mobile with relatively low diffusion barrier (0.9 eV) and migrate opposite the field. However, O_i^{2-} are more mobile than V_o^{2+} because of their much lower diffusion barriers (~0.2 eV with y approaching 2 in HfO_y) and approach BE faster than V_o^{2+} may approach TE and they recombine in regions close to BE where the filament size is smaller. The rupture of CF at its thinnest region is consistent with the quantum point contact (QPC) model which assumes the rupture of CF at its constriction [32]. In a more rigorous treatment of RESET process, the nature of HfO_y forming the CF in terms of kinetics of O through it will essentially help determine where the CF gets ruptured. Hence, this recombination process is not spontaneous because the O_i^{2-} ions have to migrate through the V_o rich CF region of type HfO_y.

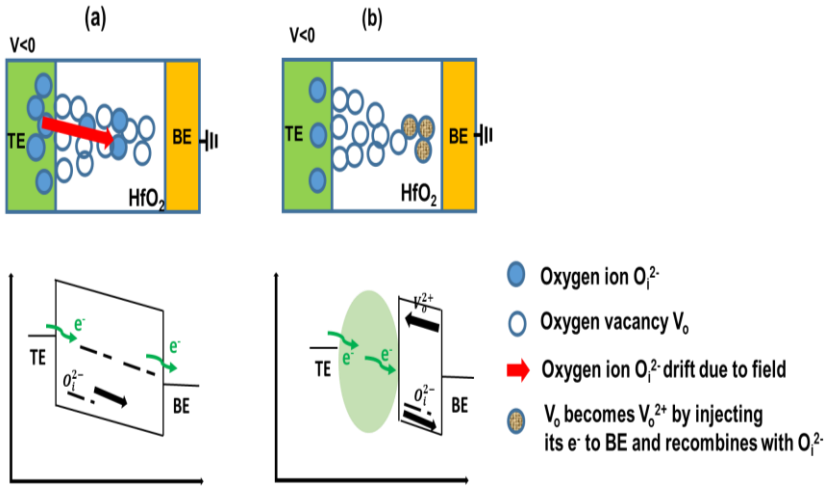

FigV.37. CF rupture model during bipolar RESET.

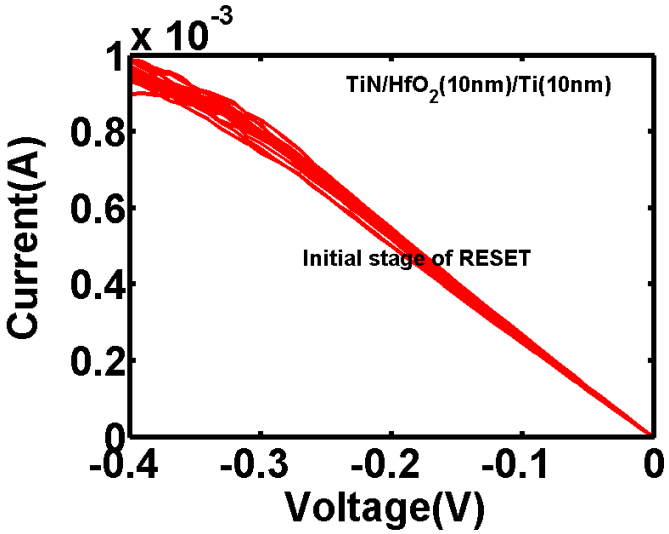

FigV.38. Initial stage of RESET for bipolar TiN/HfO2/Ti RRAM showing globally a linear trend of the current vs. voltage curves. The Y scale is linear.

For unipolar devices where in general non-reactive and symmetrical electrodes are used as top and bottom electrodes, the O ions do not have preferential sites at either BE or TE to form interfacial oxidized layer. Temperature is generally used as a parameter that helps initiate the thermal dissolution of CF [33]. It is probably true, but at this stage we do not have clearer understanding about how the RESET process is triggered for unipolar devices. Nevertheless, for these devices the O ions seem to recombine with V_o in a more abrupt process resulting in CF rupture with higher resistance values compared with bipolar RRAM devices (Chapter III: section III.3.1).

V.7 CF reconstruction: SET

The SET process is similar to the forming step in terms of the formation of a continuous conduction path between BE and TE. However, the main difference lies in the fact during the forming operation new Hf-O bonds breakage was necessary while in SET only O ions that have recombined with V_o during RESET need to be moved out of the CF region. FigV.39 shows the model we propose for the SET operation. By applying positive voltage to TE, the O ions that recombined with CF at its constriction (tip) migrate back to it and subsequently results in CF reconstruction. During SET, only few ions are involved which explains the lower voltage involved in the process compared to forming. Also the fact that the oxide is already defective with the portion of the remaining CF after RESET explains the higher current (more than 4 orders of magnitude) during the pre-SET stage compared to the pre-forming one ($R_{pristine} > 10^9$ Ohm vs. $R_{off} \sim 10^4$-10^5 Ohms).

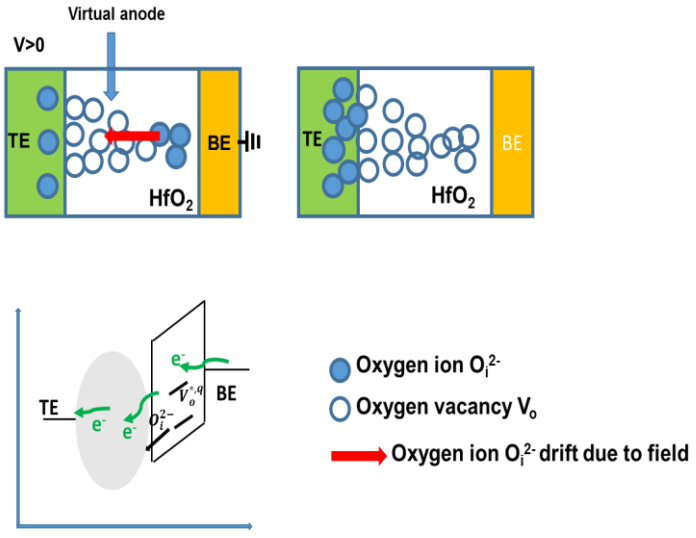

FigV.39. CF reconstruction model during SET.

V.8 CF composition/nature

V.8.1 HfO_x filament

We understand from the CF formation/rupture models described above that it is an oxygen deficient region (rich of oxygen vacancies). However, the above treatment did not provide any indication about how this O deficient region may look like. The topic is challenging and there are many open questions whether this O deficient CF is purely/essentially metallic Hf [34], a chain of oxygen vacancies inducing a conduction channel [35] [36], hafnia sub-oxides (HfO_x) [37] or a mixture Hf sub-oxides and metal ions from the TE (Ti for example). At this point, most of the hypotheses about CF composition are receivable due to the lack of clear cut experimental evidence about its nature to resolve the issue and the sensitivity of CF to experimental conditions (voltage ramp, voltage pulse, high current, low current etcetera). However, thermodynamic consideration about the stability of the different Hf sub-oxides against metal Hf can provide insightful indication about the composition of CF and what it could potentially be. This is the approach that we adopted in this work. TableV.7 summarizes the HfO_x suboxides that we investigated along with their associated space groups. When we could not find a specific sub-oxide in the literature, we constructed it ourselves by running several relaxations until a minimum energy configuration was found.

HfO_x suboxide	Space group	Reference
Hf_4O	-	-
Hf_3O	$P\bar{3}1c$	[38]
V_o^{2+}	$P\bar{3}1m$	[38]
HfO	P-62m	[39]
Hf_2O_3	P-4m2	[37]
Hf_4O_7	-	[37]
HfO_2	$P2_1/c$	[37]

TableV.7. Studied HfO_x sub oxides with their space groups.

Our thermodynamic ensemble assumes an Hf filament surrounded by HfO_2 and we evaluate its stability against other Hf sub oxides as described in the following reaction:

$$(n - \frac{m}{2})Hf + (\frac{m}{2})HfO_2 \rightarrow nHfO_{m/n} \qquad \textbf{(V.23)}$$

The formation enthalpies ($\Delta H_{suboxide}$) of the sub oxides from the above equation are shown in FigV.40 in which $x = \frac{m}{n}$. Our calculations show that the formation of Hf filament is not stable and drifts towards Hf_4O-Hf_3O sub oxides with probably some HfO spots as well. The existence of a homogenous filament with one specific HfO_x seems to be very unlikely. The filament region is probably a mixture of different HfO_x which are slightly oxidized with the predominance of Hf_4O-Hf_3O compositions surrounded by an HfO_2 matrix.

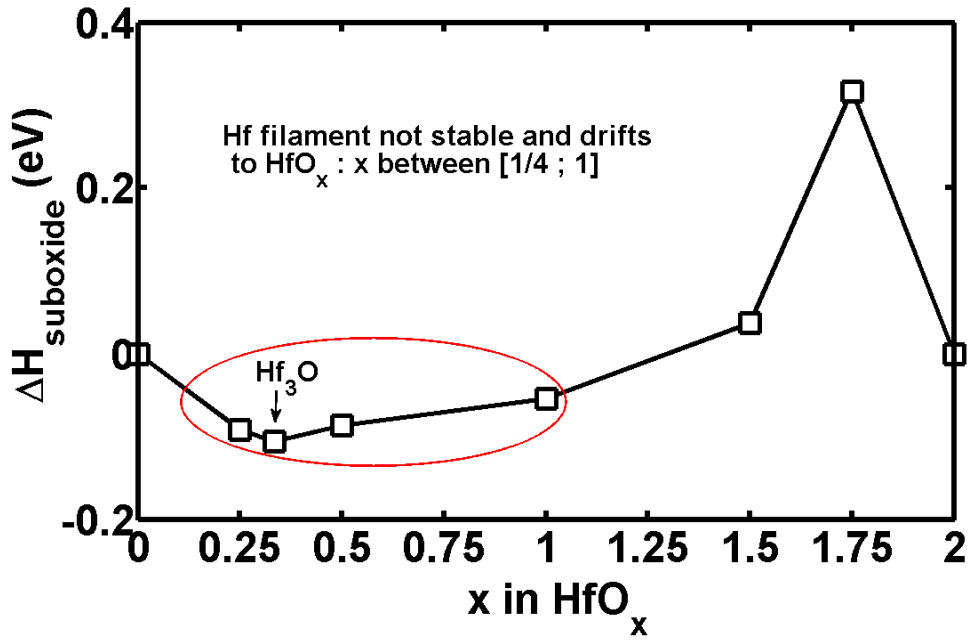

FigV.40. Stability of Hf filament surrounded by HfO_2. Hf filament is not stable and drifts towards Hf_4O-Hf_3O sub oxides.

Since Hf_3O emerges as a probable composition of the CF region, we investigated its oxidation and searched for possible Hf sub oxides that could potentially form the ruptured CF region after RESET. This is achieved by injecting the same amount of O atoms to Hf_3O as a way of modelling RESET through the following equation:

$$\left(\frac{1}{3x-1}\right)Hf_3O + \frac{1}{2}O_2 \rightarrow \left(\frac{3}{3x-1}\right)HfO_x \qquad \textbf{(V.24)}$$

FigV.41 shows the oxidation of Hf_3O and few interesting points can be observed. The ruptured region may form HfO suboxides and eventually HfO_2 with continuing injection of O into the filament. The energy difference between Hf_2O and HfO is not very important which indicates that the ruptured Hf_3O CF region form HfO_x

suboxides that are similar to itself with $1/2 \leq x \leq 1$ surrounded by HfO_2 patches. The mixture of HfO_x in the ruptured CF region is further enhanced by the non-control of current during the RESET operation. Hf_2O_3 as ruptured CF region seems unstable/improbable and even if it could form it would eventually decompose into HfO + HfO_2. In any case, the results show that Hf_4O_7 would not form the ruptured CF region at all. However, the existence of unstable phases during RRAM switching operations cannot be completely excluded because of their occurrence under non-equilibrium conditions. This may explain the origin of intrinsic variability of the high resistance state in RRAM. The possibility of forming different HfO_x in the ruptured CF region during different switching cycles induces intrinsic variability in the switching resistance.

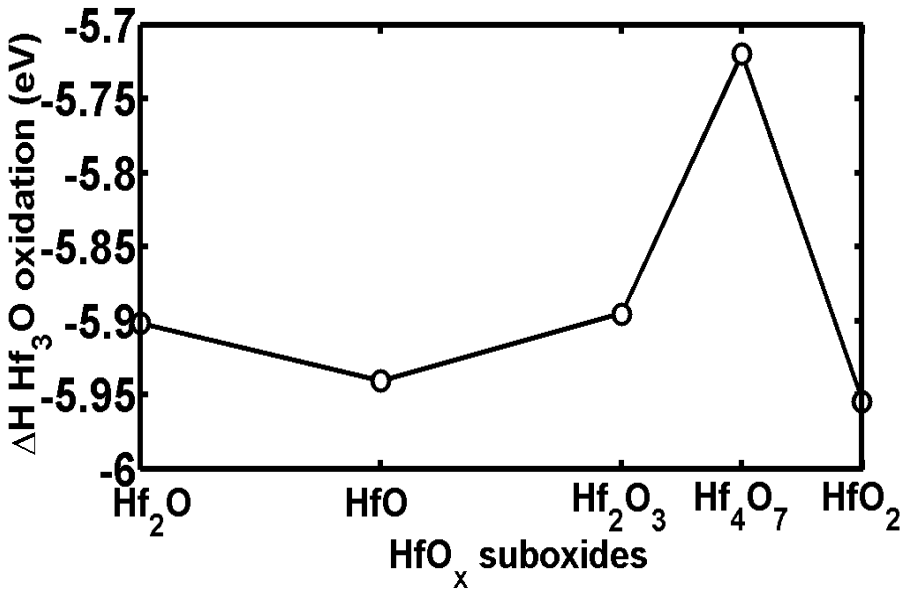

FigV.41. Hf_3O filament oxidation.

The location of the ruptured region depends on the kinetics of O_i in HfO_x forming the CF. FigV.42 shows the results of O diffusion barriers that were calculated in some of the suboxides. These barriers are not exhaustive and only short range diffusion was considered. A more complete study would involve long range diffusion in different directions. Nevertheless, the results suggest that the less oxidized is HfO_x, the lower is the diffusion barrier of O_i. The trend is somehow broken at HfO and this could probably suggest that other directions for O_i migration would need to be considered for rigorous conclusion. But, it could also mean that HfO_x forming the CF region is probably Hf_3O/Hf_4O rather than HfO. For CF rupture, one may then imagine O_i diffusing in HfO_2 like region surrounding the CF to recombine with it closer to the BE

under the applied field (FigV.43b). It is also possible that current flowing though CF during the RESET enhances the O_i diffusion in Hf_4O/Hf_3O like filament and allowing it to rupture the CF at its constriction close to BE (FigV.43a). Only exhaustive diffusion study of O_i in HfO_x surrounded by HfO_2 could help draw stronger conclusions.

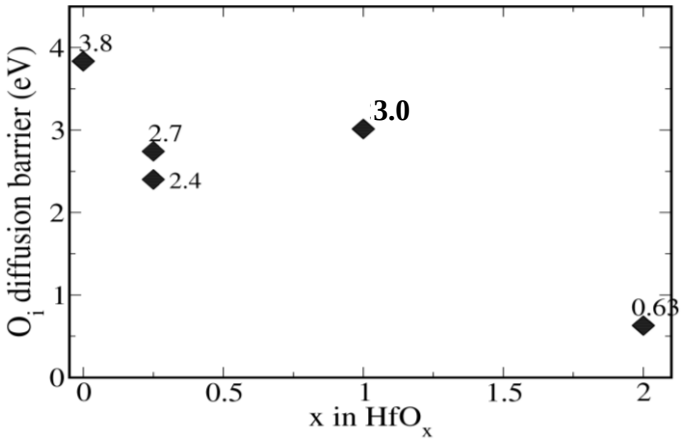

FigV.42. O_i diffusion barriers in HfO_x.

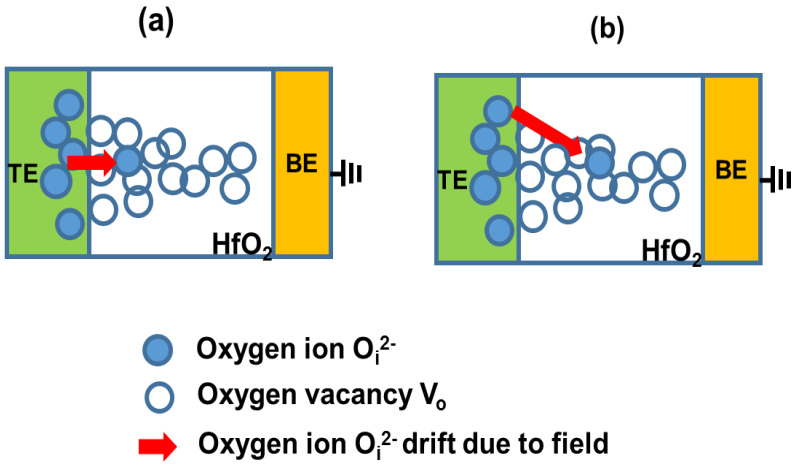

FigV.43. Possible O_i migration path during RESET (a) O_i diffusing through HfO_x to CF constriction (b) O_i diffusing along CF in HfO_2 region like towards CF constriction.

V.8.2 Possible Ti in the conductive filament

Many bipolar RRAM devices have Ti as top electrode as it is the case in this study. In our discussion about RRAM, the role of Ti has been viewed in only one direction that is, its reactivity with oxygen and its role as a buffer layer for O by forming TiO_x at the Ti/HfO_2 interface. Forming operation in RRAM occurs at relatively high voltages, quite often with relatively higher compliance current, and the possible presence of Ti in the CF may not be completely excluded. We studied this case by looking at the formation energy of Ti in perfect HfO_2 supercell, HfO_2 supercell with an oxygen vacancy, HfO_2 supercell with 4 V_o, HfO_2 with the GB model developed above

and the migration barrier of Ti in HfO_2. The formation energies of the different cases, shown in FigV.44 and summarized in TableV.8, were calculated using:

$$\Delta H^{Ti,\pm q} = E_{tot}^{Ti,supercell,\pm q} - E_{tot}^{supercell} + \mu_{Ti} \pm q(E_{VB} + E_F) \quad \text{(V.25)}$$

where $E_{tot}^{Ti,supercell,\pm q}$ the total energy of HfO_2 supercell containing Ti at charge $\pm q$, $E_{tot}^{supercell}$ total energy of the supercell without Ti, E_{VB} and E_F are defined respectively as the top of the valence band (VB) and the Fermi level measured from VB to CB of HfO_2. μ_{Ti} is the Ti chemical potential taken as relative to hcp-Ti.

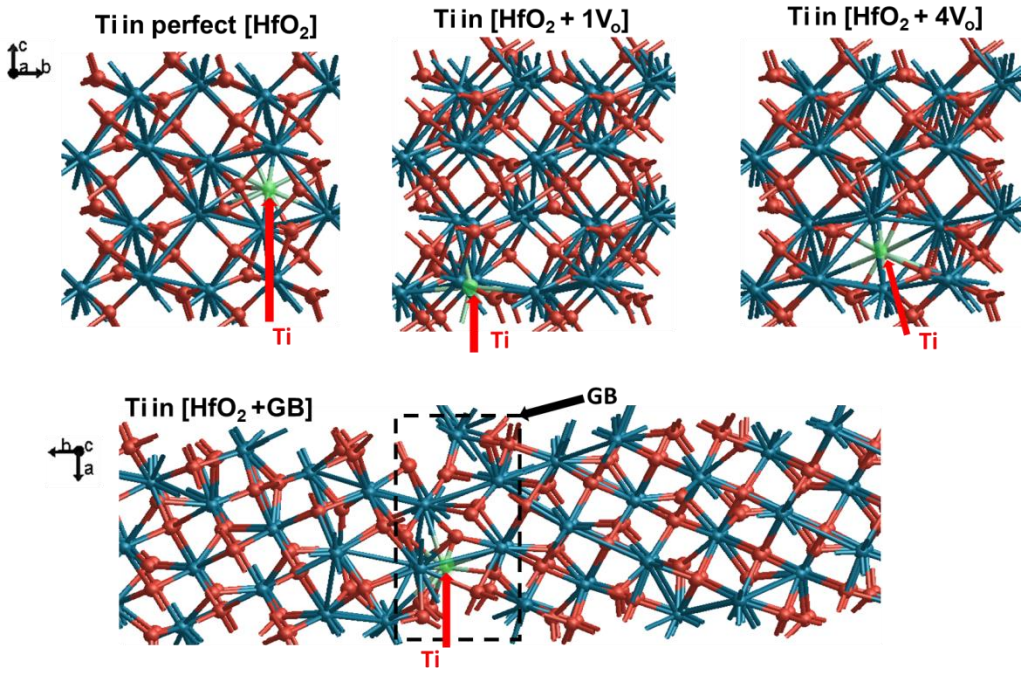

FigV.44. Optimized HfO_2 structures with Ti incorporation.

Model	Formation energy ΔH^{Ti} (eV)
Ti in perfect [HfO_2]	3.0
Ti in [HfO_2 + 1V_o]	2.4
Ti in [HfO_2 + 4V_o]	1.5
Ti in [HfO_2 + GB]	0.2

TableV.8. Formation energy of Ti in different HfO_2 models.

The formation energy ΔH^{Ti} of incorporating Ti into HfO_2 is relatively high (3 eV). However, when V_o defects are added into the HfO_2 supercell, ΔH^{Ti} decreases and this could be partly attributed to the lowering of the supercell stress with increasing V_o concentration, thus facilitating Ti incorporation. Nevertheless, the high formation energy of the different cases (> 1.5 eV) despite the presence of pre-defects indicates that the incorporation of Ti into HfO_2 cell is not favorable. For the special case of Ti incorporation into grain boundary of HfO_2, ΔH^{Ti} becomes close to zero (0.2 eV) (see section V.5 for the GB model investigated earlier). This is consistent with the results of Xue et al. [28] where the incorporation energy of Ti into the grain boundary of CSL cubic HfO_2 GB model was -0.16 eV. The difference in the two energies may be explained by the difference between the two GB models.

$\Delta H^{Ti,\pm q}$ for the incorporation of Ti into pure HfO_2 at different charge states is also calculated with respect to the Fermi level as shown in FigV.45. When the Fermi level is close to VB, the formation energy of Ti^{q+} becomes more negative with Ti^{+4} being the most favorable charge state. This scenario has to be considered mainly during the forming stage, because the applied voltage is much higher at forming operation than during SET/RESET, allowing for a sufficient barrier lowering. Therefore it is possible that Ti gets introduced into HfO_2 during forming via GB with the incorporated atoms probably remaining in place/immobile inside the dielectric layer during SET/RESET steps.

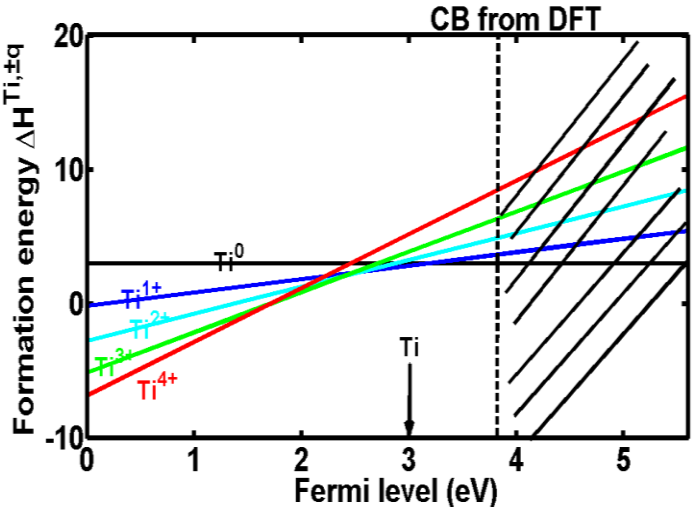

FigV.45. Formation energy of inserting Ti into mHfO_2 at different charge states with respect to the Fermi level.

In addition to $\Delta H^{Ti,\pm q}$, FigV.46 shows the DOS of the different cases tabulated in TableV.8. When Ti is inserted into HfO_2, defect states appear slightly above mid-gap

with HfO_2 remaining as insulator for cases A, B, and D. These levels are not accurate due to the band gap underestimation issue in DFT. For case C where Ti is incorporated into HfO_2 with $4V_o$, the HOMO level has finite states which indicate the emergence of some metallic/semi-metallic properties. These states may be able to carry some conduction current. The presence of extended defects like few aggregated V_o (like 4 V_o case here) or GB are expected in HfO_2 because the films are not perfect and the ALD deposition temperatures (300°C to 350°C) in RRAM applications are in general lower than the crystallization temperature of HfO_2. From thermodynamic consideration, these defects and the weak bonds at the Ti/HfO_2 interface may also facilitate the insertion of Ti into HfO_2.

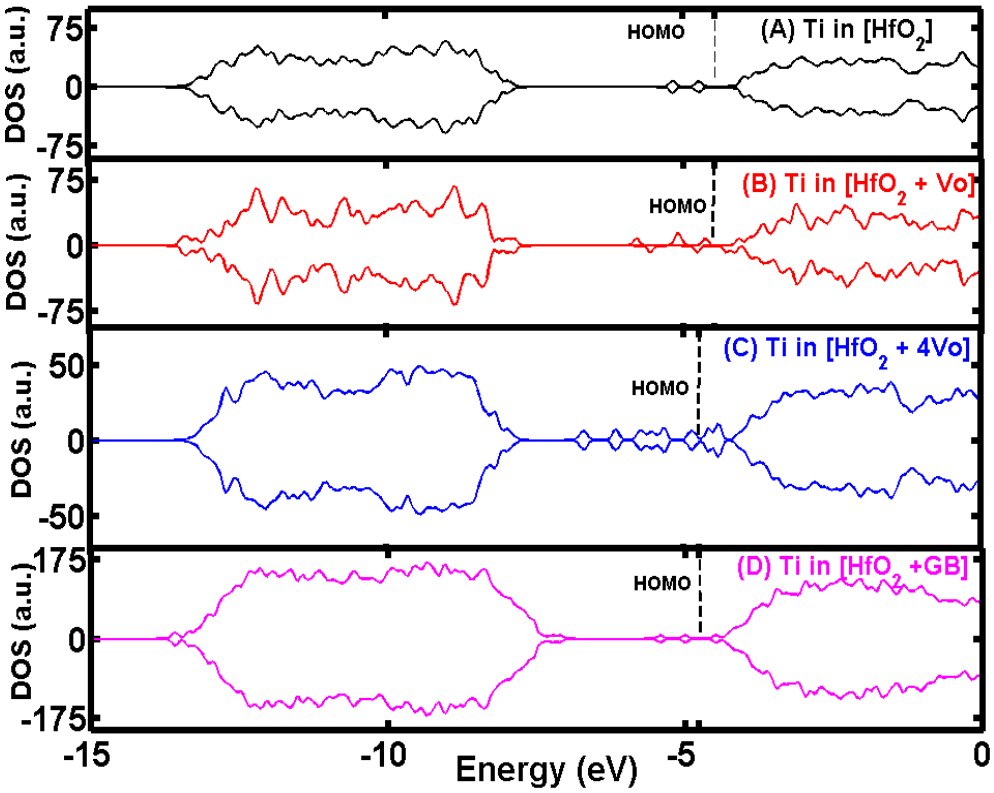

FigV.46. DOS of the different HfO_2 systems with Ti incorporation.

The migration of Ti in HfO_2 with V_{o3} was considered in order to have an idea about its diffusion barrier. The diffusing Ti atom was placed at the lattice position of the missing 3-fold coordinated O atom and was allowed to migrate to an interstitial position in HfO_2 (FigV.47). TableV.9 summarizes the diffusion results in both neutral and charged states.

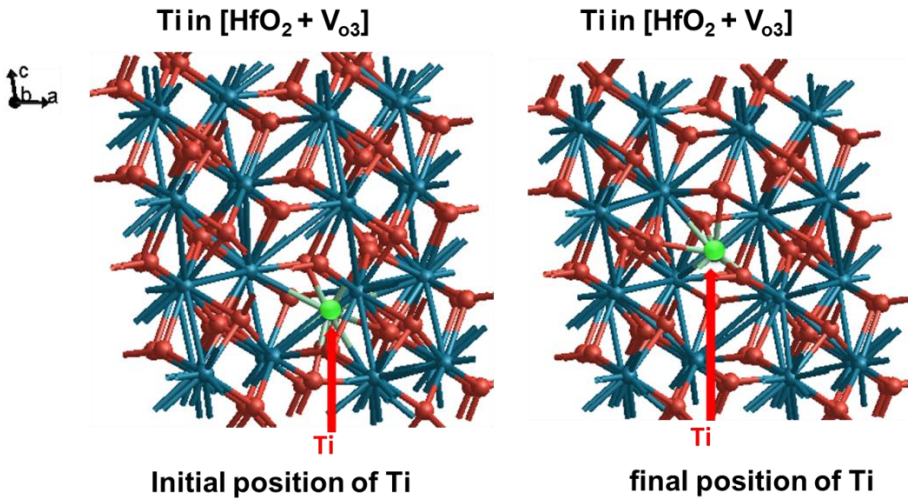

FigV.47. HfO_2 structures showing the initial and final positions considered for the Ti migration.

Ti charge state	Diffusion barrier (eV)
0	2.7
+2	2.9
+4	2.4

TableV.9. Diffusion barrier of neutral/charged Ti in HfO_2

The barrier for neutral Ti diffusion was calculated to be 2.7 eV and was reduced to 2.4 eV when Ti was charged +4. Ti does not seem to diffuse in its +2 state which presents the highest barrier of 2.9 eV. The 2.4 eV barrier may be overcome under the 2V to 3V forming voltages of TiN/HfO_2/Ti RRAM devices. Moreover, it is possible that this barrier becomes lower at the Ti/HfO_2 interface or GB near the interface. Hence, the diffusion of Ti into the CF of HfO_2 based RRAM when it is used as top electrode is a possible scenario. Indeed, the presence of Ti in the CF region has been experimentally proposed by Privitera et al. [40] working on TiN/HfO_2/Ti devices by using EELS STEM technique.

Our thermodynamic study of the CF composition did not take into account the possible presence of Ti in it because that would be very challenging. Also, the fact that we do not know what concentration of Ti to assume in the CF region would make the exploration even more difficult. At this stage, Ti in CF remains a possible case but we believe that the dominant defects making it up are oxygen interstitial and vacancies especially during SET/RESET when lower voltages are applied. Hopefully, clear experimental evidence with quantitative data on the composition of CF will see the day in the near future so as to confirm/infirm some of the theoretical predictions and shed

more light on its microscopic nature depending on the programming and set/reset conditions (voltages applied, compliance current, time scales).

V.9 Conclusions

The conductive filament formation in HfO_2 RRAM devices has been dealt with some detail. The stability of potential defects that may be at the origin of CF formation has been investigated. Oxygen interstitials have both low formation energies and low diffusion barriers and form complex O_2^{2-} in their neutral states. They are essentially inactive in terms of electronic conduction. However, some unstable neutral O_i present empty states inside HfO_2 gap which may contribute to the total current under fast transient switching conditions.

Neutral oxygen vacancies have higher formation energies (~7 eV) which are reduced with a combined effect of charge injection and with a reactive top electrode. Oxygen vacancies form defect states inside the gap that can serve as charge trapping centers. Neutral and negatively charged V_o have large diffusion barriers and are generally immobile. Charged V_o^{2+} have low diffusion barrier, their formation may be favorable with high work function electrodes.

Frenkel pairs formation and diffusion show that Hf-O bonds are stable and hard to break in pure monoclinic HfO_2. Their formation energy (4.9 eV - 5.2 eV) in neutral state is high. However this energy can be reduced by charge injection and reactive TE. Moreover, the results indicate their diffusion barrier as well as the generation of new FP could be helped by electron injection.

In addition to the point defects and extended FP, grain boundaries in HfO_2 also serve as weak spots where Hf-O bond breakage process could be facilitated. We saw that the GB region could have oxygen coordination as low as 2. These low oxygen coordination seem to be precursors for CF formation.

By combining the different scenarios that could help initiate Hf-O bond breakage process, a CF formation model was proposed which indicate that this formation in HfO_2 RRAM starts from the reactive TE/oxide interface by forming a virtual anode. This virtual anode grows from TE to BE under the applied field and ends up creating a conductive path. When inert electrodes are used as in $Pt/HfO_2/Pt$, we saw that CF formation probably starts from the BE by forming a virtual cathode. The RESET operation is attributed to the recombination of O_i^{2-} and V_o^{2+} at the point of filament where it is the thinnest.

The composition of the CF was investigated under thermodynamic equilibrium. The results show that the CF is probably an Hf sub oxide that could potentially be Hf_4O-Hf_3O. By assuming an Hf_3O as the filament and by injecting a constant amount of oxygen to it as an attempt to model RESET, a ruptured filament that would be HfO_x ($1/2 \leq x \leq 1$) surrounded HfO_2 or HfO_2 with continuous oxidation were obtained. The low energy differences between the sub oxides indicate that the ruptured CF region is probably non-homogenous and made up of a mixture of different sub oxides. This could explain the origin of intrinsic variability of R_{off} in RRAM.

The possible presence of Ti inside the CF region was looked upon and the results show that it is a scenario that cannot be excluded. Ti^{4+} ions have low formation energy with close to the valence band of HfO_2 and their diffusion into HfO_2 could be possible under the high voltages involved during forming operation only and/or at GB.

Our calculations highlight the crucial role of the electrode material choice especially the top electrode in RRAM operation. The results showed that depending on the reactivity of TE (Ti vs. Pt), not only the forming voltage changes but also the mechanisms of CF formation and its stability also change. Moreover, the energetics of defects, their charge states and diffusion barriers also change depending on the electrode material. Hence, one way of optimization of RRAM would be to continue working on the TE material through: its deposition condition by tuning its oxygen content (degree of oxidation, eg. TiO_x, $x \leq 1$), bi-layer electrodes (eg. Al/Ti), doping or alloying (TiSi, TiSe etc.).

One can see that there are many challenges involved in the process of understanding the microscopic phenomena involved in the resistive switching behavior of HfO_2 based devices. Electron transport through defects is difficult to describe because of quantum phenomena such as electron-defects coupling, electron-phonon coupling and so on which are beyond the scope of our DFT calculations. Our results give indications about processes that may be energetically favorable and some of the material optimization that could be explored. Further studies, especially a comprehensive view of the kinetics of defects in Hf-suboxides and optimization of the electrode material will surely help pave the way towards deeper understanding of RRAM.

References

[1] B. Traoré, P. Blaise, E. Vianello, H. Grampeix, A. Bonnevialle, E. Jalaguier et al., "Microscopic understanding of the low resistance retention in HfO_2 and HfAlO

based RRAM," *IEEE IEDM*, pp. 21.5.1 - 21.5.4, 2014.

[2] H. Takeuchi, D. Ha, and T.-J. King, "Observation of bulk HfO_2 defects by spectroscopic ellipsometry," *Jour. Vacuu. Scienc. Tech.*, vol. 22, 1337, 2004.

[3] J. Robertson, "High dielectric constant oxides," *Eur. Phys. J. Appl. Phys.*, vol. 28, pp. 265–291, 2004.

[4] H. Arashi, "Pressure-Induced Phase Transformation of HfO_2 ," *J. Am. Ceram. Soc.*, vol. 75, pp. 844 - 847, 1992.

[5] J. Kang, E.-C. Lee and K. J. Chang, "First-principles study of the structural phase transformation of hafnia under pressure," *Phys. Rev. B*, vol. 68, 054106, 2003.

[6] C. Zhao, G. Roebben, M. Heyns and Van Der Biest, "Crystallisation and Tetragonal-Monoclinic Transformation in ZrO_2 and HfO_2 Dielectric Thin Films," *key Eng. Mater.*, vol. 206-213, pp. 1285-1288, 2002.

[7] P. Hohenberg and W. Kohn, "Inhomogeneous electron gas" Phys. Rev., vol. 136, p. B864, 1964;W. Kohn and L. J. Sham, "Self-consistent equations including exchange and correlation effects", Phys. Rev., vol. 140, p. A1133, 1965,.

[8] J. Soler et al., "The SIESTA method for ab-initio order-N materials simulation," *J. Phys.: Condens. Matter*, vol. 14, pp. 2745-2779, 2002.

[9] N. Troullier and J. L. Martins, "Efficient pseudopotentials for plane-wave calculations," *Phys. Rev. B.*, vol. 43, pp. 1993-2006 , 1991.

[10] G. Henkelman, B. P. Uberuaga, and H. Jónsson, "A climbing image nudged elastic band method for finding saddle points and minimum energy paths," *J. Chem. Phys.*, vol. 113, p. 9901, 2001.

[11] S. R. Bahn and K. W. Jacobsen, "An Object-Oriented Scripting Interface to a Legacy Electronic Structure Code," *Comput. Sci. Eng.*, vol. 4, pp. 56-66, 2002.

[12] W. Tang, E. Sanville, and G. Henkelman, "A grid-based Bader analysis algorithm without lattice bias," *J. Phys.: Compute Mater.* , vol. 21 084204, 2009.

[13] L. Wang, T. Maxisch and G. Ceder, "Oxidation energies of transition metal oxides within the GGA+U framework," *Phy. Rev. B.*, vol. 73, no. 195107, 2006.

[14] J. X. Zheng et al., "First-principles study of native point defects in hafnia and zirconia," *Phys. Rev. B.*, vol. 75, pp. 104112-1–104112-7 , 2007.

[15] H. Jiang, R.I. Gomez-Abal, P. Rinke and M. Scheffler, "Electronic band structure of zirconia and hafnia polymorphs from the GW perspective," *Phys. Rev. B*, vol. 81, 085119, 2010.

[16] J. Heyd, G.E. Scuseria and M. Ernzerhof, "Hybrid functionals based on a screened Coulomb potential," *Journ. Chem. Phys.*, vol. 118, 8207, 2003.

[17] M. Jain, J.R. Chelikowsky and S. Louie, "Quasiparticle Excitations and Charge Transition Levels of Oxygen Vacancies in Hafnia," *Phys. Rev. Lett.* , vol. 107, 216803, 2011.

[18] L.R.C. Fonseca and A.A. Knizhnik, "First-principles calculation of the TiN effective work function on SiO_2 and on HfO_2," *Phys. Rev. B*, vol. 74, 195304, 2006.

[19] P.-Y. Proddhomme, F. Fontaine-Vive, A. Van der Geest, P. Blaise, J. Even , "Ab initio calculation of effective work functions for a TiN/HfO_2/SiO2/Si transistor stack," *Appl. Phys. Lett.*, vol. 99, no. 022101, 2011.

[20] A. V. Gavrikov, A. A. Knizhnik, A. A. Bagatur'yants, B. V. Potapkin, L. R. C. Fonseca and M. W. Stoker, "Oxidation of the Pt/HfO_2 interface: The role of the oxygen chemical potential," *Journ. Apply. Phys.*, vol. 101, 014310, 2007.

[21] N. Capron et al., "Migration of oxygen vacancy in HfO_2 and across the HfO_2/SiO_2

interface: A first-principles investigation," *Appl. Phys. Lett.*, vol. 91, no. 192905, 2007.

[22] R. Öttking, S. Kupke, E. Nadimi, R. Leitsmann, F. Lazarevic, P. Plänitz et al., "Defect generation and activation processes in HfO_2 thin films: Contributions to stress-induced leakage currents," *Phys. Status Solidi A*, pp. 1-7, 2014.

[23] Z.F. Hou, X.G. Gong, Q. Li, "Al-induced reduction of the oxygen diffusion in HfO_2 : an ab initio study," *J. Phys.Cond. Matter*, vol. 20, no. 135206, 2008.

[24] J. Blumberger and K.P. McKenna, "Constrained density functional theory applied to electron tunnelling between defects in MgO," *Phys.Chem. Chem. Phys.*, vol. 15, 2184, 2013.

[25] P. Calka, E. Martinez, V. Delaye et al., "Chemical and structural properties of conducting nanofilaments in TiN/HfO_2-based resistive switching structures," *Nanotech.*, vol. 24, no. 085706, 2013.

[26] M. Setvín, U. Aschauer, P. Scheiber, Y.F. Li, W. Hou, M. Schmid et al., "Reaction of O_2 with Subsurface Oxygen Vacancies on TiO_2 Anastase (101)," *Science*, vol. 341, pp. 988-991, 2013.

[27] B. Traoré, P. Blaise, E. Vianello et al., "Impact of electrode nature on the filament formation and variability in HfO_2 RRAM," *IEEE IRPS*, pp. 5E.2.1 - 5E.2.5, 2014.

[28] K.-H. Xue, P. Blaise, L.R.C. Fonseca, G. Molas, E. Vianello, B. Traoré et al., "Grain-boundary composition and conduction in HfO_2: An ab-initio study," *Appl. Phys. Lett.*, vol. 102, p. 201908, 2013.

[29] C. Cagli, J. Buckley, V. Jousseaume et al., "Experimental and theoretical study of electrode effects in HfO_2 based RRAM," *IEEE IEDM*, pp. 658–661, 2011.

[30] M. Lanza, K. Zhang, M. Porti, M. Nafria, Z.Y. Shen, L.F. Liu et al., "Grain boundaries as preferential sites for resistive switching in the HfO_2 resistive random access memory structures ," *Appl. Phys. Lett.*, vol. 100, pp. 123508 - 123508-4, 2012.

[31] G. Bersuker, D. C. Gilmer, D. Veksler, et al., "Metal oxide resistive memory switching mechanism based on conductive filament properties," *J. Appl. Phys.*, vol. 110, p. 124518, 2011.

[32] R. Degreave, L. Goux, S. Clima, B. Govoreanu, Y.Y. Chen, G.S. Kar et al., "Modeling and tuning the filament properties in RRAM metal oxide stacks for optimized stable cycling," *VLSI-TSA*, pp. 1-2, 2012.

[33] U. Russo, D. Jelmini, C. Cagli, A. L. Lacaita, S. Spiga, C. Wiemer et al. , "Conductive-filament switching analysis and self-accelerated thermal dissolution model for reset in NiO-based RRAM," *IEEE IEDM*, pp. 775 - 778, 2007.

[34] K. P. McKenna, "Optimal stoichiometry for nucleation and growth of conductive filaments in HfOx," *Modelling Simul. Mater. Sci.*, vol. 22, no. 025001, 2014.

[35] X. Cartoixà, R. Rurali and J. Suñé, "Transport properties of oxygen vacancy filaments in metal/crystalline or amorphous HfO_2/metal structures," *Phys. Rev. B*, vol. 86, no. 165445, 2012.

[36] S.-G. Park, B. Magyari-Köpe and Y. Nishi, "Impact of Oxygen Vacancy Ordering on the Formation of a Conductive Filament in TiO_2 for Resistive Switching Memory," *IEEE Elec. Dev. Lett.*, vol. 32, no. 2, pp. 197 - 199, 2011.

[37] K.-H. Xue, P. Blaise, L. R. C. Fonseca, and Y. Nishi, "Prediction of semi-metallic tetragonal Hf_2O_3 and Zr_2O_3 from first-principles," *Phys. Rev. Lett.*, vol. 110, no. 065502, 2013.

[38] B.P. Burton, A. Van de Walle, "First principles phase diagram calculations for the octahedral-interstitial system HfO_x, $0 \leq x \leq 0.5$," *CALPAD*, vol. 37, pp. 151-157, 2012.

[39] B. Puchala, A. Van der Ven, "Thermodynamics of the Zr-O system from first-principles calculations," *Phys.Rev.B.*, vol. 88, no. 094108, 2013.

[40] S. Privitera, G. Bersuker, B. Butcher, A. Kalantarian, S. Lombardo, C. Bongiorno et al., "Microscopy study of the conductive filament in HfO_2 resistive switching memory devices," *Microelec. Eng.*, vol. 109, pp. 75 - 78, 2013.

Conclusions and perspectives

A large number of application opportunities have opened up for semiconductor memory technologies. Among these technologies, non-volatile NAND Flash memory represents a significant portion in the IC market and has benefitted from the traditional scaling of semi-conductor industry allowing its high density integration for mass market production. However, their scaling limits seem to be approached and there seems to be serious problems beyond the 22 nm node. In an effort to go beyond this scaling limitation, alternative memory solutions are proposed of which RRAM stands out as a serious candidate for NAND Flash replacement.

In Chapter II, we studied the impact of scaling on HfO_2 based RRAM from different perspectives. A bottleneck for RRAM scaling is the forming voltage which increases with smaller device areas. There are alternative solutions to reduce this forming voltage increase with scaled devices through high temperature annealing or oxide thickness reduction. High temperature annealing may be easier to implement depending on the maximum thermal budget allowed for the devices at the cost of possible degradation of the devices' R_{off} uniformity. The reduction of the oxide thickness may be a better solution. However too thin an oxide may arise other issues such as the degradation of the devices' thermal stability. Increasing the Ti top electrode thickness not only resulted in the decrease of the forming voltage but also in the increase of R_{off}/R_{on} ratio at the 1mA compliance current used. However, it induced a degraded R_{off} uniformity. By combining the different results, our study pointed out that the optimal stack composition would be HfO_2(5nm)/Ti(10nm) because it had better yield, good switching characteristics, good thermal stability and a good compromise between R_{off}/R_{on} ratio and R_{off} variability.

The 1mA high compliance current enforced during the scaling study and its poor control in 1R structures cause some limitations on how far our conclusions may hold. This is because RRAM performance and reliability are largely influenced by the compliance current and the programming conditions. At 1mA compliance current, R_{on} was very stable during the high temperature stress while R_{off} failed towards R_{on}. On the

other hand, we saw in chapter IV that at 100 µA, R_{on} fails towards R_{off} during the high temperature data retention. Therefore, it would be highly desirable to conduct similar scaling study with low programming currents which are more suitable for low power applications.

In Chapter III, we looked at the impact of the electrode material on RRAM switching characteristics. The performance of HfO_2 based memory cells and their switching modes were largely dependent on the electrode/oxide interface rather than on the properties of the oxide layer alone. Devices showing unipolar switching mode generally had symmetrical electrodes at the bottom and top electrodes and were non-reactive with oxygen like Pt. Bipolar devices generally had non-symmetrical electrodes with one of the electrodes being oxygen reactive like Ti. W/HfO_2/Ti and W/HfO_2/TiN devices presented good switching yield with larger switching window. However they had larger forming voltage compared to TiN/HfO_2/Ti devices. Similarly, Pt/HfO_2/Pt devices also exhibited larger forming voltage compared to TiN/HfO_2/Ti memory cells. Both W/HfO_2/TiN and Pt/HfO_2/Pt devices had larger median R_{off} values with more important variability.

The introduction of Ti as top electrode not only induced the reduction of the forming voltage but also resulted in the improvement of the uniformity of the devices. This was mainly attributed to the reactivity of Ti with oxygen resulting in the formation of subs-stoichiometric TiO_y layer at the Ti/HfO_2 interface. Our study of the thermodynamics of this interface revealed that its optimal stoichiometry and composition after device fabrication would be Ti_2O/Hf_2O_3. For the devices' thermal stability and variability, the combined experimental and calculations results show that the concentration of oxygen interstitial (O_i) ions in the oxide after CF formation was larger for RRAM devices with inert electrodes (like Pt) compared with O reactive electrodes (like Ti) which resulted in degraded device performance. The lower O_i concentration in HfO_2 layer with Ti electrodes resulted in improved thermal stability and device variability.

Hence, the choice of the electrode material is very crucial in the search of optimized switching properties of HfO_2 based memory cells.

The impact of alloying HfO_2 with Al was studied from both experimental and theoretical perspectives in Chapter IV. The study pointed out the impact of the atomic

composition and structure on the resistive switching layer's thermal stability. As far as the switching characteristics were concerned, Al incorporation into HfO_2 did not have significant impact on the switching voltages and resistances except for the forming voltage which was lower for HfO_2 based devices compared with HfAlO. Low resistance state (R_{on}) retention behaviors of both HfO_2 and HfAlO were comprehensively investigated. R_{on} retention failure has shown to be highly temperature activated and Al incorporation into HfO_2 improved the thermal stability of devices. Ab initio based V_o diffusion barriers in HfO_2 and HfAlO were calculated in order to understand the microscopic picture of R_{on} retention. The calculations showed high barriers for HfAlO which were in agreement with the experimental results. The high V_o diffusion barrier for HfAlO was explained by the shorter Al-O bond lengths associated with its higher atomic concentration which hindered V_o diffusion. A further step towards understanding the impact of doping on HfO_2 based RRAM thermal stability was carried out by alloying HfO_2 with Ti within the framework of theoretical calculations. Our calculations showed that V_o diffusion barriers in HfTiO were lower compared with HfO_2 which suggested their poor R_{on} retention behaviours. Our theoretical predictions were validated by experimental data available from the literature which provided more insight on the microscopic understanding of the low resistance state retention. From our study, some hints/guidelines were provided on the alloying/doping material selection rule in order to improve R_{on} thermal stability in RRAM.

In Chapter V, the conductive filament formation in HfO_2 RRAM devices was investigated with some detail. The stability of potential defects that may be at the origin of CF formation was also studied. By combining the different scenarios that could help initiate Hf-O bond breakage process, a CF formation model in HfO_2 based RRAM was proposed which showed that electron injection plays a major role in this process. The model indicated that CF formation in $TiN/HfO_2/Ti$ RRAM starts from the reactive Ti/oxide interface by forming a virtual anode. This virtual anode grows from TE to BE under the applied field and ends up creating a conductive path. When inert electrodes were used as in $Pt/HfO_2/Pt$, we saw that CF formation probably starts from the BE by forming a virtual cathode. The RESET operation was attributed to the recombination of O_i^{2-} and V_o^{2+} at the point of filament where it was the thinnest.

The composition of the CF was investigated under thermodynamic equilibrium. The results showed that the CF is probably an Hf sub oxide that could potentially be

Hf_4O-Hf_3O. By assuming an Hf_3O as the filament and by injecting a constant amount of oxygen into it as an attempt to model RESET, a ruptured filament that would be HfO_x ($1/2 \leq x \leq 1$) surrounded HfO_2 or HfO_2 with continuous oxidation were obtained. The low energy differences between the sub oxides indicated that the ruptured CF region is probably non-homogenous and made up of a mixture of different sub oxides. We believe that the non-homogenous nature of the ruptured CF region could explain the origin of intrinsic variability in RRAM.

As mentioned above, the theoretical study also highlighted the crucial role of the electrode material choice especially the top electrode in RRAM operation. The results showed that depending on the reactivity of TE (Ti vs. Pt), not only the forming voltage changes but also the mechanisms of CF formation and its stability also changes. Moreover, the energetics of defects, their charge states and diffusion barriers also change depending on the electrode material. Hence, a way of optimization of RRAM would be to continue working on the TE material through: its deposition condition by tuning its oxygen content (degree of oxidation, eg. TiO_x, $x \leq 1$), bi-layer electrodes (eg. Al/Ti), doping or alloying (TiSi, TiSe etc.).

Throughout this study, we have tried to bring some answers to the challenges that need to be faced for RRAM to be a solid technology of choice for NAND Flash replacement and other non-volatile memory applications. There still remain many issues that need to be addressed such as variability of R_{off} and more comprehensive physical understanding.

Because of the intrinsic nature of R_{off} variability, it is likely that the problem will be resolved through engineering the HfO_2 layer in order to change the oxide layer properties such that the ruptured CF region will essentially discriminate a particular Hf-suboxide instead of combination of sub-oxides. Screening of doping/alloying materials with HfO_2 will need to be conducted via ab initio calculations in order to understand their properties and the changes they induce in the HfO_2 layer. Also, defect diffusion in these alloyed materials will also help understand their thermal stability. This work has already started this process via Al and Ti incorporation. One may project this study with Zr which is in the same column as Hf and other materials from columns 3 and 4 of the periodic table. The key point would be which material when added to HfO_2 will tend to stabilize a particular suboxide of HfO_x during RESET for a more uniform ruptured CF region.

Nevertheless, our results in Chapter II tend to indicate that Low temperature deposited HfO_2 (essentially amorphous HfO_2) bring some uniformity in R_{off} distribution. However, this will need to be validated through the fabrication of similar devices integrated in 1T1R structure with better control of the compliance current.

We hope that our study has set up the main ingredients towards more understanding of RRAM operation. However, problems such as the diffusion of oxygen in Hf-suboxides will also need to be fully studied from two directions: O diffusion in Hf-suboxides alone, O diffusion in Hf-suboxides surrounded by HfO_2. The latter will be a huge step towards modeling an actual device at atomistic level especially if the study could also be conducted under an applied field.

All of the calculations performed in this work were carried out at zero fields while actual RRAM devices operate under voltage application. Our developed calculations in Chapter V which attempt to include voltage in the formation enthalpy equations are interesting but not enough because of the limitations in trying to describe non-equilibrium systems out of results that describe equilibrium systems. Therefore, the dynamics of defects as well as their diffusion under an applied field will also help grasp the microscopic picture of resistive switching.

Finally, electron transport through defects is difficult to describe because of quantum phenomena such as electron-defects coupling, electron-phonon coupling and so on which are beyond the scope of our DFT calculations. Our results gave indications about processes that may be energetically favorable and some of the material optimization that could be explored. However, a joint cooperation/collaboration between individuals dealing with ab initio calculations, experiments and device physics modeling would be necessary to have more comprehensive view of RRAM devices. This will help create the bridge between atomistic information which are microscopic in nature and experimental data which are macroscopic such that a fully consistent picture of RRAM will be developed.

Bibliography of the author

Conferences

B. Traoré, P. Blaise, E. Vianello, H. Grampeix, A. Bonnevialle, E. Jalaguier, G. Molas, S. Jeannot, L. Perniola, B. De Salvo, and Y. Nishi "Microscopic understanding of the low resistance retention in HfO_2 and HfAlO based RRAM", *IEEE IEDM*, pp.21.5.1-21.5.4, 2014.

B. Traoré, P. Blaise, E. Vianello, E. Jalaguier, G. Molas, J.F. Nodin, L. Perniola, B. De Salvo, and Y. Nishi "Impact of electrode nature on the filament formation and variability in HfO_2 RRAM", *IEEE IRPS*, pp. 5E.2.1 - 5E.2.5, 2014.

B. Traoré, K.-H. Xue, E. Vianello, G. Molas, A. Padovani, O. Pirrotta,L. Larcher, P. Blaise, L. Fonseca, B. De Salvo, and Y. Nishi, "Investigation of the role of electrodes on the retention performance of HfO_x based RRAM cells by experiments, atomistic simulations and device physical modeling", *IEEE IRPS* , pp.5E.2.1-5E.2.6, 2013

B. Traoré, E. Vianello, G. Molas, M. Gely, J. F. Nodin, E. Jalaguier, P. Blaise, B. De Salvo, K.-H. Xue, L. R. C. Fonseca, and Y. Nishi, "On the forming-free operation of HfO_x based RRAM devices: Experiments and ab initio calculations", *IEEE ESSDERC*, pp. 170–173, 2013.

E. Vianello, O. Thomas, M. Harrand, S. Onkaraiah, T. Cabout, **B. Traoré**, T. Diokh, H. Oucheikh, L. Perniola,G. Molas, P. Blaise, J. F. Nodin, E. Jalaguier, B. De Salvo"Back-end 3D integration of HfO_2 - based RRAMs for low-voltage advanced IC digital design", *ICICDT*, pp. 235 – 238, 2013

J.F. Nodin, E. Vianello, L. Perniola, T. Cabout**, B. Traoré**, T. Diokh, H. Grampeix, G. Molas, E. Jalaguier, and B. De Salvo, "HfO_2-based RRAMS for integration on advanced CMOS technology nodes", *IEEE Faible Tension Faible Consommation (FTFC)*,p.1, 2013.

Journals

K.-H. Xue, **B. Traoré**, P. Blaise, L. R. C. Fonseca, E. Vianello, G. Molas, B. De Salvo, G. Ghibaudo, B. Magyari-Köpe and Y. Nish, "A combined ab initio and experimental study on the nature of conductive filaments in Pt/HfO_2/Pt resistive random access memory", *IEEE **Trans. Electron Dev**, pp. 1394 – 1402, 2014.*

E. Vianello, P. Blaise, **B. Traoré**, K.-H. Xue, "Investigation of Frenkel-Pair Formation in HfO_2 and Its Influence on Oxram Memory Reliability", *ECS Trans*., vol. 64 (8), pp.141-146, 2014

K.-H. Xue, P. Blaise, L.R.C. Fonseca, G. Molas, E. Vianello, **B. Traoré**, B. De Salvo, G. Ghibaudo and Y. Nishi, "Grain-boundary composition and conduction in HfO_2: An ab-initio study," *Appl. Phys. Lett*., vol. 102, p. 201908, 2013

Poster/Mini-conference:

B. Traoré, E. Vianello and P. Blaise, "HfO_2 based RRAM: Insight from experiment and ab-initio calculations", Oral presentation at Congrès National d'Analyse Numérique (*CANUM*) held at Carry-le-Rouet in April 2014.

B. Traoré and K.-H. Xue, "Investigating the role of electrodes on the thermal stability of HfO_x based RRAM devices", poster presented at the workshop on Density functional theory and beyond: Computational materials science for real materials held at the International Center for Theoretical Physics (*ICTP*) at Trieste in August 2013.

Investigation of HfO_2-based Resistive RAM cells by electrical characterization and atomistic simulations

Among non-volatile memory technologies, NAND Flash represents a significant portion in the IC market and has benefitted from the traditional scaling of semiconductor industry allowing its high density integration. However, this scaling seems to be problematic beyond the 22 nm node. In an effort to go beyond this scaling limitation, alternative memory solutions are proposed among which Resistive RAM (RRAM) stands out as a serious candidate for NAND Flash replacement. Hence, in this PhD thesis we try to respond to many open questions about RRAM devices based on hafnium oxide (HfO_2), in particular, by addressing the lack of detailed physical comprehension about their operation and reliability. The impact of scaling, the role of electrodes, the process of defects formation and diffusion are investigated. The impact of alloying/doping HfO_2 with other materials for improved RRAM performance is also studied. Finally, our study attempts to provide some answers on the conductive filament formation, its stability and possible composition.

Etude de cellules mémoires résistives RRAM à base de HfO_2 par caractérisation électrique et simulations atomistiques

La mémoire NAND Flash représente une part importante dans le marché des circuits intégrés et a bénéficié de la traditionnelle miniaturisation de l'industrie des sémiconducteurs lui permettant un niveau d'intégration élevé. Toutefois, cette miniaturisation semble poser des sérieux problèmes au-delà du nœud 22 nm. Dans un souci de dépasser cette limite, des solutions mémoires alternatives sont proposées parmi lesquelles la mémoire résistive (RRAM) se pose comme un sérieux candidat pour le remplacement de NAND Flash. Ainsi, dans cette thèse nous essayons de répondre à des nombreuses questions ouvertes sur les dispositifs RRAM à base d'oxyde d'hafnium (HfO_2) en particulier en adressant le manque de compréhension physique détaillée sur leur fonctionnement et leur fiabilité. L'impact de la réduction de taille des RRAM, le rôle des électrodes et le processus de formation et de diffusion des défauts sont étudiés. L'impact de l'alliage/dopage de HfO_2 avec d'autres matériaux pour l'optimisation des RRAM est aussi abordé. Enfin, notre étude tente de donner quelques réponses sur la formation du filament conducteur, sa stabilité et sa possible composition.